

**COMPARISON OF 2D AND 3D MODELS IN APPLICATION TO LONG WAVE
MOTION AND ITS INTERACTION WITH A VERTICAL WALL**

A THESIS SUBMITTED TO
THE GRADUATE SCHOOL OF NATURAL AND APPLIED SCIENCES
OF
MIDDLE EAST TECHNICAL UNIVERSITY

BY

GİZEM EZGİ ÇINAR

IN PARTIAL FULFILLMENT OF THE REQUIREMENTS
FOR
THE DEGREE OF MASTER OF SCIENCE
IN
CIVIL ENGINEERING

JULY 2018

Approval of the thesis:

**COMPARISON OF 2D AND 3D MODELS IN APPLICATION TO LONG
WAVE MOTION AND ITS INTERACTION WITH A VERTICAL WALL**

submitted by **GİZEM EZGİ ÇINAR** in partial fulfillment of the requirements for the degree of **Master of Science in Civil Engineering Department, Middle East Technical University** by,

Prof. Dr. Halil Kalıpçılar
Dean, Graduate School of **Natural and Applied Sciences**

Prof. Dr. İsmail Özgür Yaman
Head of Department, **Civil Engineering**

Prof. Dr. Ahmet Cevdet Yalçınar
Supervisor, **Civil Engineering Department, METU**

Assist. Prof. Dr. Cüneyt Baykal
Co-Supervisor, **Civil Engineering Department, METU**

Examining Committee Members:

Assist. Prof. Dr. Gülizar Özyurt Tarakçıoğlu
Civil Engineering Dept., METU

Prof. Dr. Ahmet Cevdet Yalçınar
Civil Engineering Dept., METU

Assist. Prof. Dr. Cüneyt Baykal
Civil Engineering Dept., METU

Assoc. Prof. Dr. Utku Kanoğlu
Aerospace Engineering Dept., METU

Assist. Prof. Dr. Aslı Numanoğlu Genç
Civil Engineering Dept., Atılım University

Date: 05.07.2018

I hereby declare that all information in this document has been obtained and presented in accordance with academic rules and ethical conduct. I also declare that, as required by these rules and conduct, I have fully cited and referenced all material and results that are not original to this work.

Name, Last Name: Gizem Ezgi Çınar

Signature : 

ABSTRACT

COMPARISON OF 2D AND 3D MODELS IN APPLICATION TO LONG WAVE MOTION AND ITS INTERACTION WITH A VERTICAL WALL

ÇINAR, Gizem Ezgi

M.S., Department of Civil Engineering

Supervisor: Prof. Dr. Ahmet Cevdet Yalçıner

Co-Supervisor: Asst. Prof. Dr. Cüneyt Baykal

July 2018, 167 pages

Tsunami-structure interaction is an important issue in the design of coastal structures. Numerical modeling of the tsunami-structure interaction has a vital importance in this manner to understand the behavior of the long wave motion around structures in a more detailed way.

In this study, physical model experiments on solitary wave-vertical wall interaction performed by Arikawa (2015) are numerically studied using two-dimensional depth-averaged non-linear shallow water equations model, NAMI DANCE and three-dimensional Navier-Stokes models, IHFOAM solver of OpenFOAM and CADMAS-SURF/3D. Using Navier-Stokes models, turbulence modeling is addressed with $k-\varepsilon$ and $k-\omega$ -SST turbulence models in comparison with laminar flow assumption to investigate the effect of turbulence models.

The results of the numerical models are compared with the experimental data considering the time series of water surface elevations and water particle velocities.

Keywords: Tsunami, long wave, vertical wall, turbulence, numerical modeling

ÖZ

UZUN DALGA HAREKETİ VE DİKEY DUVAR İLE ETKİLEŞİMİNE UYGULANAN 2B VE 3B MODELLERİN KARŞILAŞTIRILMASI

ÇINAR, Gizem Ezgi
Yüksek Lisans, İnşaat Mühendisliği Bölümü
Tez Yöneticisi: Prof. Dr. Ahmet Cevdet Yalçın
Ortak Tez Yöneticisi: Dr. Öğr. Üyesi Cüneyt Baykal

Temmuz 2018, 167 sayfa

Tsunami-yapı etkileşimi kıyı yapılarının tasarım sürecinde önemli bir yere sahiptir. Bu bağlamda tsunami-yapı etkileşiminin sayısal modellenmesi, uzun dalga hareketinin yapı çevresindeki davranışının daha detaylı bir şekilde anlaşılmasına olanak sağlar.

Bu çalışmada, tekil dalga-dikey duvar etkileşimi üzerine Arikawa (2015) tarafından yapılan fiziksel model deneylerinin, iki boyutlu derinliğe göre ortalaması alınmış doğrusal olmayan sığ su denklemlerini kullanan, NAMI DANCE ve üç boyutlu Navier-Stokes modelleri olan OpenFOAM ve CADMAS-SURF/3D kullanılarak sayısal modellemesi yapılmıştır. Navier-Stokes modellerini kullanarak, türbülans modellerinin etkisini araştırmak amacıyla laminer akış varsayımlına kıyasla $k-\varepsilon$ ve $k-\omega$ -SST türbülans modelleri de türbülans modellemesi içerisinde ele alınmıştır.

Sayısal modellerden elde edilen sonuçlar su seviyesi değişimi zaman serisi ve su parçacık hızları dikkate alınarak deneyel verilerle karşılaştırılmıştır.

Anahtar Kelimeler: Tsunami, uzun dalga, dikey duvar, türbülans, sayısal modelleme

To my beloved family...

ACKNOWLEDGEMENTS

I would like to express my deepest gratitude to Prof. Dr. Ahmet Cevdet Yalçiner for supervising this thesis study and giving me the chance to become a part of this amazing laboratory. He always believed in me for my research, supported me when I am in need and guided me with his broad knowledge and experience. It is always an honor to be his student and assistant.

I would like to extend my sincere thanks to Assist. Prof. Dr. Cüneyt Baykal for co-supervising this study. I learned so many things from him through my graduate years. He has always supported and encouraged me to think and do one step further.

I would like to express my special thanks to Prof. Dr. Ayşen Ergin who has a great influence on me with her kindness and optimism. She always encouraged me and believed in me for my studies. She was the reason for me to choose Coastal Engineering and I find myself very lucky to be her student and assistant.

I would like to express my gratitude to Dr. Işıkhan Güler and Assist. Prof. Dr. Gülizar Özyurt Tarakçıoğlu for sharing their knowledge and experience with me through my M.Sc. period and their valuable contributions to my coastal engineering education. I also thank the examining committee members Assoc. Prof Dr. Utku Kânoğlu and Assist. Prof. Dr. Aslı Numanoğlu Genç for their valuable comments and suggestions to improve my thesis.

I would like to extend my sincere thanks to Prof. Dr. Taro Arikawa for sharing his experimental data and the numerical model. His knowledge and guidance also made it easier to conduct my research in Japan.

One of the biggest thanks belongs to Hasan Gökhan Güler who was with me in every step of this thesis study. He always supported me in this journey and help me without hesitation whenever I need it. He is one of the kindest, most intelligent and humble people I've ever met. He will always be a dear friend, colleague, and mentor to me.

I would like to thank the Coastal Engineering Lab Family; Emrecaan Işık, Bora Yalçınar, Nilay Doğulu, Arif Kayışlı, Yusuf Korkut and Nuray Çimen for their support and sincerity. It is always a pleasure to work with them.

I would like to express my sincere thanks to my dearest friends; Cansu Demir, Ali Can Doğan, Elif Bal, Ulaş Can and Miray Mazlumoğlu for the memories we shared and their support in these times even most of them are away from Ankara. Their presence in my life means a lot. I also would like to thank my friends Yağmur Topçuoğlugil, Gökberk Işık and Burak Okan Özmen for their friendship and encouragements from the beginning of our undergraduate years till today. Last but not least, I would like to thank my oldest friends Ali Karakaya and Çağatay Taşçı for their gayness and great support! I know they will be always right beside me.

Finally, my biggest gratitude is for my beloved family. I would like to thank my mother Sona Çınar, my father Metin Çınar and my sister Berfin Su Çınar for their endless love and support. There are not enough words to express my gratefulness. I owe them everything I achieved.

TABLE OF CONTENTS

ABSTRACT	v
ÖZ.....	vi
ACKNOWLEDGEMENTS	viii
TABLE OF CONTENTS	x
LIST OF TABLES	xii
LIST OF FIGURES.....	xiii
CHAPTERS	
1. INTRODUCTION.....	1
2. LITERATURE SURVEY	3
2.1. Overview of the Physical Model Experiments	4
2.1.1. Overview of Solitary Wave Experiments	4
2.1.2. Overview of Tsunami Overflow Experiments	5
2.1.3. Overview of Tsunami Bore Experiments	7
2.1.5. Reference Experiments: Vertical Wall-Solitary Wave Interactions (Arikawa, 2015)	8
2.2. Overview of Numerical Modeling Studies	13
2.2.1. Overview of NSWE Applications of Tsunami Structure Interaction	13
2.2.2. Overview of the Applications of 3D CFD Solvers to Tsunami-Structure Interactions.....	14
2.2.3. Overview of Application of Turbulence Models	16
3. NAMI DANCE	21
3.1. Numerical Scheme of NAMI DANCE.....	22
3.2. Numerical Setup of the Experiments for NAMI DANCE.....	24
3.2.1. Case 1	24
3.2.2. Case 2.....	25

3.2.3. Case 3.....	26
3.3. Results and Discussions of NAMI DANCE Simulations	27
4. IHFOAM SOLVER OF OPENFOAM	47
4.1. Numerical Scheme of IHFOAM	48
4.2. Turbulence Models.....	49
4.2.1. k- ϵ Turbulence Model.....	49
4.2.2. k- ω -SST Turbulence Model.....	51
4.3. Numerical Setup of the Experiments for IHFOAM	52
4.3.1. Case 1.....	53
4.3.2. Case 2.....	54
4.3.3. Case 3.....	54
4.4. Results and Discussions of the Simulations of IHFOAM	54
5. CADMAS-SURF/3D	79
5.1. Numerical Scheme of the CADMAS-SURF/3D	79
5.2. Numerical Setup of the Experiments for CADMAS-SURF/3D	83
5.2.1. Case 1.....	84
5.2.2. Case 2.....	85
5.2.3. Case 3.....	85
5.3. Results and Discussions on CADMAS-SURF/3D Simulations.....	86
6. COMPARISON OF THE NUMERICAL MODELS	109
6.1. Estimation of Splash Height on the Vertical Wall	110
6.2. Comparison for Laminar Approach	113
6.3. Comparison for k- ϵ Turbulence Model	131
6.4. Comparison for k- ω -SST Turbulence Model	149
7. CONCLUSION.....	153
REFERENCES.....	157

LIST OF TABLES

TABLES

Table 6.1. Numerical Simulations Performed for Each Three Physical Model Experiments	109
Table 6.2. Peak Surface Water Elevation (in cm) of Each Wave Gauge for All Cases Under Laminar Approach	115
Table 6.3. Percent Error of Each Wave Gauge for Laminar Approach in Case 1 ...	120
Table 6.4. Percent Error of Each Wave Gauge for Laminar Approach in Case 2 ...	121
Table 6.5. Percent Error of Each Wave Gauge for Laminar Approach in Case 3 ...	131
Table 6.6. Peak Surface Water Elevation (in cm) of Each Wave Gauge for All Cases Under k- ϵ Approach.....	133
Table 6.7. Percent Error of Each Wave Gauge for k- ϵ Approach in Case 1	138
Table 6.8. Percent Error of Each Wave Gauge for k- ϵ Approach in Case 2	139
Table 6.9. Percent Error of Each Wave Gauge for k- ϵ Approach in Case 3	149
Table 6.10. Peak Surface Water Elevation (in cm) of Each Wave Gauge for All Cases Under k- ω -SST Approach.....	150
Table 6.11. Percent Error of Each Wave Gauge for k- ω -SST Approach in All Cases	151

LIST OF FIGURES

FIGURES

Figure 2.1. (1) First position of the vertical wall, (2) Second position of the vertical wall, (3) Third position of the vertical wall (Arikawa, 2015).....	9
Figure 2.2. Plan view and the cross-section of the experimental setup for horizontal case (Arikawa, 2015)	10
Figure 2.3. Snapshots from Experiment Video of Case 1 (Arikawa, 2015)	11
Figure 2.4. Snapshots from Experiment Video of Case 2 (Arikawa, 2015)	12
Figure 2.5. Snapshots from Experiment Video of Case 3 (Arikawa, 2015)	12
Figure 3.1. Orientation of the coordinate system and top view computational domain of the Case 1 for NAMI DANCE model	24
Figure 3.2. Three-dimensional representation of the computational domain of Case 1 in NAMI DANCE	25
Figure 3.3. Orientation of the coordinate system and top view computational domain of the Case 2 for NAMI DANCE model	25
Figure 3.4. Three-dimensional representation of the computational domain of Case 2 in NAMI DANCE	26
Figure 3.5. Orientation of the coordinate system and top view computational domain of the Case 3 for NAMI DANCE model	26
Figure 3.6. Three-dimensional representation of the computational domain of Case 3 in NAMI DANCE	27
Figure 3.7. Comparison of Water Surface Elevations of NAMI DANCE with Experimental Measurements for Case 1	29
Figure 3.8. Comparison of Water Surface Elevations of NAMI DANCE with Experimental Measurements at WG8 for Case 1.....	30
Figure 3.9. Comparison of Particle Velocities in x-direction, U of NAMI DANCE with Experimental Measurements for Case 1	31

Figure 3.10. Comparison of Particle Velocities in x-direction, U of NAMI DANCE with Experimental Measurements at V4 for Case 1	32
Figure 3.11. Snapshots from Simulation of Case 1 with NAMI DANCE	33
Figure 3.12. Comparison of Water Surface Elevations of NAMI DANCE with Experimental Measurements for Case 2	35
Figure 3.13. Comparison of Water Surface Elevations of NAMI DANCE with Experimental Measurements at WG9 for Case 2.....	36
Figure 3.14. Comparison of Particle Velocities in x-direction, U of NAMI DANCE with Experimental Measurements for Case 2	37
Figure 3.15. Comparison of Particle Velocities in x-direction, U of NAMI DANCE with Experimental Measurements at V5 for Case 2	38
Figure 3.16. Snapshots from Simulation of Case 2 with NAMI DANCE	39
Figure 3.17. Comparison of Water Surface Elevations of NAMI DANCE with Experimental Measurements for Case 3	41
Figure 3.18. Comparison of Water Surface Elevations of NAMI DANCE with Experimental Measurements at WG10 for Case 3.....	42
Figure 3.19. Comparison of Particle Velocities in x-direction, U of NAMI DANCE with Experimental Measurements for Case 3	43
Figure 3.20. Comparison of Particle Velocities in x-direction, U of NAMI DANCE with Experimental Measurements at V6 for Case 3	44
Figure 3.21. Snapshots from Simulation of Case 3 with NAMI DANCE	45
Figure 4.1. Orientation of the coordinate system and two-dimensional computational domain of the Case 1 for IHFOAM model	53
Figure 4.2. Orientation of the coordinate system and two-dimensional computational domain of the Case 2 for IHFOAM model	54
Figure 4.3. Orientation of the coordinate system and two-dimensional computational domain of the Case 3 for IHFOAM model	54
Figure 4.4. Comparison of Water Surface Elevations of IHFOAM with Experimental Measurements for Case 1	56

Figure 4.5. Comparison of Water Surface Elevations of IHFOAM with Experimental Measurements at WG8 for Case 1	57
Figure 4.6. Snapshots from (a) the video of the experiment (Arikawa, 2015) and (b) simulation video of the k- ω -SST turbulence model for Case 1	58
Figure 4.7. Comparison of Particle Velocities in x-direction, U of IHFOAM with Experimental Measurements for Case 1	59
Figure 4.8. Comparison of Particle Velocities in x-direction, U of IHFOAM with Experimental Measurements at V4 for Case 1	60
Figure 4.9. Snapshots from Simulation of Case 1 with laminar model	61
Figure 4.10. Snapshots from Simulation of Case 1 with k- ϵ model.....	61
Figure 4.11. Snapshots from Simulation of Case 1 with k- ω -SST model	62
Figure 4.12. Comparison of Water Surface Elevations of IHFOAM with Experimental Measurements for Case 2.....	64
Figure 4.13. Comparison of Water Surface Elevations of IHFOAM with Experimental Measurements at WG9 for Case 2	65
Figure 4.14. Snapshots from (a) the video of the experiment (Arikawa, 2015) and (b) simulation video of the k- ω -SST turbulence model for Case 2	66
Figure 4.15. Comparison of Particle Velocities in x-direction, U of IHFOAM with Experimental Measurements for Case 2	67
Figure 4.16. Comparison of Particle Velocities in x-direction, U of IHFOAM with Experimental Measurements at V5 for Case 2	68
Figure 4.17. Snapshots from Simulation of Case 2 with laminar model	69
Figure 4.18. Snapshots from Simulation of Case 2 with k- ϵ model.....	70
Figure 4.19. Snapshots from Simulation of Case 2 with k- ω -SST model	70
Figure 4.20. Comparison of Water Surface Elevations of IHFOAM with Experimental Measurements for Case 3.....	72
Figure 4.21. Comparison of Water Surface Elevations of IHFOAM with Experimental Measurements at WG10 for Case 3	73
Figure 4.22. Snapshots from (a) the video of the experiment (Arikawa, 2015) and (b) simulation video of the k- ω -SST turbulence model for Case 3	74

Figure 4.23. Comparison of Particle Velocities in x-direction, U of IHFOAM with Experimental Measurements for Case 3	75
Figure 4.24. Comparison of Particle Velocities in x-direction, U of IHFOAM with Experimental Measurements at V6 for Case 3	76
Figure 4.25. Snapshots from Simulation of Case 3 with laminar model	77
Figure 4.26. Snapshots from Simulation of Case 3 with k- ϵ model.....	77
Figure 4.27. Snapshots from Simulation of Case 3 with k- ω -SST model	78
Figure 5.1. Orientation of the coordinate system and two-dimensional computational domain of the Case 1 for CADMAS-SURF/3D model	84
Figure 5.2. Orientation of the coordinate system and two-dimensional computational domain of the Case 2 for CADMAS-SURF/3D model	85
Figure 5.3. Orientation of the coordinate system and two-dimensional computational domain of the Case 3 for CADMAS-SURF/3D model	85
Figure 5.4. Comparison of Water Surface Elevations of CADMAS-SURF/3D with Experimental Measurements for Case 1	88
Figure 5.5. Comparison of Water Surface Elevations of CADMAS-SURF/3D with Experimental Measurements at WG8 for Case 1.....	89
Figure 5.6. Comparison of Water Particle Velocities in x-direction, U of CADMAS-SURF/3D with Experimental Measurements for Case1	90
Figure 5.7. Comparison of Water Particle Velocities in x-direction, U of CADMAS-SURF/3D with Experimental Measurements at V4 for Case 1	91
Figure 5.8. Snapshots from Simulation of Case 1 with laminar model	92
Figure 5.9. Snapshots from Simulation of Case 1 with k- ϵ turbulence model.....	92
Figure 5.10. Comparison of Water Surface Elevations of CADMAS-SURF/3D with Experimental Measurements for Case 2	95
Figure 5.11. Comparison of Water Surface Elevations of CADMAS-SURF/3D with Experimental Measurements at WG9 for Case 2.....	96
Figure 5.12. Comparison of Water Particle Velocities in x-direction, U of CADMAS-SURF/3D with Experimental Measurements for Case 2	97

Figure 5.13. Comparison of Water Particle Velocities in x-direction, U of CADMAS-SURF/3D with Experimental Measurements at V5 for Case 2	98
Figure 5.14. Snapshots from Simulation of Case 2 with laminar model	99
Figure 5.15. Snapshots from Simulation of Case 2 with k- ϵ turbulence model.....	99
Figure 5.16. Comparison of Water Surface Elevations of CADMAS-SURF/3D with Experimental Measurements for Case 3	102
Figure 5.17. Comparison of Water Surface Elevations of CADMAS-SURF/3D with Experimental Measurements at WG10 for Case 3.....	103
Figure 5.18. Comparison of Water Particle Velocities in x-direction, U of CADMAS-SURF/3D with Experimental Measurements for Case 2	104
Figure 5.19. Comparison of Water Particle Velocities in x-direction, U of CADMAS-SURF/3D with Experimental Measurements at V6 for Case 3	105
Figure 5.20. Snapshots from Simulation of Case 3 with laminar model	106
Figure 5.21. Snapshots from Simulation of Case 3 with k- ϵ turbulence model.....	106
Figure 6.1. Snapshots from the experimental video of Case 1 (a) before the incident of impact of the solitary wave and (b) at the incident of impact of the solitary wave (Arikawa, 2015)	111
Figure 6.2. Snapshots from the experimental video of Case 2 (a) before the incident of impact of the solitary wave and (b) at the incident of impact of the solitary wave (Arikawa, 2015)	111
Figure 6.3. Snapshots from the experimental video of Case 3 (a) before the incident of impact of the solitary wave and (b) at the incident of impact of the solitary wave (Arikawa, 2015)	112
Figure 6.4 Comparison of Water Surface Elevations of All Models with Experimental Measurements for Case 1 with Laminar Approach	116
Figure 6.5 Comparison of Water Surface Elevations of All Models with Experimental Measurements at WG8 for Case 1 with Laminar Approach.....	117
Figure 6.6 Comparison of Particle Velocities in x-direction, U of All Model with Experimental Measurements for Case 1 with Laminar Approach.....	118

Figure 6.7 Comparison of Particle Velocities in x-direction, U of All Models with Experimental Measurements at V4 for Case 1 with Laminar Approach	119
Figure 6.8 Comparison of Water Surface Elevations of All Models with Experimental Measurements for Case 2 with Laminar Approach	122
Figure 6.9 Comparison of Water Surface Elevations of All Models with Experimental Measurements at WG9 for Case 2 with Laminar Approach	123
Figure 6.10 Comparison of Particle Velocities in x-direction, U of All Model with Experimental Measurements for Case 2 with Laminar Approach.....	124
Figure 6.11 Comparison of Particle Velocities in x-direction, U of All Models with Experimental Measurements at V5 for Case 2 with Laminar Approach	125
Figure 6.12 Comparison of Water Surface Elevations of All Models with Experimental Measurements for Case 3 with Laminar Approach	127
Figure 6.13 Comparison of Water Surface Elevations of All Models with Experimental Measurements at WG10 for Case 3 with Laminar Approach.....	128
Figure 6.14 Comparison of Particle Velocities in x-direction, U of All Model with Experimental Measurements for Case 3 with Laminar Approach.....	129
Figure 6.15 Comparison of Particle Velocities in x-direction, U of All Models with Experimental Measurements at V6 for Case 3 with Laminar Approach	130
Figure 6.16 Comparison of Water Surface Elevations of IHFOAM and CADMAS-SURF/3D with Experimental Measurements for Case 1 with k- ϵ Turbulence Model	134
Figure 6.17 Comparison of Water Surface Elevations of IHFOAM and CADMAS-SURF/3D with Experimental Measurements at WG8 for Case 1 with k- ϵ Turbulence Model.....	136
Figure 6.18 Comparison of Particle Velocities in x-direction, U of IHFOAM and CADMAS-SURF/3D with Experimental Measurements for Case 1 with k- ϵ Turbulence Model.....	136
Figure 6.19 Comparison of Particle Velocities in x-direction, U of IHFOAM and CADMAS-SURF/3D with Experimental Measurements at V4 for Case 1 with k- ϵ Turbulence Model	137

Figure 6.20 Comparison of Water Surface Elevations of IHFOAM and CADMAS-SURF/3D with Experimental Measurements for Case 2 with k- ϵ Turbulence Model.....	140
Figure 6.21 Comparison of Water Surface Elevations of IHFOAM and CADMAS-SURF/3D with Experimental Measurements at WG9 for Case 2 with k- ϵ Turbulence Model.....	141
Figure 6.22 Comparison of Particle Velocities in x-direction, U of IHFOAM and CADMAS-SURF/3D with Experimental Measurements for Case 2 with k- ϵ Turbulence Model.....	142
Figure 6.23 Comparison of Particle Velocities in x-direction, U of IHFOAM and CADMAS-SURF/3D with Experimental Measurements at V5 for Case 2 with k- ϵ Turbulence Model	143
Figure 6.24 Comparison of Water Surface Elevations of IHFOAM and CADMAS-SURF/3D with Experimental Measurements for Case 3 with k- ϵ Turbulence Model.....	145
Figure 6.25 Comparison of Water Surface Elevations of IHFOAM and CADMAS-SURF/3D with Experimental Measurements at WG10 for Case 3 with k- ϵ Turbulence Model.....	146
Figure 6.26 Comparison of Particle Velocities in x-direction, U of IHFOAM and CADMAS-SURF/3D with Experimental Measurements for Case 3 with k- ϵ Turbulence Model.....	147
Figure 6.27 Comparison of Particle Velocities in x-direction, U of IHFOAM and CADMAS-SURF/3D with Experimental Measurements at V6 for Case 3 with k- ϵ Turbulence Model	148

CHAPTER 1

INTRODUCTION

Tsunami is a Japanese word combination of the two characters *tsu-* means harbor and *-nami* means wave. Tsunamis are series of long waves generated by the large displacements of a water body caused by different factors such as earthquakes, landslides, volcanic eruptions, atmospheric pressure changes etc.

Throughout the history, tsunamis have left a mark in the common memory of mankind through the destruction they have caused. In recent history, the 2004 Indian Ocean tsunami and the 2011 Great East Japan Earthquake (GEJE) tsunami can be considered as one of the most important examples of this destruction. The 2011 GEJE tsunami could not be prevented by the coastal defense structures and it destructed many bridges, breakwaters, and other coastal infrastructure in an unexpected manner (Suppasri et al., 2016). This event highlighted the fact that more detailed studies (both physical and numerical) are required to understand the tsunami behavior around structures and to determine the structure failure mechanisms.

In numerical modeling of tsunamis, Non-linear Shallow Water Equations (NSWE) are often preferred to generally investigate the transformation, propagation, inundation and partly tsunami-structure interaction. On the other hand, in general, three-dimensional computational fluid dynamics (CFD) models can perform more detailed and accurate analyses for tsunami-structure interaction and have a key role in understanding the physical processes in detailed.

Models solving NSWE and three-dimensional full Navier-Stokes equations should be compared in order to understand the performances of these models in modeling

tsunami-structure interaction. Therefore, in this study, physical model experiments on solitary wave-vertical wall interaction are numerically studied using three different numerical models named as NAMI DANCE, IHFOAM solver of OpenFOAM® and CADMAS-SURF/3D to compare the results and understand the performances of these models under such challenging cases.

In Chapter 2, a brief literature survey on both physical and numerical modeling studies focusing on tsunami-structure interaction is presented. The reference experiments selected to be modeled in this study are explained in detail. This chapter also includes a brief literature overview of some turbulence models used in this study.

NAMI DANCE model is introduced and the numerical background of the model is explained in Chapter 3. Later the numerical setup for the three experimental cases are introduced and the results of the simulations are presented providing graphical comparisons with the experimental data considering the time series of water surface elevations and water particle velocities.

Chapter 4 includes the brief information about IHFOAM solver of OpenFOAM® and explanation of numerical schemes used in the model. Then, the numerical setup of each experiment is introduced. This chapter is ended with the comparisons of the numerical simulation results with the use of several turbulence models with physical model experiment data focusing on the water surface elevations and particle velocities.

In Chapter 5, CADMAS-SURF/3D model is introduced and numerical background of the model is explained. After providing numerical setup for the experimental cases used in this model, graphical comparisons of the numerical results with the experimental data for the time series of water surface elevations and water particle velocities are presented.

Finally, Chapter 6 concludes the study including overall comparisons of the numerical models and future recommendations.

CHAPTER 2

LITERATURE SURVEY

Numerical simulations of tsunami-structure interaction have become one of the key components of tsunami research as it permits calculating the wave motion around the structures, and the pressure distribution on them accurately. Thus, it becomes easier to understand the behavior of the structures under tsunami attack enhancing the structure resilience against tsunami disaster. In this Chapter, previous physical and numerical modeling studies of tsunami-structure interactions are reviewed.

In Section 2.1, a brief overview of physical modeling studies for tsunami-structure interaction is given. The main focus in this section is the experiments conducted by Arikawa (2015) as these experiments are used as reference tests in this thesis study.

In numerical modeling studies, tsunami-structure interaction is generally investigated with the help of numerical models that solve Navier-Stokes (NS) equations. On the other hand, Non-linear Shallow Water Equations (NSWE) and Boussinesq equations are usually solved by numerical models that are used to assess tsunami propagation, inundation and amplification studies. However, models solving NSWE and Boussinesq equations are also used in solving tsunami-structure interaction problems. Therefore, it is important to understand the accuracy of NSWE or Boussinesq equations in tsunami-structure interaction problems. In Section 2.2, a brief information on the NSWE will be given in the scope of this thesis and common numerical modeling studies using NSWE will be summarized. Then, the 3D Navier-Stokes solvers which are simply called Computational Fluid Dynamics (CFD) models will be discussed.

2.1. Overview of the Physical Model Experiments

Physical modeling is an important tool to gain insight and improve understanding in physics of tsunami-structure interactions, supply data sets for developing and advancing numerical models and testing proposed designs.

In the following sections, a brief overview of the physical model experiments will be summarized. Then, the laboratory experiments used as a reference in this thesis will be explained in detail.

In the present state of art, completely representing the tsunami wave in physical model experiments is a very challenging problem since the wave length is very long. Solitary wave experiments are a very common way in the literature to illustrate the tsunami wave. Furthermore, tsunami overflow experiments are also used with solitary wave to represent the effect of duration during the overflow of tsunamis. Lastly mentioned here is the bore experiments in tsunami modeling studies. The literature review on physical model experiments is confined to tsunami-structure interaction experiments as much as possible while explaining these three type of physical experiments used to represent tsunamis. However, selected pioneering experiments in tsunami research are also presented for completeness of the discussions.

2.1.1. Overview of Solitary Wave Experiments

Hall and Watts (1953) measured the maximum runup of solitary waves on five different beaches. In this study, a runup formula as a function of beach slope and incident wave height was proposed based on the experimental results. Although there were earlier studies on tsunami runup onto sloping beaches, Synolakis (1987) was one of the pioneering studies of solitary waves to demonstrate a meticulous validation of the theory with his experiments to investigate the runup of solitary waves on plane beaches (Briggs et al., 2009). Laboratory experiments supported the theory and an asymptotic result for the maximum runup is presented in this study. Briggs et al. (1995) conducted another study on the three-dimensional form of solitary wave runup experiments. This study shows that the runup of non-breaking waves in a basin was

smaller than the ones in a tank. It also showed that there is not much difference in case of breaking waves. Liu et al. (1995) performed a study on a circular island to investigate the runup of solitary waves. This study reported that on the front side of the island where facing the attack of the wave direction, first maximum runup is largest. It also showed that a dramatic increase in the runup is observed at the back side of the island when the length of the wave generator or crest length of the wave is increased. In Synolakis et al. (2008), five laboratory benchmark cases are described and discussed. These cases are named as solitary wave experiments on a 1:20 sloping beach (Synolakis, 1987), solitary wave runup on a composite beach (Kânoğlu, 1998; Kânoğlu and Synolakis, 1998), on a conical island (Liu et al., 1995; Kânoğlu, 1998; Kânoğlu and Synolakis, 1998), tsunami runup on a complex three-dimensional beach (Takahashi, 1996) and tsunami generation and runup due to three-dimensional landslide (Liu et al., 2005). Another study performed by Esteban et al. (2012) on laboratory experiments using solitary waves to investigate the stability of a breakwater. A design formula is proposed based on these experiments and field research. Moreover, Guler et al. (2015) studied the performance level of Haydarpasa Breakwater under the possible attack of a tsunami event. The experiments are conducted at Port and Airport Research Institute (PARI), Japan in a 105 m wave channel using a solitary wave. Arikawa (2015) conducted a series of experiments to investigate the tsunami wave forces on structures using solitary waves. Since these experiments are used as a reference in this thesis, detailed information is given in Section 2.1.4.

2.1.2. Overview of Tsunami Overflow Experiments

After the devastating effects of major tsunamis such as 2004 Indian Ocean Tsunami and 2011 Great East Japan Earthquake (GEJE) Tsunami, overflow experiments played a very important role to understand the failure mechanisms of structures and effect of duration of tsunami overflow. Madsen et al. (2008) indicated that the solitary waves do not have enough capability to express the impact of tsunami attacks alone. Therefore, overflow experiments are used in addition to solitary wave experiments to represent the effect of duration during tsunami overflow. Arikawa et al. (2012) stated

that due to the water level difference between the seaside and the harbor side, duration of the tsunami overflow plays a crucial role in the stability of breakwaters. After a large number of breakwaters damaged by GEJE Tsunami, Arikawa et al. (2013) performed several physical experiments using different breakwater cross-sections to analyze the exact failure mechanisms caused by tsunami overflows. This study revealed that bearing capacity of rubble mounds decreases due to the scouring by overflows. Another study performed by Arikawa et al. (2014b) aimed to find the relationship between scouring depth and vortex due to overflow. This study showed that scouring depth can be evaluated by the scale of the vortex. Takahashi et al. (2014) aimed to describe the stability of a breakwater foundation under the action of seepage created by tsunami-induced difference between the water levels of the seaside and rear side of breakwaters. They applied the centrifuge technique and the results of the experiments showed that scouring due to seepage and boiling occur and that the seepage force decreases the bearing capacity of the rubble foundation. Guler et al. (2015) also conducted overflow experiments in addition to solitary wave experiments previously mentioned to have a better understanding and create a realistic effect of a tsunami. Harbitz et al. (2016) tested similar cross-sections to the cross-section used in Guler et al. (2015) considering similar wave conditions. Also, breakwater model damages are investigated in the bore experiments. In Sassa et al. (2016) several experiments are conducted to investigate simultaneous processes and to explain in detail the mechanism of the instability involving the scour of the mound/sandy seabed, bearing capacity and flow of the foundation and the failure of caisson breakwaters by using a tsunami overflow-seepage centrifuge experimental system. Aniel-Quiroga et al. (2018) carried out laboratory experiments on Mediterranean rubble-mound breakwaters under tsunami waves. In this study, breakwater damages are investigated focusing on the two different effects of the tsunamis: 1) the first impact of solitons and 2) tsunami overflow by applying a pump-driven wave maker. As a result, development of a set of formula that provides the value of the damage parameter is presented.

2.1.3. Overview of Tsunami Bore Experiments

Broken tsunami waves inundate shoreline as a hydraulic bore which is a fast moving body of water with an abrupt front. These bores create forces on structures such as hydrodynamic (drag) force, buoyant force, surge force and impact of debris. Accurate estimation of these impact forces in laboratory experiments is a very challenging and difficult work (Nistor et al., 2009). Ramsden, (1993) conducted a comprehensive experimental investigation on determining the forces on a vertical wall by solitary waves, bores, and surges. In these experiments, forces and overturning moments due to bores and dry-bed surges were recorded and calculated respectively. Also, Arnason (2005) conducted a study and measured the forces exerted on various shapes of structures due to a hydraulic bore on a dry bed. These studies observed that the upper limit of the impulsive force caused by a bore is much higher of the subsequent maximum hydrodynamic force. It is emphasized that the findings are empirically based on the small-scale laboratory works. Robertson et al. (2008) performed a series of experiments to determine the effect of tsunami bores on coastal and nearshore structures, especially buildings and bridges. The experimental results provide data for validation of CFD models to be used in the estimation of tsunami forces on structures. To build a better understanding of the tsunami-induced forces and structures, Nistor et al. (2010) carried out several laboratory experiments in the scope of a comprehensive research project. Al-Faesly et al. (2012) presented the results of a comprehensive experimental program investigating the hydrodynamic forces on structural models generated by a turbulent hydraulic bore similar to those induced by broken tsunami waves. Rahman and Nakaza (2016) conducted series of experiments for different initial tsunami bore heights in the laboratory to investigate the tsunami impact on a simple building model structure. They compared the experimental results with numerical simulations. Chen et al. (2016) carried out a detailed experimental study to quantify the tsunami bore uplift loads on a deck, representing a typical wharf structure. The effects of bore height, deck height and slope angle on uplift loads were studied. This study showed that bore height correlates with bore velocity.

2.1.5. Reference Experiments: Vertical Wall-Solitary Wave Interactions (Arikawa, 2015)

In GEJE Tsunami, it is seen that damage of the Nuclear Power Plants (NPPs) has very serious consequences apart from the loss of human life and property. Although there were many discussions about the availability of the prevention of this kind of an accident is possible or not, there is one certain thing which is the vital significance of ensuring the nuclear safety against tsunamis. Since the flooding hazard is a serious issue at NPP sites, International Atomic Energy Agency (IAEA) makes an effort to prepare detailed guidelines on tsunami hazard assessment.

Benchmark problems are designed and used to test the accuracy of numerical models including idealized scenarios as well as actual situations. There are several benchmark cases to test the accuracy of tsunami models. IAEA prepared a supporting technical document named as “*Tsunami and Seiche Hazard Assessment*” for the specific safety guide; SSG-18 “*Meteorological and Hydrological Hazards in Site Evaluation of Nuclear Installations*”. This supporting document is about the providing a detailed guidance on tsunami hazard assessment and highlight the importance of benchmarking on tsunami for the validation and verification of the numerical models. In this document, the laboratory experiments conducted by Arikawa (2015) is selected as one of the benchmark problems to be used in the validation and verification of tsunami models.

Arikawa (2015) carried out several systematic laboratory experiments to investigate the forces on the vertical wall structure due to solitary wave. These experiments are conducted in the 105 m long, 25 m wide and 2 m depth wave channel of PARI, Japan. The channel is divided into two and the width of the channel where the slope is set is 0.80 m.

In the experiments, four different bottom slopes as 0 (horizontal), 1/10, 1/20 and 1/40 just in front of the vertical wall are tested. However, since it is more general not to have a slope in front of the structures, the one with the horizontal case is selected to be

used in this thesis. At the end of the channel, three vertical blocks of 1m height located side by side like a vertical wall obtaining a total width of 0.80 m. Experiments are conducted for three different locations of this vertical wall. The positions of the vertical wall can be seen in Figure 2.1 Numerical simulations are carried out for all of these three different vertical wall positions to see the breaking effect and they are stated as Case 1, Case 2 and Case 3 from now on in the thesis. In Case 1, vertical wall is placed on the small step at the end of the horizontal part of the channel and the solitary wave breaks right on the vertical wall. For Case 2, position of the vertical wall slides 1 m behind of the previous case and solitary wave reaches the vertical wall as a breaking wave. Lastly, Case 3 indicates the situation where the vertical wall located 2 m behind of the first position and solitary wave comes as a broken wave.



Figure 2.1. (1) First position of the vertical wall, (2) Second position of the vertical wall, (3) Third position of the vertical wall (Arikawa, 2015)

The time histories of water elevation and velocities are measured at different locations in the channel and on the wall with 13 wave gauges (WGs) and 6 electromagnetic velocity meters (Vs). Figure 2.2 shows the plan and cross-sectional view of the channel with the locations of wave and velocity gauges.

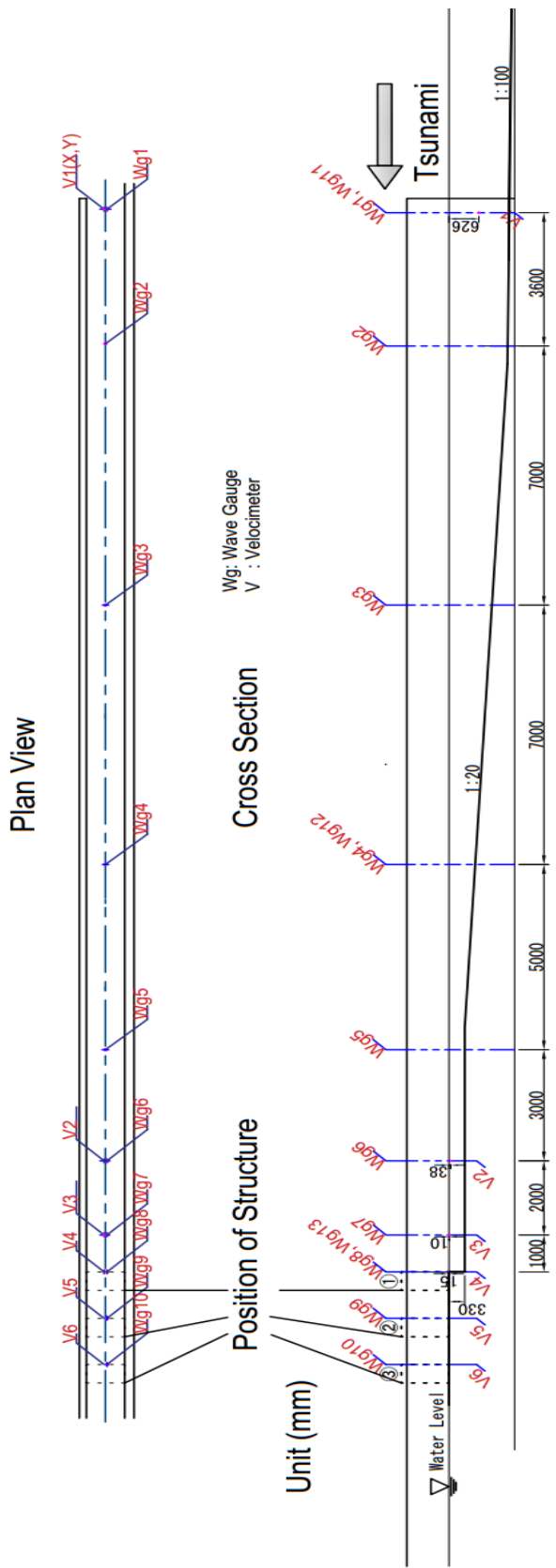


Figure 2.2. Plan view and the cross-section of the experimental setup for horizontal case
(Arikawa, 2015)

The depth of water is measured as 1.252 m at the inlet boundary in front of the wave maker reducing to 0.33 m in front of the vertical wall (Figure 2.2). Experiment duration is kept as 90 seconds.

The same solitary wave is used in all the configurations generated by the wavemaker using Boussinesq theory. The solitary wave height at the first wave gauge (WG1) is approximately 0.2 m whereas the peak velocity under the solitary wave at the same location (V1) is around 0.55 m/s. The solitary wave height increases as it approaches the vertical wall, and a splash occurs as it hits to the vertical wall. The water particle velocity is also increasing as the wave propagates along the channel. The snapshots taken from the experiment videos of Case 1, Case 2 and Case 3 showing the before and after the motion of the solitary wave hits the vertical wall are presented in Figure 2.3, 2.4 and 2.5 respectively.

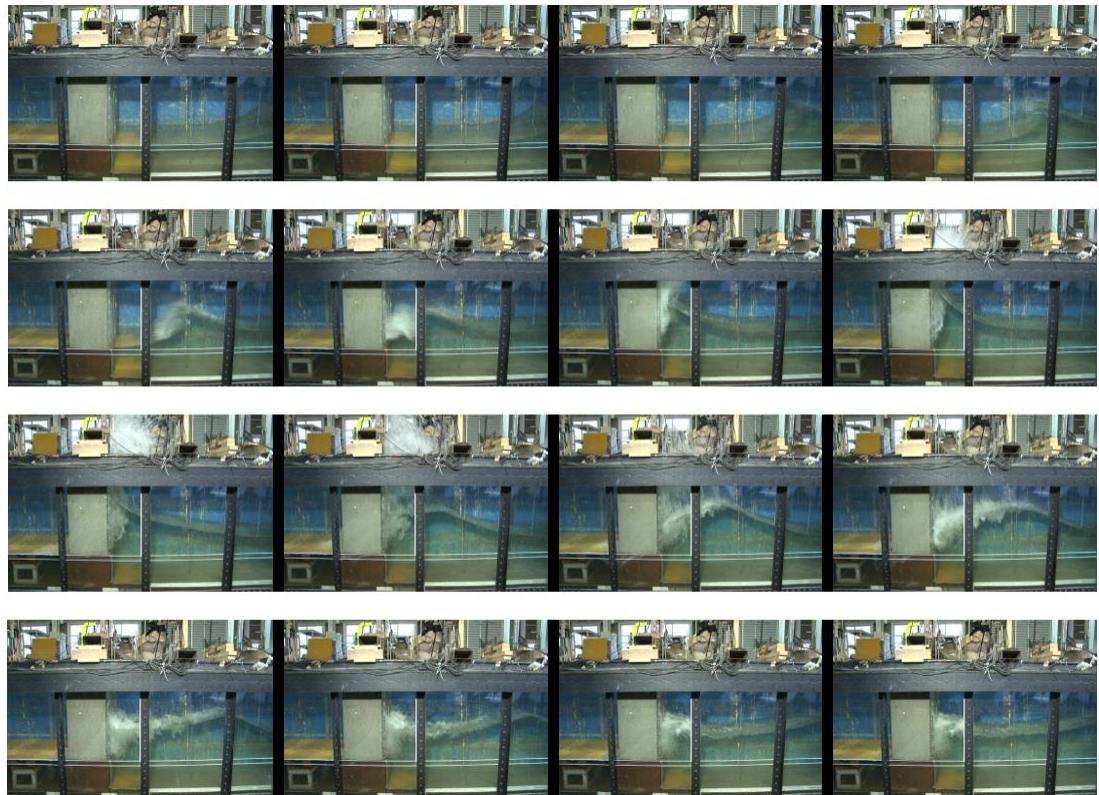


Figure 2.3. Snapshots from Experiment Video of Case 1 (Arikawa, 2015)

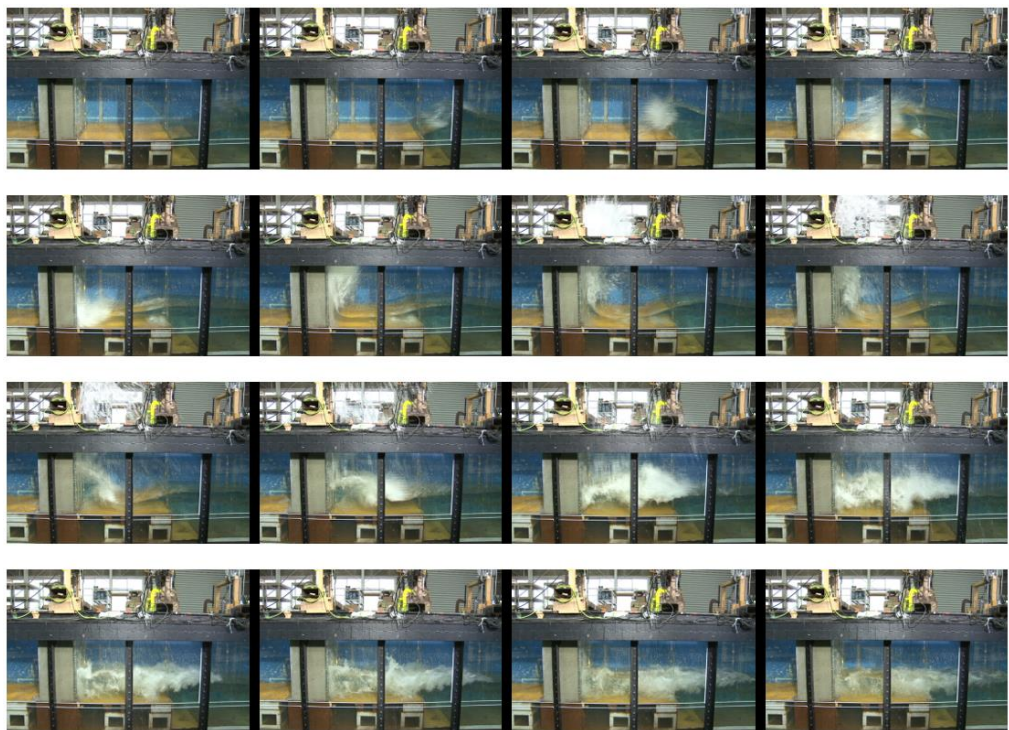


Figure 2.4. Snapshots from Experiment Video of Case 2 (Arikawa, 2015)

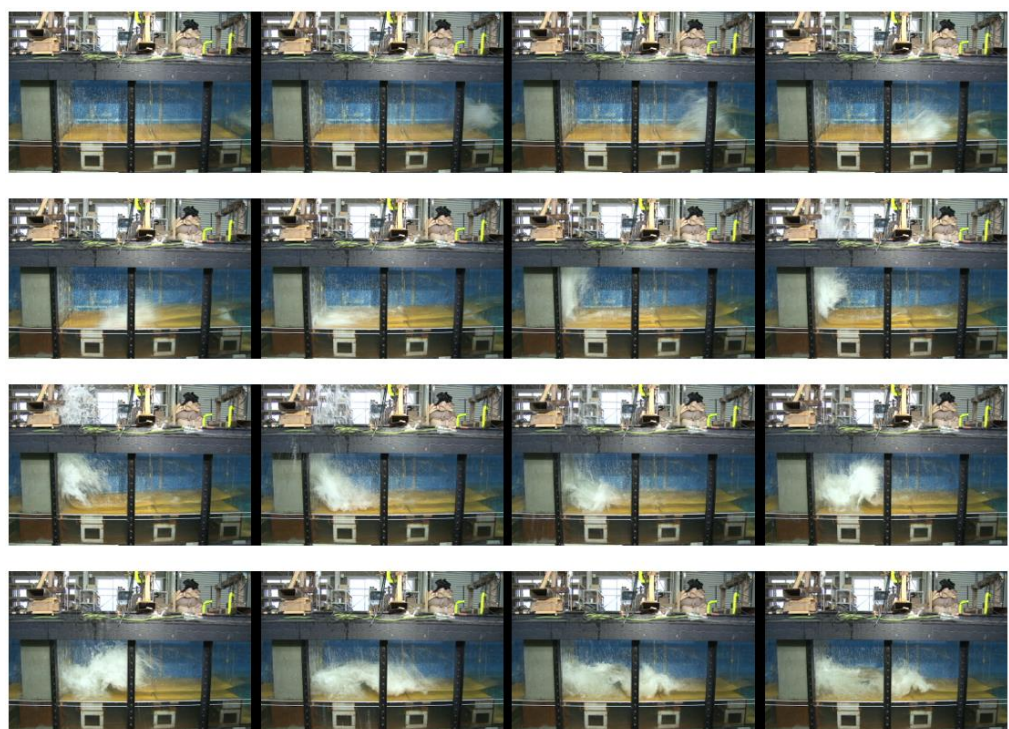


Figure 2.5. Snapshots from Experiment Video of Case 3 (Arikawa, 2015)

2.2. Overview of Numerical Modeling Studies

In the scope of this thesis, an overview of the studies related to models that solve depth-averaged NSWE which is a simplified version of Navier-Stokes equations and 3D Navier-Stokes equations are summarized. After that, a brief info and present studies of turbulence models are presented.

2.2.1. Overview of NSWE Applications of Tsunami Structure Interaction

Although a tsunami-structure interaction is not considered particularly, Horrillo et al. (2006) conducted a numerical study with using three different numerical models including the nondispersive NSWE, the non-linear Boussinesq and the full Navier-Stokes aided by the Volume of Fluid (VOF) method to capture the free surface. The results of these three models compared and discussed considering the dispersion effect. This is an important study to understand the limits of NSWE, and to predict its performance of tsunami-structure interaction. Guzzo et al. (2007) developed a numerical model to study tsunamis generated by landslides. This model solves NSWE using the Smoothed Particle Hydrodynamics (SPH) method. A dam break wave-structure interaction experimental benchmark case is modeled and good accuracy and low computational time is observed. Ozer and Yalciner (2011) presented a new term named as hydrodynamic demand which is a parameter to evaluate the tsunami drag force on structures. Several simulations with different regular-shaped basins and bottom slopes are performed using a model that solves depth-averaged NSWE. Sozdinler et al. (2014) conducted a study to analyze the relative value of the drag force which is named as hydrodynamic demand in the previous study of Ozer and Yalciner (2011) in tsunami inundation zones using a depth-averaged NSWE solver. Many tsunami parameters and several different tsunami inundation scenarios are considered in this study. Results of this study give information related to damage and safety levels of residential areas under a possible tsunami attack. Sozdinler et al. (2015) performed a numerical modeling study to investigate the damage in terms of Froude number on the structures in Kamaishi Bay due to tsunami using a depth-averaged NSWE solver. In the doctorate thesis of Velioglu (2017) investigation of the performances of a depth-

averaged NSWE solver and a 3D Reynolds Averaged Navier Stokes (RANS) solver using analytical, experimental and field benchmark cases are conducted. The differences between those two models are presented through statistical error analysis and recommendations regarding the efficient usage of the models in tsunami problems are made.

2.2.2. Overview of the Applications of 3D CFD Solvers to Tsunami-Structure Interactions

CFD simulations provide users a better understanding of the failure and damage mechanisms and more accurate force estimation on structures since it considers all physical aspects including the effect of turbulence. CFD enables researchers and engineers to perform numerical experiments in a virtual laboratory. With the increasing power of high-performance computing tools hence lowering the computational cost, the usage of CFD simulations is increasing all over the world. To investigate the damage mechanisms of bridges or coastal defense structures due to tsunami impact or to estimate the forces on these structures both Eulerian and Lagrangian CFD solvers are used. Hsiao and Lin (2010) has used a RANS solver tracking the free surface using VOF method to simulate tsunami-like solitary waves impinging and overtopping impermeable seawall. In Nistor et al. (2010), numerical modeling with using three-dimensional SPH model was performed as another component of the research project for previously mentioned physical experiments in the same study. Several researches have focused on damage mechanism of Kamaishi Breakwater, Japan due to 2011 Tsunami using RANS solvers tracking free surface using VOF method (Arikawa et al., 2012; Bricker et al., 2013; Pringle et al., 2016). St-Germain et al. (2012) have used weakly compressible smoothed particle hydrodynamics (WCSPH) method to investigate the hydrodynamic forces induced by the impact of tsunami bores on a freestanding column of square cross-section. Sakakiyama (2013) has presented both physical and numerical experiments investigating flow fields of tsunamis passing over a rubble mound breakwater. In the numerical part of Sakakiyama (2013), a RANS solver using VOF method for free-

surface tracking Isobe et al. (1999) has been used. Analyses on tsunami forces acting on bridges and damage mechanisms of bridges due to tsunami impact have also been carried out in the literature. Bricker and Nakayama (2014) has estimated forces on a bridge in Tohoku Region, Japan due to 2011 Tsunami solving RANS Equations, and tracking free surface by the VOF method. Arikawa et al. (2014a) verified the applicability of empirical formula to estimate the lateral force on the structures under tsunami overflow by using numerical simulations with a model solving RANS and capturing free surface using VOF method. Azadbakht and Yim (2015) has used finite element method to solve NS Equations, and tracked free surface using an arbitrary Lagrangian-Eulerian (ALE) method to estimate tsunami forces on several bridges located in California, USA. Xu and Cai (2015) has used a RANS solver tracking the free surface using VOF method coupled with a spring-damper model to study lateral restraining stiffness effect on bridge deck-wave interaction. Scouring around the coastal structures due to tsunami overflow has also been studied. Wang et al. (2016) have studied scouring at the rear side of a seawall due to tsunami overflow using incompressible smoothed particle hydrodynamics (ISPH) method. Chella et al. (2017) used a RANS solver with a free surface tracking algorithm called level set method to investigate breaking solitary wave forces on a vertically mounted cylinder. Chen et al. (2017) investigate the solitary wave vertical cylinder interaction using PIC method based solver PICIN which combines the advantages of both Eulerian and Lagrangian methods. Cho et al. (2017) investigates the tsunami force on a vertical wall for different wave (tsunami) heights and cross-shore locations of vertical walls by using hydrodynamic and numerical model simulations. The numerical model solves RANS Equations and tracking free surface by the VOF method. A predictive formula of the tsunami force on a vertical wall was proposed in terms of wave heights and the cross-shore locations of vertical walls based on a regression analysis for the numerical simulation results. Guler et al. (2018) numerically studied the forces acting on the crown-wall and the stoned at the rear side of the rubble mound breakwater of tsunami attack on rubble mound breakwater of Haydarpasa Port, Istanbul after calibrating and validating the numerical solver based on the physical model experiments presented in

Guler et al. (2015) consisting of both solitary wave and tsunami overflow experiments. In this study, Volume Averaged RANS (VARANS) equations are solved tracking the free surface using the VOF method. In addition to solitary wave and tsunami overflow experiments, the attack of a long single sinusoidal wave is also studied representing a potential tsunami wave that could not be generated in a physical model experiment with the present-state-of-art technology to understand the differences in acting mechanisms of these waves.

2.2.3. Overview of Application of Turbulence Models

Turbulence plays a very significant role in hydraulics. The importance of the turbulence in hydraulic problems has been realized a long time ago and from then to now it is studied with an eagerness by many scientist and engineers. In this section, application of some turbulence models used in tsunami-structure interaction is reviewed.

Turbulent motion contains different size of eddies which symbolize the vortices stretching each other thus creating smaller size eddies and transmit the kinetic energy to them until viscous forces damp the energy at the smallest eddies (Rodi, 2017).

There are many different types of methods to treat the turbulence. Two equation models are one of the simplest turbulence models that can work with Reynolds Averaged Navier-Stokes (RANS) equations and Volume Averaged RANS (VARANS) equations which do not need an empirical formula for the length scale or for any order turbulence quantity inside the calculation domain. In addition to the k -equation, two equation models are used to solve a second transport equation to determine the length scale, L .

In the scope of this thesis, only the $k-\varepsilon$, $k-\omega$, and $k-\omega$ -SST two-equation turbulence models will be discussed and earlier applications of these methods will be presented in the following sections.

2.2.3.1. *k-ε* Turbulence Model

This model is one of the most widely used turbulence models in CFD applications. Many tests and applications proved that $k-\epsilon$ turbulence model is applicable to a wide variety of flows with reasonable success yet, in some certain situations the model does not provide satisfactory results (Rodi, 2017). It provides a better performance in the free flow regions. Detailed information can be found in Casey and Wintergerste (2000). Xiao and Huang (2008) conducted a numerical study based on the RANS and $k-\epsilon$ equations to estimate the impact of a solitary wave on an idealized beachfront house. Hsiao and Lin (2010) investigated the tsunami-like solitary waves impinging and overtopping an impermeable seawall using a two-dimensional VOF type model based on RANS equations and the $k-\epsilon$ turbulence closure solver. del Jesus et al. (2012) performed a numerical study to investigate the tsunami wave interaction with porous and impermeable vertical barriers using a model that solves VARANS equations to simulate the wave flow within the porous structures and VOF method to track the free surface. $k-\epsilon$ turbulence model is used and volume-averaged to provide a closure for turbulent terms. Bricker et al. (2013) studied the turbulence model effects on the analysis of breakwater overtopping during the 2011 GEJE Tsunami. In this study, a RANS solver capturing free surface using VOF method with $k-\epsilon$ turbulence model is used to simulate the unsteady overtopping. Bricker and Nakayama (2014) also investigated the failure of Utatsu concrete girder highway bridge in Minamisanriku during the 2011 GEJE Tsunami. In this study, two-dimensional analysis with a model that solves RANS equations with employing VOF method for free surface is used. Turbulence is modeled with $k-\epsilon$ turbulence model. Dao et al. (2014) conducted a sensitivity analysis on the relationship of the tsunami and coastal embankment structure. In this study, a model based on the RANS equations with $k-\epsilon$ turbulence model for closure is used for simulations. Douglas et al. (2015) reproduce the physical experiments conducted by Al-Faesly et al. (2012) to investigate the tsunami-induced hydrodynamic loading on nearshore structures using a three-dimensional multiphase model that solves RANS equations and employs VOF method to capture free surface with $k-\epsilon$ turbulence model. Douglas and Nistor (2015) performed a numerical study to

understand the effect of bed condition on the tsunami-like bores and their interactions with the structures using a multiphase three-dimensional numerical model that solves RANS equations and uses VOF method for free surface. $k-\epsilon$ turbulence model is employed to provide closure for the turbulent terms. Kawasaki et al. (2015) carried out a numerical analysis on two-dimensional multiphase turbulence flow using a numerical model based on RANS equations and $k-\epsilon$ turbulence model for closure. Ghosh et al. (2016) conducted a numerical study on the effectiveness of different opening sizes in buildings to mitigate the structural damages due to tsunamis. Under the solitary wave impact, a CFD analysis is performed. Three-dimensional RANS solving model with VOF method to track the free surface is used. Turbulence is modeled with the readily available $k-\epsilon$ model. Sarjamee (2016) investigated the tsunami-induced hydrodynamic loading on freestanding structures numerically using a model that solves RANS equations with VOF method to trace the free surface. In this work, $k-\epsilon$ turbulence model is used to provide a closure for turbulence terms. The previously mentioned study in Section 2.2.2 by (Cho et al. 2017) used the $k-\epsilon$ turbulence model for the turbulence closure to simulate the hydrodynamic forces induced by tsunami on a vertical wall structure.

2.2.3.2. $k-\omega$ Turbulence Model

The use of $k-\omega$ turbulence model is increased due to the unsatisfactory results provided by the $k-\epsilon$ model in large adverse pressure gradient boundary layers and flow separation zones. Turbulence frequency ω , is used to determine the length scale, L instead of ϵ -equation. The model was originally proposed by Wilcox (1993). This model performs better near wall regions and adverse-pressure-gradient flows; but, at free stream, the model suffers from the excessive sensitivity to the boundary condition for ω . Williams and Fuhrman (2016) investigated the boundary layer flow and properties induced by tsunami-scale waves. For this aim, an existing one-dimensional vertical boundary layer model based on RANS equations is extended to work with the $k-\omega$ turbulence model. Model is validated and used for transient wave boundary layers at full tsunami scales. Xu et al. (2017) performed a numerical study on predicting

forces on a coastal bridge deck with girders due to a solitary wave to find an alternative approach for accurate estimation of solitary wave forces. $k-\omega$ model is used as the turbulent closure for RANS equations in the CFD model. In the previously mentioned study in Section 2.2.2 conducted by Chella et al. (2017), $k-\omega$ turbulence model is used to describe the turbulence effect in breaking solitary waves. Larsen et al. (2017) presented a hydrodynamic and morphologic coupled numerical model used to assess tsunami-induced scour around a monopile structure solving RANS equations coupled with $k-\omega$ turbulence closure.

2.2.3.3. $k-\omega$ -SST Turbulence Model

The $k-\omega$ -SST model combines the best features of $k-\varepsilon$ and $k-\omega$ turbulence models. By using a set of blending functions, $k-\omega$ -SST turbulence model provides the best results for different zones where $k-\varepsilon$ and $k-\omega$ turbulence models function the best. It was proposed by Menter (1994) to solve the turbulence problem near walls with $k-\omega$ and away from the walls in free flow region with $k-\varepsilon$ turbulence model. Leschka and Oumeraci (2011) performed a numerical study on the influence of an artificial reef and emerged cylinder on the propagation of solitary waves using a two- and three-dimensional two-phase RANS model and the VOF method applied with the $k-\omega$ -SST model. Leschka et al. (2014) studied the effect of structural arrangements and distances among them on hydrodynamic forces for a group of three emerged cylinders by solitary waves and bores. $k-\omega$ -SST turbulence closure is used for estimation of the turbulence. Kawasaki et al. (2015) used $k-\omega$ -SST turbulence model for their study in addition to $k-\varepsilon$ model. The authors concluded that the results obtained from the simulation where the $k-\omega$ -SST turbulence model is used showed better agreement with the experiments conducted for tsunami loading. Another previously mentioned study in Section 2.2.2 conducted by Xu and Cai (2015) applied the $k-\omega$ -SST turbulence model to simulate the turbulent characters of the incoming waves and those generated from the bridge deck-wave interaction. The previously mentioned study in Section 2.2.2 performed by Guler et al. (2018) used the $k-\omega$ -SST turbulence model to investigate the performance of Haydarpasa Breakwater under tsunami attack.

CHAPTER 3

NAMI DANCE

NAMI DANCE is a numerical model developed by the collaboration of scientist - *Andrey Zaytsev, Ahmet Cevdet Yalciner, Anton Chernov, Efim Pelinovsky and Andrey Kurkin-* from Middle East Technical University Civil Engineering Department Ocean Engineering Research Center, Turkey and Special Research Bureau for Automation of Marine Researches, Far Eastern Branch of Russian Academy of Sciences, Russia. Later, NAMI DANCE is re-implemented to work with Graphics Processing Unit (GPU) by *Bora Yalciner, Andrey Zaytsev, Ahmet Cevdet Yalciner, Efim Pelinovsky and Andrey Kurkin.* NAMI DANCE is a United Nations Educational, Scientific and Cultural Organization (UNESCO) recommended computational tool used especially in tsunami modeling. It is written in C++ programming language and it follows the identical computational procedures of TUNAMI-N2 (Tōhoku University's Numerical Analysis Model for Investigation of Near-field tsunamis, No.2) which is developed by Profs. Shuto and Imamura (Imamura, 1989, Shuto, Goto, & Imamura 1990, Goto & Ogawa, 1991).

In addition to tsunami parameters NAMI DANCE also computes; tsunami source from both rupture characteristics and pre-determined waveform, propagation, arrival time of the tsunami, amplification, inundation based on the accuracy of grid size, directions and distributions of current velocities, distribution of water surface elevations, time histories of water surface fluctuations, 3D plot of sea state and animation of tsunami propagation (Yalciner et al., 2006b, 2007b).

NAMI DANCE solves the NSWE using initial and boundary conditions. Detailed information about the numerical solution is given in Section 3.1. NAMI DANCE has been validated via benchmarks that commonly used among coastal scientists.

NAMI DANCE provides users an option to choose between two different coordinate system such as spherical or Cartesian and also two equation types of linear or non-linear shallow water equations. It can create the tsunami initial wave either from tsunamigenic rupture parameters or an initial water surface disturbance area defined by the user. Input can be given to the program as a static source initial wave or a dynamic source initial wave such as time history of water elevation.

3.1. Numerical Scheme of NAMI DANCE

In the theory of long waves, the vertical acceleration of water particles is often neglected against the gravitational acceleration. Thus, it is assumed that the vertical motion of the water particles has no effect on the pressure distribution. Based on this approximation, the fundamental equations of NAMI DANCE are obtained using necessary dynamic and kinematic conditions and also bottom friction terms (for nonlinearity). They are discretized by means of the staggered leapfrog scheme.

There are certain assumptions to be applied in order to get the NSWE such as neglecting the surface tension force between air and water (dynamic boundary condition at free surface), a water particle on the free surface keeps its position throughout the motion (kinematic boundary condition at free surface) etc. Also, in case of tsunami propagation in shallow waters, horizontal eddy turbulence can be neglected against the bottom friction except for runup on the land. Details of the derivation of NSWE can be found in Imamura et al. (2006).

After the assumptions and substitutions, the fundamental equations of NAMI DANCE which is the NSWE in the spherical coordinate system, are expressed in the Equations 3.1-3.3 by Imamura et al. (2006):

$$\frac{\partial \eta}{\partial t} + \frac{1}{R \cos \phi} \left[\frac{\partial M}{\partial \lambda} + \frac{\partial (N \cos \phi)}{\partial \phi} \right] = 0 \quad [3.1]$$

$$\begin{aligned} \frac{\partial M}{\partial t} + \frac{1}{R \cos \phi} \frac{\partial}{\partial \lambda} \left(\frac{M^2}{D} \right) + \frac{1}{R} \frac{\partial}{\partial \phi} \left(\frac{MN}{D} \right) + \frac{gD}{R \cos \phi} \frac{\partial \eta}{\partial \lambda} + \frac{\tau_\lambda}{\rho} = \\ (2\omega \sin \phi) N + \frac{gD}{R \cos \phi} \frac{\partial d}{\partial \lambda} + \frac{1}{R \cos \phi} \frac{\partial D \psi}{\partial \phi} \end{aligned} \quad [3.2]$$

$$\begin{aligned} \frac{\partial N}{\partial t} + \frac{1}{R \cos \phi} \frac{\partial}{\partial \lambda} \left(\frac{MN}{D} \right) + \frac{1}{R} \frac{\partial}{\partial \phi} \left(\frac{N^2}{D} \right) + \frac{gD}{R} \frac{\partial \eta}{\partial \phi} + \frac{\tau_\phi}{\rho} = \\ -(2\omega \sin \phi) M + \frac{gD}{R} \frac{\partial d}{\partial \phi} + \frac{1}{R} \frac{\partial D \psi}{\partial \phi} \end{aligned} \quad [3.3]$$

where λ and ϕ are longitude and latitude respectively, t is time, η is vertical displacement of water above the still water level, M and N are the discharge fluxes in longitude and latitude, τ_λ and τ_ϕ are the bottom shear stresses in longitude and latitude, D is the total depth (summation of η and water depth from still water), R is Earth radius, ω is Earth's rotation (they are taken as 6378.137 km and 7.27×10^{-5} rad/s. respectively) and g is the gravitational acceleration. Finite differences is one of the most widely used numerical methods in Eulerian framework to solve NSWE. NAMIDANCE employs the staggered leap-frog finite difference scheme to solve the NSWE. These equations are valid only in the spherical coordinate system, and they are non-dispersive which means the spreading of the energy in the direction of wave advance is neglected. For the boundary conditions, the open boundary conditions are used to allow the reflected waves to pass through the boundary without causing any additional water surface elevation. Wavefront condition is controlled by the condition to determine if the cell is submerged or dry. Stability is determined via Courant-Friedrichs-Lowy (CFL) condition to ensure the numerical speed of the wave $\Delta \lambda / \Delta t$, is equal or larger than the actual speed passing through each grid at each time step.

3.2. Numerical Setup of the Experiments for NAMI DANCE

The physical experiments of Arikawa (2015) are reproduced in a 2D domain using NAMI DANCE. The reader can refer to Section 2.1.5 for details of the physical model experiments. The spherical coordinate system is used to create the bathymetry for the simulations. Longitude and latitude are stated as x and y from now on for the simplicity. The positive x -direction is towards the wave maker and positive y -direction is perpendicular to the direction of propagation of the solitary wave. The gravitational force is in the downward direction.

3.2.1. Case 1

In Case 1, the vertical wall is located on top of the small step which is 6 m away from the end of the slope. Figure 3.1 indicated the coordinate system and the top view of the computational domain of Case 1.

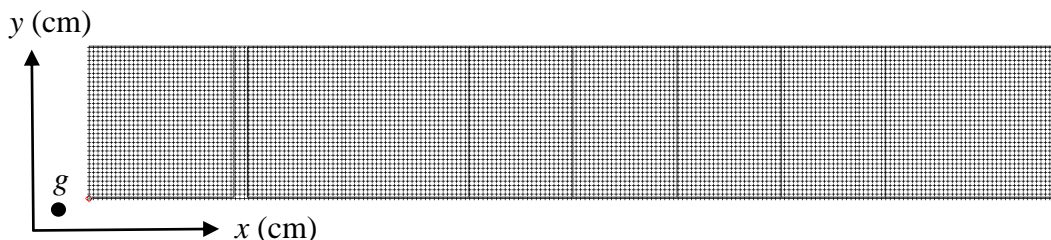


Figure 3.1. Orientation of the coordinate system and top view computational domain of the Case 1 for NAMI DANCE model

Δx and Δy which are the grid sizes of the computational domain represented by a structured mesh covers the whole flume are uniform throughout the mesh. Δx and Δy , both are set as 1 cm for the simulation. Thus, the total of 3701 grid points in x -direction and 670 grid points in y -direction is obtained. In Case 1, the vertical wall is positioned just above the small step that is located at the end of the horizontal ground. The three-dimensional view of the computational domain is given in Figure 3.2.

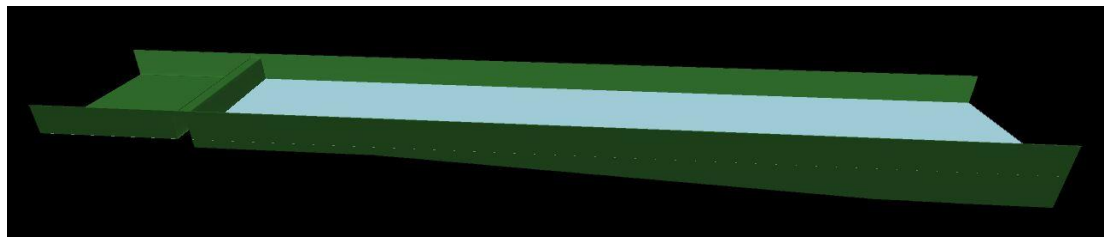


Figure 3.2. Three-dimensional representation of the computational domain of Case 1 in NAMI DANCE

To shorten the wave channel and decrease the computational time, the water surface elevation time series and velocity values measured at the location of WG1 and V1 gauges are used exactly as the input to the system at the upstream end of the computational domain. Therefore, the simulation duration is kept as 20 sec. The maximum and minimum y boundaries are defined as rigid walls. NAMI DANCE calculates the maximum time step that satisfies the CFL stability criteria automatically considering the bathymetry. According to this limitation, time step for the simulation, Δt is selected as 0.0005 seconds.

3.2.2. Case 2

In Case 2, the vertical wall is 1 m moved back from the small step that is located at the end of the horizontal ground. The computational domain is the same with Case 1 except the change of the location of the vertical wall. Figure 3.3 shows the coordinate system and top view of the computational domain.

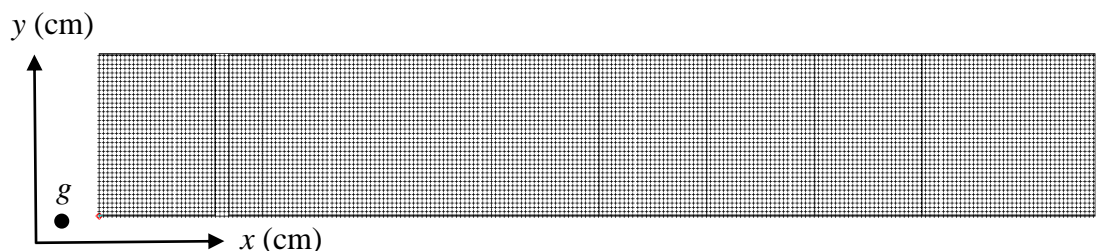


Figure 3.3. Orientation of the coordinate system and top view computational domain of the Case 2 for NAMI DANCE model

The water surface elevation time series and velocity values measured at the location of WG1 and V1 gauges are used exactly as the input to the system at the upstream end of the computational domain like in the Case 1. Simulation duration is same with the previous case as 20 sec. The maximum and minimum y boundaries are defined as rigid walls.

According to CFL stability limitation, time step for the simulation, Δt is selected as 0.0005 seconds. Three-dimensional representation of the computational domain can be seen in Figure 3.4.

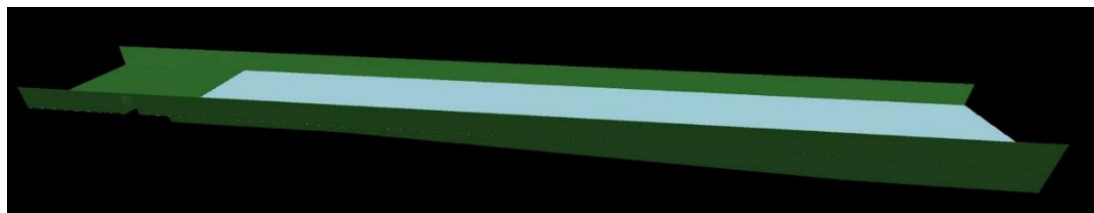


Figure 3.4. Three-dimensional representation of the computational domain of Case 2 in NAMI DANCE

3.2.3. Case 3

In Case 3, the new position of the vertical wall is 2 m away from the small step that is located at the end of the horizontal ground. The computational domain is the same with Case 1 and Case 2 except the change of the location of the vertical wall. The coordinate system and top view of the computational domain are given in Figure 3.5.

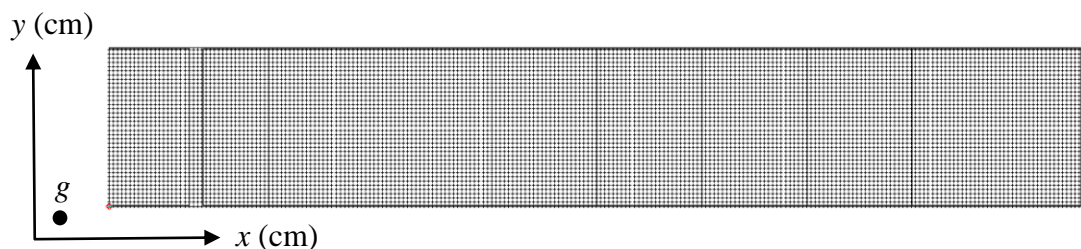


Figure 3.5. Orientation of the coordinate system and top view computational domain of the Case 3 for NAMI DANCE model

The water surface elevation time series and velocity values measured at the location of WG1 and V1 gauges are used exactly as the input to the system at the upstream end of the computational domain like in the Case 1 and Case 2. Simulation duration is same with the previous cases as 20 sec. The maximum and minimum y boundaries are defined as rigid walls.

Time step for the simulation, Δt is selected as 0.0005 seconds based on the CFL stability limitation. Three-dimensional representation of the computational domain can be seen in Figure 3.6.

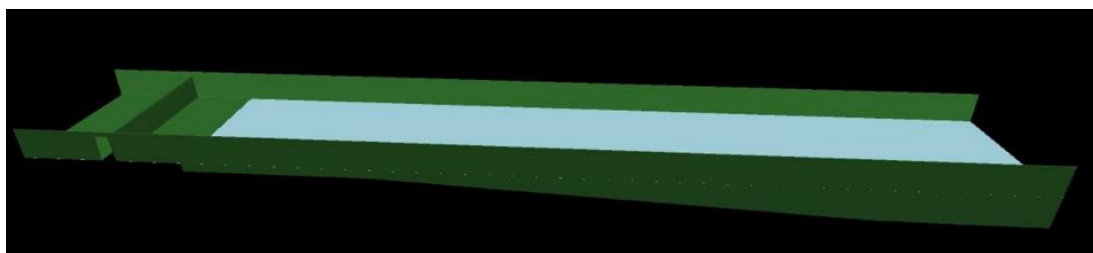


Figure 3.6. Three-dimensional representation of the computational domain of Case 3 in NAMI DANCE

3.3. Results and Discussions of NAMI DANCE Simulations

The results and discussions of the simulations are presented in this section. The time interval for the experimental data and the output time interval for numerical simulations are both 0.0005 sec.

Comparison of the time histories of water surface elevations obtained from the NAMI DANCE simulation for Case 1 and the measured data of time histories in physical model experiments is presented in Figure 3.7 for wave gauges from WG1 to WG8. The results show that the time histories are in a fairly well agreement with the measured data along the wave channel. Minor time lag occurred in the computation of the reflected waves in WG5 and WG6. In these gauges, it can be seen that the peak values are estimated with reasonable accuracy. In WG 7, the trend of the numerical model is in consistency with the general trend of the solitary wave experiment. At

WG8 which is the critical gauge since it is located just in front of the vertical wall, it is clearly seen that NAMI DANCE could not compute the water surface elevation correctly. The closer look of the results of WG8 is given in Figure 3.8 to see the differences in detail. The results indicate that the peak value computed by NAMI DANCE at the incident where the solitary wave hits the vertical wall is nearly half of the measured experimental data. The flat part of the experimental data indicates that the wave gauge at that location could not measure the water surface elevation correctly due to the extremely high splashes over the vertical wall. This means that the actual splash reaches much higher value than the measurements. Detailed investigation about this issue is given in Chapter 4 with snapshots from the videos of the physical model experiments. Comparison between the time histories of the horizontal component of particle velocities in the x-direction and the measured time histories in physical experiments at velocity gauges (V1-V4) are presented in Figure 3.9. It is seen that the trend of the numerical results matches with the experimental data throughout the channel. However, especially at V4 which is the velocity gauge located right in front of the vertical wall NAMI DANCE was not capable to capture the particle velocities since the impact is a highly complicated phenomenon (Figure 3.10).

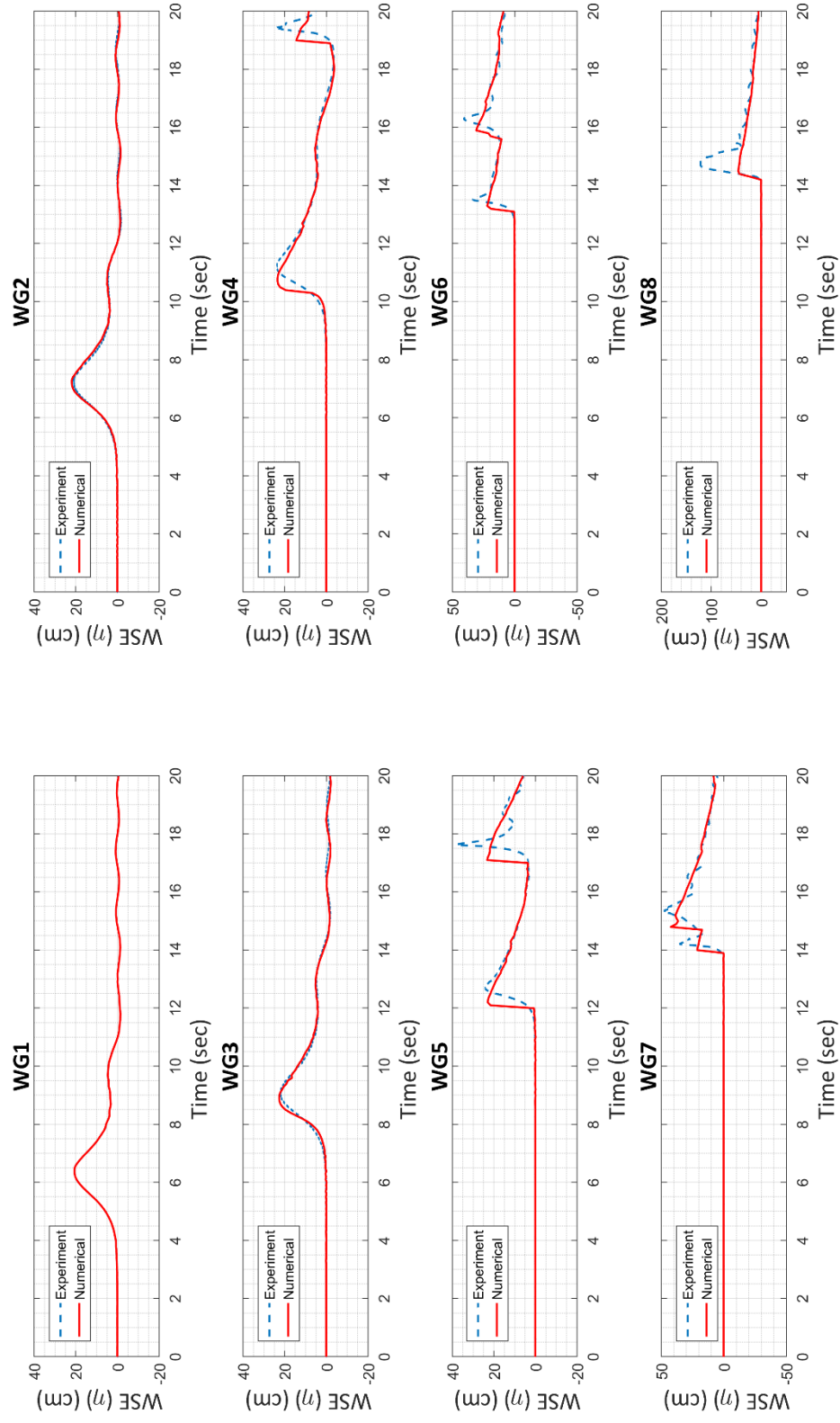


Figure 3.7. Comparison of Water Surface Elevations of NAMI DANCE with Experimental Measurements for Case 1

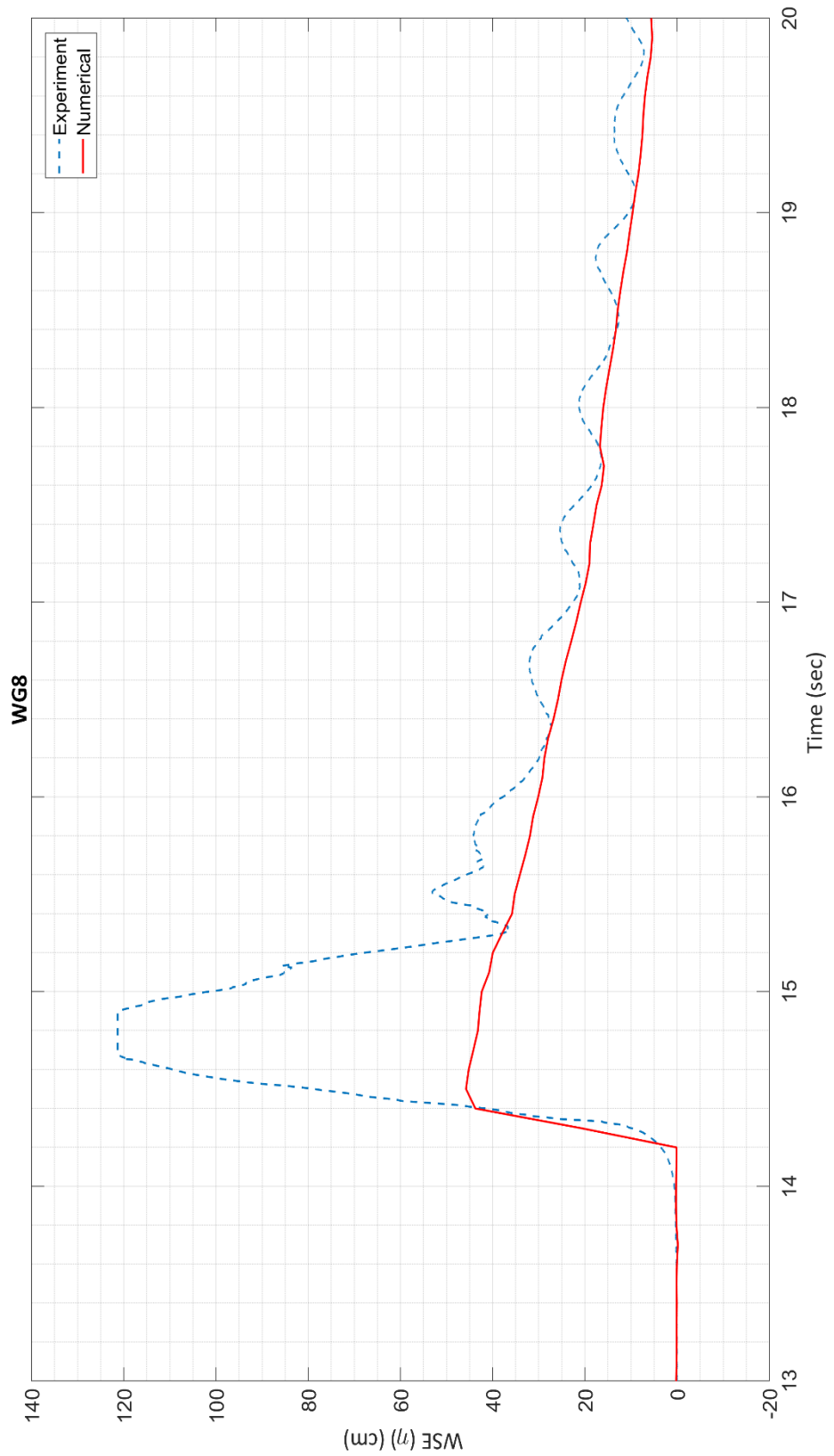


Figure 3.8. Comparison of Water Surface Elevations of NAMIDANCE with Experimental Measurements at WG8 for Case 1

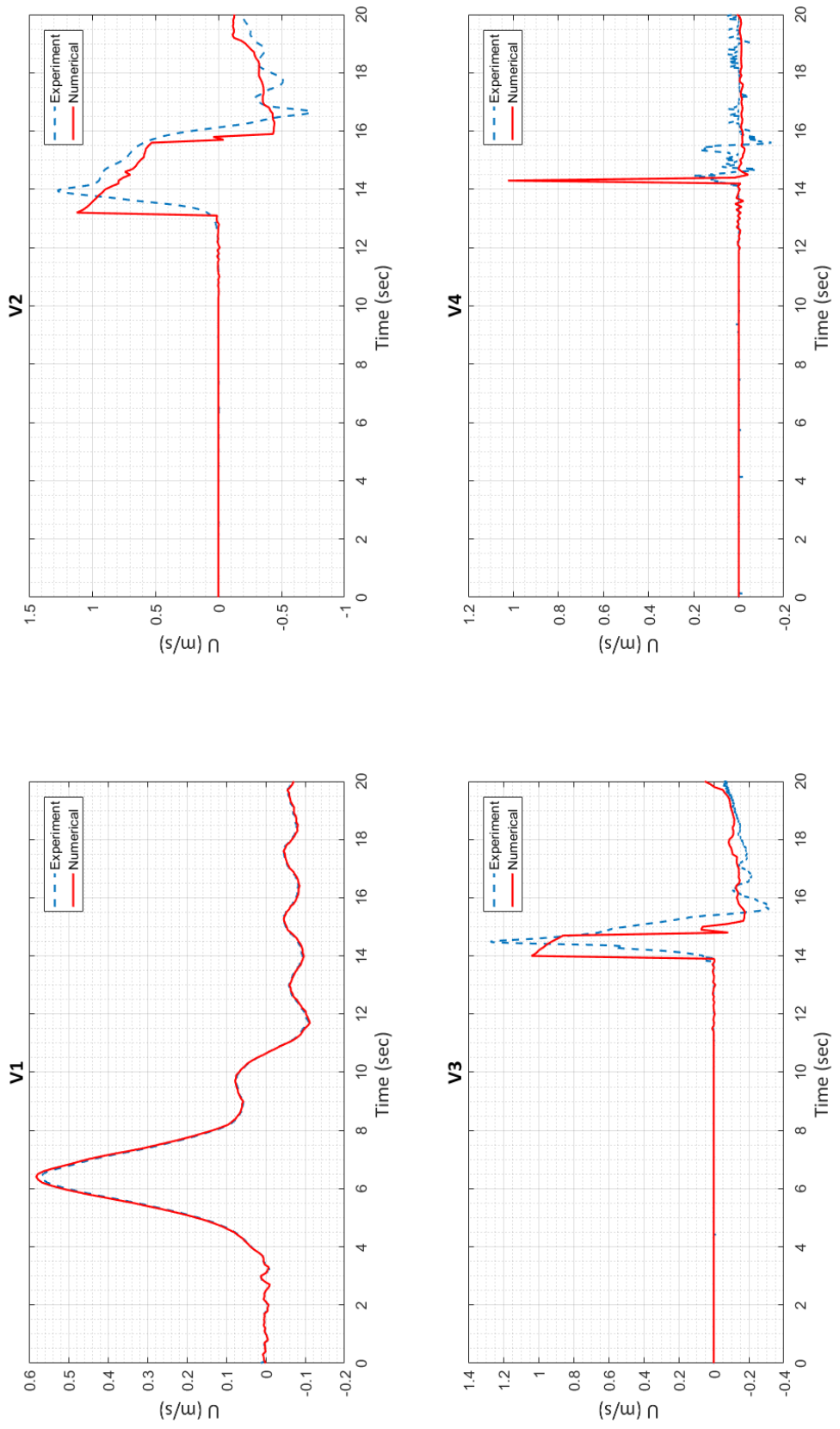


Figure 3.9. Comparison of Particle Velocities in x-direction, U of NAMI DANCE with Experimental Measurements for Case 1

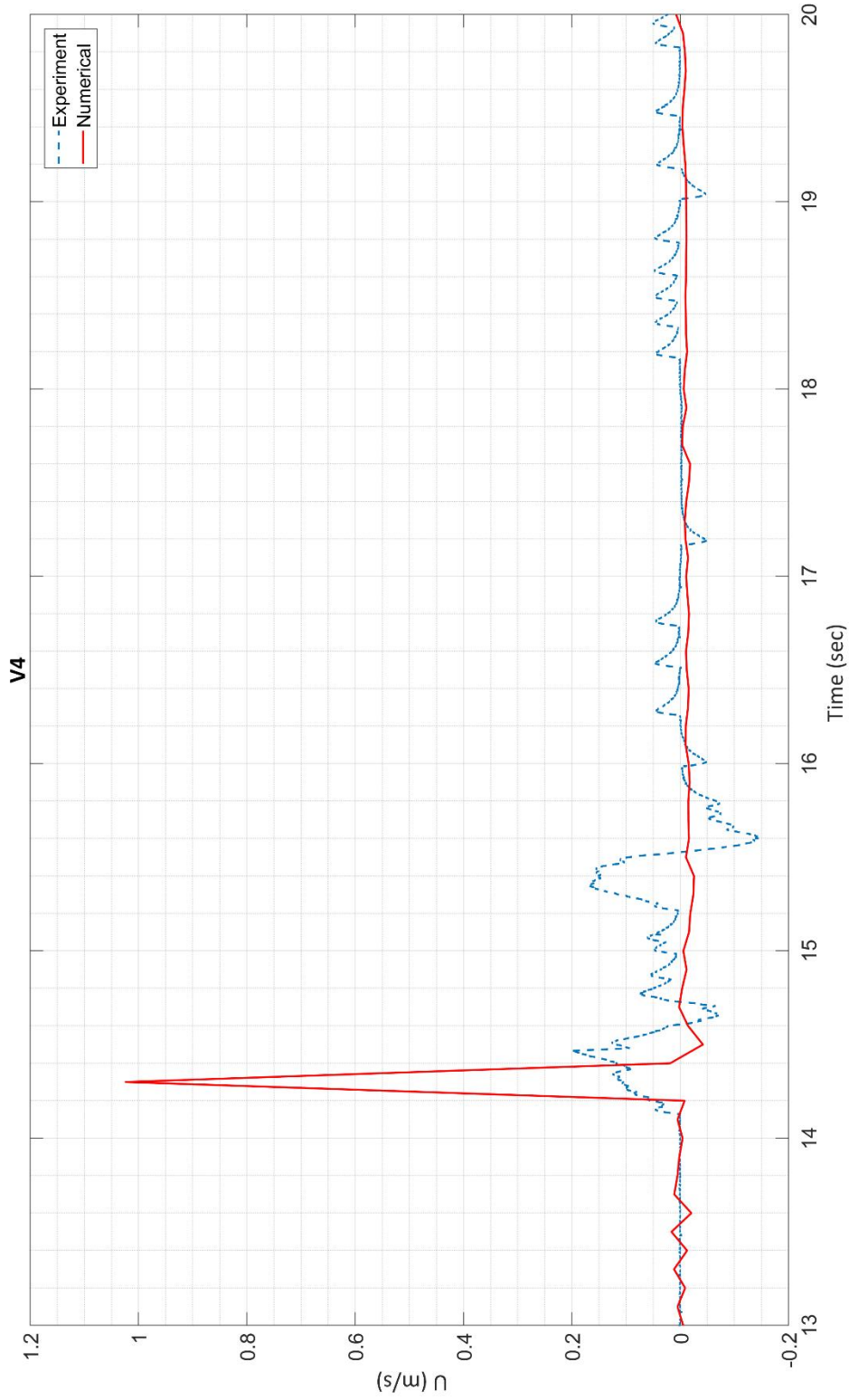


Figure 3.10. Comparison of Particle Velocities in x-direction, U of NAMI DANCE with Experimental Measurements at V4
for Case 1

Snapshots from simulations of NAMI DANCE for Case 1 are given in Figure 3.11.

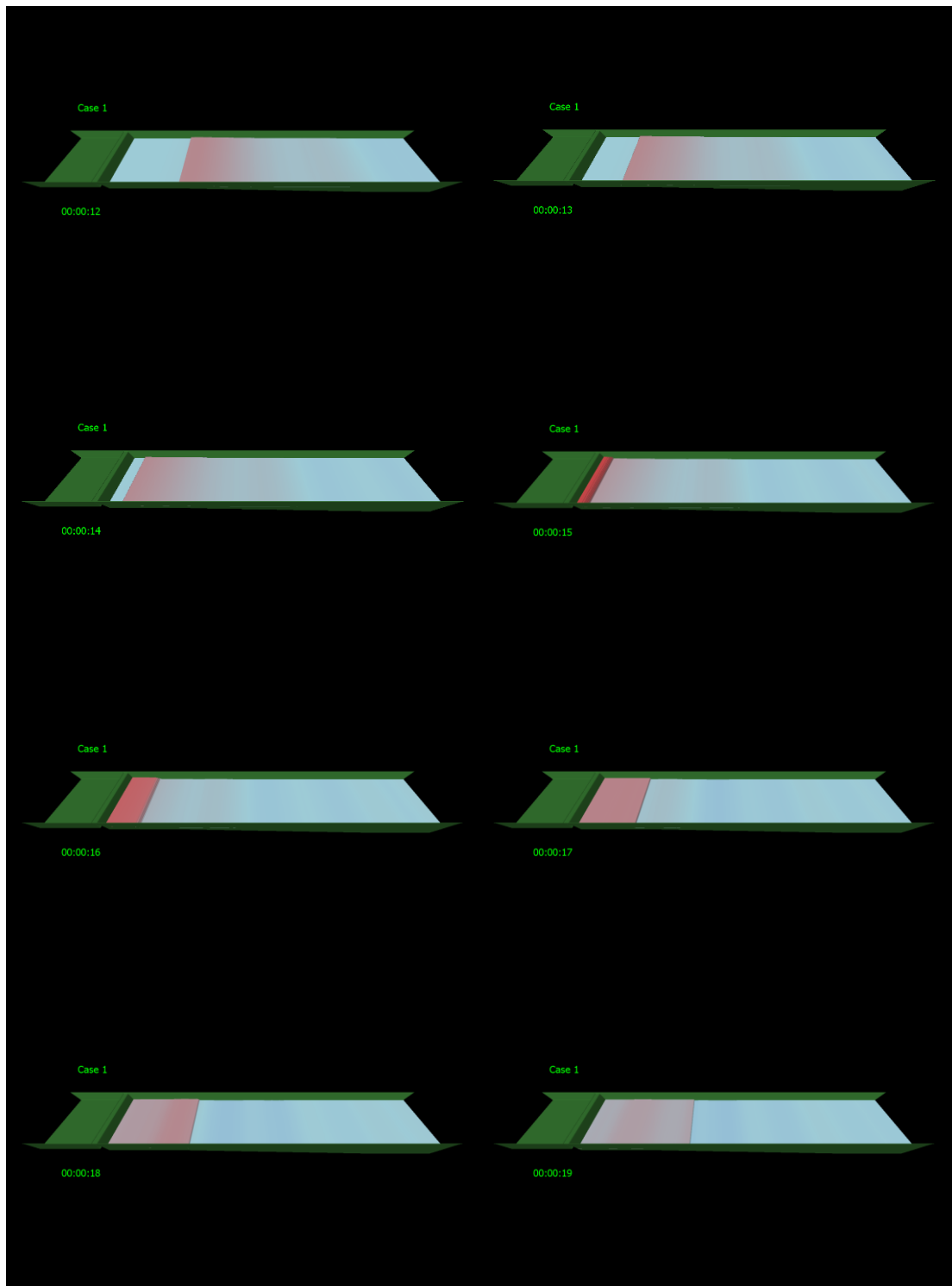


Figure 3.11. Snapshots from Simulation of Case 1 with NAMI DANCE

Similar comparisons for Case 2 on the time histories of water surface elevations obtained from NAMI DANCE simulation and the time histories in physical model experiments are presented in Figure 3.12 for wave gauges from WG1 to WG9. The results of the gauges from WG1 to WG7 demonstrate that the time histories are satisfactorily represented considering the measured data along the wave channel. At WG7, the general trend of the experimental data is achieved but NAMI DANCE underestimated the first peak of the incoming solitary wave. The same situation is valid for WG8 and WG9. Also, it is seen that NAMI DANCE could not properly model the water surface elevation under the reflected wave effect. Also it can be seen that there is a time lag between the results. A closer look to the WG9 which is the wave gauge located in front of the vertical wall can be seen in detail in Figure 3.13 to distinguish the difference. The Figure 3.13 clearly shows that NAMI DANCE was not able to compute splashes occurred due to the slamming of the solitary wave to the vertical wall at this location as expected.

Comparison between the time histories of the horizontal component of particle velocities in the x-direction and the measured time histories in physical experiments at velocity gauges (V1-V5) are presented in Figure 3.14. Again, it is seen that the trend of the computed time histories of the particle velocities is consistent with the trend of the physical model experiments along the channel at velocity gauges V1, V2, and V3. At the location of V4, solitary wave starts breaking. NAMI DANCE could not represent the particle velocities correctly at that location. In Figure 3.15 a detailed look is provided for the V5 which is the critical velocity gauge located just in front of the vertical wall. It is seen that NAMI DANCE failed to compute the velocities accurately. The time lag occurred since the water particle velocities underestimated at V4 located just in front of the small step. Therefore, the time required for solitary wave to reach the V5 is longer than the experiment. These results were expected since the incident impact of the wave and the vertical wall is a highly nonlinear turbulence dominant phenomenon, and NAMI DANCE is a depth-averaged model.

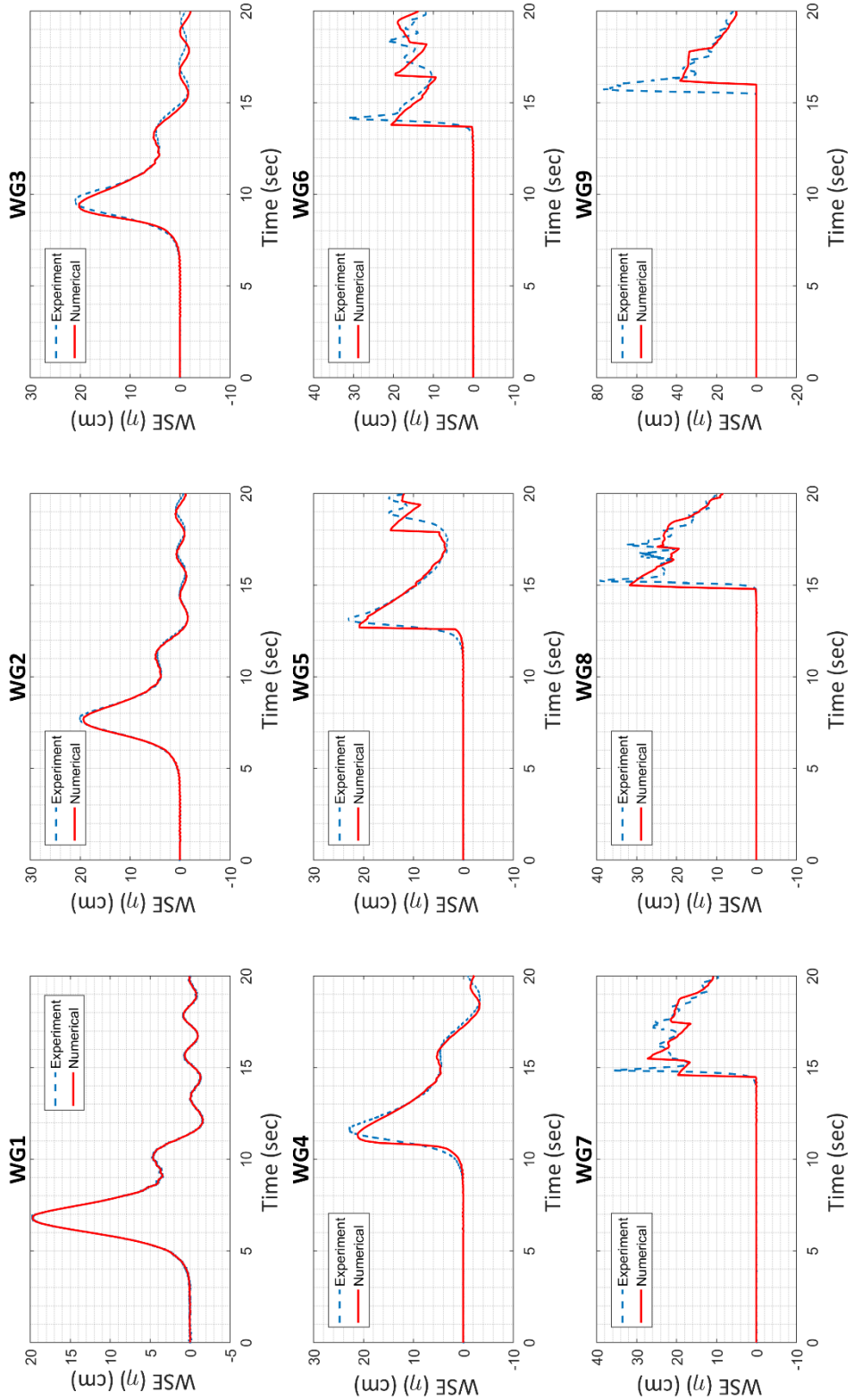


Figure 3.12. Comparison of Water Surface Elevations of NAMI DANCE with Experimental Measurements for Case 2

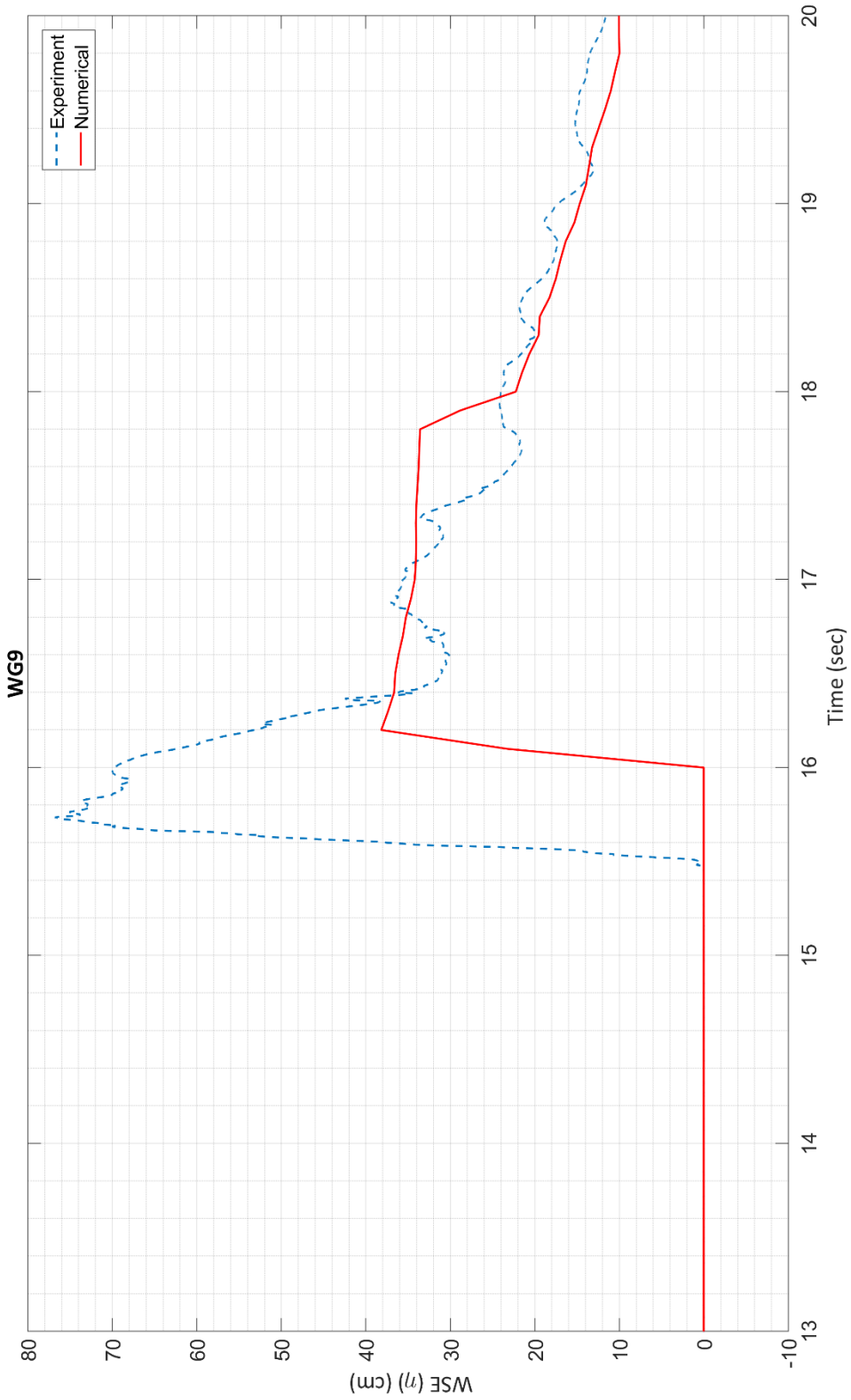


Figure 3.13. Comparison of Water Surface Elevations of NAMIDANCE with Experimental Measurements at WG9 for Case 2

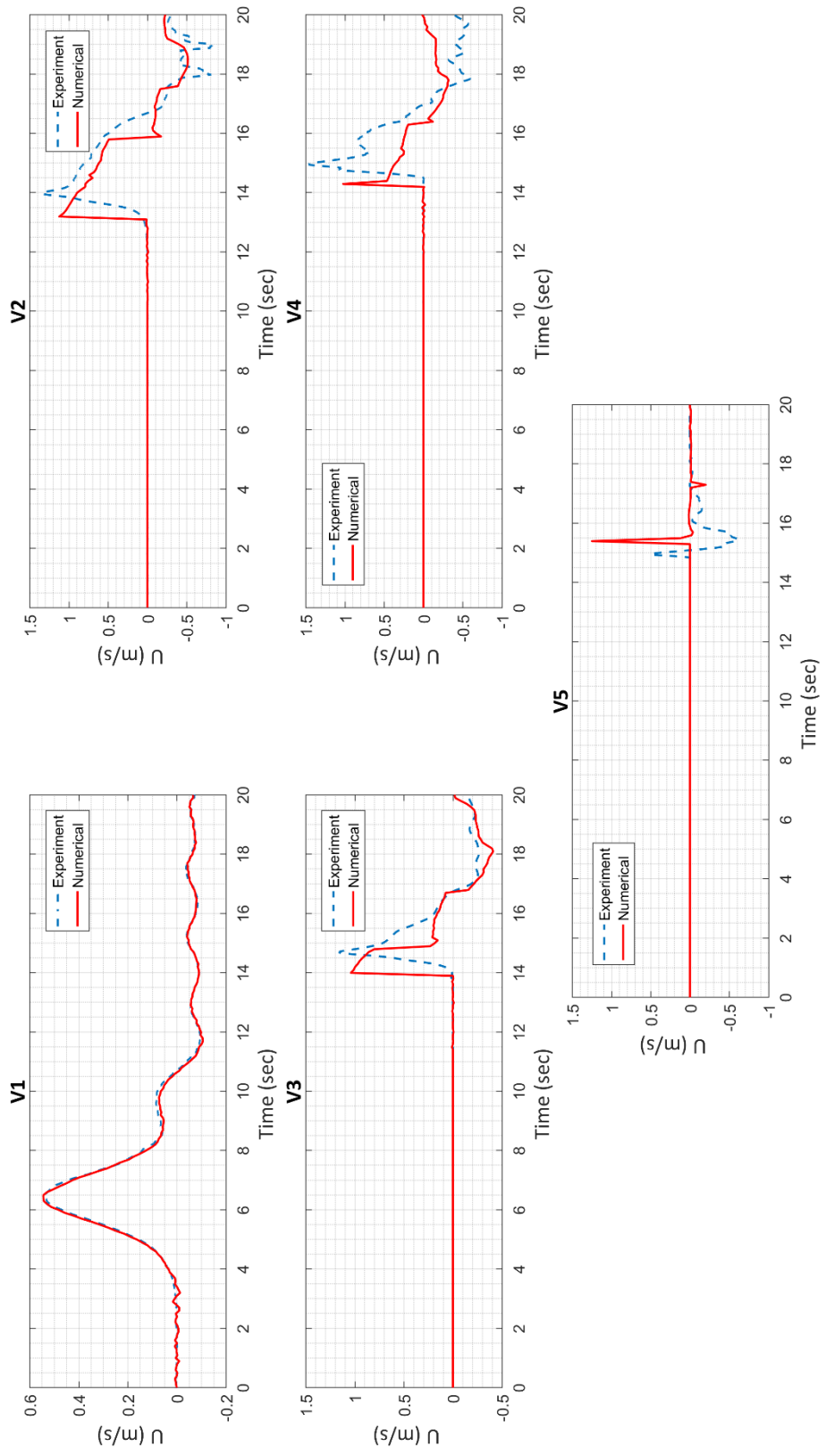


Figure 3.14. Comparison of Particle Velocities in x-direction, U of NAMI DANCE with Experimental Measurements for Case 2

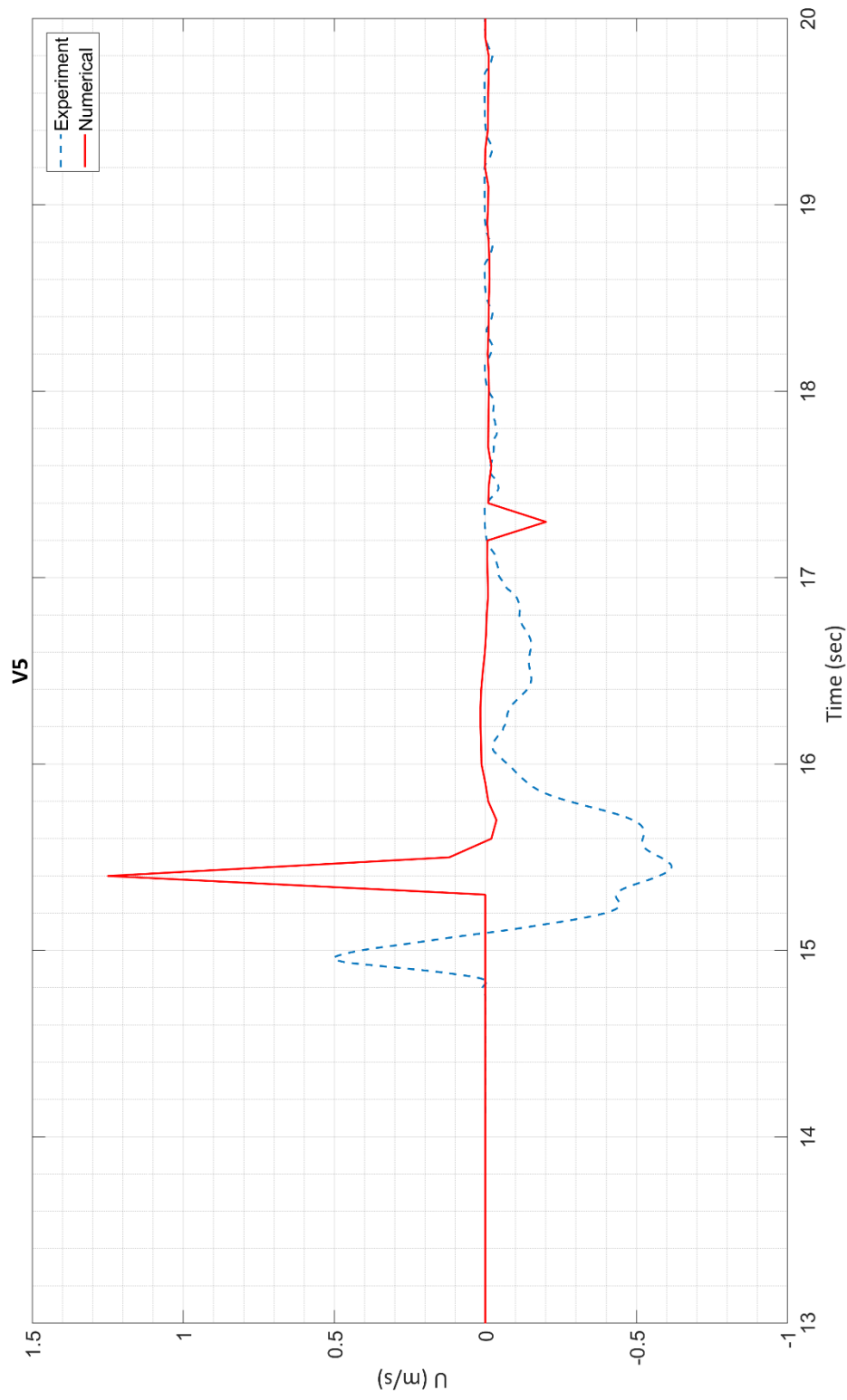


Figure 3.15. Comparison of Particle Velocities in x-direction, U of NAMIDANCE with Experimental Measurements at V5 for Case 2

Snapshots from simulations of NAMI DANCE for Case 2 are given in Figure 3.16.

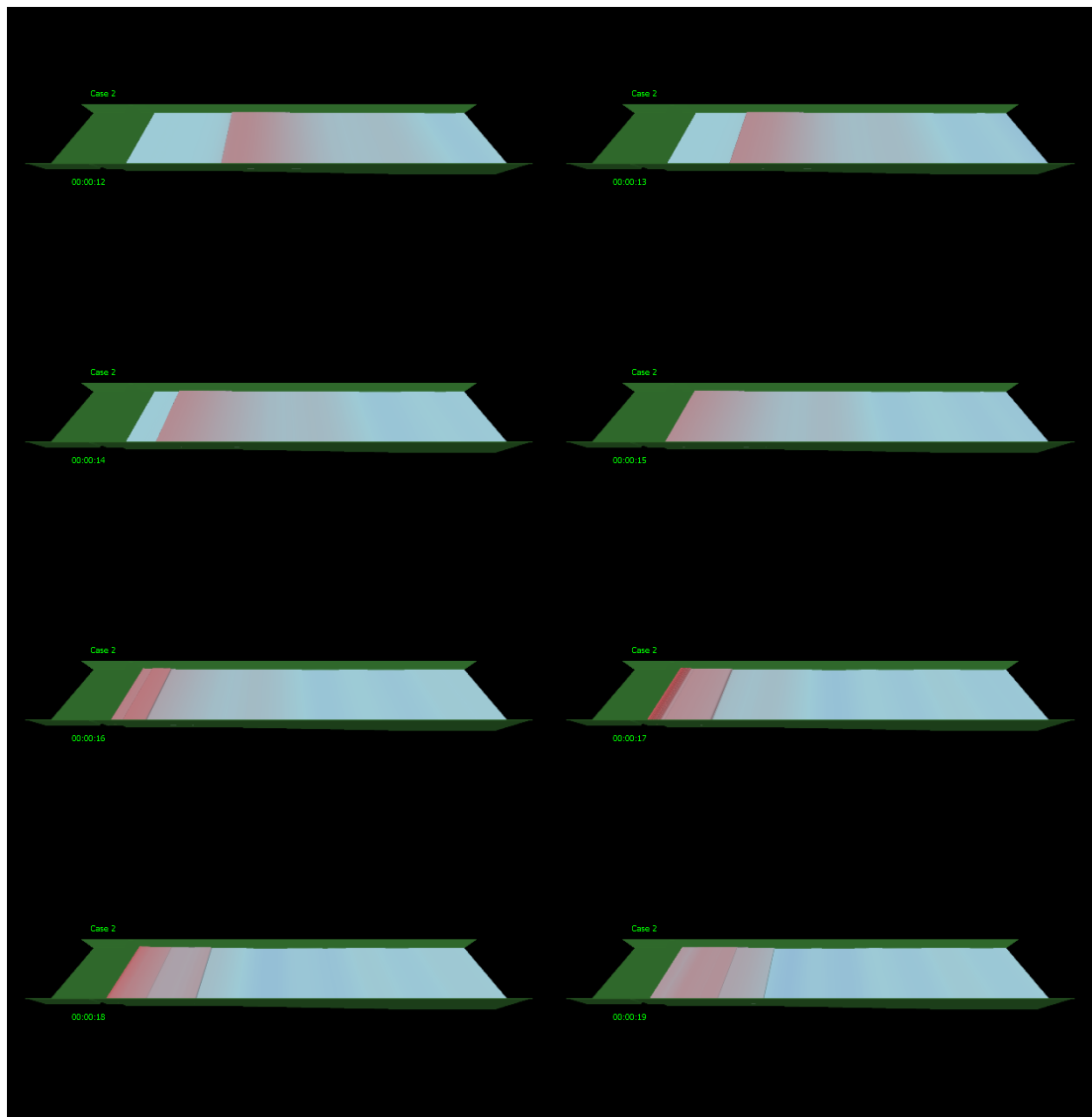


Figure 3.16. Snapshots from Simulation of Case 2 with NAMI DANCE

Lastly, for Case 3, the time histories of water surface elevations obtained from NAMI DANCE simulation and the time histories in physical model experiments are compared and presented in Figure 3.17 for wave gauges from WG1 to WG10. The results of the gauges from WG1 to WG8 demonstrate that along the wave channel the time histories are satisfactorily represented trend of the measured data. However, the peak value of the water surface elevation at WG 7 could not compute accurately by the NAMI DANCE. The solitary wave reaches the WG9 as a breaking wave. The mechanism is highly complex at this location and as expected NAMI DANCE results are not accurate against the experimental data. Also, it can be seen that there is a time lag between the results. For the wave gauge in front of the vertical wall, WG10, a detailed look is provided in Figure 3.18. It is certain that NAMI DANCE could not solve the maximum splash height occurred in front of the vertical wall correctly. This result was predictable since it is highly complicated to solve the incident of the impact of the solitary wave with the vertical wall accurately even for the 3D Navier-Stokes models.

Comparison between the time histories of the horizontal component of particle velocities in the x-direction and the measured time histories in physical experiments at velocity gauges (V1-V6) are presented in Figure 3.19. Although the general trend of the numerical model is matched with the experimental trend along the channel, at gauges V4 and V5 NAMI DANCE underestimated the particle velocities. Since the V5 located at the same point with WG9, the discussions related to it valid for V5 too. In Figure 3.20 a detailed look is provided for the V6 which is the critical velocity gauge located just in front of the vertical wall. Similar with Case 2, the time lag occurred since the water particle velocities underestimated at V4 located just in front of the small step. Therefore, the time required for solitary wave to reach the V6 is longer than the experiment. Even if the computed results are similar with the experimental data for the rising motion of the solitary wave on the vertical wall, NAMI DANCE failed to compute the velocities accurately under the effect of downward motion. The results at this location were expected since the NAMI DANCE is a depth-averaged model.

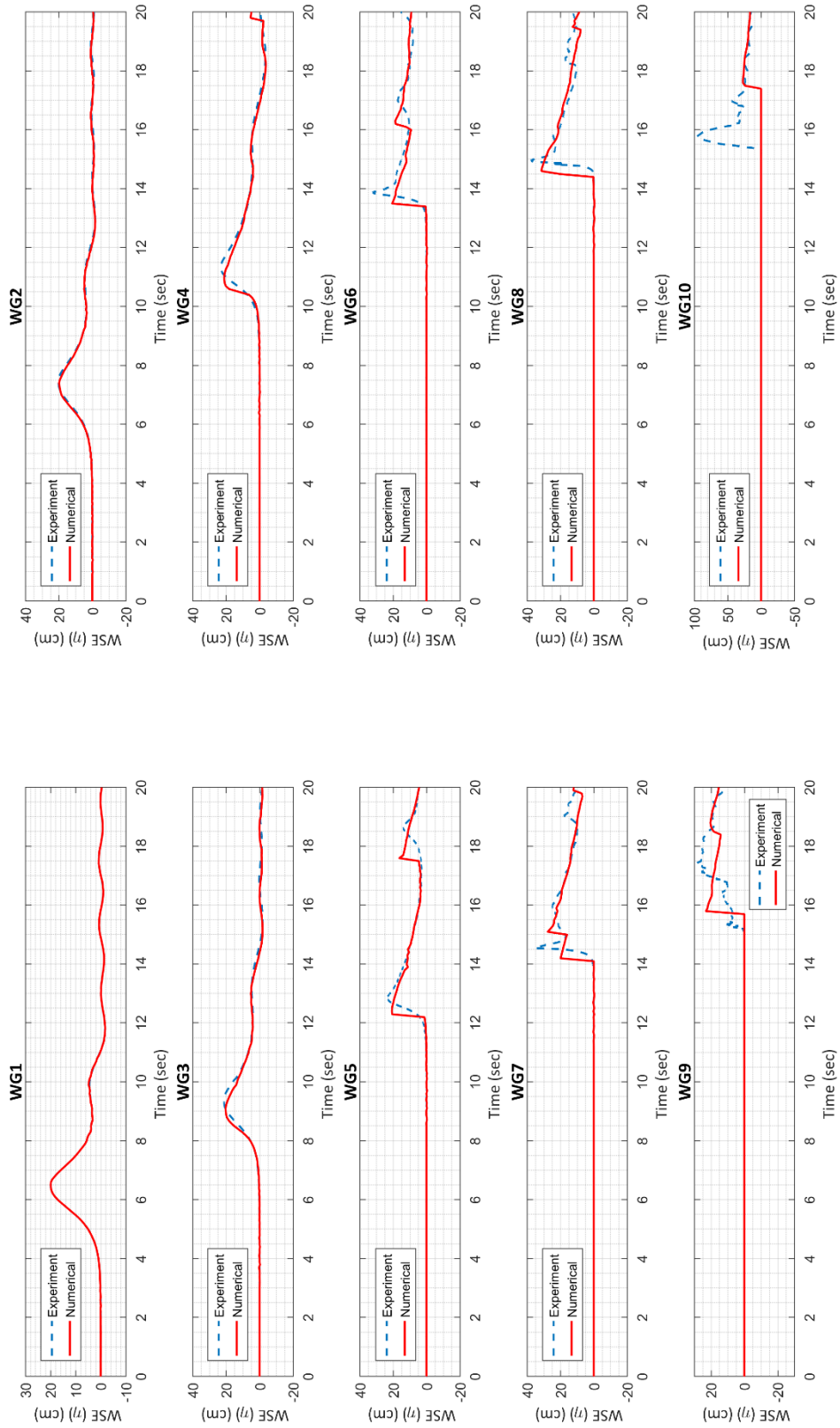


Figure 3.17. Comparison of Water Surface Elevations of NAMI DANCE with Experimental Measurements for Case 3

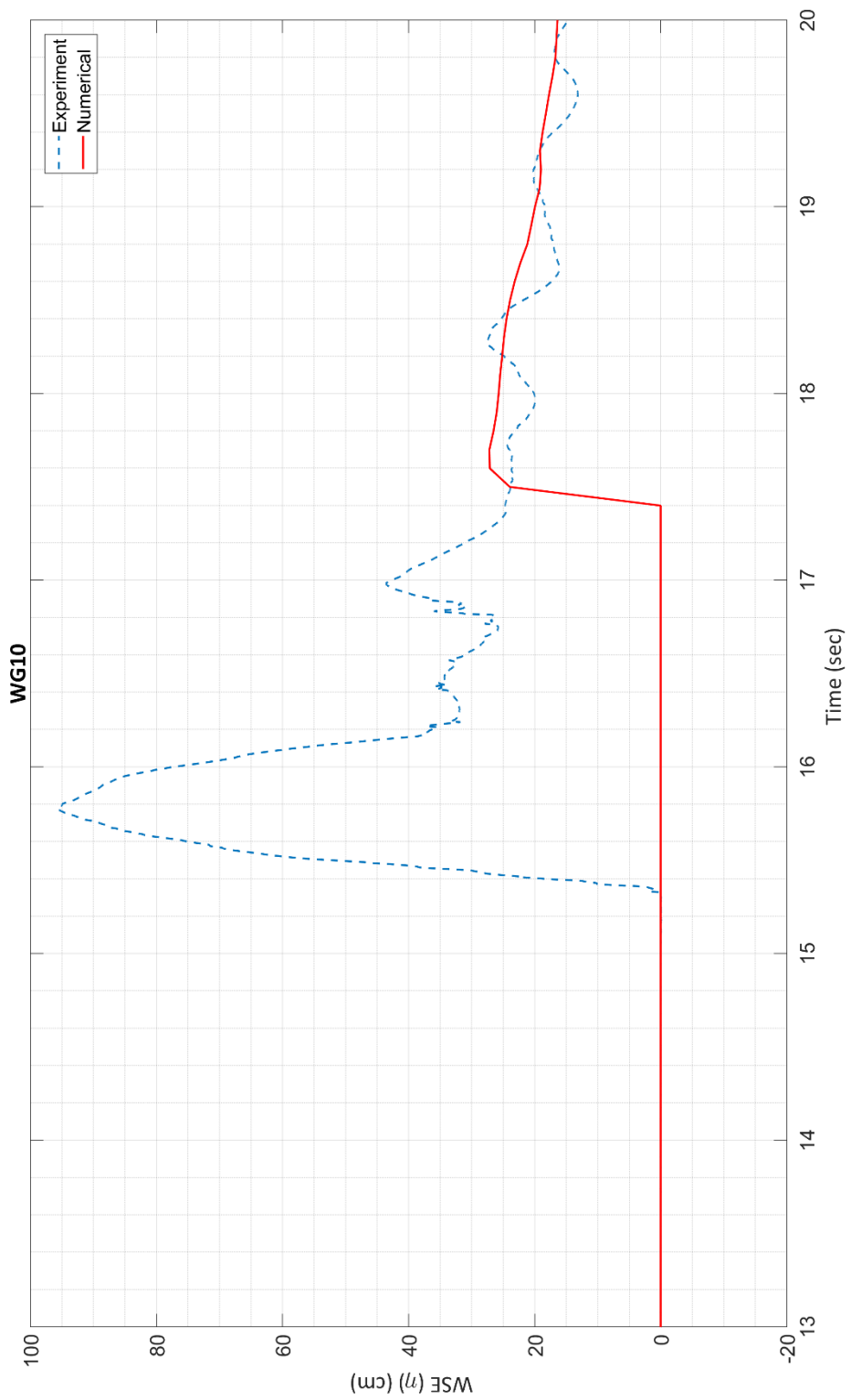


Figure 3.18. Comparison of Water Surface Elevations of NAMIDANCE with Experimental Measurements at WG10 for Case 3

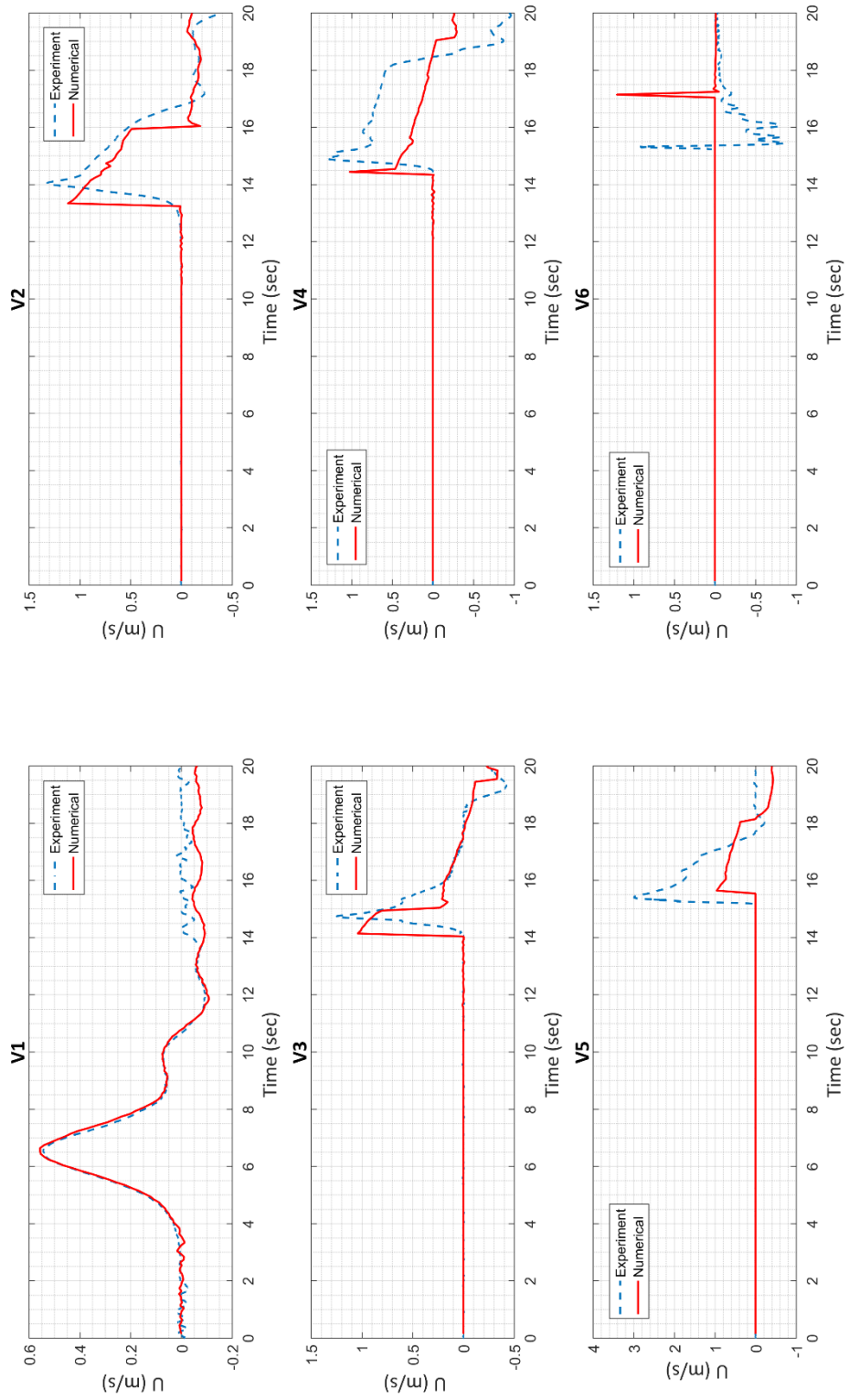


Figure 3.19. Comparison of Particle Velocities in x-direction, U of NAMIDANCE with Experimental Measurements for Case 3

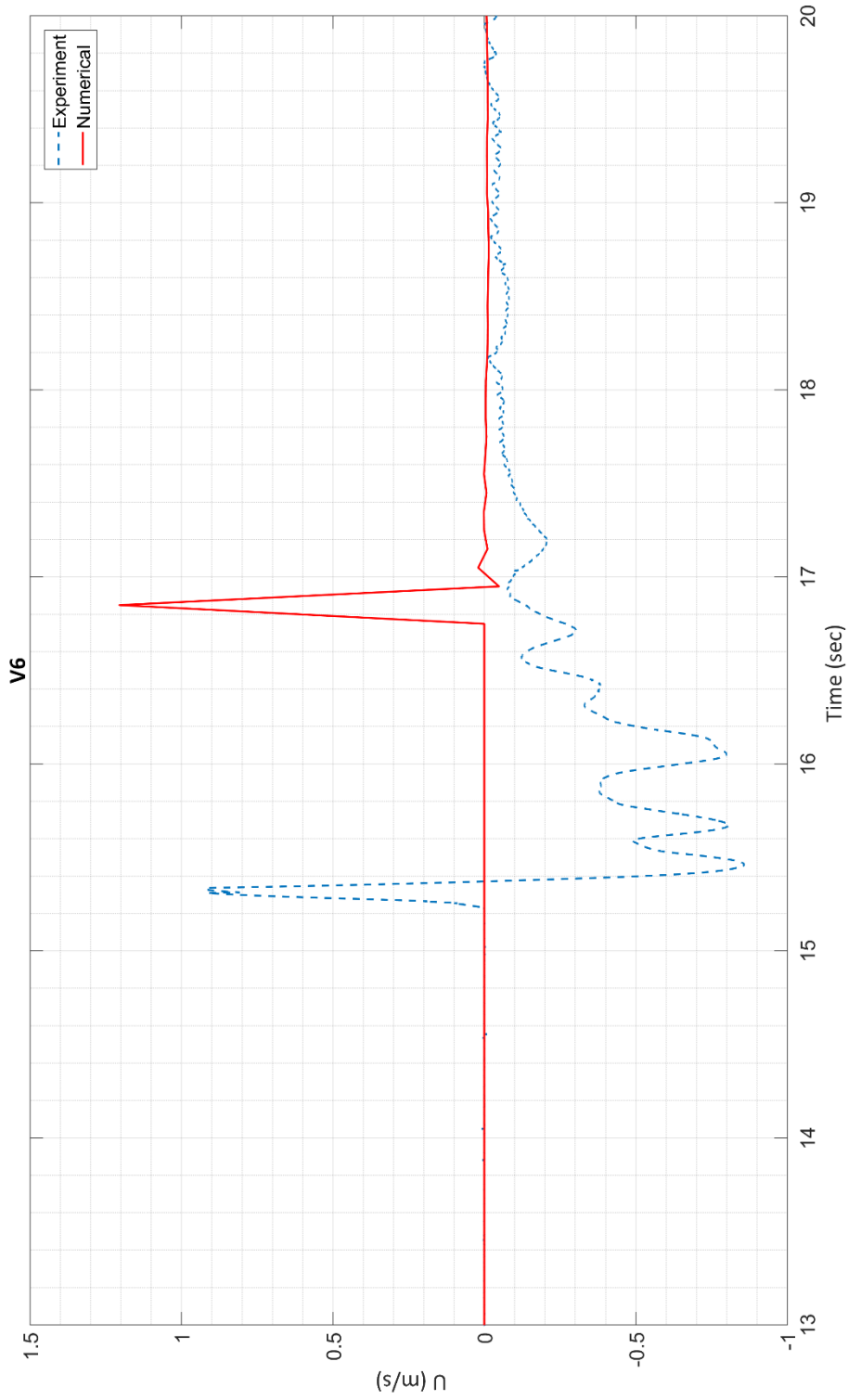


Figure 3.20. Comparison of Particle Velocities in x-direction, U of NAMI DANCE with Experimental Measurements at V6 for Case 3

Snapshots from simulations of NAMI DANCE for Case 3 are given in Figure 3.21.

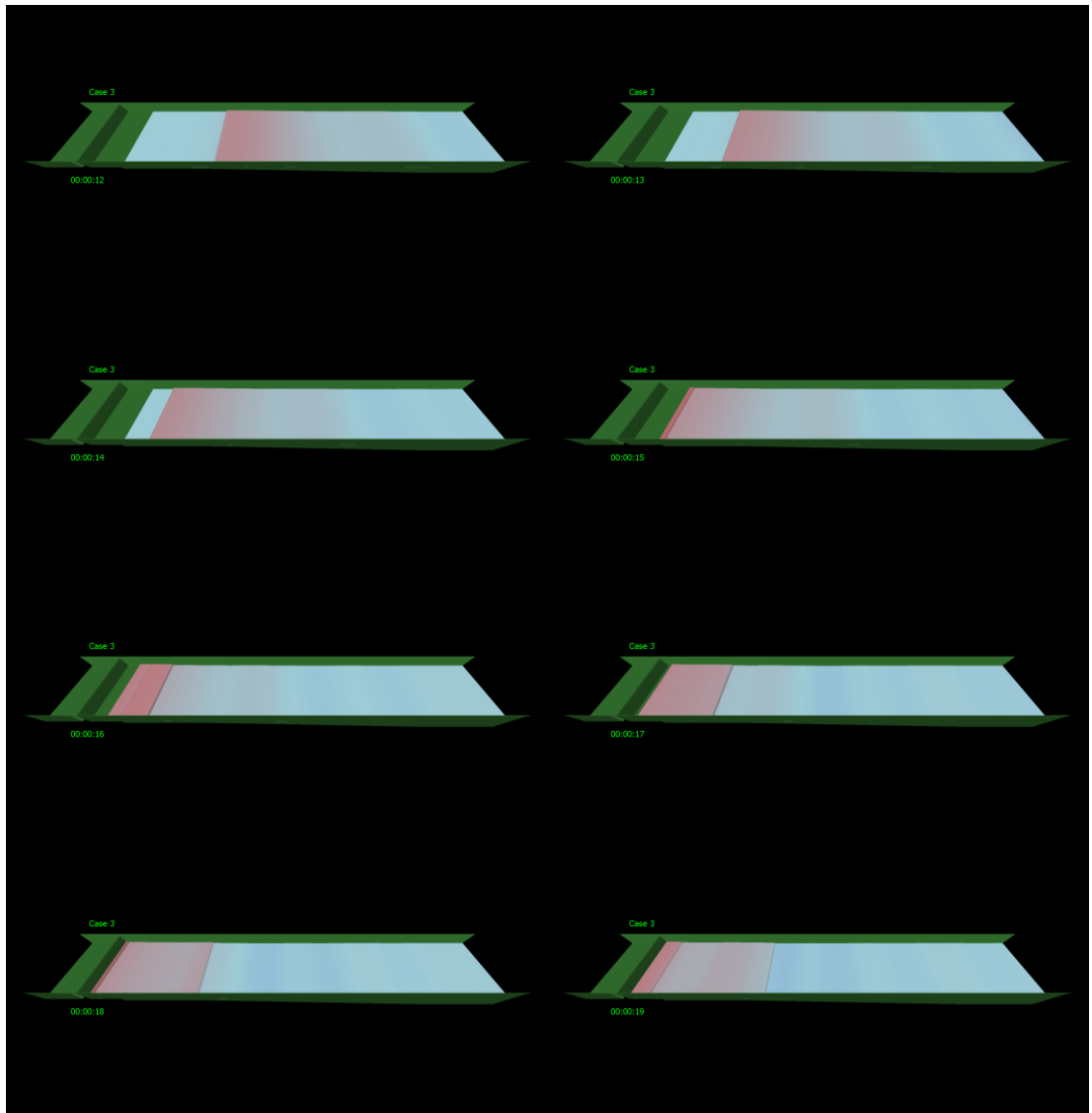


Figure 3.21. Snapshots from Simulation of Case 3 with NAMI DANCE

In this Chapter, three physical model experiments are numerically modeled in 2D with depth-averaged NSWE solver NAMI DANCE. For all three cases, it is seen that NAMI DANCE performed well computing the wave propagation along the channel. The results of the time series of water surface elevations are reasonably good until the solitary wave starts breaking at the end of the slope. For the wave gauges in front of the vertical wall, it is clearly seen that NAMI DANCE could not solve the peak water surface elevations caused by the splashes at the incident of wave impact. In all cases, NAMI DANCE underestimates the water particle velocity along the channel. For the velocity gauges in front of the vertical wall, NAMI DANCE could not provide accurate results and highly overestimated the water particle velocities since it is a depth-averaged model.

CHAPTER 4

IHFOAM SOLVER OF OPENFOAM

OpenFOAM® (Open Field Operation And Manipulation) is an open source CFD toolbox includes several C++ libraries to solve complex problems using finite volume discretization. Accessibility of the source code is one of the biggest advantages of OpenFOAM®. With this distinctive feature, users can control and modify each step of the solving process. It also has some features that help pre- and post-process the cases. OpenFOAM® allows users prepare and run their cases in parallel and provide an easy approach to handle the decomposition and reconstruction (optional) process. “interFoam” is one of the solvers in OpenFOAM® solving 3D Navier-Stokes equations for two incompressible phases (water and air) with the VOF method. In the VOF method, phases are described by a fraction occupied by the volume of fluid. This method enables to capture free surface. Turbulence modeling is often generic in OpenFOAM®. One may use two-equation turbulence models with RANS equations or Large Eddy Simulation to take turbulence effect into account.

IHFOAM is firstly used as a numerical tool that is based on interFoam solver of OpenFOAM®. It was developed by Higuera et al. (2013a) to be used in coastal engineering applications by the implementation of realistic boundary conditions of wave generation and absorption in OpenFOAM® environment. In Higuera et al. (2013b) the model applied to coastal engineering problems. After that, IHFOAM was presented and validated as a solver of OpenFOAM® by Higuera et al. (2014a) for porous media flow solving the VARANS equations. The VARANS equations are a modified version of RANS proposed by del Jesus et al. (2012). Treating each medium

as homogeneous and ignoring the complex geometry, this technique distinguishes the mean flow inside the porous media. IHFOAM solver also has some key features like wave generation and active wave absorption for both static and dynamic meshes and an enhanced version of dynamic meshing. Several test cases are tested with this solver and presented in Higuera et al. (2014b).

4.1. Numerical Scheme of IHFOAM

The fundamental equations of IHFOAM solver are continuity equation, momentum equation, and the VOF function advection equation given in Equations 4.1-4.3.

$$\frac{\partial}{\partial x_i} \frac{u_i}{n} = 0 \quad [4.1]$$

$$(1+c) \frac{\partial}{\partial t} \left(\frac{\rho u_i}{n} \right) + \frac{u_j}{n} \frac{\partial}{\partial x_j} \left(\frac{\rho u_i}{n} \right) = - \frac{\partial p}{\partial x_i} + \rho g_i \\ + \frac{\partial}{\partial x_j} \left(\mu_{eff} \frac{\partial}{\partial x_i} \left(\frac{u_i}{n} \right) \right) - A \frac{u_i}{n} - B \frac{u_i}{n} \left| \frac{u_i}{n} \right| \quad [4.2]$$

$$\frac{\partial \alpha}{\partial t} + \frac{1}{n} \frac{\partial \alpha u_i}{\partial x_i} + \frac{1}{n} \frac{\partial \alpha (1-\alpha) u_i}{\partial x_i} = 0 \quad [4.3]$$

where u_i is the extended averaged or Darcy velocity, n is the porosity, ρ is the density, p is the pressure, g is the gravitational acceleration, μ_{eff} is the efficient dynamic viscosity defined as $\mu_{eff} = \mu + \rho v_{turb}$ where μ is the molecular dynamic viscosity and v_{turb} is turbulent kinetic viscosity computed by the selected turbulence model, α is the VOF function which takes value between 0 and 1 (0 means the cell is empty and 1 means cell is full of water). A , B and c are the closure parameters for friction forces, pressure forces and added mass due to the individual elements of the porous media respectively. del Jesus et al. (2012) commented on that as a recommended value c should be taken as 0.34. Formulas of these parameters presented in Engelund (1953) are modified by van Gent (1995) is given in Equations 4.4 and 4.5:

$$A = \alpha \frac{(1-n)^3}{n^2} \frac{\mu}{D_{n50}^2} \quad [4.4]$$

$$B = b \left(1 + \frac{7.5}{KC} \right) \frac{1-n}{n^2} \frac{\rho}{D_{n50}} \quad [4.5]$$

where α and b are the friction parameters, D_{n50} is the material's nominal mean diameter, KC is the Keulegan-Carpenter number for additional friction considering the oscillatory nature and unsteadiness of the system.

In this thesis, since the vertical wall structure is impervious, n is used as 1 and c is taken as 0. This means A and B are both zero so that the porous calculation is out of the concept. In other words, regular RANS equations are solved.

In OpenFOAM®, to solve the coupled field of velocity and pressure a two-step unique methodology called PIMPLE which is the combined version of Pressure Implicit Split Operator (PISO) and Semi-Implicit Method of Pressure Linked Equations (SIMPLE) algorithms is used. Moreover, VOF advection equation is solved by a special solver called Multidimensional Universal Limiter for Explicit Solution (MULES) using a limiter factor and bound the solution between 0 and 1. In IHFOAM, a new version of MULES called IHMULES enables the users to account for the porous media flow.

4.2. Turbulence Models

In this thesis, volume averaged k- ϵ and k- ω -SST turbulence models in IHFOAM are used to calculate the turbulent kinetic energy, v_{turb} . The equations of these turbulence models are briefly explained in this section.

4.2.1. k- ϵ Turbulence Model

The details of the volume-averaging process of this model can be found in del Jesus (2011). Based on the work of del Jesus (2011), the volume-averaged modified (i.e.

$u_i^* = \frac{u_i}{n}$) expressions are given in Equations 4.6-4.11:

$$\frac{\partial}{\partial t} k^* + u_j^* \frac{\partial}{\partial x_j} k^* = \frac{1}{\rho} \tau_{ij}^* S_{ij}^* - \varepsilon^* + \frac{\partial}{\partial x_j} \left[\left(\nu + \frac{\nu_t^*}{\sigma_k} \right) \frac{\partial}{\partial x_j} k^* \right] + \frac{1}{\rho} [CT]_k \quad [4.6]$$

$$\begin{aligned} \frac{\partial}{\partial t} \varepsilon^* + u_j^* \frac{\partial}{\partial x_j} \varepsilon^* &= \frac{1}{\rho} C_{\varepsilon 1} \frac{\varepsilon^*}{k^*} \tau_{ij}^* S_{ij}^* - C_{\varepsilon 2} \frac{\varepsilon^{*2}}{k^*} \\ &\quad + \frac{\partial}{\partial x_j} \left[\left(\nu + \frac{\nu_t^*}{\sigma_\varepsilon} \right) \frac{\partial}{\partial x_j} \varepsilon^* \right] + \frac{1}{\rho} [CT]_\varepsilon \end{aligned} \quad [4.7]$$

where

$$\tau_{ij}^* S_{ij}^* = \left[2 \frac{\mu_t}{n} S_{ij}^* - \frac{2}{3} \rho \frac{k}{n} \delta_{ij} \right] S_{ij}^* \quad [4.8]$$

$$S_{ij}^* = \frac{1}{2} \left(\frac{\partial}{\partial x_j} \frac{u_i}{n} + \frac{\partial}{\partial x_i} \frac{u_j}{n} \right) \quad [4.9]$$

$$\mu_t = \rho C_\mu \frac{k^2}{\varepsilon} \quad [4.10]$$

$$\nu_t^* = C_\mu \frac{k^{*2}}{\varepsilon^*} \quad [4.11]$$

k is the turbulent kinetic energy, ε is turbulent dissipation rate, σ_k is a model constant, $\tau_{ij} S_{ij}$ is the production term, S_{ij} refers to the average of the rate of strain tensor, μ_t is turbulent dynamic viscosity, ν_t is turbulent kinematic viscosity, C_μ is the model coefficient and [CT] makes reference to closure term expressed in the Equations 4.12 - 4.15.

For the closure terms;

$$[CT]_k = \varepsilon_\infty \quad [4.12]$$

$$[CT]_\varepsilon = C_{\varepsilon 2} \frac{\varepsilon_\infty^2}{k_\infty} \quad [4.13]$$

$$k_\infty = 3.7(1-n)n^{\frac{7}{2}} \sum_i u_i^{*2} \quad [4.14]$$

$$\varepsilon_\infty = 39.0(1-n)^{\frac{5}{2}} n^5 \sum_i u_i^{*2} \frac{1}{D_{50}} \quad [4.15]$$

4.2.2. *k*- ω -SST Turbulence Model

The *k*- ω -SST model combines the *k*- ε and *k*- ω turbulence models using some blending functions. The aim of this model to obtain the results as good as *k*- ω when modeling the boundary layer flow and as good as *k*- ε in free flow modeling.

The expressions of the *k*- ω -SST model are given in Equations 4.16-4.18:

$$\frac{\partial}{\partial t} k^* + u_j^* \frac{\partial}{\partial x_j} k^* = \frac{1}{\rho} \tau_{ij}^* S_{ij}^* - \beta^* \omega^* k^* + \frac{\partial}{\partial x_j} \left[(\nu + \sigma_k \nu_t) \frac{\partial}{\partial x_j} k^* \right] + \frac{1}{\rho} [CT_{SST}]_k \quad [4.16]$$

$$\begin{aligned} \frac{\partial}{\partial t} \omega^* + u_j^* \frac{\partial}{\partial x_j} \omega^* &= \frac{1}{\rho \nu_t} \tau_{ij}^* S_{ij}^* - \beta^* \omega^{*2} + \frac{\partial}{\partial x_j} \left[(\nu + \sigma_\omega \nu_t) \frac{\partial}{\partial x_j} \omega^* \right] \\ &+ 2(1-F_1) \sigma_{\omega 2} \frac{1}{\omega^*} \frac{\partial}{\partial x_j} k^* \frac{\partial}{\partial x_j} \omega^* + \frac{1}{\rho} [CT_{SST}]_\omega \end{aligned} \quad [4.17]$$

$$\nu_t = \frac{\alpha_1 k^*}{\max[\alpha_1 \omega^*, \Omega^* F_2]} \quad [4.18]$$

where k is the turbulent kinetic energy, ω is the specific rate of dissipation of turbulent kinetic energy to internal thermal energy, $\tau_{ij} S_{ij}$ is the production term, β and σ_k are model constants and Ω is the mean rate of rotation tensor.

Blending functions bounded from 0 to 1 appear in the equations as $F_1 = \tanh(\arg_1^4)$ and $F_2 = \tanh(\arg_2^2)$. The arguments are calculated in Equations 4.19-4.21:

$$\arg_1 = \min \left\{ \min \left[\max \left(\frac{\sqrt{k^*}}{\beta^* \omega^* y}; \frac{500\nu}{\omega^* y^2} \right); \frac{4\sigma_{\omega^2} k^*}{CD_{k\omega} y^2} \right]; 10 \right\} \quad [4.19]$$

$$CD_{k\omega} = \max \left(2n\sigma_{\omega^2} \frac{1}{\omega^*} \frac{\partial}{\partial x_j} k^* \frac{\partial}{\partial x_j} \omega^*; 10^{-10} \right) \quad [4.20]$$

$$\arg_2 = \min \left[\max \left(\frac{2\sqrt{k^*}}{\beta^* \omega^* y}; \frac{500\nu}{\omega^* y^2} \right); 100 \right] \quad [4.21]$$

4.3. Numerical Setup of the Experiments for IHFOAM

The physical experiments of Arikawa (2015) are reproduced in a two-dimensional domain using IHFOAM solver of OpenFOAM®. The reader can refer to Section 2.1.5 for details of the physical model experiments. The cartesian coordinate system is used to create the bathymetry for the simulations. The positive x-direction is towards the vertical wall and same with the direction of propagation of the solitary wave. On the other hand, positive z-direction is opposite of the gravitational force.

Although the length of the flume is 105 m, to decrease the computational time of the simulation, time series of water surface elevation and velocity measured at the location of WG1 and V1 gauges are used as an input to the system at 0.6 m behind of the location of the gauges. Thus, the total length of the computational domain is determined as 29.5 m, 30.75 m and 32 m for Case 1, Case 2 and Case 3 respectively.

The mesh sizes are same for all three cases. Maximum mesh size is 5 cm along the x-axis starting from the beginning of the channel to the location of WG1 as a constant value. From there to the end of the 1/10 slope (see Figure 2.2) the mesh size along x (Δx) is decreasing from 5 cm to 1 cm. After that, it is fixed and minimum Δx is 1 cm. Mesh size along the y-axis (Δy) is determined as 2 cm and limited to only one cell as these simulations are carried out as a 2D case. Mesh size of 0.5 cm along the z-axis (Δz) used as a fixed value through the whole computational domain.

In this simulations, generic boundary conditions given in OpenFOAM® are used except for the inlet boundary condition. The inlet boundary condition is selected as measured surface water elevation at WG1 and water particle velocity at V1 forced by the boundary conditions given by IHFOAM. Also, wave absorption condition is applied at the inlet. The upper boundary condition is set as ‘atmosphere’, the bottom and the vertical wall boundary condition is used as ‘wall’ and the side walls are selected as ‘empty’. Selecting ‘empty’ boundary condition along a selected direction converts the simulations to 2D as the momentum equation is not solved in this selected direction.

The water depth at the inlet of the computational domain is 1.252 meters. Water density is 1000 kg/m^3 and gravitational acceleration is 9.81 m/s^2 . The simulation duration is set as 20 sec for all three cases. Three simulations with laminar, k- ϵ and k- ω -SST turbulence models are carried out and the results of the simulations are compared for each case.

4.3.1. Case 1

The total length of the computational domain is 29.5 meters in the x-direction and 3.4 meters in the z-direction. The vertical wall is located on the small step at the end of the horizontal floor. The side view of the channel can be seen in Figure 4.1. The total of approximately 700.000 cells are present in this simulation.

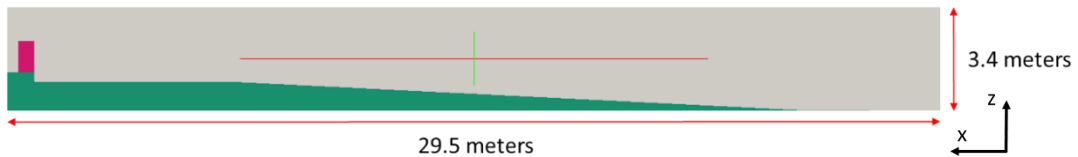


Figure 4.1. Orientation of the coordinate system and two-dimensional computational domain of the Case 1 for IHFOAM model

4.3.2. Case 2

The total length of the computational domain is 30.75 meters in the x-direction and 3.0 meters in the z-direction. Vertical wall position is shifted 1 meter away from the small step at the end of the horizontal floor. The side view of the channel can be seen in Figure 4.2. The total number of cells is approximately 650.000 in this simulation.

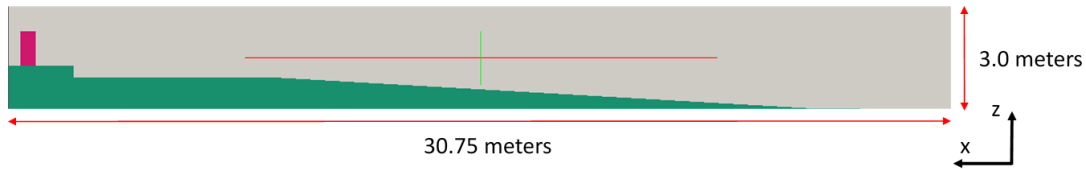


Figure 4.2. Orientation of the coordinate system and two-dimensional computational domain of the Case 2 for IHFOAM model

4.3.3. Case 3

The total length of the computational domain is 32.0 meters in x-direction and 3.0 meters in z-direction. In this case, the vertical wall is located 2 meters away from the small step at the end of the horizontal floor. The side view of the channel can be seen in Figure 4.3. The total number of cells is approximately 690.000 in this simulation.

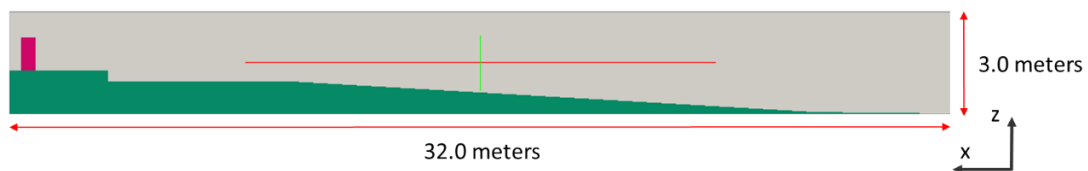


Figure 4.3. Orientation of the coordinate system and two-dimensional computational domain of the Case 3 for IHFOAM model

4.4. Results and Discussions of the Simulations of IHFOAM

The results of the simulations and the detailed discussions on them are presented in this section. The sampling interval for the experimental data is 2000 Hz. On the other

hand, the output time interval for numerical simulations are kept as 0.1 sec in order to optimize storage requirements.

Comparison of the time histories of water surface elevations obtained from each simulation (laminar, $k-\epsilon$ and $k-\omega$ -SST) for Case 1 and the measured data of time histories in physical model experiments is presented in Figure 4.4 for wave gauges from WG1 to WG8. The results show that along the wave channel the time histories are in a good agreement with the measured data. The differences between the computed and measured data at these gauges (WG1-WG7) start due to the reflection occurred by hitting of the solitary wave to the vertical wall structure. There is no major difference between the results of turbulence models at the gauges located along the channel. Different results obtained at the WG8 which is the wave gauge located just in front of the vertical wall. In general, it can be said that the simulations have the same trend as the experimental data with no major differences. The closer look of the results of WG8 is given in Figure 4.5 to distinguish the differences. It can be seen that all of the three simulations (laminar, $k-\epsilon$ and $k-\omega$ -SST) resulted in higher water surface elevation than the measured data. The flat part of the experimental data indicates that the wave gauge could not measure the water surface elevation correctly due to the extremely high splashes over the vertical wall. Videos of the experiment are reviewed to validate this statement. Snapshots from the video of the experiment and the simulation with $k-\omega$ -SST turbulence model for Case 1 are presented and the height of the vertical wall is shown in Figure 4.6. It is concluded that the splashes reached much higher values (more than 130 cm) than the measured one. However, it might not be possible to compare the computed peak water surface elevation with the experimental data accurately as the wave gauge could not catch the splash sufficiently.

Comparison between the time histories of the horizontal component of particle velocities in the x-direction and the measured time histories in physical experiments at velocity gauges (V1-V4) are presented in Figure 4.7. Again, it is seen that particle velocities are in fairly good agreement with the physical model experiments along the channel until the reflected waves arrive.

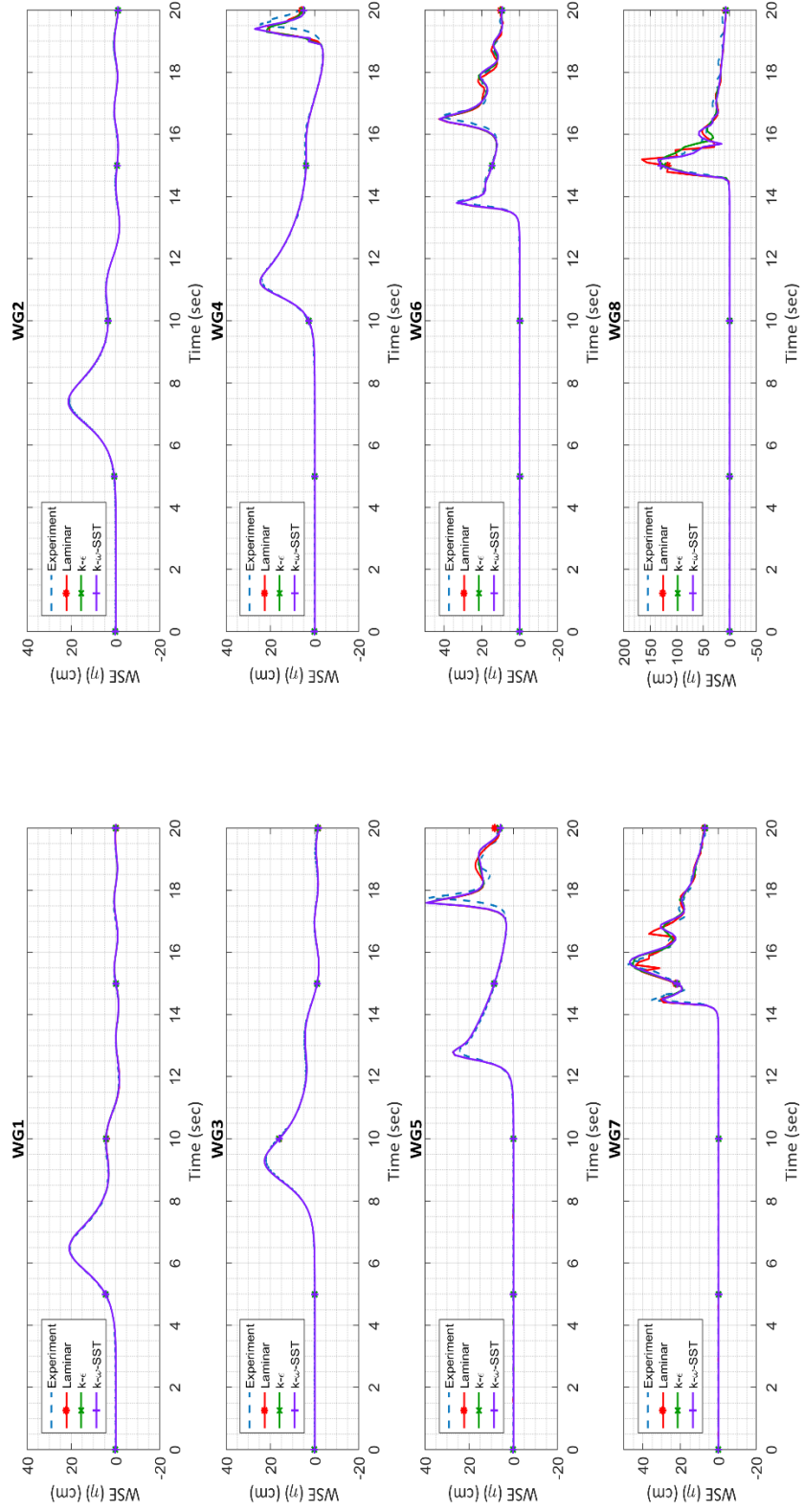


Figure 4.4. Comparison of Water Surface Elevations of IINFOAM with Experimental Measurements for Case 1

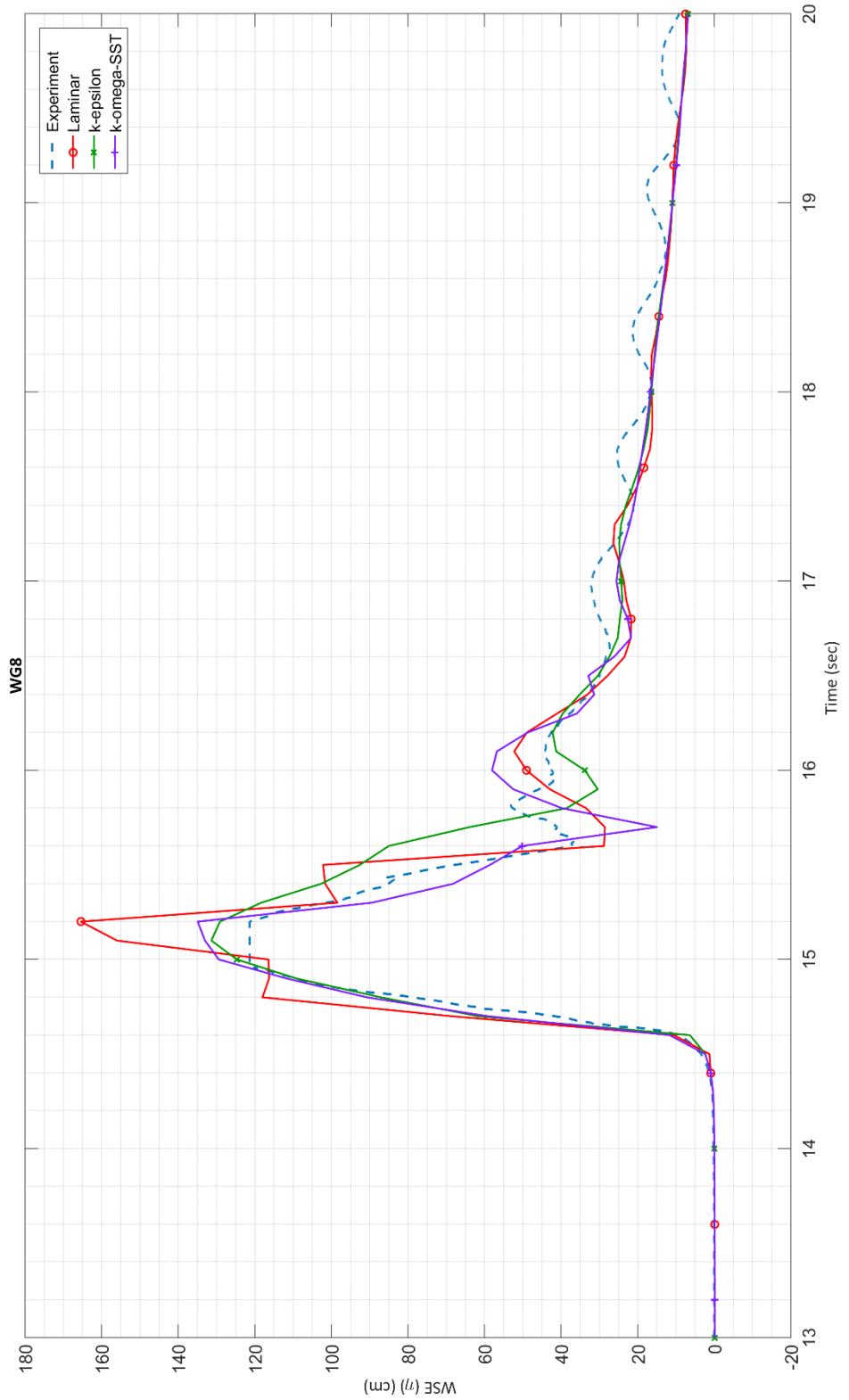


Figure 4.5. Comparison of Water Surface Elevations of IHAOAM with Experimental Measurements at WG8 for Case 1

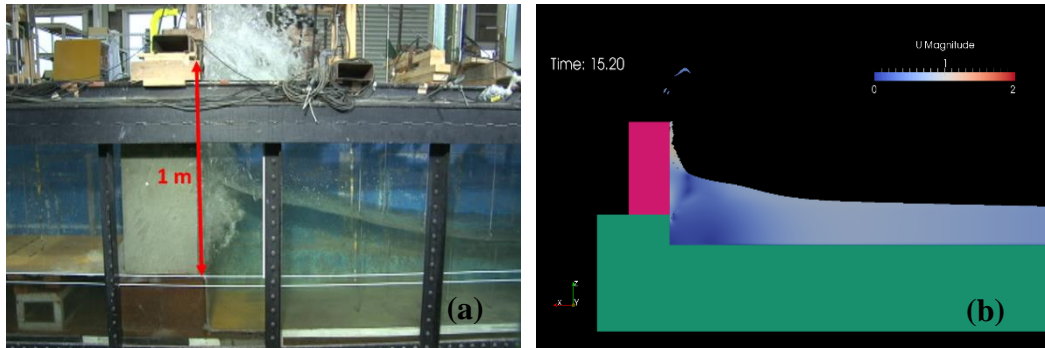


Figure 4.6. Snapshots from (a) the video of the experiment (Arikawa, 2015) and (b) simulation video of the $k-\omega$ -SST turbulence model for Case 1

One of the possible reasons for the differences between the simulations calculating particle velocities is the 2D/3D effects after the wave reflection. Although the difference between the models is not very critical, it can be said from the results of the velocity gauges located along the channel (V1, V2, and V3) that $k-\epsilon$ turbulence model works best for estimating the particle velocities at those locations under the effect of the reflected wave. However, as expected there are some non-negligible deviations at V4. A closer look to the V4 is given in Figure 4.8. It is seen that laminar model could not solve properly the particle velocities on the vertical wall properly. This result was expected since a highly turbulent phenomenon is present at this location when the solitary wave hits the wall. Also, $k-\epsilon$ underestimated the velocities and did not provide a sufficient result. Among the three turbulence models, $k-\omega$ -SST performed the best in this case but it has also some apparent deviations from the experimental data.

Snapshots from simulations performed using laminar, $k-\epsilon$ and $k-\omega$ -SST models for Case 1 indicating the velocity distribution during solitary wave attack are given in Figures 4.9, 4.10 and 4.11, respectively.

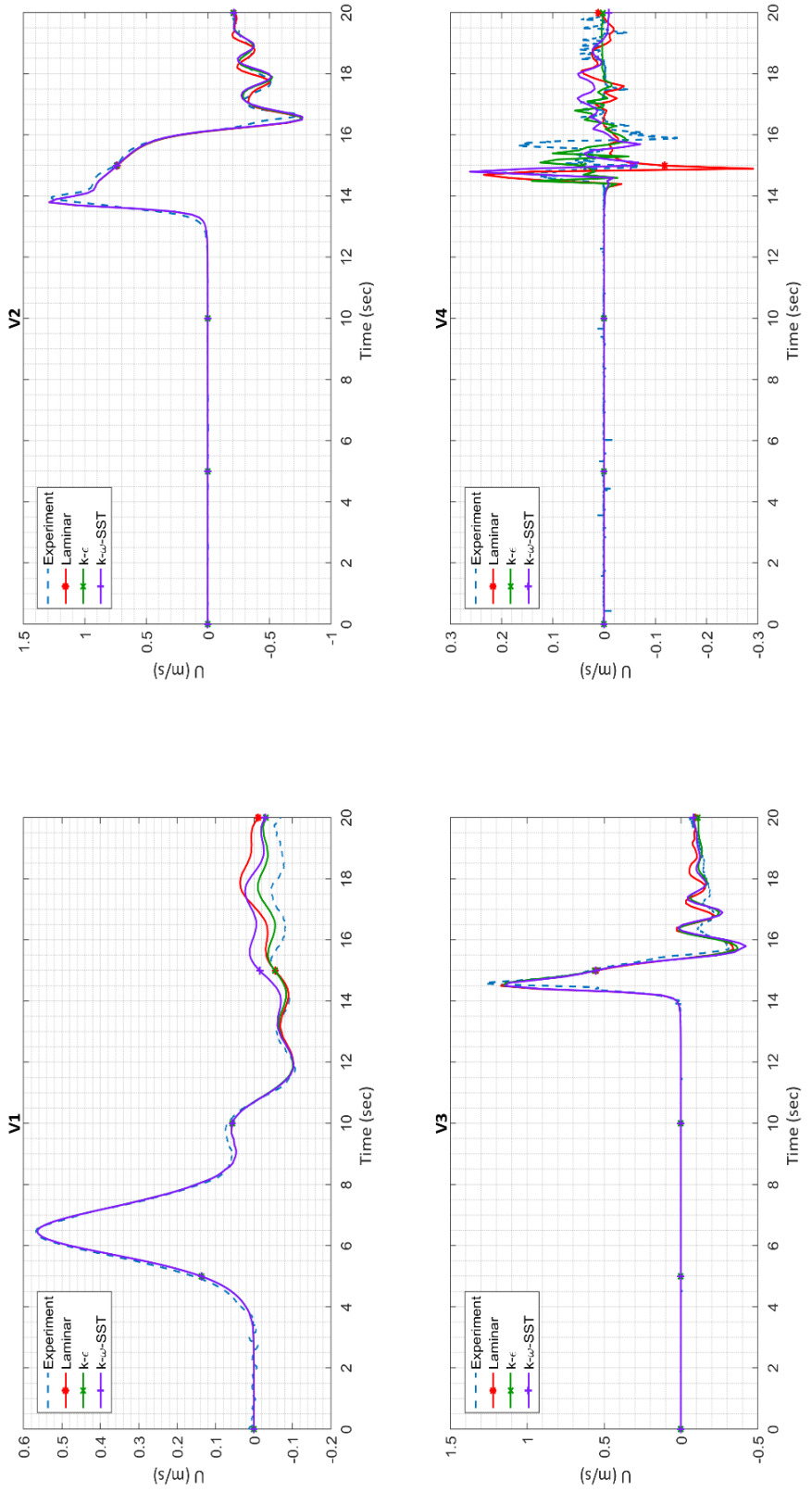


Figure 4.7. Comparison of Particle Velocities in x-direction, U of IHFOAM with Experimental Measurements for Case 1

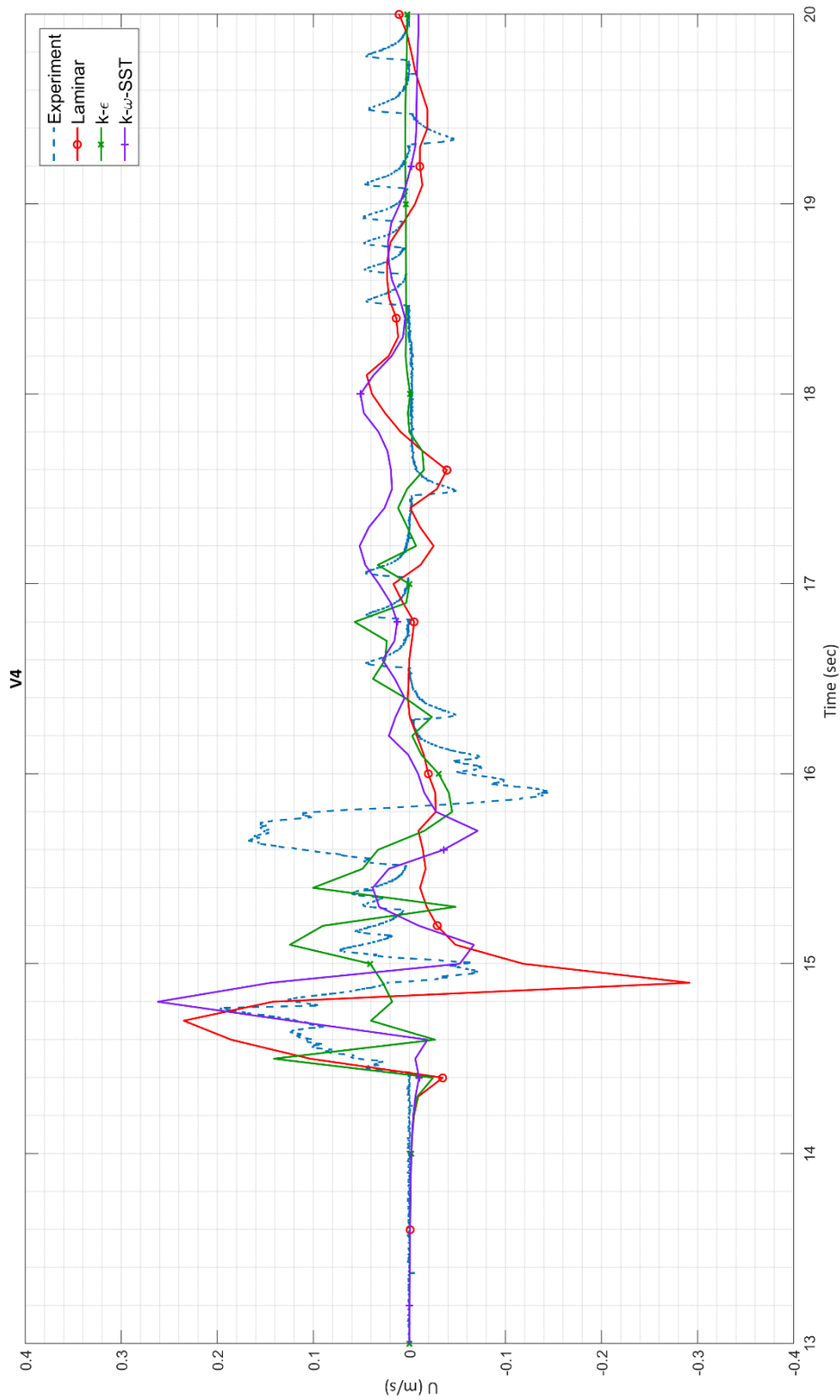


Figure 4.8. Comparison of Particle Velocities in x-direction, U of IHFOAM with Experimental Measurements at V4 for Case 1

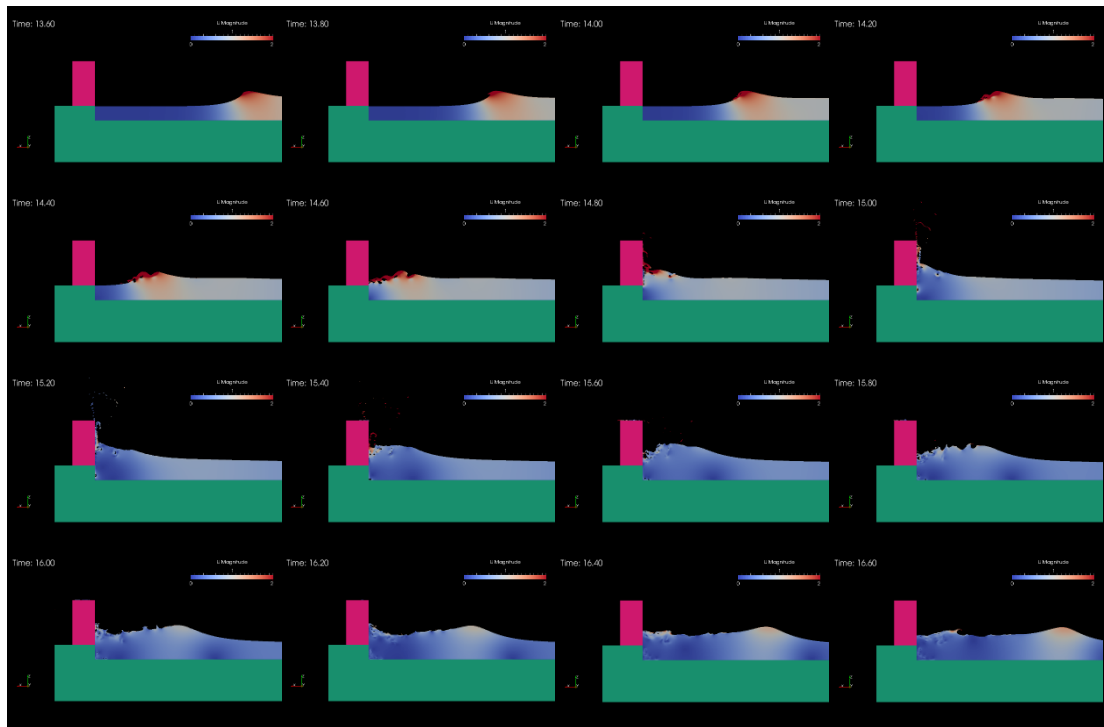


Figure 4.9. Snapshots from Simulation of Case 1 with laminar model

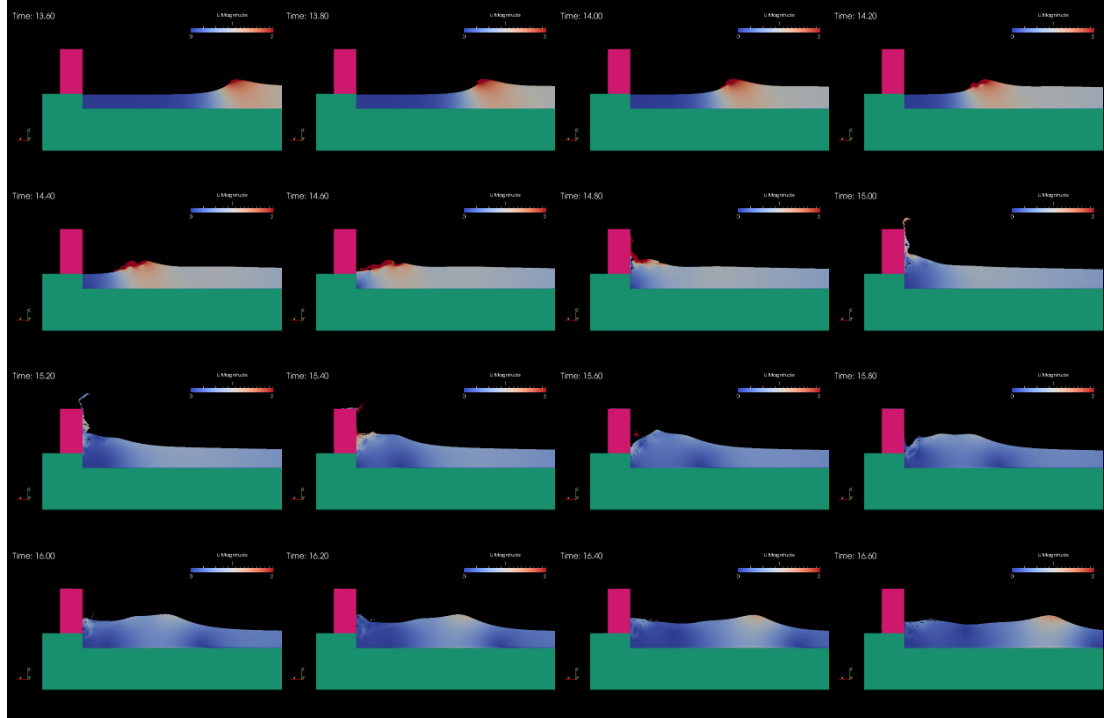


Figure 4.10. Snapshots from Simulation of Case 1 with k-ε model

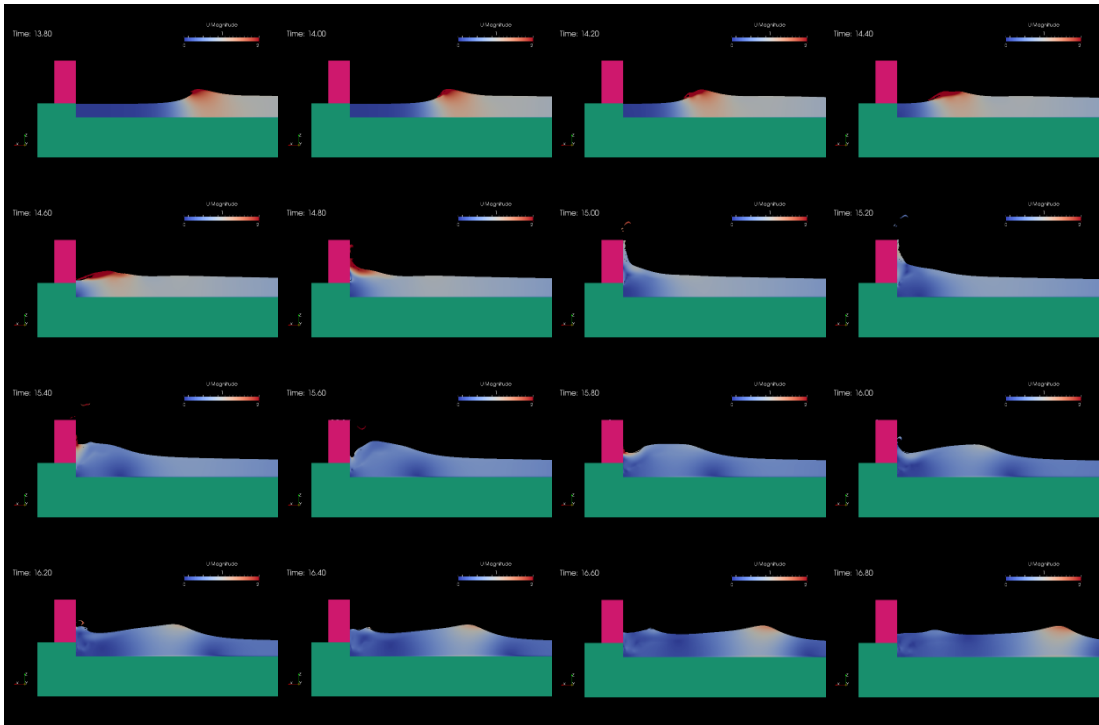


Figure 4.11. Snapshots from Simulation of Case 1 with $k-\omega$ -SST model

Similar comparisons for Case 2 on the time histories of water surface elevations obtained from each simulation (laminar, $k-\epsilon$ and $k-\omega$ -SST) and the time histories in physical model experiments are presented in Figure 4.12 for wave gauges from WG1 to WG9. The results of the gauges from WG1 to WG6 demonstrate that along the wave channel the time histories are in a good agreement with the measured data. At WG7, the general trend of the experimental data is in fairly good agreement with the numerical trend; but, all models underestimated the first peak of the incoming solitary wave and overestimated the second peak due to reflections. The same situation is also valid for the WG8. Overestimation of the water surface elevation by all models at WG9 which is the wave gauge located just in front of the vertical wall can be seen in detail in Figure 4.13 to distinguish the differences. It can be seen that all of the three simulations resulted in higher water surface elevation than the measured data. There is a significant difference between the results of the experimental data and $k-\omega$ -SST model. To check the accuracy of the measured data from the physical experiments,

videos of the experiment are reviewed and snapshot at the incident where the splash reaches its higher value is presented in Figure 4.14 with the snapshot from the simulation video of the $k-\omega$ -SST numerical model at the same incident. When the height of the vertical wall is scaled, it is concluded that the splashes reached much higher values (more than 140 cm) than the measured one. Therefore, due to the extreme splashes, the measurement instruments also faced with difficulties to measure the data correctly. As expected, $k-\omega$ -SST works better and estimated more realistic values for the water surface elevation than the $k-\epsilon$ turbulence model around the wall. It is clearly seen that $k-\epsilon$ turbulence model shows extra dissipative behavior near wall region. Moreover, another comparison between the time histories of the horizontal component of particle velocities in the x-direction and the measured time histories in physical experiments at velocity gauges (V1-V5) are presented in Figure 4.15. Again, it is seen that particle velocities are in fairly good agreement with the physical model experiments along the channel until the reflected waves arrive.

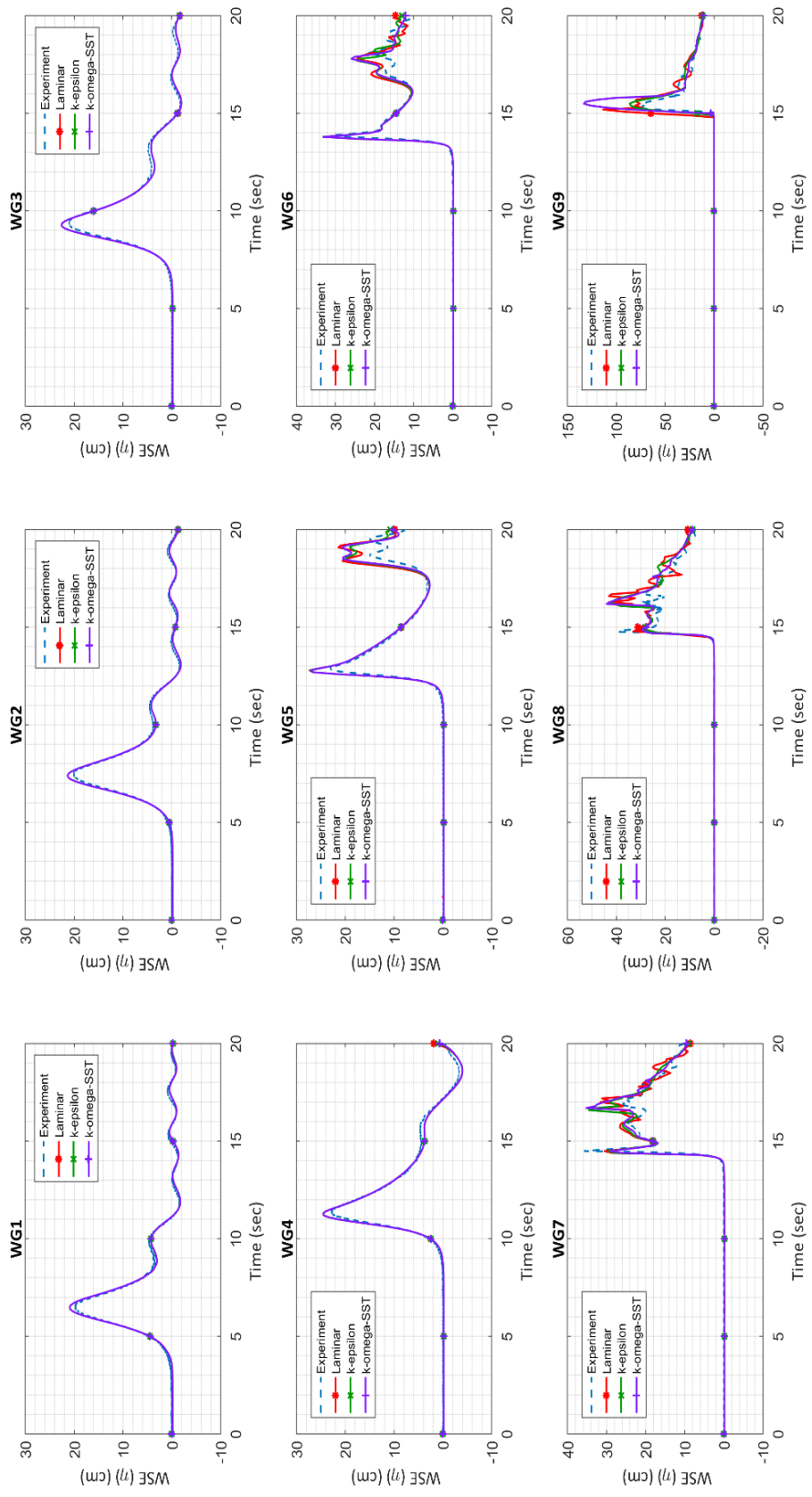


Figure 4.12. Comparison of Water Surface Elevations of IHFOAM with Experimental Measurements for Case 2

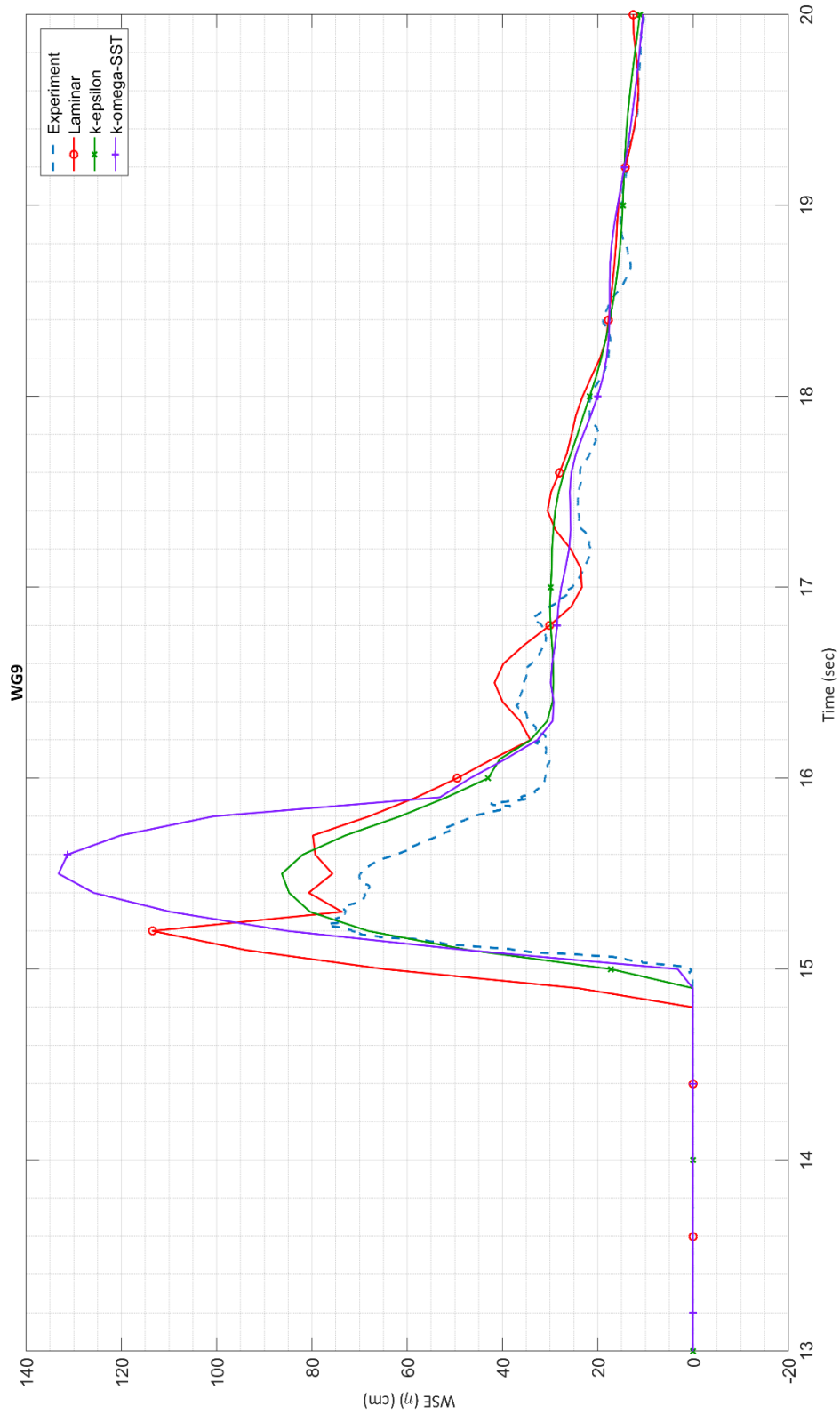


Figure 4.13. Comparison of Water Surface Elevations of IHFOAM with Experimental Measurements at WG9 for Case 2

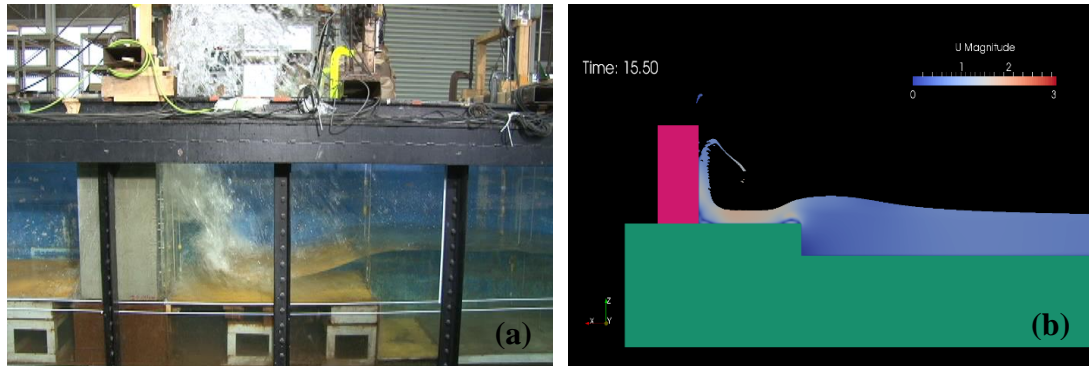


Figure 4.14. Snapshots from (a) the video of the experiment (Arikawa, 2015) and (b) simulation video of the $k-\omega$ -SST turbulence model for Case 2

For this case, the breaking of the solitary wave starts at V4 and continues until the wave reaches the velocity gauge, V5. Again, the 2D/3D effects deviated from the numerical results of the particle velocities from the experimental data. In V4, it is clearly seen that the laminar model is insufficient to solve the particle velocities accurately where turbulence plays a critical role in breaking. Although there is not much difference between the $k-\epsilon$ and $k-\omega$ -SST models, it can be said from the results of the V4 that $k-\epsilon$ turbulence model works better for estimating the particle velocities at that location under the effect of the reflected wave. The critical velocity gauge is V5 in this case since it is located just in front of the vertical wall. A closer look to the V5 is given in Figure 4.16.

It is seen that the $k-\epsilon$ and $k-\omega$ -SST results are in consistency with the general trend of the experimental data. However, $k-\omega$ -SST turbulence model significantly overestimated the peak velocity and did not provide accurate results. In this case, the $k-\epsilon$ turbulence model performed much better than the $k-\omega$ -SST contrary to the expectations since this gauge is located near wall region. For the laminar model, it could not solve properly the particle velocities on the vertical wall. This result was expected since a highly turbulent phenomenon is present at this location when the solitary wave hits the wall.

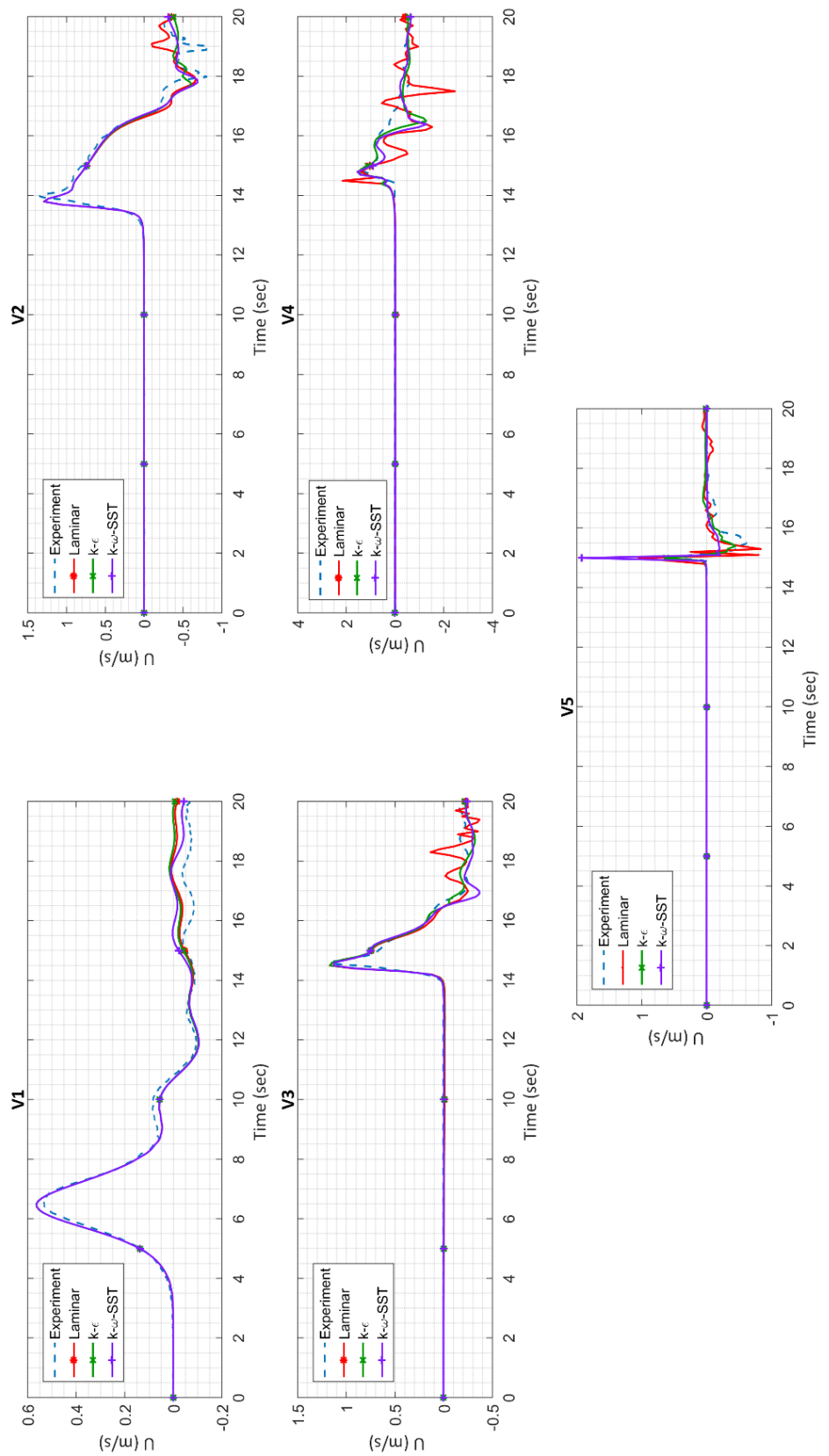


Figure 4.15. Comparison of Particle Velocities in x-direction, U of IINFOAM with Experimental Measurements for Case 2

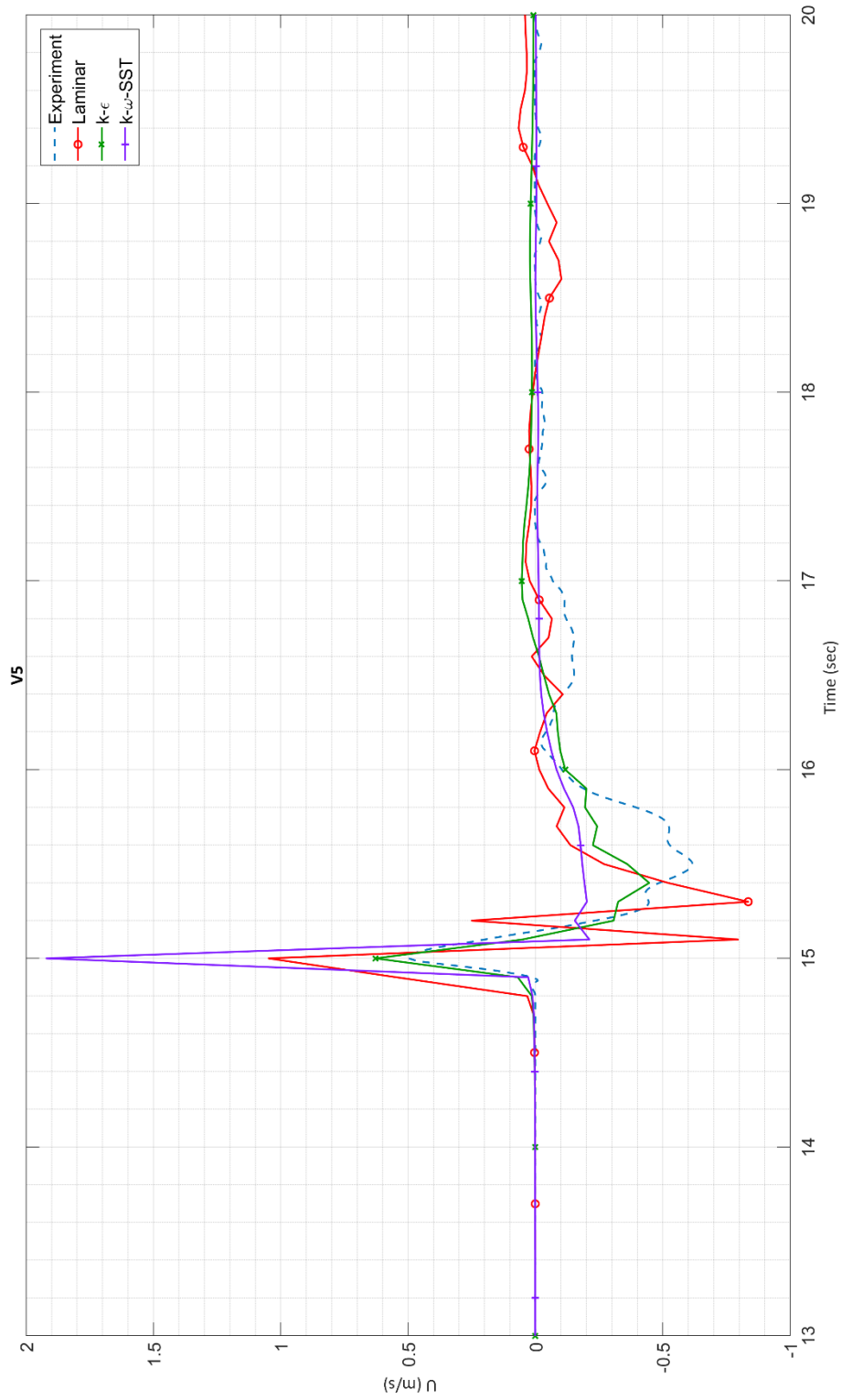


Figure 4.16. Comparison of Particle Velocities in x-direction, U of IHFOAM with Experimental Measurements at V5 for Case 2

Snapshots from simulations performed using laminar, k- ϵ and k- ω -SST models for Case 2 indicating the velocity distribution during solitary wave attack are given in Figures 4.17, 4.18 and 4.19, respectively.

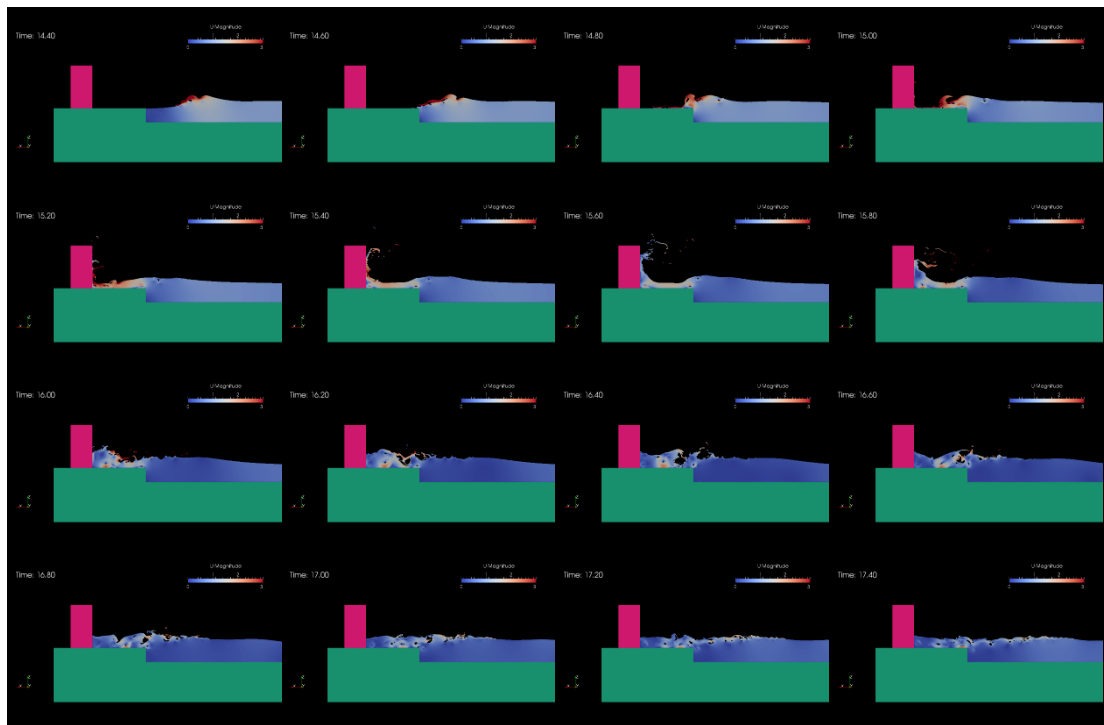


Figure 4.17. Snapshots from Simulation of Case 2 with laminar model

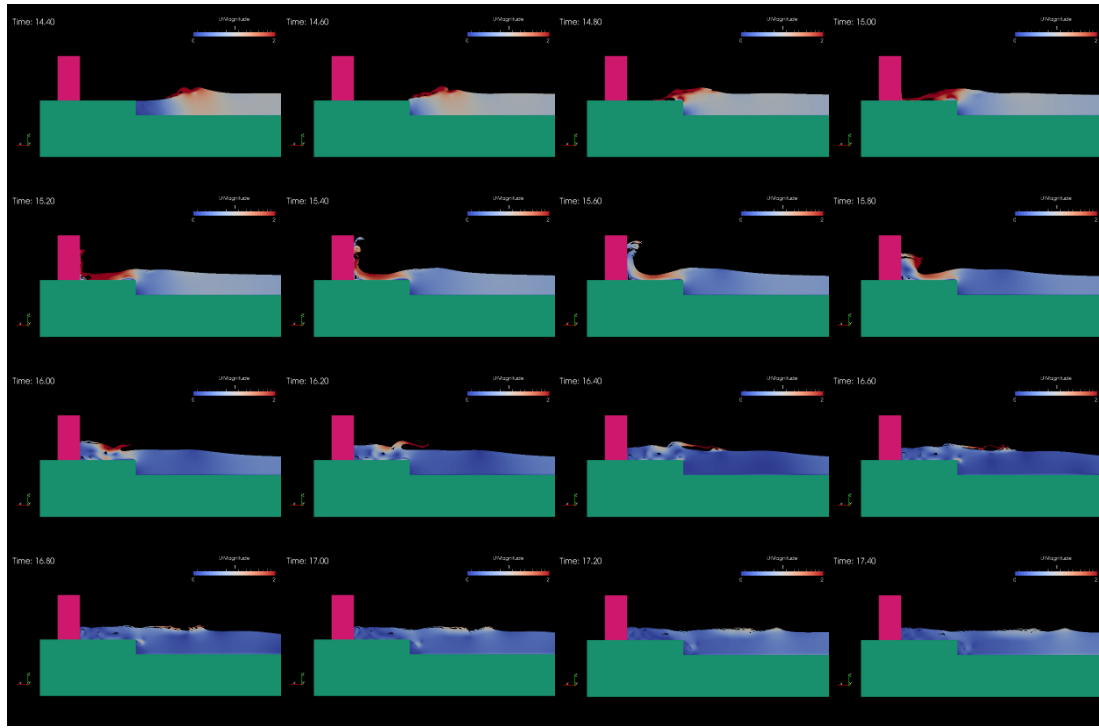


Figure 4.18. Snapshots from Simulation of Case 2 with $k-\epsilon$ model

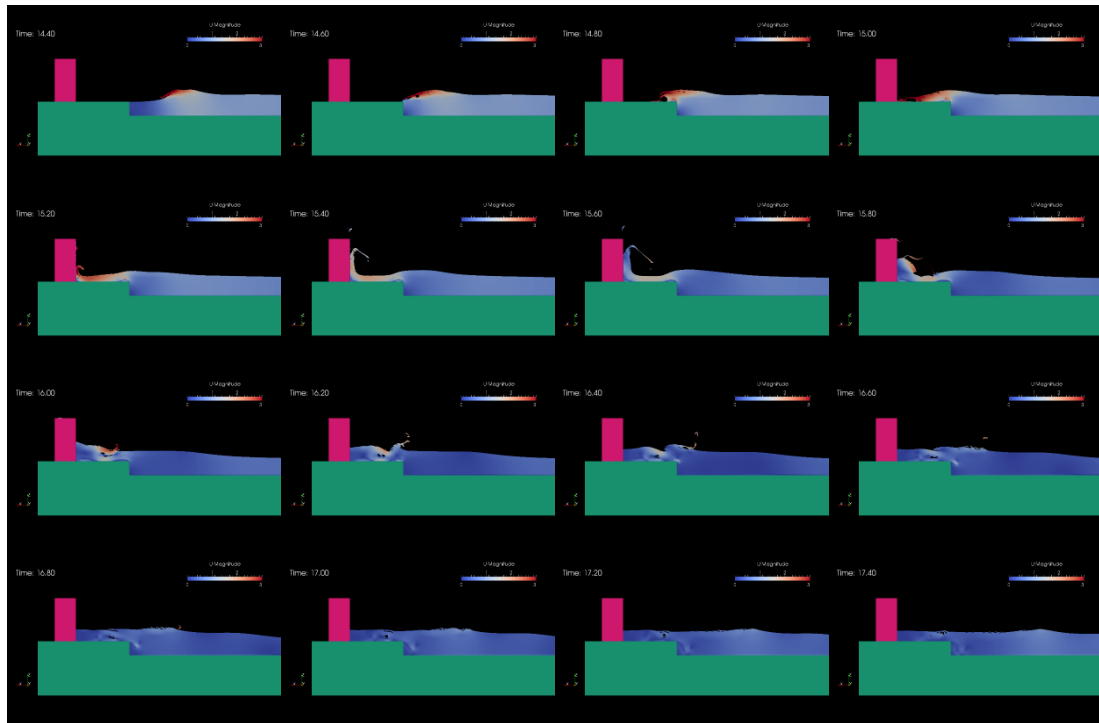


Figure 4.19. Snapshots from Simulation of Case 2 with $k-\omega$ -SST model

Lastly, for Case 3, the time histories of water surface elevations obtained from each simulation (laminar, $k-\epsilon$ and $k-\omega$ -SST) and the time histories in physical model experiments are compared and presented in Figure 4.20 for wave gauges from WG1 to WG10. The results of the gauges from WG1 to WG8 show that although there are some discrepancies between the results due to the wave reflection from the vertical wall, the time histories are in a good agreement with the measured data along the wave channel. At WG9, the general trend of the experimental data is in fairly good agreement with the numerical trend. However, between the seconds 16-17, where the breaking waves reflecting back from the vertical wall dominate the flow, $k-\omega$ -SST overestimated the water surface elevations. The performances of the numerical models at WG10 which is the wave gauge located just in front of the vertical wall can be seen in detail in Figure 4.21 to distinguish the differences. Figure 4.21 indicates that $k-\epsilon$ turbulence model shows extra dissipate behavior near the wall region and could not solve the water surface elevation accurately in this case as expected. On the other hand, it seems that $k-\omega$ -SST model overestimated the peak value for the time histories of water surface elevations. In that point, to check the accuracy of the measured data from the physical experiments, videos of the experiment are reviewed and snapshot at the incident where the splash reaches its higher value is presented in Figure 4.22 with the snapshot from the simulation video of the $k-\omega$ -SST numerical model at the same incident. When the height of the vertical wall is scaled, it is concluded that the splashes reached much higher values (more than 130 cm) than the measured one. This means due to the extreme splashes the measurement instruments could not measure the data correctly and also, the $k-\omega$ -SST numerical model could not catch the exact peak value. However, $k-\omega$ -SST works better and computed more realistic values for the water surface elevation than the $k-\epsilon$ turbulence and laminar models around the wall. The laminar model performed well in the rising motion of the splashes but it could not solve the reflected wave motion accurately afterward. Moreover, another comparison between the time histories of the horizontal component of particle velocities in the x-direction and the measured time histories in physical experiments at velocity gauges (V1-V6) are presented in Figure 4.23.

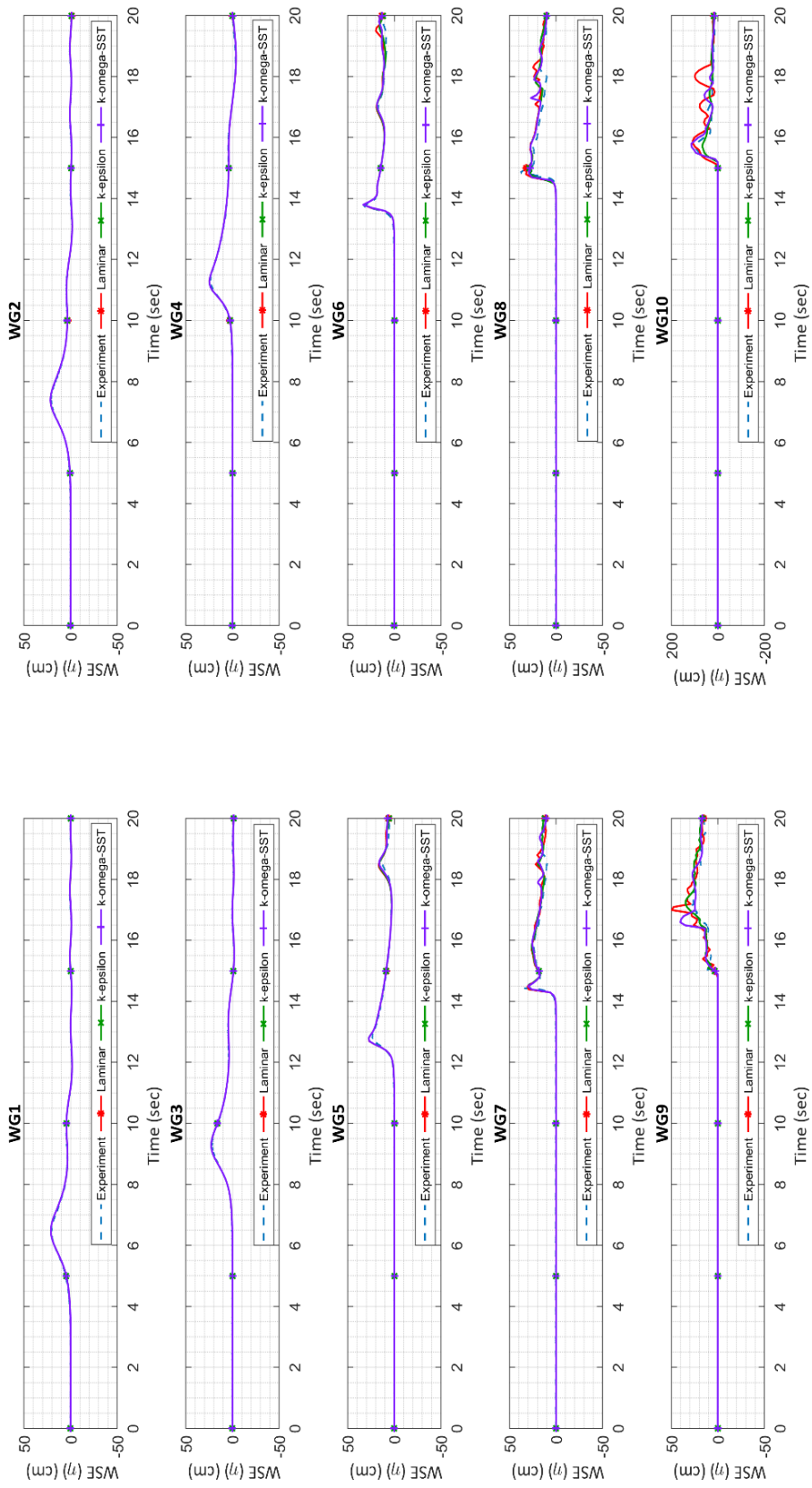


Figure 4.20. Comparison of Water Surface Elevations of IHFOAM with Experimental Measurements for Case 3

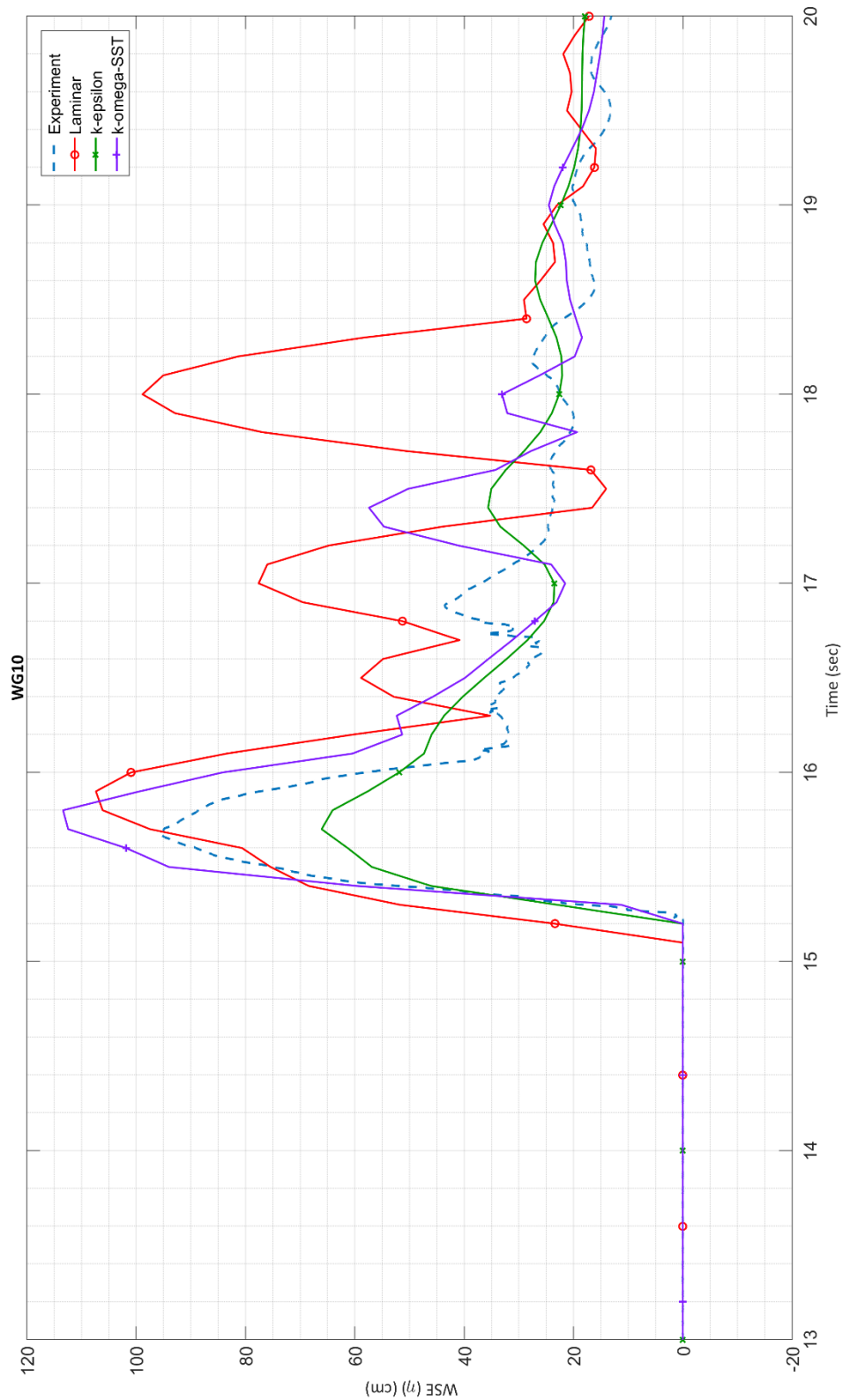


Figure 4.21. Comparison of Water Surface Elevations of IHFOAM with Experimental Measurements at WG10 for Case 3



Figure 4.22. Snapshots from (a) the video of the experiment (Arikawa, 2015) and (b) simulation video of the $k-\omega$ -SST turbulence model for Case 3

Figure 4.23 indicates that the particle velocities are in fairly good agreement with the physical model experiments along the channel until the reflected waves arrive. For this case, the breaking of the solitary wave starts at V4 and continues until the wave reaches the velocity gauge, V6. The 2D/3D effects caused a deviation in the numerical results of the particle velocities compared to the experimental data. In V4, it is clearly seen that the laminar model had some problems to solve the particle velocities accurately for the incoming wave. Although there is not much difference between the $k-\epsilon$ and $k-\omega$ -SST models, it can be said from the results of the V4 that $k-\epsilon$ turbulence model provided closer values for particle velocities at that location under the effect of the reflected wave. For the V5, both $k-\epsilon$ and $k-\omega$ -SST turbulence models worked well. However, the laminar model could not solve the particle velocities accurately under turbulence effect after reflection. A closer look to the V6 to see the performance of the models in detail in front of the vertical wall is given in Figure 4.24. It is seen that the laminar model could not solve the particle velocities at the impact incident and overestimated the peak value. $k-\epsilon$ turbulence model underestimated the peak water particle velocities however, $k-\omega$ -SST results are in consistency with the experimental data for the rising part of the water. It can be said that $k-\omega$ -SST turbulence model provided closer results comparing the experimental data in this highly turbulent case. Snapshots from simulations performed using laminar, $k-\epsilon$ and $k-\omega$ -SST models for Case 3 indicating the velocity distribution during solitary wave attack are given in Figures 4.25, 4.26 and 4.27, respectively.

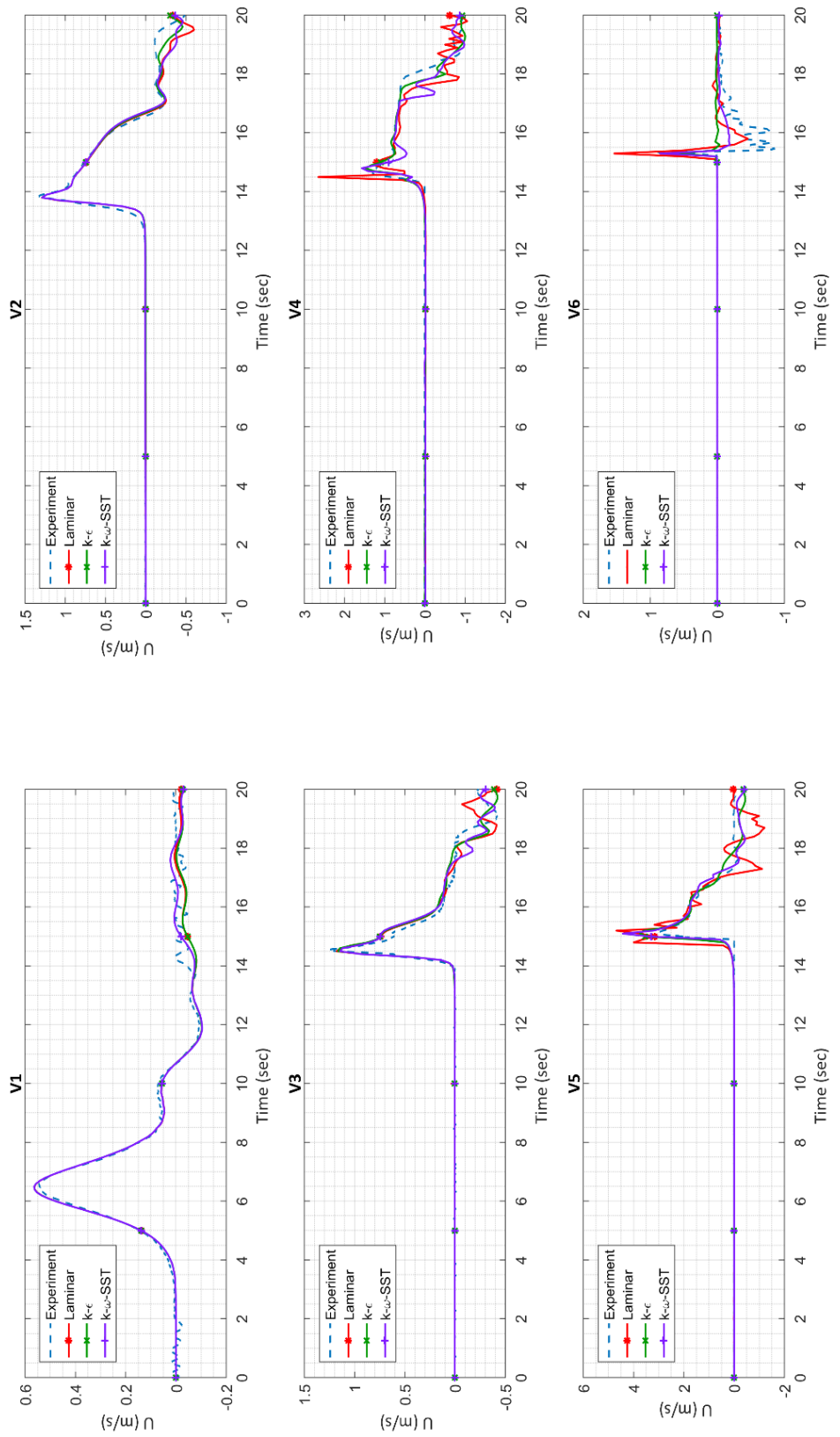


Figure 4.23. Comparison of Particle Velocities in x-direction, U of IHAFOAM with Experimental Measurements for Case 3

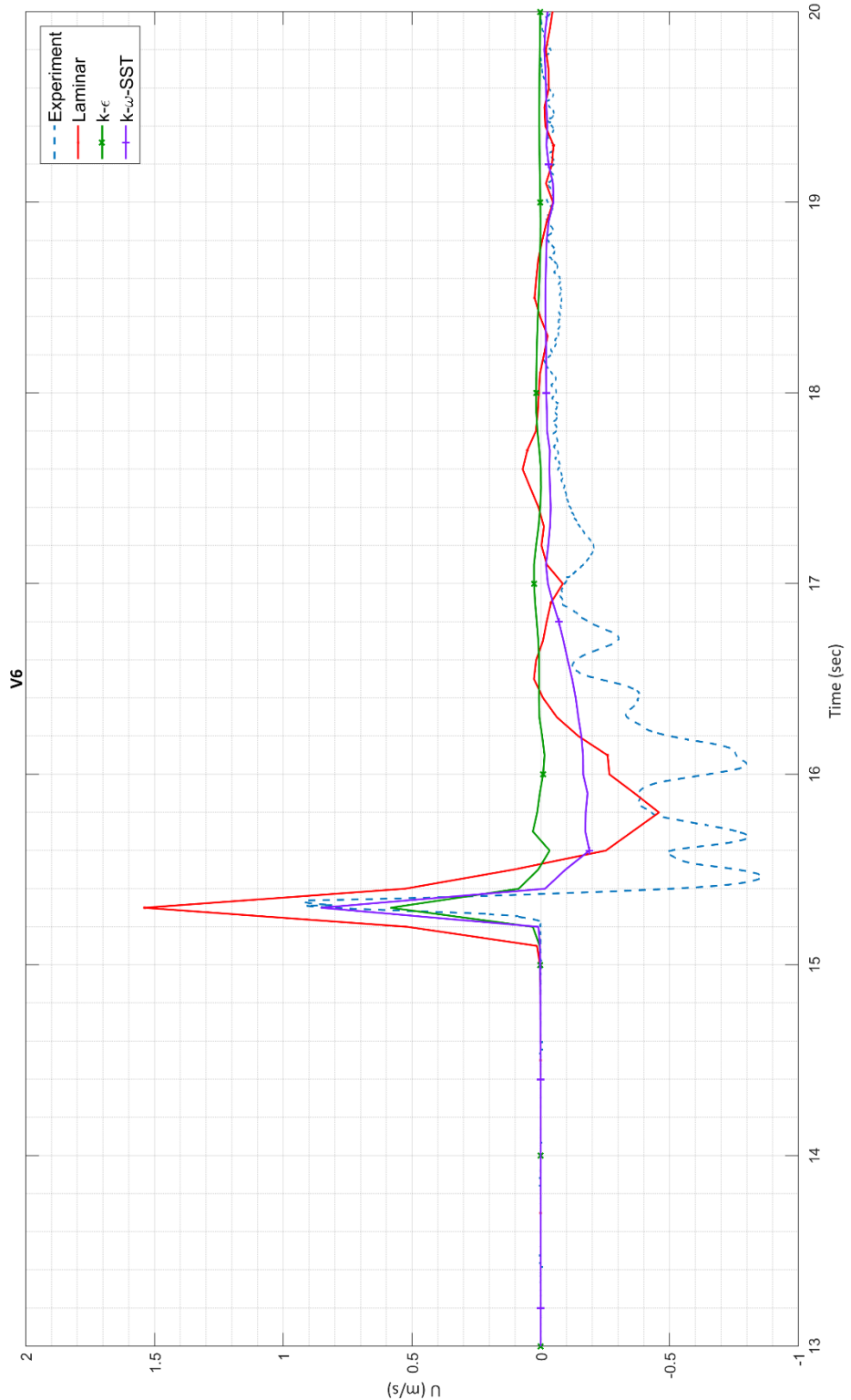


Figure 4.24. Comparison of Particle Velocities in x-direction, U of IHFOAM with Experimental Measurements at V6
for Case 3

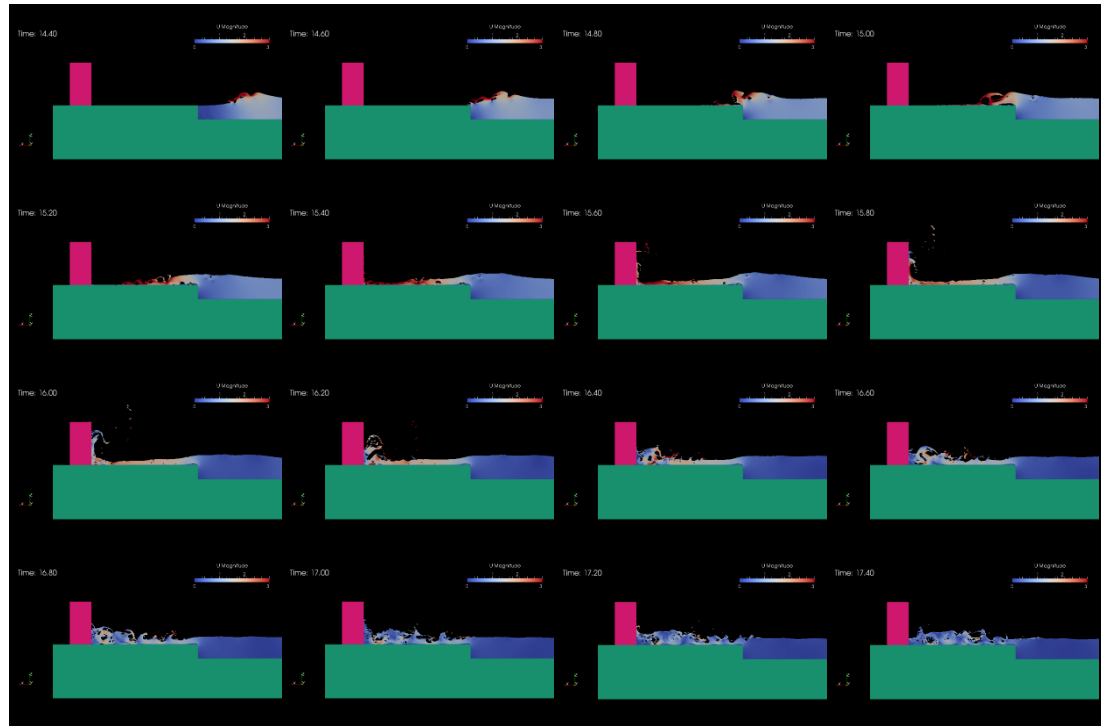


Figure 4.25. Snapshots from Simulation of Case 3 with laminar model

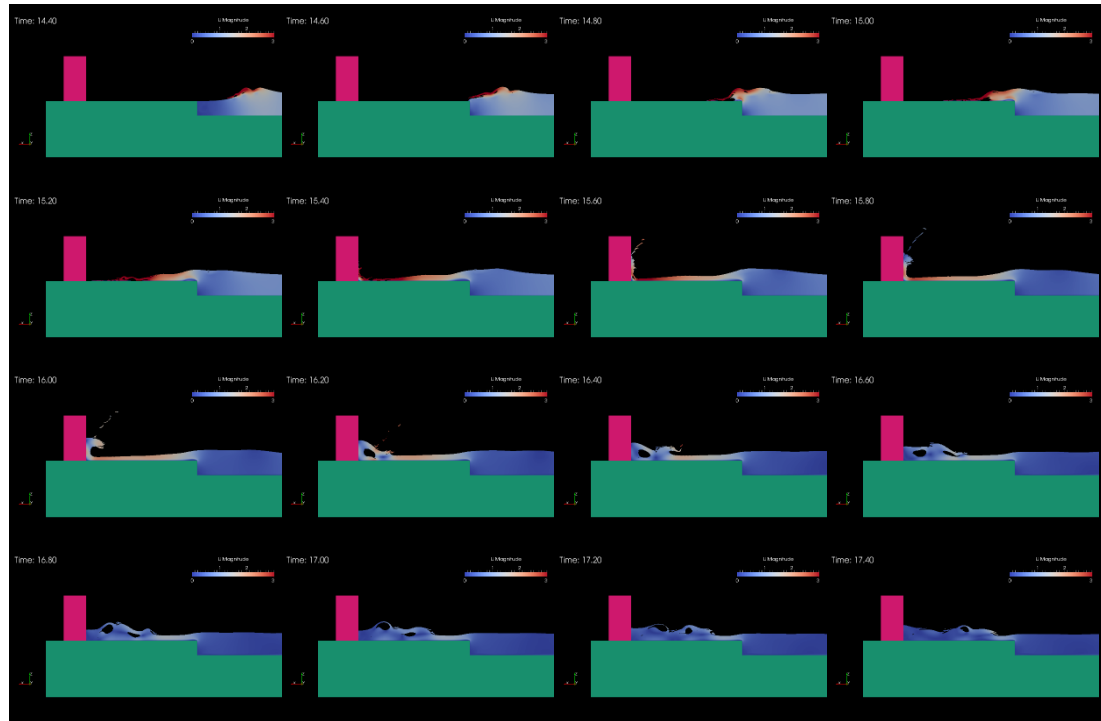


Figure 4.26. Snapshots from Simulation of Case 3 with $k-\epsilon$ model

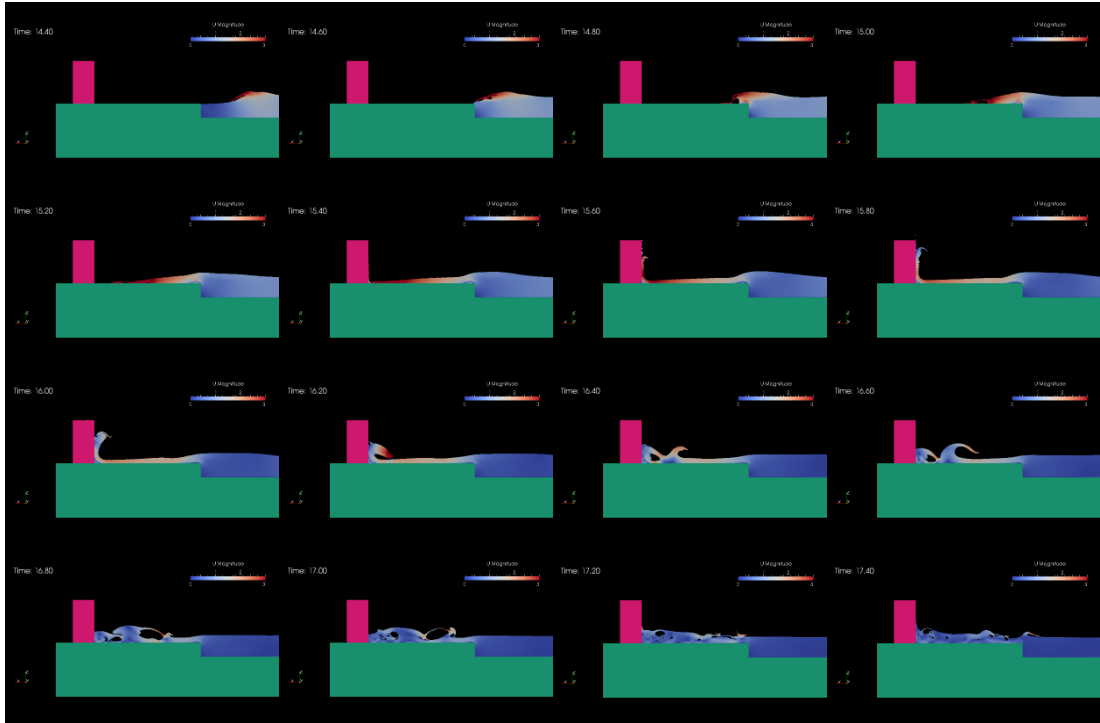


Figure 4.27. Snapshots from Simulation of Case 3 with k- ω -SST model

In this Chapter, physical model experiments on solitary wave-vertical wall interaction are numerically studied in 2D using IHFOAM solver of OpenFOAM®. For all three cases, it can be said that IHFOAM results from each turbulence model are fairly well agreement with the experimental data along the channel. The discrepancies start with the breaking of the solitary wave. In front of the vertical wall at the incident of wave impact, laminar assumption overestimated the water surface elevations and provided the highest values among the models. It is also seen from the gauges located in front of the vertical wall that k- ϵ turbulence model is much dissipative than the k- ω -SST model. The k- ω -SST turbulence model performed well in estimating peak water surface elevations at the incident of wave impact and provided reasonably good results for water particle velocities.

CHAPTER 5

CADMAS-SURF/3D

The “Research Group on Application of Numerical Wave Flume to Maritime Structure Design” involving 30 researchers from different universities, government, and non-government institutes was established in 1998, Japan. As one of the outcomes, CADMAS-SURF was developed to evaluate the effect and stability of structures considering the effect of wave breaking and complicated free surface accurately enough. CADMAS-SURF solves the RANS for three-dimensional incompressible fluid based on porous body model with using VOF method to trace the free surface. It is applicable to not only wave transformation but also the interaction of wave, current, structure, and foundation. It uses the high Reynolds number $k-\epsilon$ two-equation turbulence model. CADMAS-SURF has wave generating boundary conditions. To make a non-reflecting boundary, both Sommerfield’s radiation condition and the energy dissipation zone are available in the model.

CADMAS-SURF/3D (Arikawa et al., 2005, 2007) is developed for three-dimensional numerical simulations by PARI based on the CADMAS-SURF. It solves the RANS for three-dimensional incompressible fluid based on porous body model with using a three-dimensional VOF model to capture the free surface.

5.1. Numerical Scheme of the CADMAS-SURF/3D

CADMAS-SURF/3D uses the Cartesian coordinate system. Finite differences is used to subdividing the whole domain into smaller parts. The model adopted the staggered grid system as a discretization scheme. Outside the analytical domain, virtual cells are

used to deal with the boundary conditions. Like CADMAS-SURF, CADMAS-SURF/3D also has two options named as Sommerfeld's radiative boundary and energy dissipation band for a non-reflective boundary. For turbulence calculations, CADMAS-SURF/3D has k- ϵ turbulence model. Euler method is used for the time discretization to calculate the physical quantities in the old and new time step. To couple the continuity equation and equation of motion, Simplified Marker and Cell (SMAC) method is adopted.

The expanded equations that CADMAS-SURF/3D solves for 3D incompressible fluid based on porous body model as given below in Equations 5.1-5.4:

$$\frac{\partial \gamma_x u}{\partial x} + \frac{\partial \gamma_y v}{\partial y} + \frac{\partial \gamma_z w}{\partial z} = \gamma_v S_\rho \quad [5.1]$$

$$\begin{aligned} \lambda_v \frac{\partial u}{\partial t} + \frac{\partial \lambda_x uu}{\partial x} + \frac{\partial \lambda_y vu}{\partial y} + \frac{\partial \lambda_z wu}{\partial z} &= -\frac{\gamma_v}{\rho} \frac{\partial p}{\partial x} + \frac{\partial}{\partial x} \left\{ \gamma_x V_e \left(2 \frac{\partial u}{\partial x} \right) \right\} \\ &+ \frac{\partial}{\partial y} \left\{ \gamma_y V_e \left(\frac{\partial u}{\partial y} + \frac{\partial v}{\partial x} \right) \right\} + \frac{\partial}{\partial z} \left\{ \gamma_z V_e \left(\frac{\partial u}{\partial z} + \frac{\partial w}{\partial x} \right) \right\} + \gamma_v D_x u - R_x + \gamma_v S_u \end{aligned} \quad [5.2]$$

$$\begin{aligned} \lambda_v \frac{\partial v}{\partial t} + \frac{\partial \lambda_x uv}{\partial x} + \frac{\partial \lambda_y vv}{\partial y} + \frac{\partial \lambda_z wv}{\partial z} &= -\frac{\gamma_v}{\rho} \frac{\partial p}{\partial y} + \frac{\partial}{\partial x} \left\{ \gamma_x V_e \left(\frac{\partial v}{\partial x} + \frac{\partial u}{\partial y} \right) \right\} \\ &+ \frac{\partial}{\partial y} \left\{ \gamma_y V_e \left(2 \frac{\partial v}{\partial y} \right) \right\} + \frac{\partial}{\partial z} \left\{ \gamma_z V_e \left(\frac{\partial v}{\partial z} + \frac{\partial w}{\partial y} \right) \right\} + \gamma_v D_y v - R_y + \gamma_v S_v \end{aligned} \quad [5.3]$$

$$\begin{aligned} \lambda_v \frac{\partial w}{\partial t} + \frac{\partial \lambda_x uw}{\partial x} + \frac{\partial \lambda_y vw}{\partial y} + \frac{\partial \lambda_z ww}{\partial z} &= -\frac{\gamma_v}{\rho} \frac{\partial p}{\partial x} + \frac{\partial}{\partial x} \left\{ \gamma_x V_e \left(\frac{\partial w}{\partial x} + \frac{\partial u}{\partial z} \right) \right\} \\ &+ \frac{\partial}{\partial y} \left\{ \gamma_y V_e \left(\frac{\partial w}{\partial y} + \frac{\partial v}{\partial x} \right) \right\} + \frac{\partial}{\partial z} \left\{ \gamma_z V_e \left(2 \frac{\partial w}{\partial z} \right) \right\} + \gamma_v D_z w - R_z + \gamma_v S_w + \frac{\gamma \rho^* g}{\rho} \end{aligned} \quad [5.4]$$

where x , y and z are horizontal, transverse and vertical axes, u , v , and w are the velocities in x , y and z -direction respectively, t is time, ρ is the density of water, p is

pressure, ν_e is the effective viscosity (summation of the molecular viscosity, ν and eddy viscosity, ν_t), γ_v is the porosity, γ_x , γ_y and γ_z are permeability in x, y and z directions respectively, D_x , D_y and D_z are coefficients for energy dissipation in x, y and z directions respectively, S_ρ , S_u , S_v and S_w are source terms for wave generation and g is the gravitational acceleration. λ_v , λ_x , λ_y and λ_z are expressed by using the inertia coefficient C_M and permeability coefficients as below.

$$\begin{aligned}\lambda_v &= \gamma_v + (1 - \gamma_v)C_M \\ \lambda_x &= \gamma_x + (1 - \gamma_x)C_M \\ \lambda_y &= \gamma_y + (1 - \gamma_y)C_M \\ \lambda_z &= \gamma_z + (1 - \gamma_z)C_M\end{aligned}\quad [5.5]$$

R_x , R_y and R_z are resistance terms for a porous structure where Δx , Δy and Δz are the size of the calculation grid and C_D is the drag coefficient.

$$\begin{aligned}R_x &= \frac{1}{2} \frac{C_D}{\Delta x} (1 - \gamma_x) u \sqrt{u^2 + v^2 + w^2} \\ R_y &= \frac{1}{2} \frac{C_D}{\Delta y} (1 - \gamma_y) v \sqrt{u^2 + v^2 + w^2} \\ R_z &= \frac{1}{2} \frac{C_D}{\Delta z} (1 - \gamma_z) w \sqrt{u^2 + v^2 + w^2}\end{aligned}\quad [5.6]$$

Since the experiments carried out with the impermeable vertical wall (non-porous media), the effect of λ and R is not considered in this thesis.

For the tracing of water surface, advection equation of F (the ratio of fluid volume to cell volume) in VOF method based on porous body model given in Equation 5.7 is solved in 3D where the S_F is a source term of wave generation. With the solution of this equation cells are distinguished as “full-cell”, “surface-cell” and “empty-cell”.

$$\gamma_v \frac{\partial F}{\partial t} + \frac{\partial \gamma_x u F}{\partial x} + \frac{\partial \gamma_y v F}{\partial y} + \frac{\partial \gamma_z w F}{\partial z} = \gamma_v S_F \quad [5.7]$$

CADMAS-SURF/3D uses k - ε (two-equation) turbulence model for turbulence calculations. k is the turbulence kinetic energy and ε is defined as dissipation rate given in Equations 5.8 and 5.9, respectively.

$$k = \frac{1}{2}(u'^2 + v'^2 + w'^2) \quad [5.8]$$

$$\begin{aligned} \varepsilon = & \nu \left[2 \left\{ \left(\frac{\partial u'}{\partial x} \right)^2 + \left(\frac{\partial v'}{\partial y} \right)^2 + \left(\frac{\partial w'}{\partial z} \right)^2 \right\} \right] \\ & + \left(\frac{\partial u'}{\partial y} + \frac{\partial v'}{\partial x} \right)^2 + \left(\frac{\partial v'}{\partial z} + \frac{\partial w'}{\partial y} \right)^2 + \left(\frac{\partial w'}{\partial x} + \frac{\partial u'}{\partial z} \right)^2 \end{aligned} \quad [5.9]$$

For the computation of k and ε convection-diffusion equations given in Equation 5.10 and 5.11 are solved:

$$\begin{aligned} & \lambda_v \frac{\partial k}{\partial t} + \frac{\partial \lambda_x u k}{\partial x} + \frac{\partial \lambda_y v k}{\partial y} + \frac{\partial \lambda_z w k}{\partial z} \\ &= \frac{\partial}{\partial x} \left(\gamma_x V_k \frac{\partial k}{\partial x} \right) + \frac{\partial}{\partial y} \left(\gamma_y V_k \frac{\partial k}{\partial y} \right) + \frac{\partial}{\partial z} \left(\gamma_z V_k \frac{\partial k}{\partial z} \right) + \gamma_v (G_s + G_T - \varepsilon) \end{aligned} \quad [5.10]$$

$$\begin{aligned} & \lambda_v \frac{\partial \varepsilon}{\partial t} + \frac{\partial \lambda_x u \varepsilon}{\partial x} + \frac{\partial \lambda_y v \varepsilon}{\partial y} + \frac{\partial \lambda_z w \varepsilon}{\partial z} \\ &= \frac{\partial}{\partial x} \left(\gamma_x V_\varepsilon \frac{\partial \varepsilon}{\partial x} \right) + \frac{\partial}{\partial y} \left(\gamma_y V_\varepsilon \frac{\partial \varepsilon}{\partial y} \right) + \frac{\partial}{\partial z} \left(\gamma_z V_\varepsilon \frac{\partial \varepsilon}{\partial z} \right) \\ &+ \gamma_v \left\{ C_1 \frac{\varepsilon}{k} (G_s + G_T) (1 + C_3 R_f) - C_2 \frac{\varepsilon^2}{k} \right\} \end{aligned} \quad [5.11]$$

where G_s , G_T , R_f , V_t , V_k and V_ε are given in Equations 5.12-5.17.

$$G_s = V_t \left[2 \left\{ \left(\frac{\partial u}{\partial x} \right)^2 + \left(\frac{\partial v}{\partial y} \right)^2 + \left(\frac{\partial w}{\partial z} \right)^2 \right\} \right] \quad [5.12]$$

$$+ \left(\frac{\partial u}{\partial y} + \frac{\partial v}{\partial x} \right)^2 + \left(\frac{\partial v}{\partial z} + \frac{\partial w}{\partial y} \right)^2 + \left(\frac{\partial w}{\partial x} + \frac{\partial u}{\partial z} \right)^2$$

$$G_T = - \frac{v_t}{\rho \sigma_t} \left(g \frac{\partial \rho^*}{\partial z} \right) \quad [5.13]$$

$$R_f = - \frac{-G_T}{G_s + G_T} \quad [5.14]$$

$$\nu_t = C_\mu \frac{k^2}{\epsilon} \quad [5.15]$$

$$\nu_k = \nu + \frac{\nu_t}{\sigma_k} \quad [5.16]$$

$$\nu_\epsilon = \nu + \frac{\nu_t}{\sigma_\epsilon} \quad [5.17]$$

In Equations 5.11, 5.15, 5.16 and 5.17, the empirical values are used as default for C_μ , σ_k , σ_ϵ , C_1 , C_2 and C_3 respectively as 0.09, 1.00, 1.30, 1.44, 1.92 and 0.0.

The calculated effect of turbulence obtained from above equations is inserted in Equations 5.2, 5.3 and 5.4 as given in Equations 5.18 and 5.19.

$$\nu_e = \nu + \nu_t \quad [5.18]$$

$$p' = p + \frac{2}{3} \rho k \quad [5.19]$$

5.2. Numerical Setup of the Experiments for CADMAS-SURF/3D

The physical model experiments of Arikawa (2015) is reproduced in a two-dimensional domain using CADMAS-SURF/3D. The Cartesian coordinate system is used to create the bathymetry for the simulations. The positive x-direction is towards the vertical wall and same with the direction of propagation of the solitary wave. and positive z-direction is opposite of the gravitational force which is in the downward direction.

The mesh sizes are same for all three cases. Maximum Δx is 5 cm starting from the beginning of the channel to the location of WG1 as a constant mesh size. From there to the end of the 1/10 slope Δx is decreasing from 5 cm to 1 cm. After that, it is fixed and minimum Δx is 1 cm. Δy is determined as 2 cm and there is only one cell along the y-direction. Δz is 0.5 cm as a fixed value along the z-direction.

Although the length of the flume is 105 m, to decrease the computational time of the simulation, time series of water surface elevation and velocity measured at the location of WG1 and V1 gauges are used as an input to the system at 0.6 m behind of the location of the gauges. Simulation duration is kept as 20 seconds.

The water depth at the inlet of the computational domain is 1.252 meters. Water density is 1000 kg/m^3 and gravitational acceleration is 9.81 m/s^2 . For the velocity and pressure, the no-slip boundary condition and for the VOF function F, the free boundary condition is used.

For all three cases, two simulations with laminar and k- ϵ turbulence model are carried out.

5.2.1. Case 1

The total length of the computational domain is 29.5 meters in the x-direction and 3.4 meters in the z-direction. The vertical wall is located on the small step at the end of the horizontal floor. The side view of the channel can be seen in Figure 5.1. The total of approximately 700.000 cells is present in this simulation.

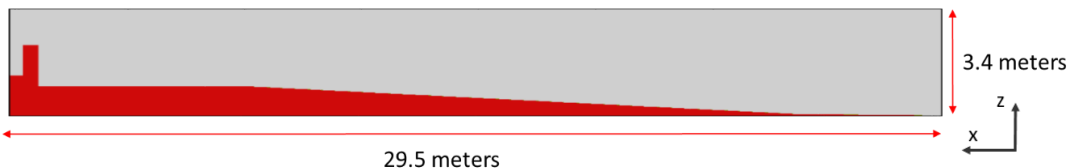


Figure 5.1. Orientation of the coordinate system and two-dimensional computational domain of the Case 1 for CADMAS-SURF/3D model

5.2.2. Case 2

The total length of the computational domain is 30.75 meters in the x-direction and 3.0 meters in the z-direction. Vertical wall position is shifted 1 meter away from the small step at the end of the horizontal floor. The side view of the channel can be seen in Figure 5.2. The total number of cells is approximately 650.000 in this simulation.

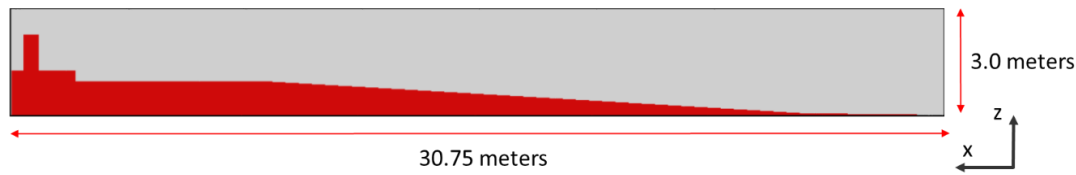


Figure 5.2. Orientation of the coordinate system and two-dimensional computational domain of the Case 2 for CADMAS-SURF/3D model

5.2.3. Case 3

The total length of the computational domain is 32.0 meters in the x-direction and 3.0 meters in the z-direction. In this case, the vertical wall is located 2 meters away from the small step at the end of the horizontal floor. The side view of the channel can be seen in Figure 5.3. The total number of cells is approximately 690.000 in this simulation.

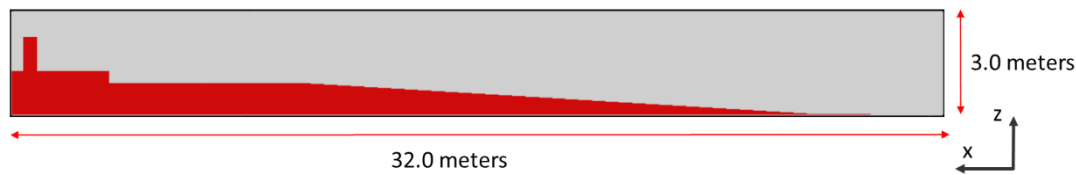


Figure 5.3. Orientation of the coordinate system and two-dimensional computational domain of the Case 3 for CADMAS-SURF/3D model

5.3. Results and Discussions on CADMAS-SURF/3D Simulations

The results and discussions of the simulations performed using CADMAS-SURF/3D are presented in this section. To optimize the limit of storage for the results of the numerical simulations, the output time interval is selected as 0.1 sec whereas the sampling interval of the physical model experimental data is 2000 Hz.

Comparison of the time histories of water surface elevations obtained from each simulation (laminar and $k-\epsilon$) for Case 1 and the measured data of time histories in physical model experiments is presented in Figure 5.4 for the wave gauges from WG1 to WG8. The results show that along the wave channel the time histories are in a quite good agreement with the measured data both for the laminar and $k-\epsilon$ models. The differences between the results of laminar and $k-\epsilon$ simulations compared to the measured data at these gauges (WG1-WG7) start due to the reflection occurred by hitting of the solitary wave to the vertical wall structure. However, it is seen that there is no major difference between the turbulence and no-turbulence numerical computations. Different results for the peak water surface elevations obtained at WG8 which is the wave gauge located just in front of the vertical wall. In this location, it is not very simple to catch the exact height of the splashes occurred by the slamming of the solitary wave to the vertical wall. In general, it can be said that the simulations have the same trend with the experimental data.

The closer look of the results of WG8 is given in Figure 5.5 to distinguish the differences. It is clearly seen that both simulations (laminar and $k-\epsilon$) resulted in higher water surface elevation than the measured data. As discussed in the previous chapter, the flat part of the experimental data indicates the lack of accurate measurement at the impact incident. The trend of the two numerical simulations is quite similar to each other. However, laminar model resulted in higher water surface elevations at the incident of impact and computes lower water surface elevation values for the downward motion and reflection. It might not be reasonable to compare the computed peak water surface elevation with the experimental data as the wave gauge could not catch the splash accurately.

Comparison between the time histories of the horizontal component of particle velocities in the x-direction and the measured time histories in physical experiments at velocity gauges (V1-V4) are presented in Figure 5.6. Again, it can be seen that the particle velocities are in fairly good agreement with the physical model experiments along the channel until the reflected waves arrive. Differences between the laminar and $k-\epsilon$ models can be observed for the computation of the reflected wave motion that 2D/3D effects and turbulence after reflection has a high influence on the flow.

A closer look to the V4 is given in Figure 5.7. Both models (laminar and $k-\epsilon$) had difficulties in solving the water particle velocities accurately. It also became apparent that laminar model has a time lag and could not solve the water particle velocities for the impact time and later on properly. Although $k-\epsilon$ model performed better and provide more accurate results for the impact velocity, there are some apparent discrepancies in the reflected wave motion part.

Snapshots from simulations performed using laminar and $k-\epsilon$ models for Case 1 indicating the velocity distribution during solitary wave attack are given in Figures 5.8 and 5.9, respectively.

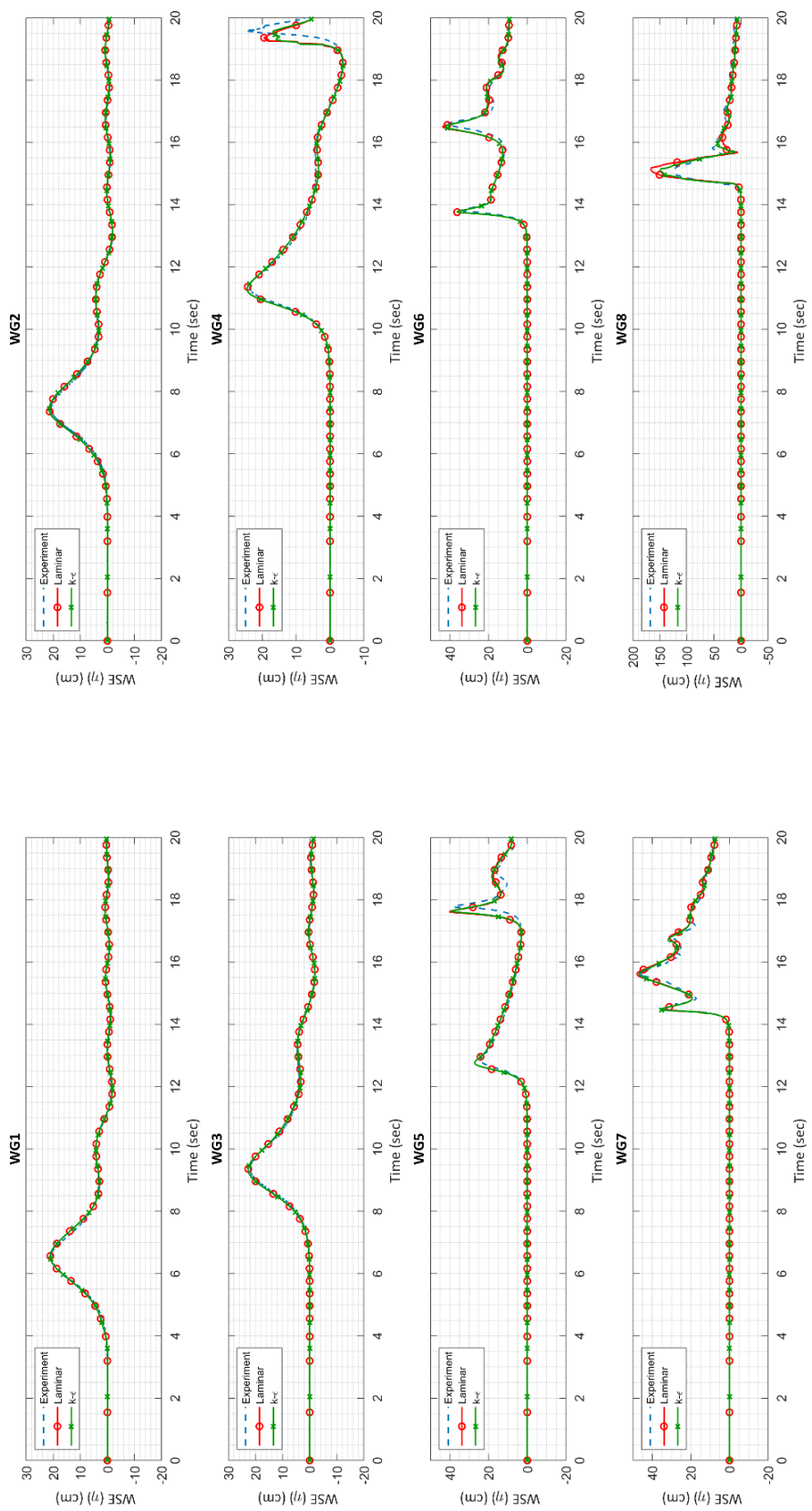


Figure 5.4. Comparison of Water Surface Elevations of CADMAS-SURF/3D with Experimental Measurements for Case 1

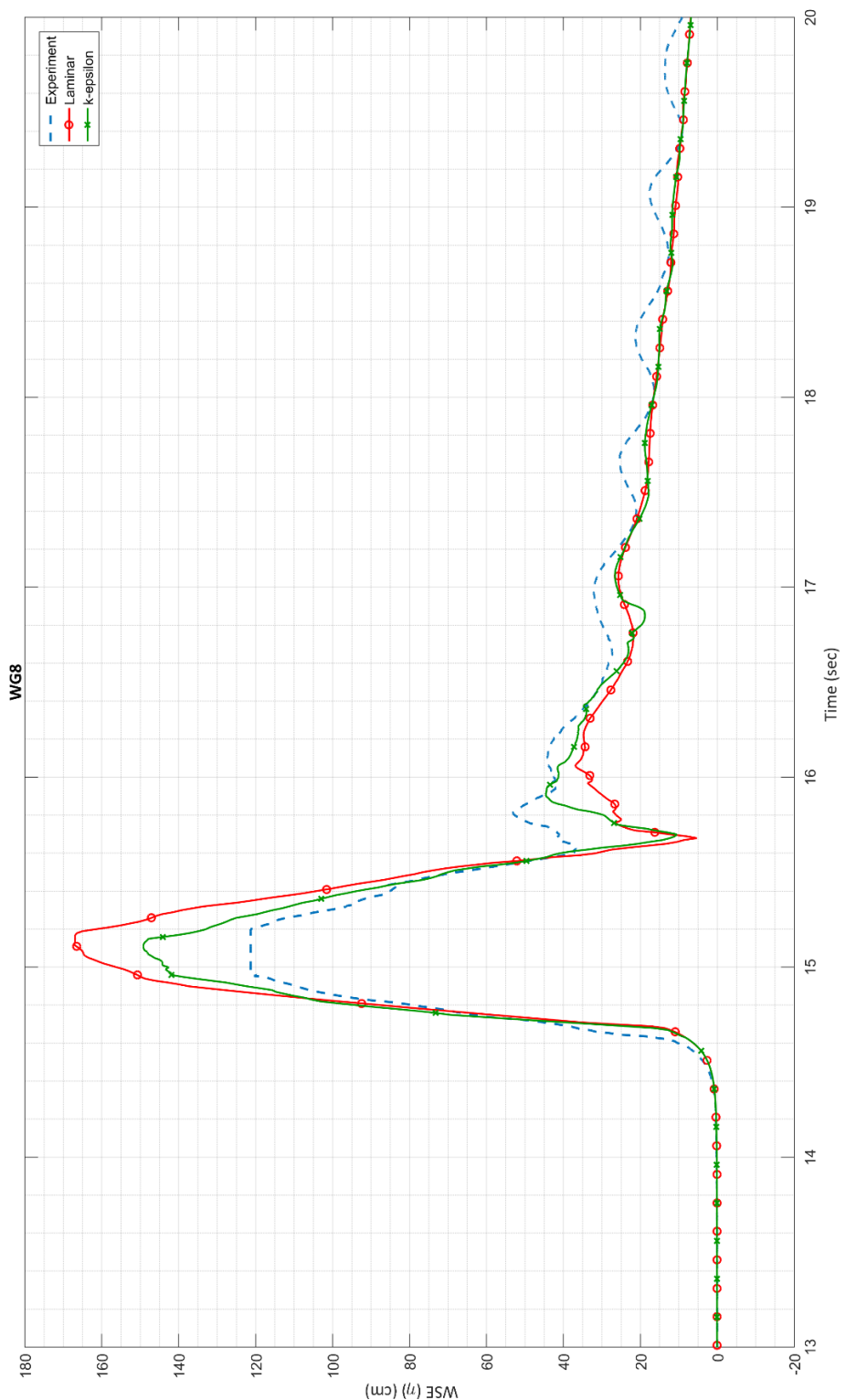


Figure 5.5. Comparison of Water Surface Elevations of CADMAS-SURF/3D with Experimental Measurements at WG8 for Case 1

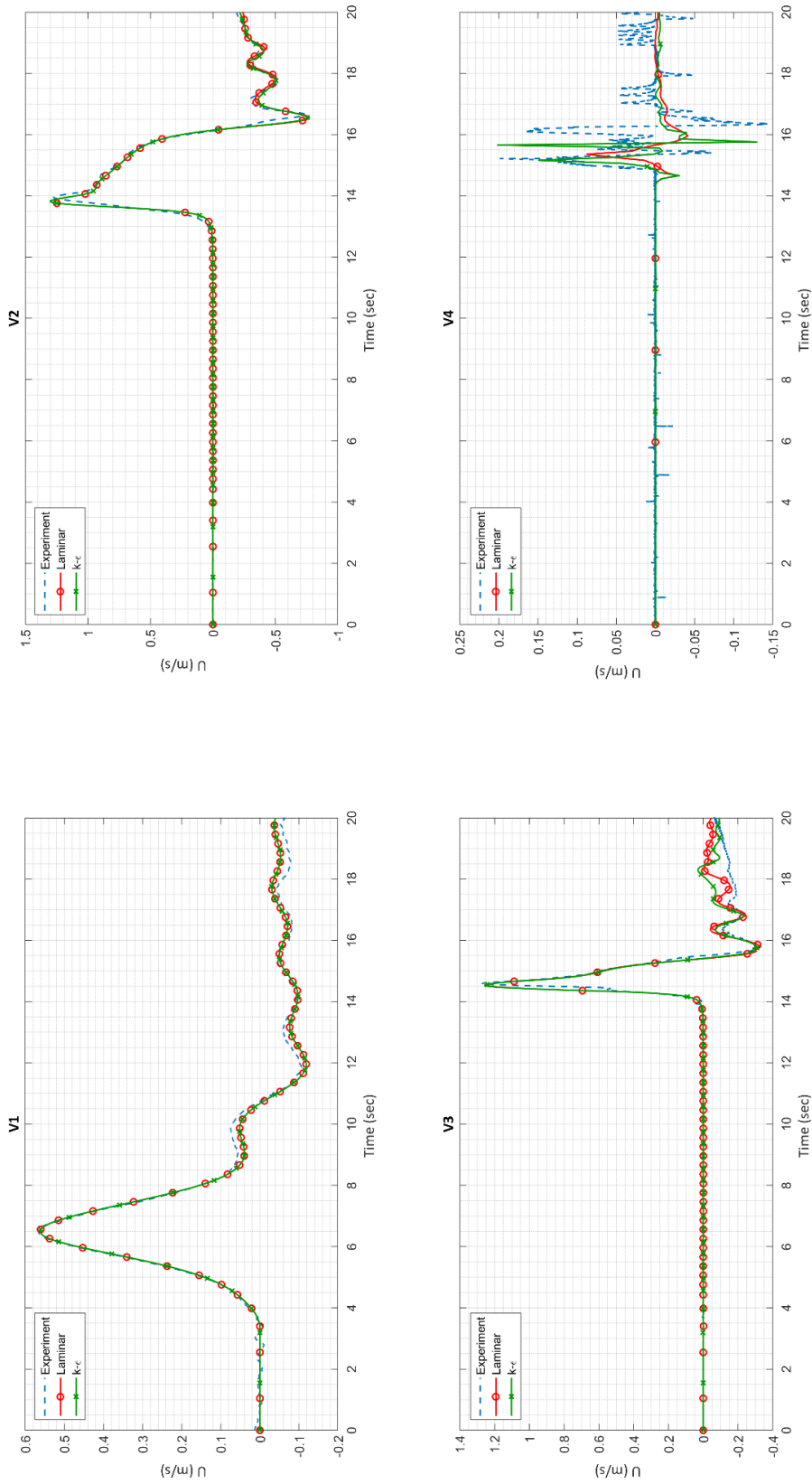


Figure 5.6. Comparison of Water Particle Velocities in x-direction, U of CADMAS-SURF/3D with Experimental Measurements for Case 1

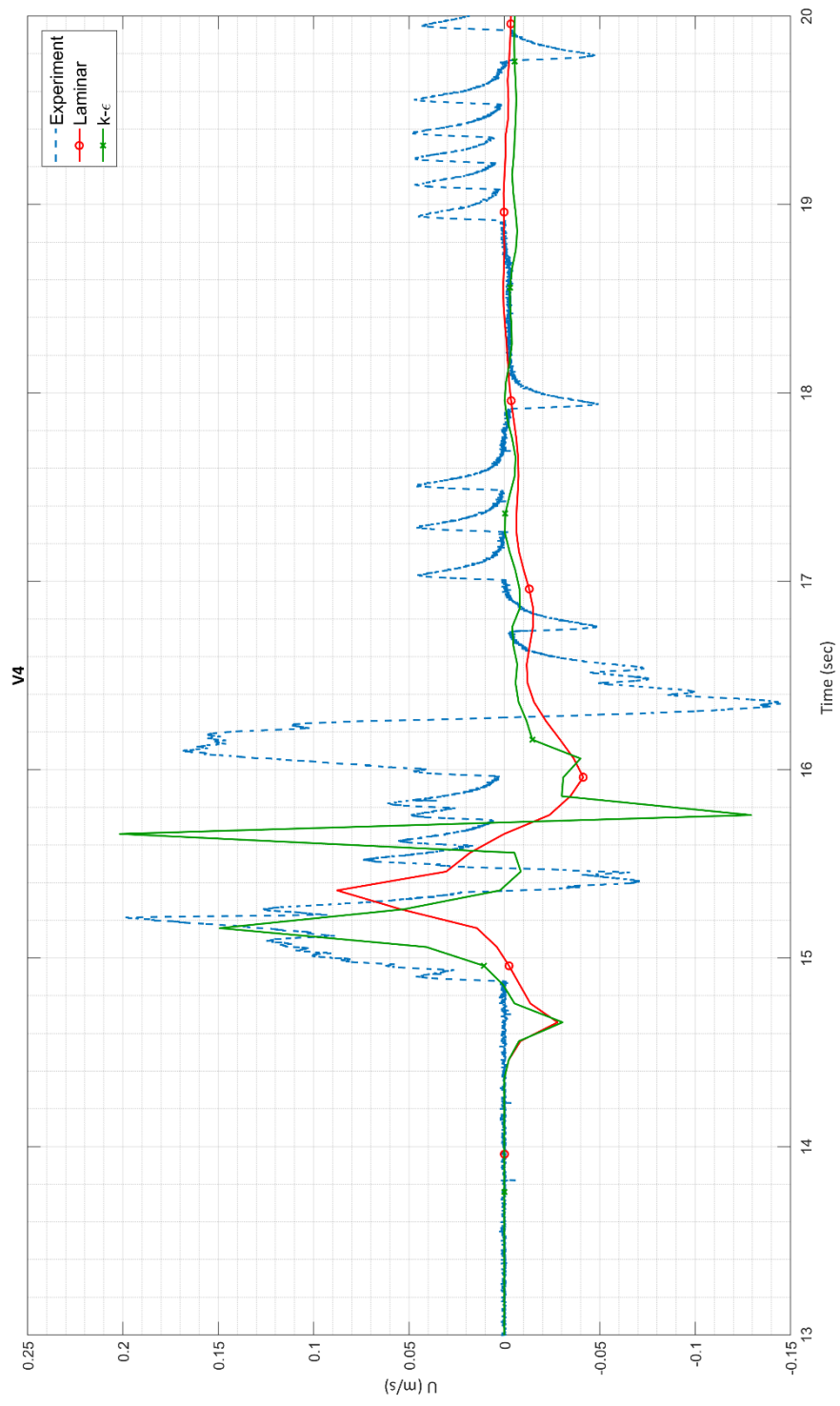


Figure 5.7. Comparison of Water Particle Velocities in x-direction, U of CADMAS-SURF/3D with Experimental Measurements at V4 for Case 1

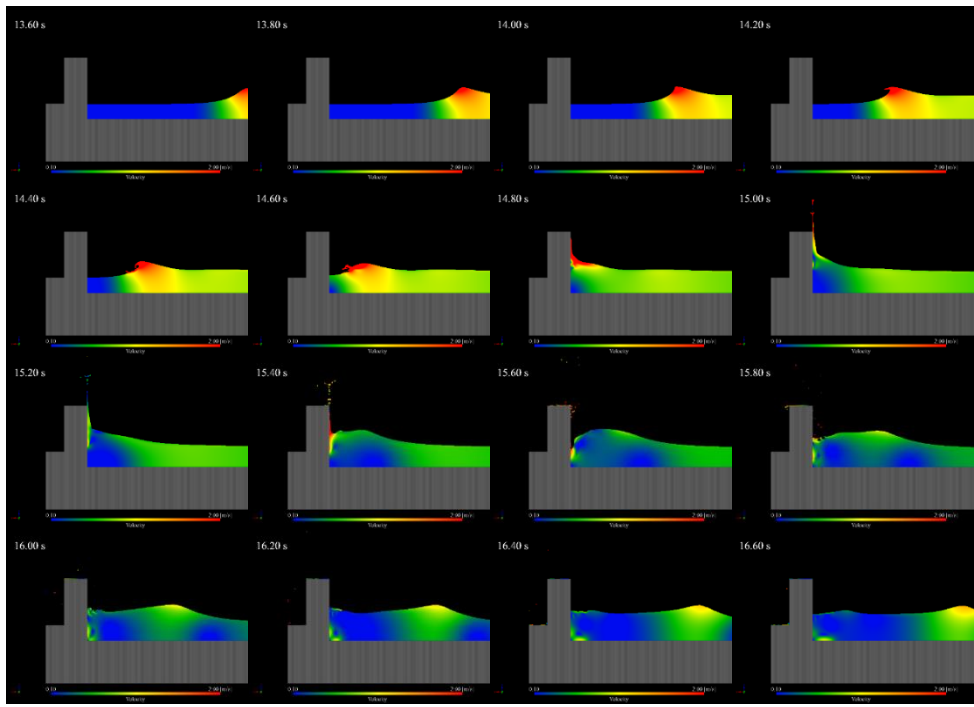


Figure 5.8. Snapshots from Simulation of Case 1 with laminar model

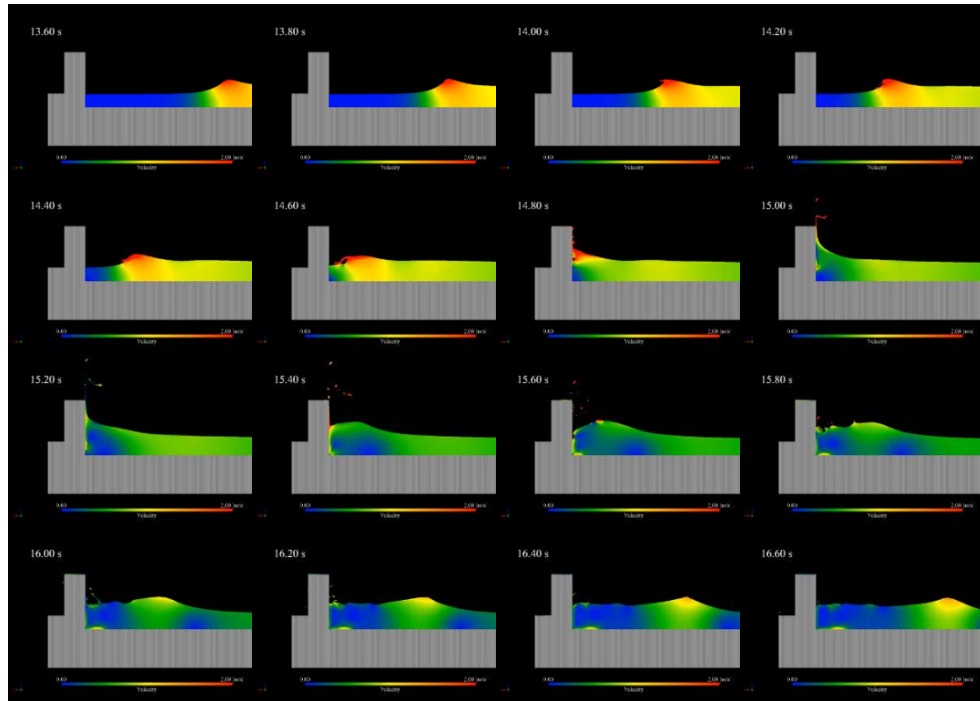


Figure 5.9. Snapshots from Simulation of Case 1 with k- ϵ turbulence model

Similar comparisons for Case 2 on the time histories of water surface elevations obtained from each simulation (laminar and $k-\varepsilon$) and the time histories in physical model experiments are presented in Figure 5.10 for wave gauges from WG1 to WG10. The results of the gauges from WG1 to WG7 demonstrate that along the wave channel the time histories are in a good agreement with the measured data. Discrepancies start to be apparent computing the reflected wave motion. At WG5, it is clearly seen that both models overestimated the water surface elevation caused by the reflected wave from the vertical wall. The same situation is valid also valid for WG6. However, there is not much difference between the results of the laminar and $k-\varepsilon$ models. At WG7, it is observed that peak water surface elevation at the incident of wave impact is underestimated by both models. One of the reasons for that could be the selected time output in this study. Decreasing the output time interval might be effective to catch the peak water surface elevation. At the location of WG8 where the solitary wave starts breaking, both models underestimated the peak value of the water surface elevation for incoming solitary wave and overestimated the second peak caused by the reflected wave.

The most significant difference is observed again in front of the vertical wall at WG9. Overestimation of the water surface elevation for the incident of impact by both models at this gauge can be seen in detail in Figure 5.11. Both laminar and $k-\varepsilon$ models resulted in higher values than the measured data for the water surface elevation. The difference between the model results and experimental data is quite significant for the splash height at the time of impact. When the experimental videos reviewed, it is seen that the splash reached much higher values than the measured data. Therefore, it can be inferreded that numerical model results are more likely to be reasonable. Although it seems like laminar model performed better for the peak water surface elevation, it might be not healthy to draw conclusions like that since the experimental data is not accurate.

Furthermore, another comparison between the time histories of the horizontal component of particle velocities in the x-direction and the measured time histories in

physical experiments at velocity gauges (V1-V5) are presented in Figure 5.12. The results of the numerical models are in a fairly well agreement with the experimental data along the wave channel until the time that reflected wave is present. For this case, the breaking of the solitary wave starts at V4 and continues until the wave reaches the velocity gauge, V5. Again, the 2D/3D effects deviated from the numerical results of the particle velocities from the experimental data.

A closer look to the V5 which is the critical gauge located in front of the vertical wall is given in Figure 5.13. It is clearly seen that laminar simulation has a time lag and could not solve the particle velocities accurately. For the $k-\varepsilon$ model, it can be said that overestimation for the particle velocities at impact time is observed. It is also seen that it could not solve the falling motion of the solitary wave accurately. Snapshots from simulations performed using laminar and $k-\varepsilon$ models for Case 2 indicating the velocity distribution during solitary wave attack are given in Figures 5.14 and 5.15, respectively.

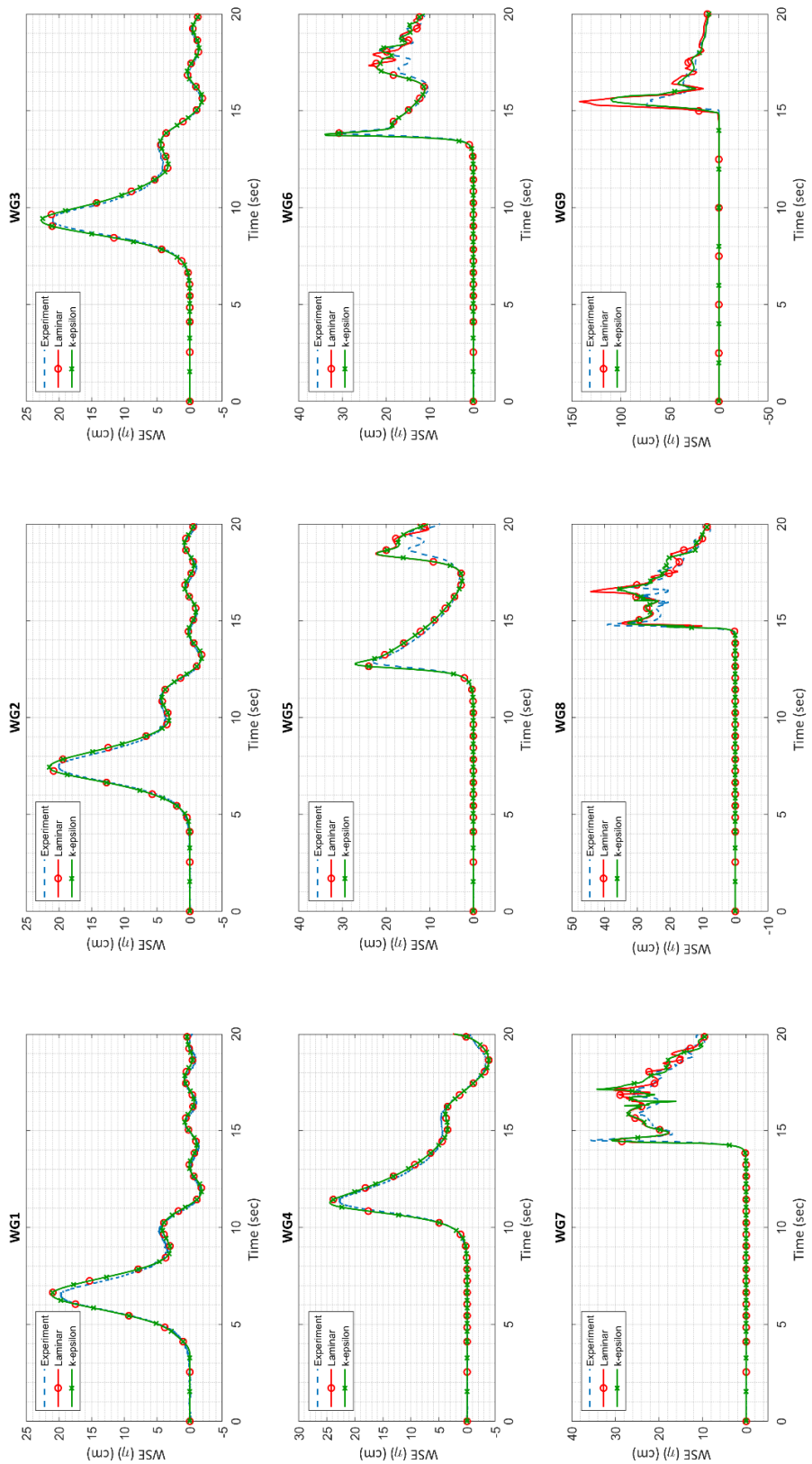


Figure 5.10. Comparison of Water Surface Elevations of CADMAS-SURF/3D with Experimental Measurements for Case

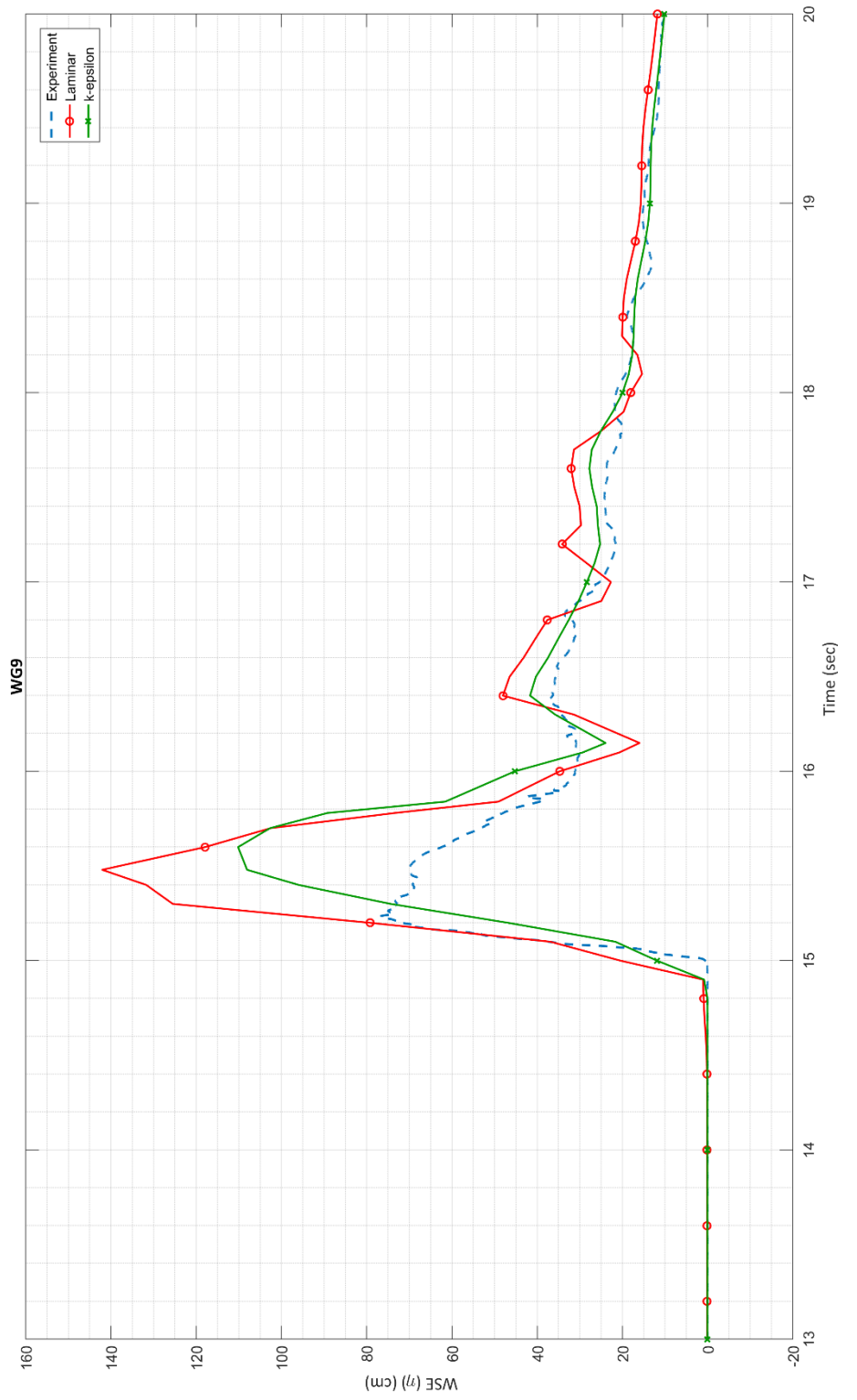


Figure 5.11. Comparison of Water Surface Elevations of CADMAS-SURF/3D with Experimental Measurements at WG9 for Case 2

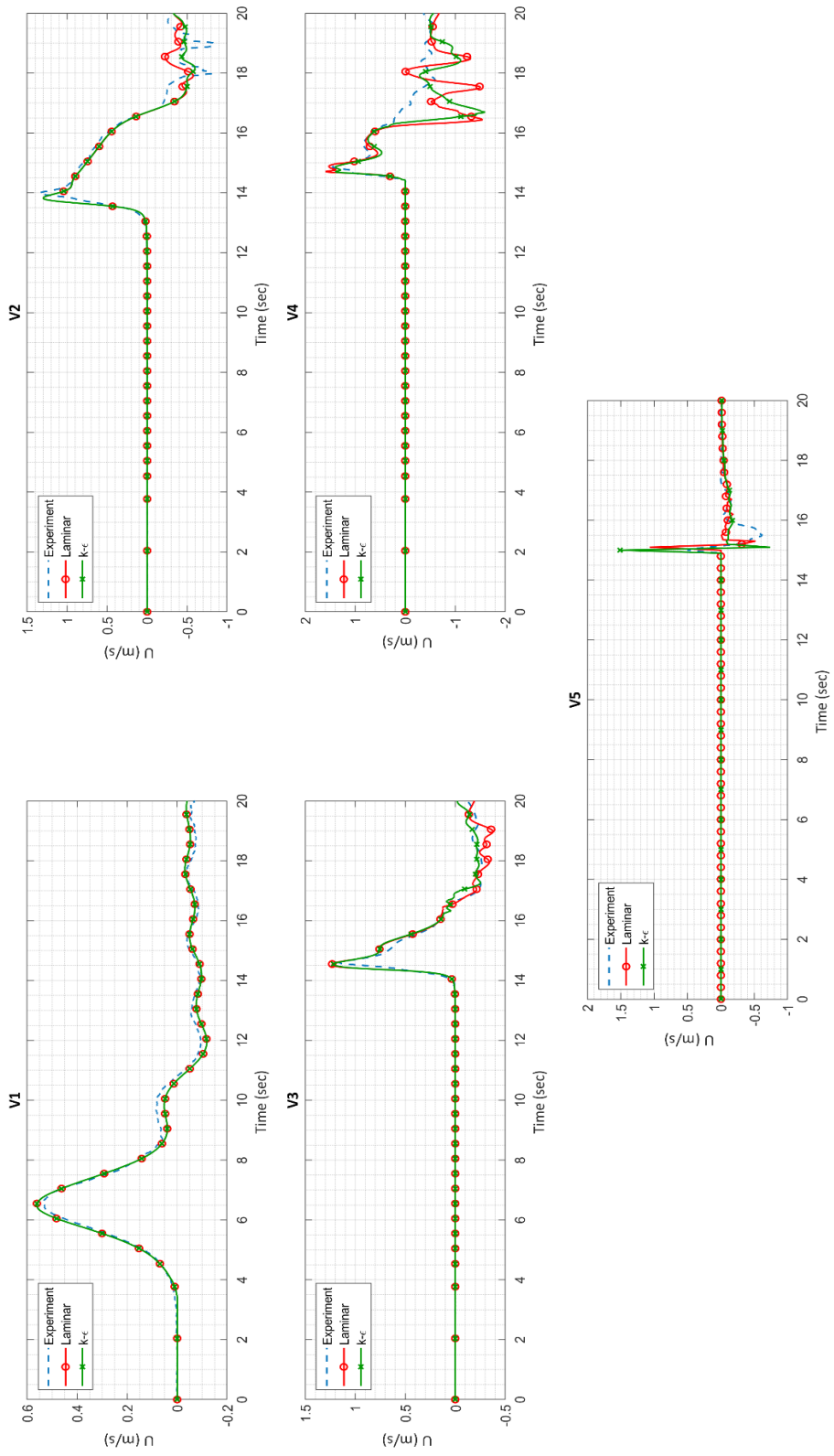


Figure 5.12. Comparison of Water Particle Velocities in x-direction, U of CADMAS-SURF/3D with Experimental Measurements for Case 2

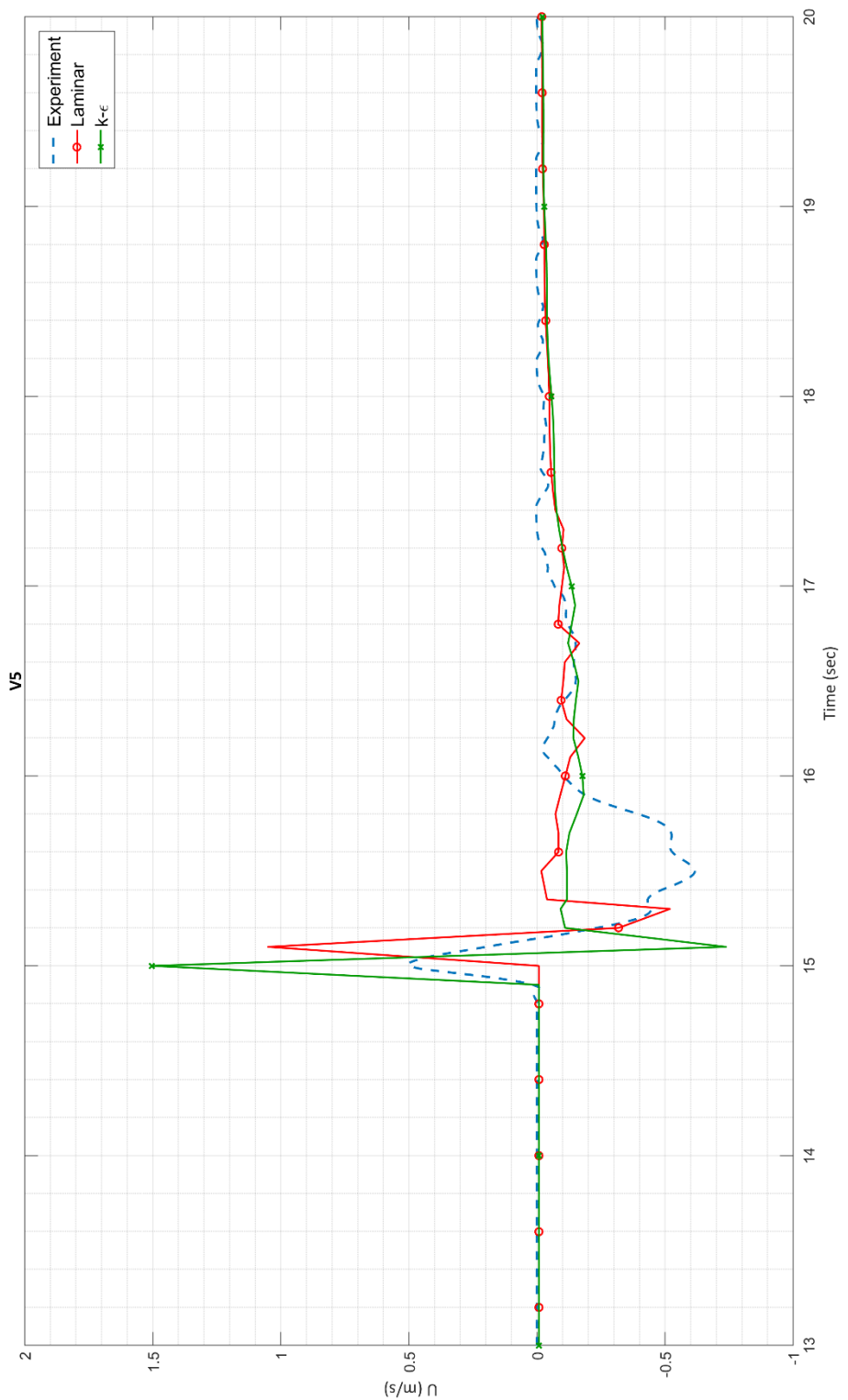


Figure 5.13. Comparison of Water Particle Velocities in x-direction, U of CADMAS-SURF/3D with Experimental Measurements at V5 for Case 2

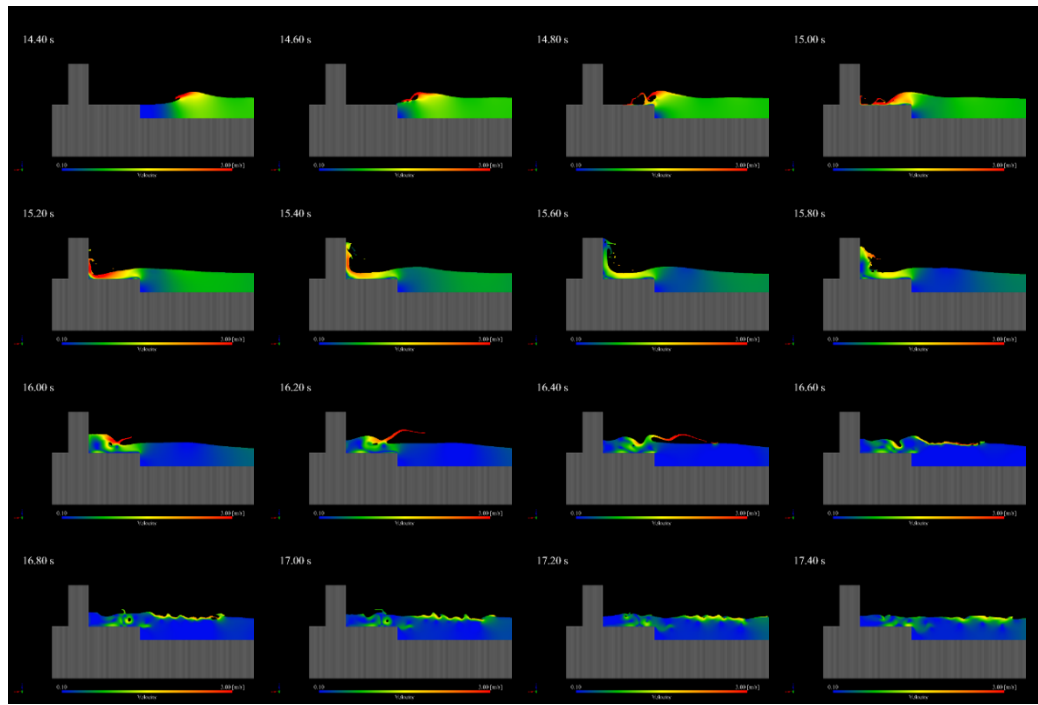


Figure 5.14. Snapshots from Simulation of Case 2 with laminar model

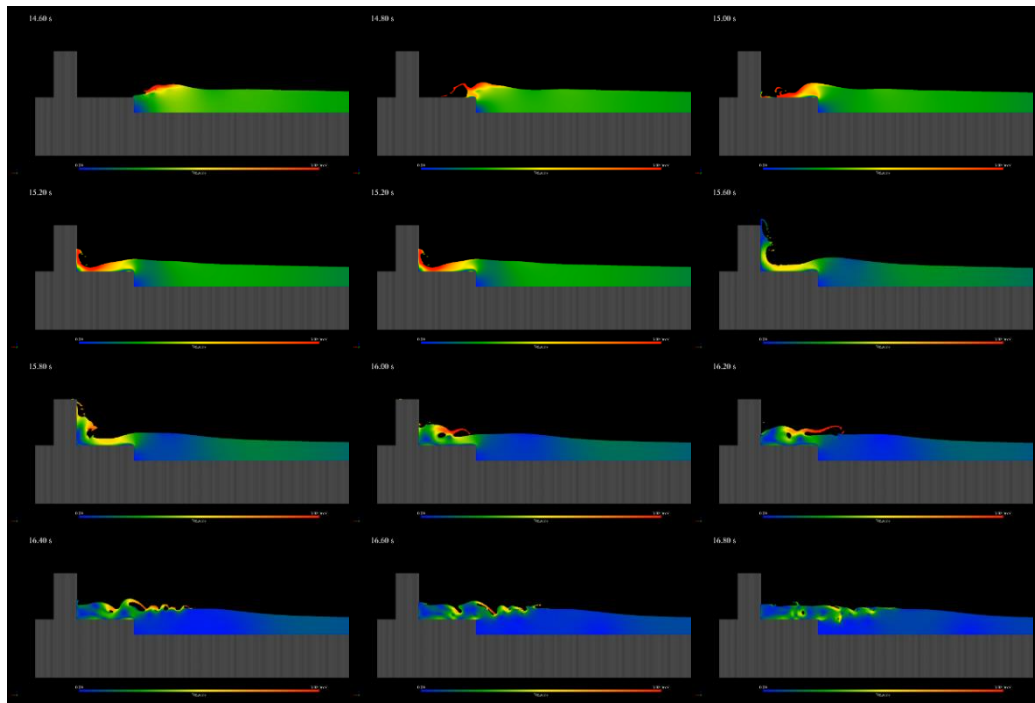


Figure 5.15. Snapshots from Simulation of Case 2 with $k-\epsilon$ turbulence model

Lastly, for Case 3, the time histories of water surface elevations obtained from each simulation (laminar and $k-\epsilon$) and the time histories in physical model experiments are compared and presented in Figure 5.16 for wave gauges from WG1 to WG10. Again the results of the wave gauges located along the channel showed a fairly well agreement with the measured data. The discrepancies occurred due to the wave reflection from the vertical wall. At WG9, the general trend of the experimental data is in fairly good agreement with the numerical trend. Around the seconds 16-17, where the breaking waves reflecting back from the vertical wall and falling motion created a circulation where the turbulence dominates the flow very much, the $k-\epsilon$ model performed better than the laminar as expected but provided slightly overestimated values for the water surface elevations.

The performances of the numerical models at WG10 which is the wave gauge located just in front of the vertical wall can be seen in detail in Figure 5.17 to distinguish the differences. Figure 5.17 indicates that $k-\epsilon$ turbulence model performed much better to catch the splash height. However, as it is discussed in the previous chapter, experimental measurement could not catch the splash height accurately. Therefore, $k-\epsilon$ turbulence model actually underestimated the peak value for water surface elevation at the incident of wave impact. The laminar model provides higher water surface elevations for the splash height, however, remains insufficient to calculate the falling motion and reflected wave behavior. To emphasize once more, it might be not reasonable to compare the performances of the models based on their calculation of the splash height since the experimental measurements could not catch the exact value of the water surface elevation at this location.

Moreover, another comparison between the time histories of the horizontal component of particle velocities in the x-direction and the measured time histories in physical experiments at velocity gauges (V1-V6) are presented in Figure 5.18. It can be seen that the general trend of the particle velocities is similar with the trend of the measured data from physical model experiments along the channel until the reflected waves arrive. In this case, the breaking of the solitary wave starts at V4 and continues until

the wave reaches the velocity gauge, V6. The 2D/3D effects caused apparent deviations in the numerical results of the particle velocities compared to the experimental data. In V4, it is clearly seen that both models could not solve the reflected wave motion accurately. In V5, $k-\epsilon$ model overestimated the peak velocity occurred at the incident of wave impact and also had some problems calculating the reflected wave motion. Although the trend of the experimental data seems to match with the trend of the computed data by laminar model, there are some problems in the solution of the particle velocities accurately under the turbulence effect for the reflected wave.

A closer look to the V6 to see the performance of the models in detail in front of the vertical wall is given in Figure 5.19. Although the peak particle velocities at the impact incident seem to be reasonably estimated by the laminar model, it can be seen that there is a time lag and laminar model could not solve the water particle velocities accurately after the falling motion and under strong turbulence effect. The $k-\epsilon$ model overestimated the peak particle velocities and this model also failed to solve the particle velocities after reflection of the solitary wave.

Snapshots from simulations performed using laminar and $k-\epsilon$ models for Case 3 indicating the velocity distribution during solitary wave attack are given in Figures 5.20 and 5.21, respectively.

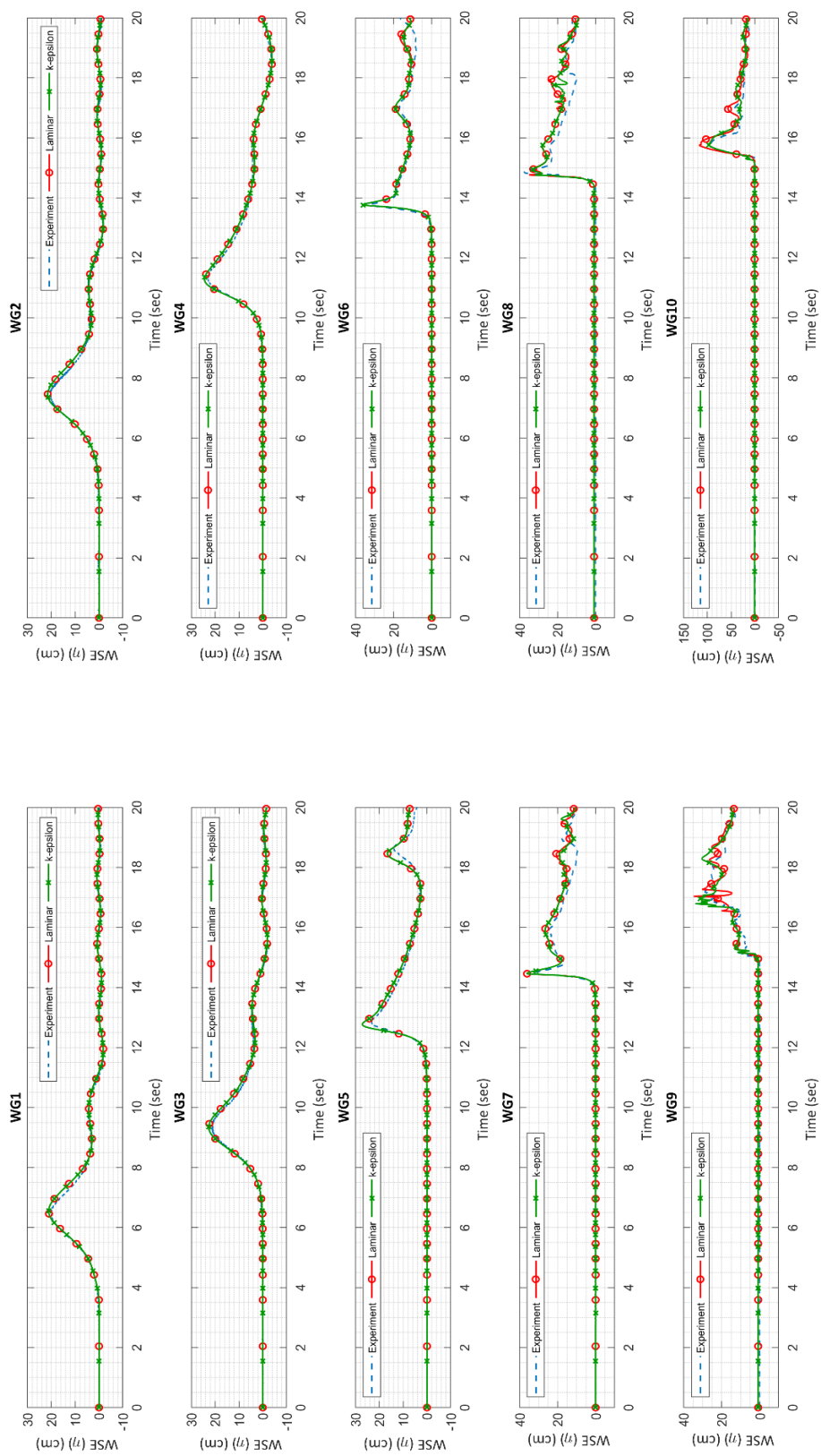


Figure 5.16. Comparison of Water Surface Elevations of CADMAS-SURF/3D with Experimental Measurements for Case 3

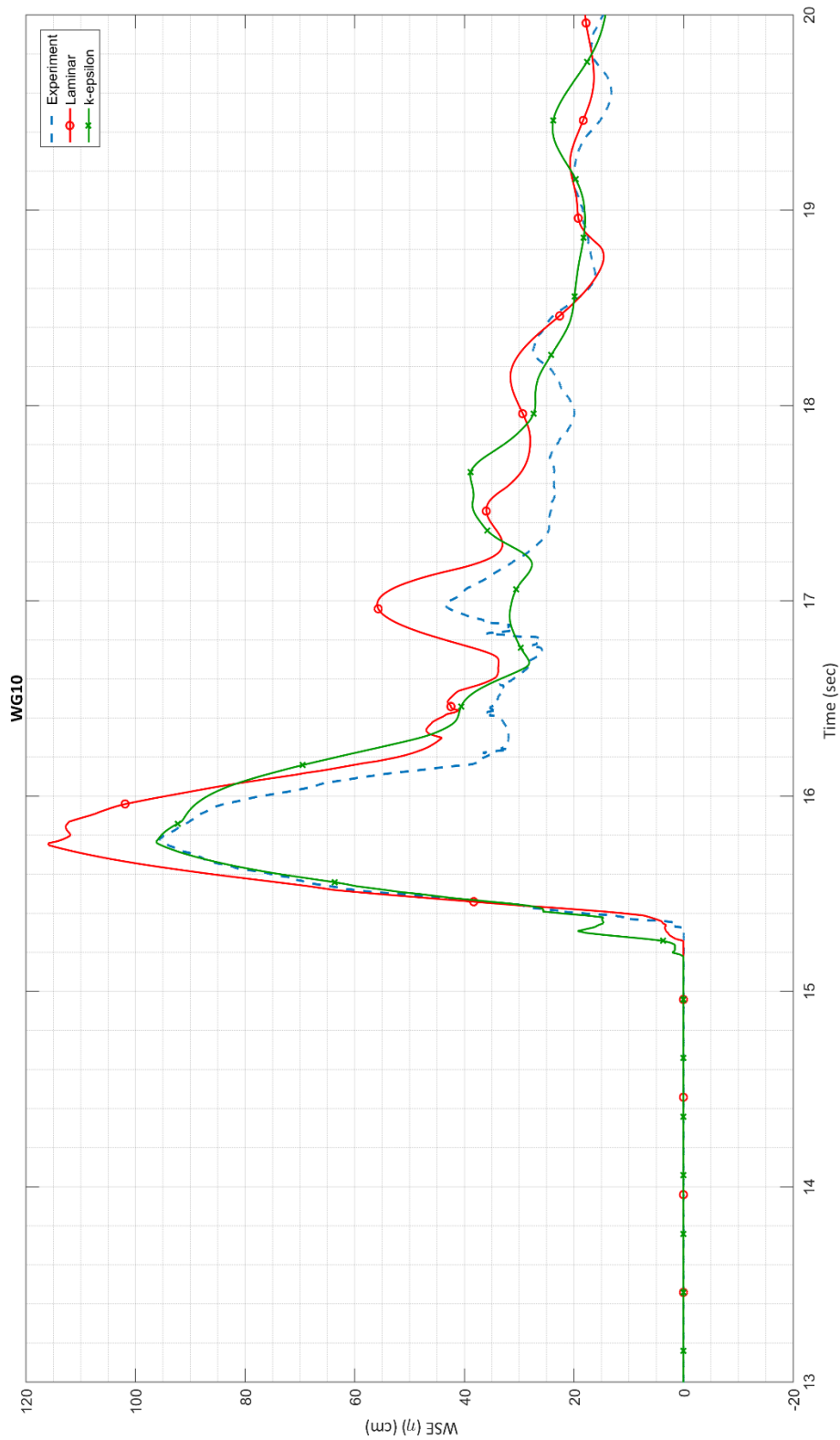


Figure 5.17. Comparison of Water Surface Elevations of CADMAS-SURF/3D with Experimental Measurements at WG10 for Case 3

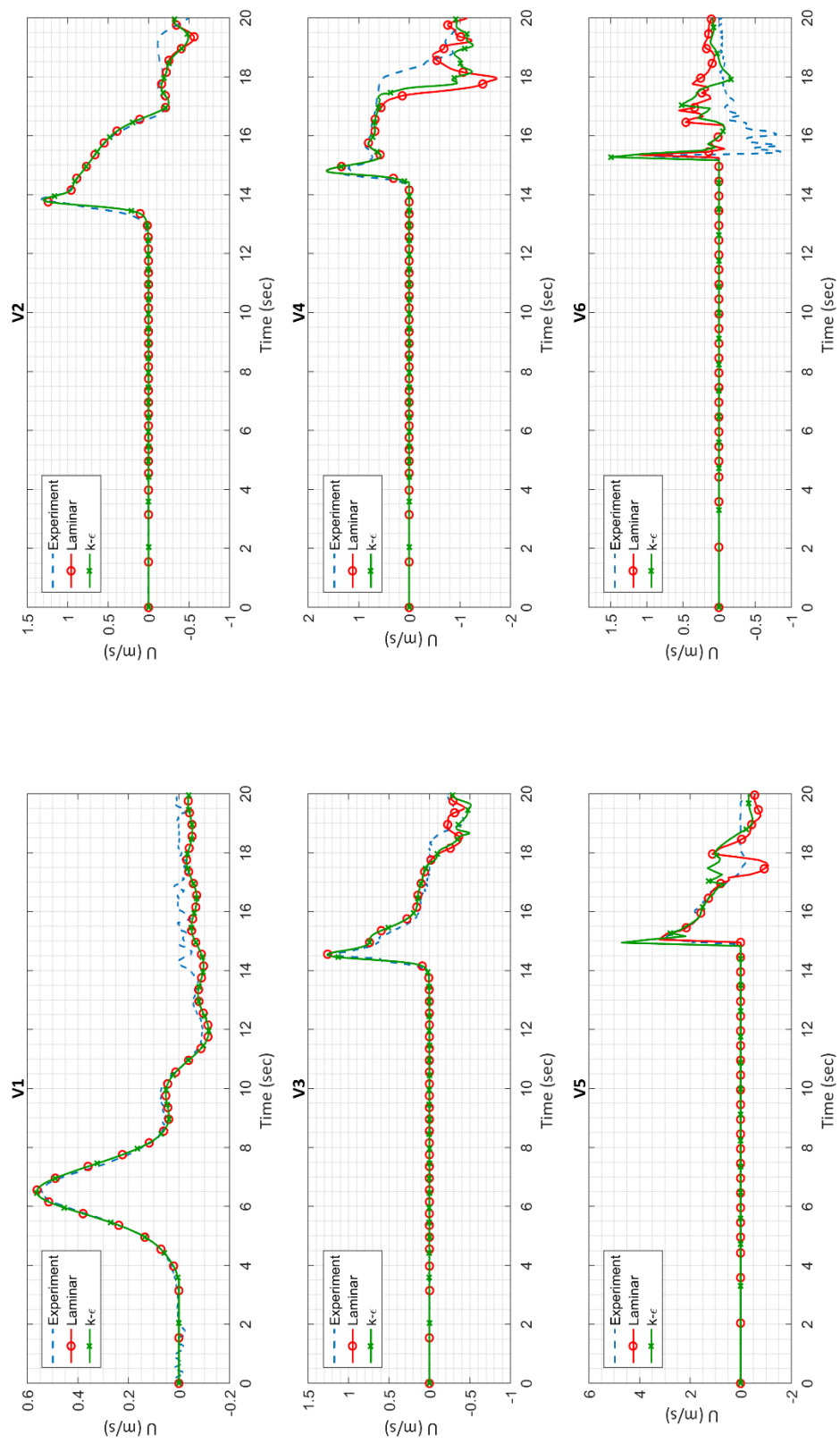


Figure 5.18. Comparison of Water Particle Velocities in x-direction, U of CADMAS-SURF/3D with Experimental Measurements for Case 2

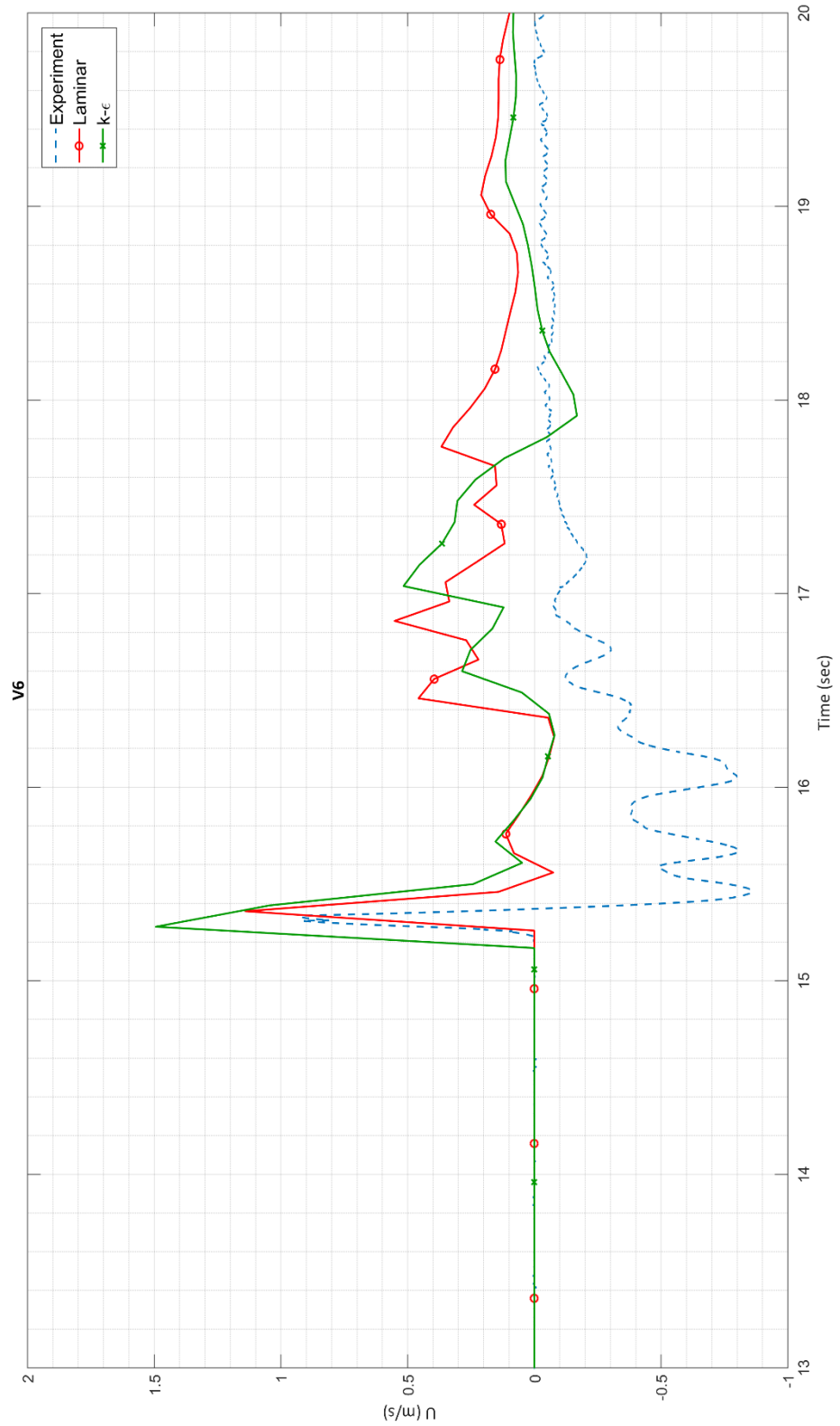


Figure 5.19. Comparison of Water Particle Velocities in x-direction, U of CADMAS-SURF/3D with Experimental Measurements at V6 for Case 3

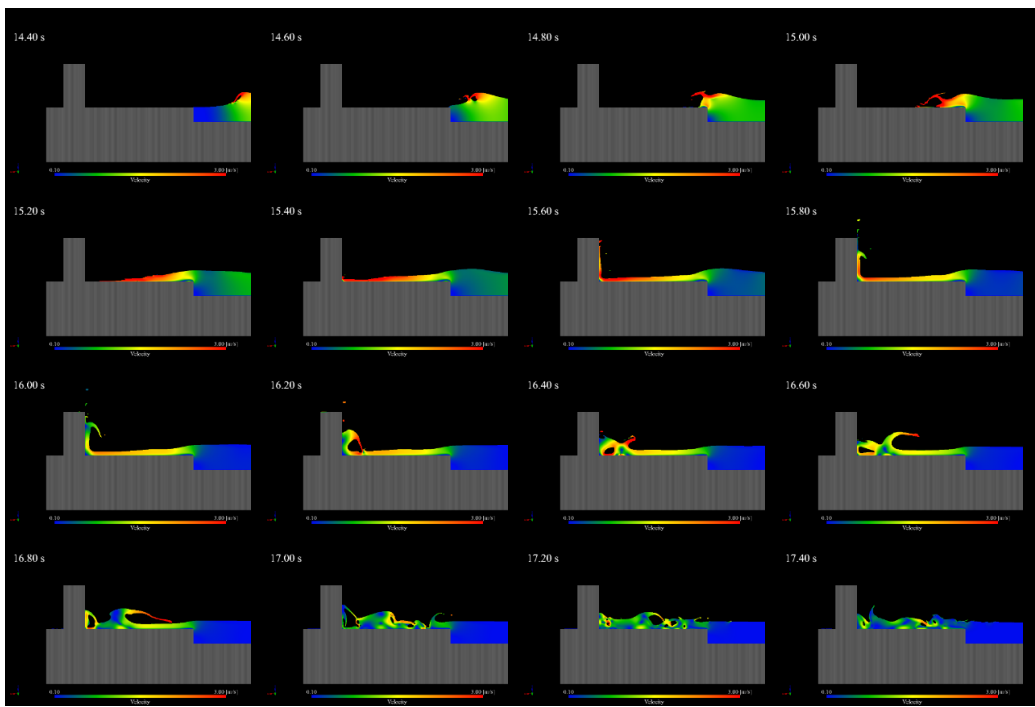


Figure 5.20. Snapshots from Simulation of Case 3 with laminar model

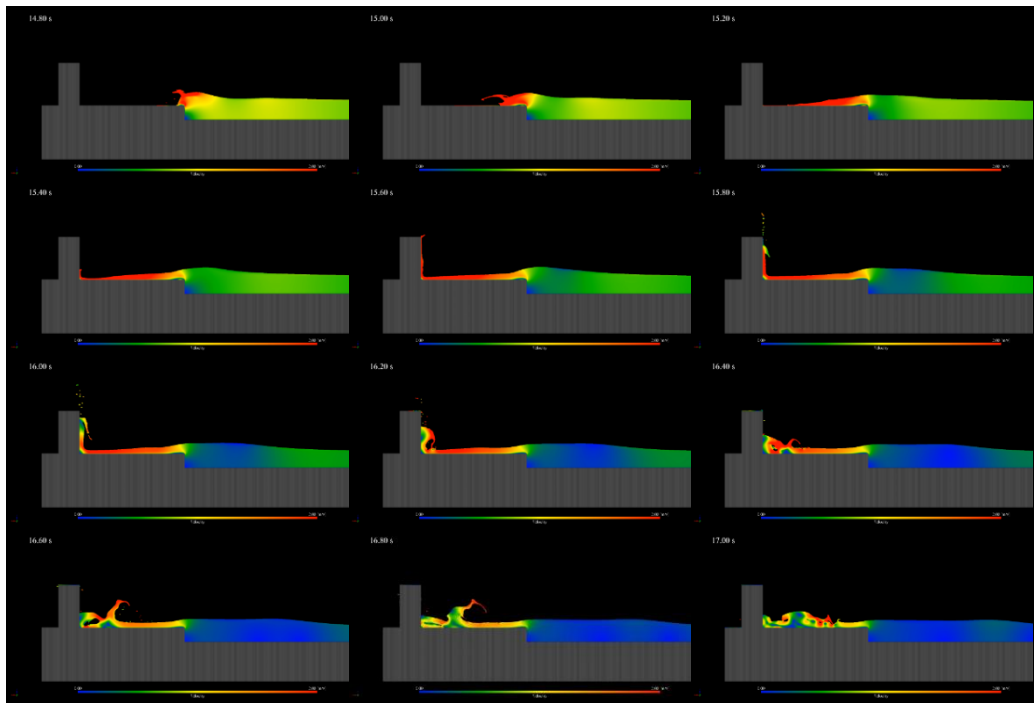


Figure 5.21. Snapshots from Simulation of Case 3 with k- ϵ turbulence model

In this Chapter, 2D numerical modeling of the physical model experiments for three cases using CADMAS-SURF/3D is presented. For all three cases, it can be concluded that CADMAS-SURF/3D performed well using both laminar and $k-\epsilon$ modeling approach to compute the water surface elevations and water particle velocities at the gauges located along the channel. The discrepancies are observed after the reflection of the solitary wave from the vertical wall. In all cases, it is seen laminar model provided smaller values of the peak particle velocities at the incident of wave impact compared to the results of the $k-\epsilon$ model. However, for the peak water surface elevation just in front of the vertical wall, the laminar model gives much higher values than the ones computed by $k-\epsilon$ model.

CHAPTER 6

COMPARISON OF THE NUMERICAL MODELS

In this chapter, performances of the three different numerical model and the effects of turbulence are presented by comparing them with experimental data and providing error limits in addition to graphical comparison of all models. Percent error analysis is performed to compare the numerical model performances and turbulence effect.

The overall view of the numerical simulations performed in this study to regenerate the three physical model experiments using three different numerical models with several turbulence models are shown in the Table 6.1.

Table 6.1. Numerical Simulations Performed for Each Three Physical Model Experiments

Models	NAMI DANCE	IHFOAM	CADMAS-SURF/3D
Laminar	✓	✓	✓
k-ε	-	✓	✓
k-ω-SST	-	✓	-

Table 6.1 indicates that the results obtained from NAMI DANCE, IHFOAM and CADMAS-SURF/3D are compared for each case considering only for the laminar model since the NAMI DANCE does not solve the turbulence. For the k-ε case, CADMAS-SURF/3D and IHFOAM results are compared with each other and experiments. Lastly, for k-ω-SST turbulence model, IHFOAM results are compared

with the experiment and the effect of using different turbulence models is investigated in its own merit.

Results of each numerical model are compared with the experimental data and a percent error is provided only for the peak water surface elevation of the incoming solitary wave. The percent error is the absolute value of the difference divided by the “correct” value times 100. The percent error analysis is carried out for each case at every wave gauge to compare the numerical simulation results with the experimental data by applying the below formula.

$$\% Error = \left| \frac{E - M}{E} \right| \times 100 \quad [6.1]$$

where E refers the experimental data which is considered the “correct” value and M is the model quantity.

6.1. Estimation of Splash Height on the Vertical Wall

As it is discussed in the Chapter 4, wave gauge in front of the vertical wall in every case could not measure the exact water surface elevation at the incident of the wave impact. Since the comparisons in this chapter based on the peak water surface elevations of the incoming wave, the experimental model videos are reviewed in detail to provide a reasonable peak splash height in front of the vertical wall for each case. It is known that the height of the vertical wall is 1m. Measuring the vertical wall height from the snapshots of experimental videos and scaling the value, the approximate peak water surface elevations are presented. To determine the reasonable splash height, continuous body vertical movement of the solitary wave at the incident of impact is considered rather than the small scale individual water splashes.

Figure 6.1 contains the two snapshots from the video of the physical model experiment of Case 1. Since the video taken from the side view (used in Chapter 4) has limited

angle of view to determine the maximum splash height, another video providing a broader angle is used for the snapshots. The first snapshot (a), shows the height of the vertical wall and the second one (b) indicates the peak water surface elevation at the incident of the solitary wave impact. The scaled value of the splash height assumed to be correct and used in the comparisons as 152 cm.

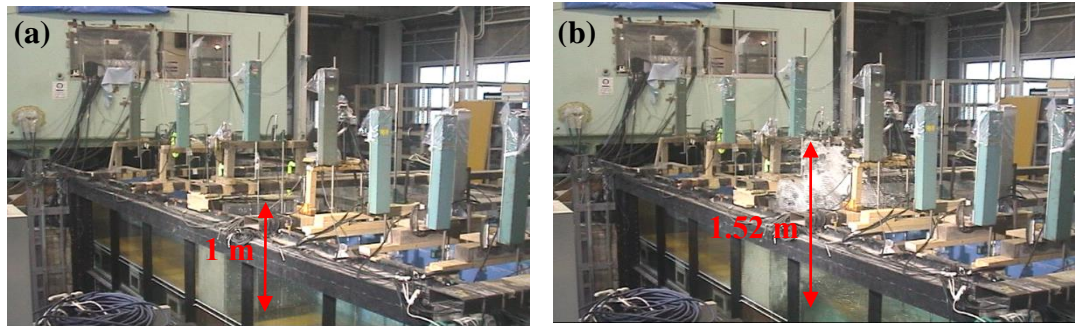


Figure 6.1. Snapshots from the experimental video of Case 1 (a) before the incident of impact of the solitary wave and (b) at the incident of impact of the solitary wave (Arikawa, 2015)

Figure 6.2 similarly shows the two snapshots from the video of the physical model experiment of Case 2. The first snapshot (a), shows the height of the vertical wall and the second one (b) indicates the peak water surface elevation at the incident of the solitary wave impact. The scaled value of the splash height assumed to be correct and used in the comparisons as 150 cm.

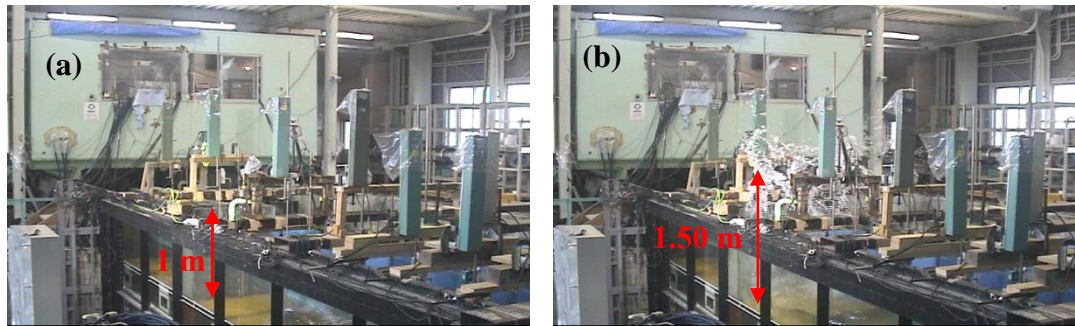


Figure 6.2. Snapshots from the experimental video of Case 2 (a) before the incident of impact of the solitary wave and (b) at the incident of impact of the solitary wave (Arikawa, 2015)

Lastly in Figure 6.3, two snapshots from the video of the physical model experiment of Case 2 are presented. The first snapshot (a), shows the height of the vertical wall and the second one (b) indicates the peak water surface elevation at the incident of the solitary wave impact. The scaled value of the splash height assumed to be correct and used in the comparisons as 133 cm. In this case particularly, small scale splashes reach much higher elevation than the determined one. However, these splashes are extremely difficult to be measured in the physical modeling experiments and also they require much smaller mesh sizes to be accurately modelled in numerical simulations. Furthermore, these smaller splashes are not effective on the design of coastal structures in the engineering point of view. Therefore, the main water body splash is traced and the maximum water surface elevation is determined accordingly.

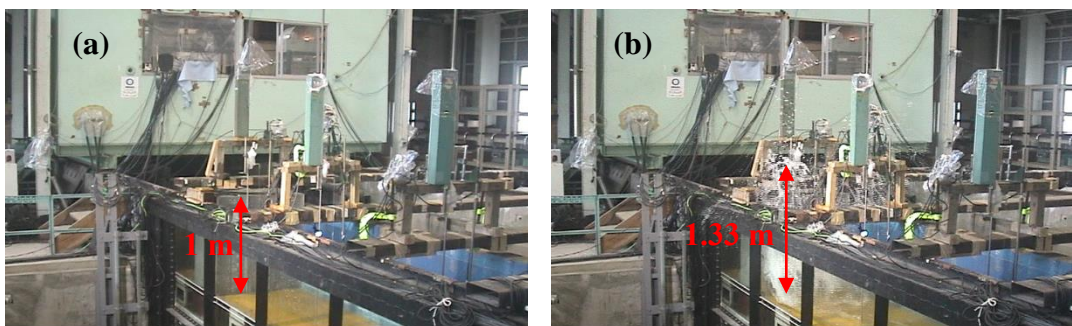


Figure 6.3. Snapshots from the experimental video of Case 3 (a) before the incident of impact of the solitary wave and (b) at the incident of impact of the solitary wave
(Arikawa, 2015)

Since the analyses presented above to estimate the peak water surface elevation in front of the vertical wall is highly depends on the person who performs the analyses, camera position and angle, resolution of the recorded videos etc., the given percent errors for the performance comparisons should not be taken as a solid quantitative comparison. It is provided to have some understanding and qualitative thought about the differences of numerical models.

6.2. Comparison for Laminar Approach

Results of the peak values of water surface elevations computed by NAMI DANCE, IHFOAM and CADMAS-SURF/3D simulations with laminar approach and the measured maximum water surface elevation data of physical model experiments are presented in Table 6.2 for all cases at each wave gauge for comparisons.

The graphical comparison of water surface elevation for Case 1 is given in Figure 6.4 for all wave gauges and a closer look for the wave gauge located just in front of the vertical wall is given in Figure 6.5 to see the differences between the numerical model result and the experimental data. Similarly, graphical comparison of the water particle velocities for the three models are given in Figure 6.6 and a closer look of the velocity gauge located right in front of the vertical wall is presented in Figure 6.7. To have a better understanding of the differences between the experimental data and the results of the different numerical models with laminar approach, the percent errors of each wave gauge for Case 1 are presented in Table 6.3 only for the peak water surface elevations.

For Case 1 results it is seen that, all models performed well along the channel considering the wave propagation and computed the water surface elevations and water particle velocities with sufficient accuracy from the engineering point of view. The averaged percent errors along the channel are around 2.5%, 2.55% and 2.7% for NAMI DANCE, IHFOAM and CADMAS-SURF/3D respectively excluding the WG1. As the solitary wave approaches to the vertical wall, the vertical velocity starts to affect the motion and the NAMI DANCE starts to provide underestimated values for the water surface elevations and water particle velocities. The percent error is increased and around 64% error is calculated for estimating the maximum water surface elevation in front of the vertical wall. Because of the nature of depth averaged NSW equations (which do not consider vertical motion), the water surface elevations in front of the vertical wall are underestimated and in contrary, the horizontal component of the water particle velocities are overestimated comparing to experimental data as expected.

The results of the IHFOAM and CADMAS-SURF/3D are very similar both along the channel and in front of the vertical wall considering the water surface elevation and water particle velocities. At WG7, it can be seen from the Table 6.3 that the percent error for IHFOAM results is higher than the CADMAS-SURF/3D. One of the reasons for that could be the output interval. Increasing the sampling rate for the output may improve the results of the water surface elevations measured at this wave gauge. Another difference observed at the wave and velocity gauges located just in front of the vertical wall. For this case, it can be said that CADMAS-SURF/3D underestimated the water particle velocities and IHFOAM provides closer peak value comparing to experimental data. It should be noted that, due to the location of the V4 and complicated process of the wave breaking, it is quite difficult to measure the exact water particle velocities even for the measurement device. For the water surface elevations just in front of the vertical wall, percent errors calculated for IHFOAM and CADMAS-SURF/3D are 8.82% and 10%, respectively.

It is worth to discussed the WG5 results in particularly since there is a constant issue observed for the results of the water surface elevations. It can be seen from the percent error tables that, IHFOAM and CADMAS-SURF/3D results shows an abrupt increase at the location of WG5 where it is located at the end of the slope. Detailed analysis on WG5 results should be performed to investigate the cause of this behavior.

Table 6.2. Peak Surface Water Elevation (in cm) of Each Wave Gauge for All Cases Under Laminar Approach

Wave Gauges	NAMIDANCE			IHFOAM			CADMAS-SURF/3D			EXPERIMENT		
	Case 1	Case 2	Case 3	Case 1	Case 2	Case 3	Case 1	Case 2	Case 3	Case 1	Case 2	Case 3
WG1	20.51	19.7	19.9	20.89	20.88	21.1	21.11	21.31	20.51	19.7	19.9	
WG2	21.82	19.37	19.97	21.34	21.31	21.3	21.48	20.68	21	19.99	20.22	
WG3	22.58	20.16	20.24	22.59	22.56	22.56	22.66	22.67	21.87	22.07	20.93	21.17
WG4	23.39	21.1	21.1	24.57	24.53	24.52	24.46	24.47	23.67	23.7	22.75	22.97
WG5	23.29	20.99	21.01	27.31	27.27	27.26	27.12	27.13	26.34	24.22	22.95	23.25
WG6	23.01	21.08	20.99	33.17	33.09	33.11	36.37	33.69	35.6	33.61	31.43	32.26
WG7	21.97	20.43	20.37	30.31	30.51	30.44	35.96	30.25	35.41	35.35	35.72	34.63
WG8	54.74	31.81	31.56	165.4	33.05	32.11	167.2	34.72	34.24	152	39.04	37.4
WG9	-	41.91	25.58	-	113.4	16.11	-	142	12.36	-	150	11.61
WG10	-	-	30.14	-	-	107.3	-	-	115.9	-	-	133

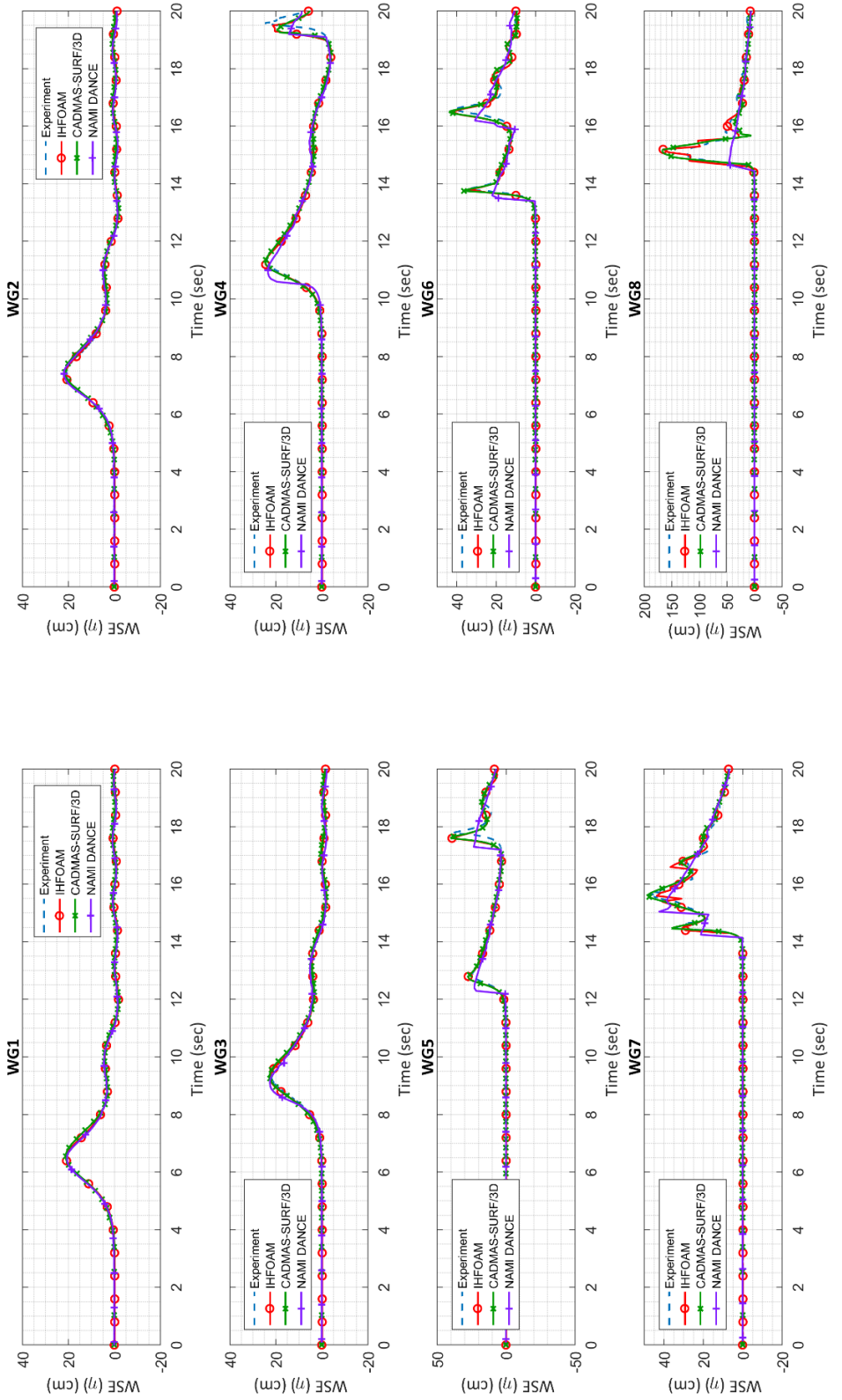


Figure 6.4 Comparison of Water Surface Elevations of All Models with Experimental Measurements for Case 1 with Laminar Approach

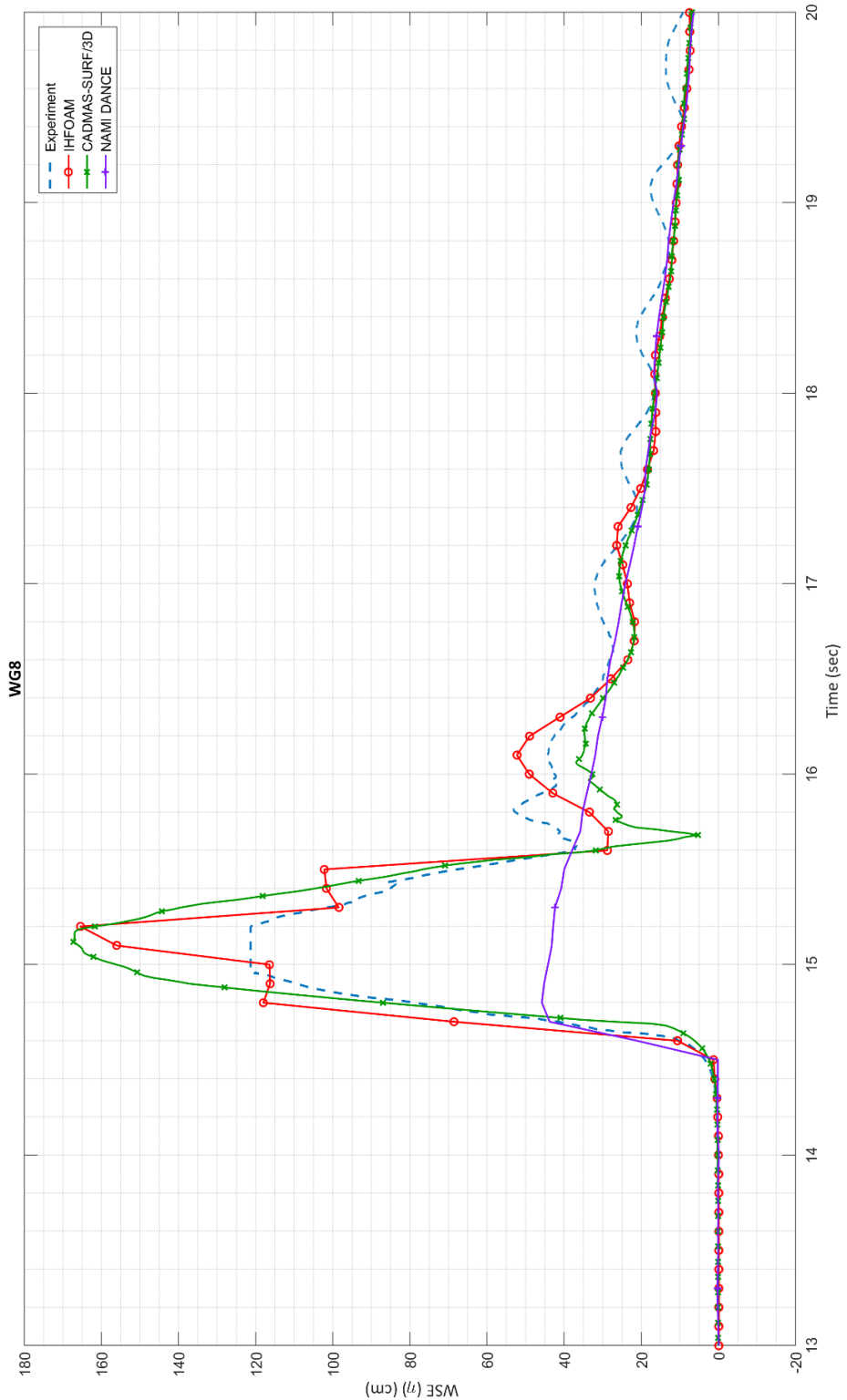


Figure 6.5 Comparison of Water Surface Elevations of All Models with Experimental Measurements at WG8 for Case 1 with Laminar Approach

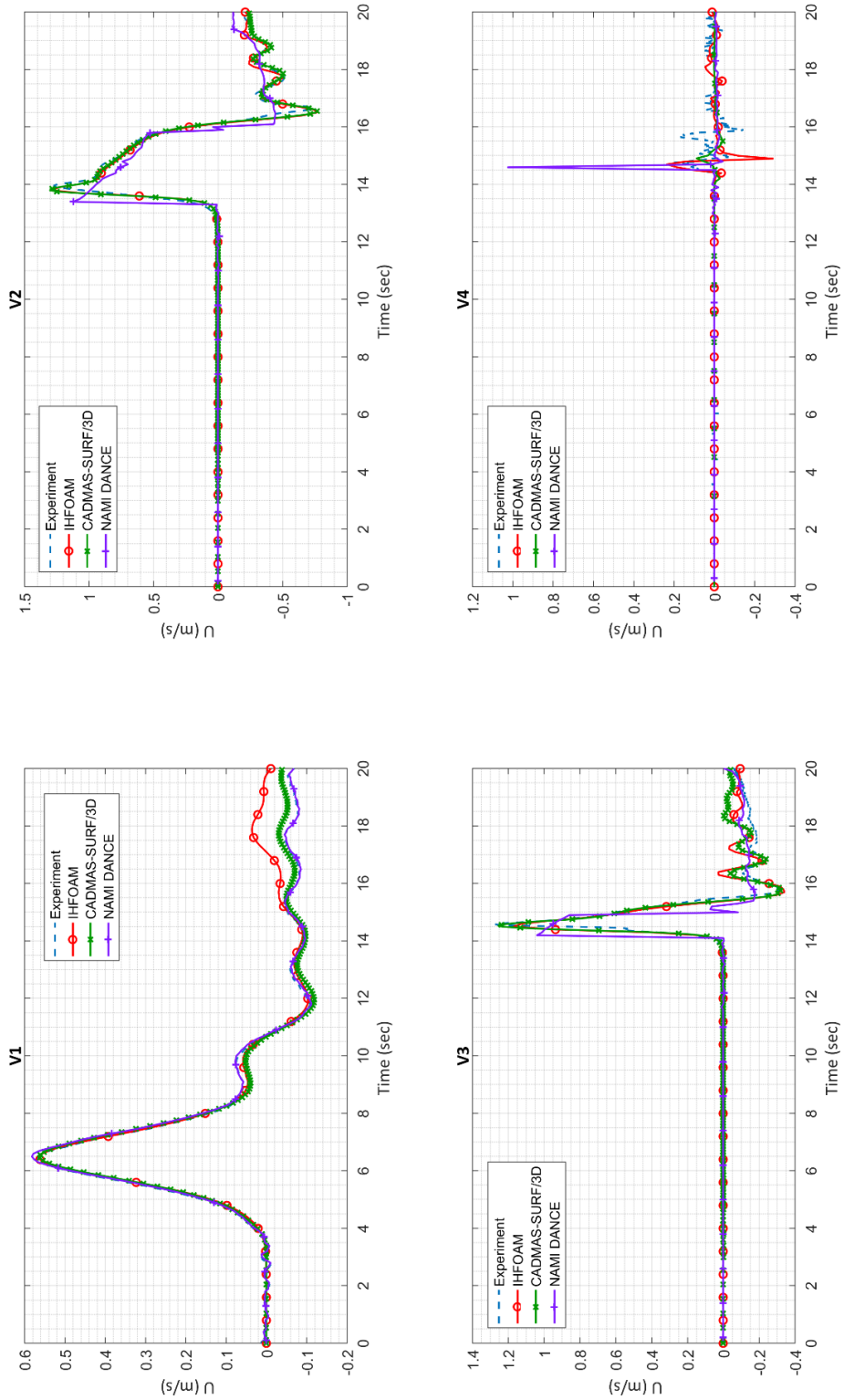


Figure 6.6 Comparison of Particle Velocities in x-direction, U of All Model with Experimental Measurements for Case 1 with Laminar Approach

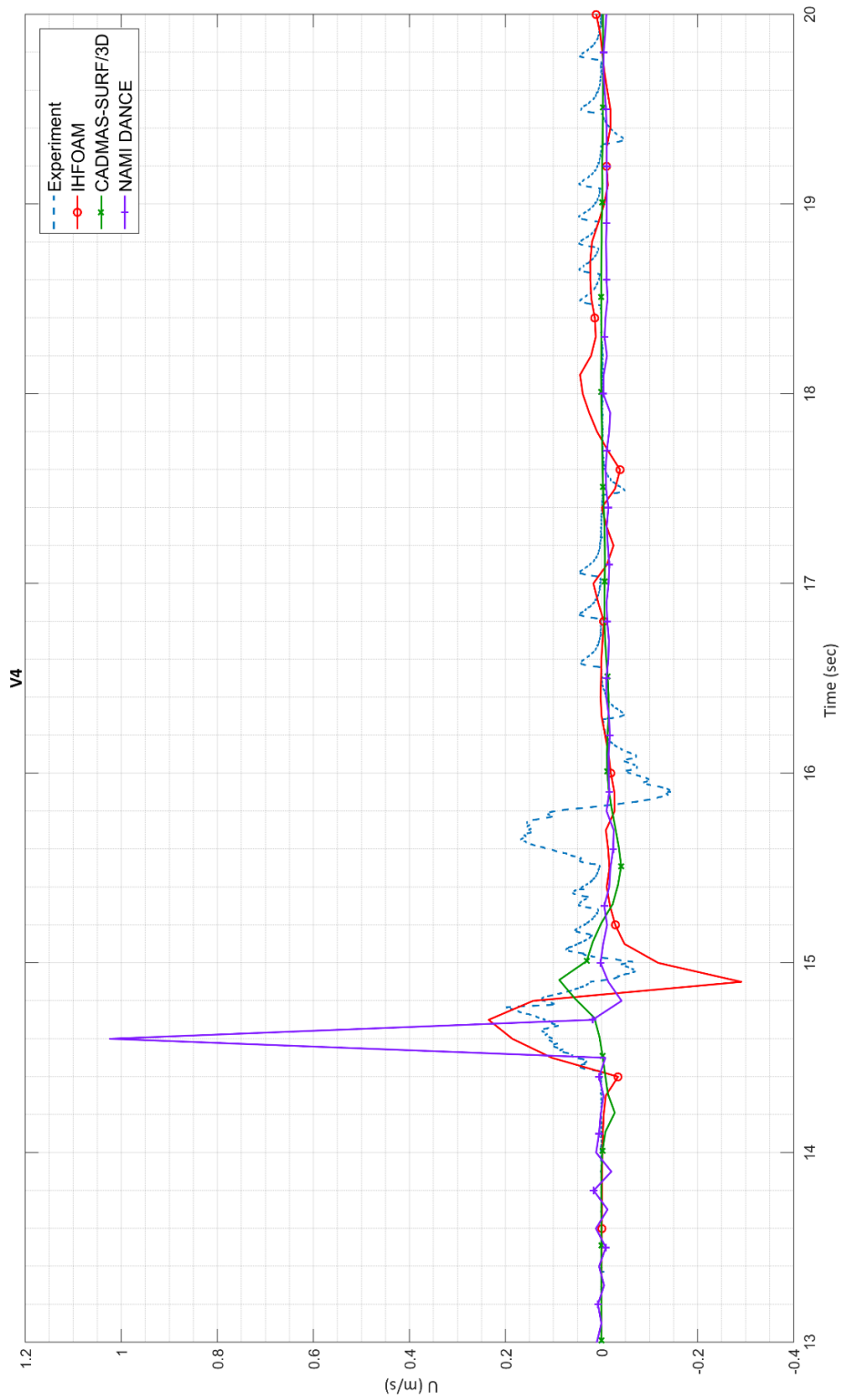


Figure 6.7 Comparison of Particle Velocities in x-direction, U of All Models with Experimental Measurements at V4 for Case 1 with Laminar Approach

Table 6.3. Percent Error of Each Wave Gauge for Laminar Approach in Case 1

Wave Gauges	Case 1		
	NAMI DANCE	IHFOAM	CADMAS- SURF/3D
	Percent Error	Percent Error	Percent Error
WG1	0.00	1.85	2.88
WG2	3.90	1.62	2.29
WG3	2.31	2.36	2.67
WG4	1.31	3.67	3.21
WG5	3.84	12.76	11.97
WG6	31.54	1.31	8.21
WG7	37.85	14.26	1.73
WG8	63.99	8.82	10.00

The graphical comparison of water surface elevation for Case 2 is given in Figure 6.8 for all wave gauges and a closer look for the wave gauge located just in front of the vertical wall is given in Figure 6.9 to see the differences between the numerical model result and the experimental data. Similarly, graphical comparison of the water particle velocities for the three models are given in Figure 6.10 and a closer look of the velocity gauge located right in front of the vertical wall is presented in Figure 6.11. To have a better understanding of the differences between the experimental data and the results of the different numerical models with laminar approach, the percent errors of each wave gauge for Case 2 are presented in Table 6.4 only for the peak water surface elevations.

It can be seen from the Figure 6.8 that all models are reasonably well agreement along the channel for both water surface elevations and water particle velocities. For NAMI DANCE results it can be said that underestimation of the peak water surface elevations starts with the vertical velocity component governs the motion. At the WG9, there is a time lag for the NAMI DANCE results. Since NAMI DANCE underestimated the water particle velocities at the V4 location where the wave passes through the small

step at the end of the horizontal part, the time required for the solitary wave to reach the WG9 and V5 is longer than the experiment and other two model results. For Case 2, the percent error for the peak water surface elevations results of NAMI DANCE at WG9 is calculated as 64%. It can be inferred that, higher percent errors are obtained near the wall area because of the effect of wave breaking which the turbulence has a significant role in the process.

For IHFOAM and CADMAS-SURF/3D, it is seen that the water surface elevations and water particle velocities results are very similar with each other. When the wave breaking starts, the differences between these two numerical models become more distinguishable. At the wave gauge located just in front of the vertical wall (WG9), CADMAS-SURF/3D provided higher peak water surface elevations results than IHFOAM. While the percent error for CADMAS-SURF/3D is around 5%, IHFOAM shows nearly 25% error. For the water particle velocities at V5, it is seen that both models give the same peak particle velocity. However, for the negative velocities IHFOAM provided overestimated values.

Table 6.4. Percent Error of Each Wave Gauge for Laminar Approach in Case 2

Wave Gauges	Case 2		
	NAMI DANCE Percent Error	IHFOAM Percent Error	CADMAS- SURF/3D Percent Error
WG1	0.00	5.99	7.16
WG2	3.10	6.60	7.45
WG3	3.68	7.79	8.31
WG4	7.25	7.82	7.56
WG5	8.54	18.82	18.21
WG6	32.93	5.28	7.19
WG7	42.81	14.59	15.31
WG8	18.52	15.34	11.07
WG9	72.06	24.40	5.33

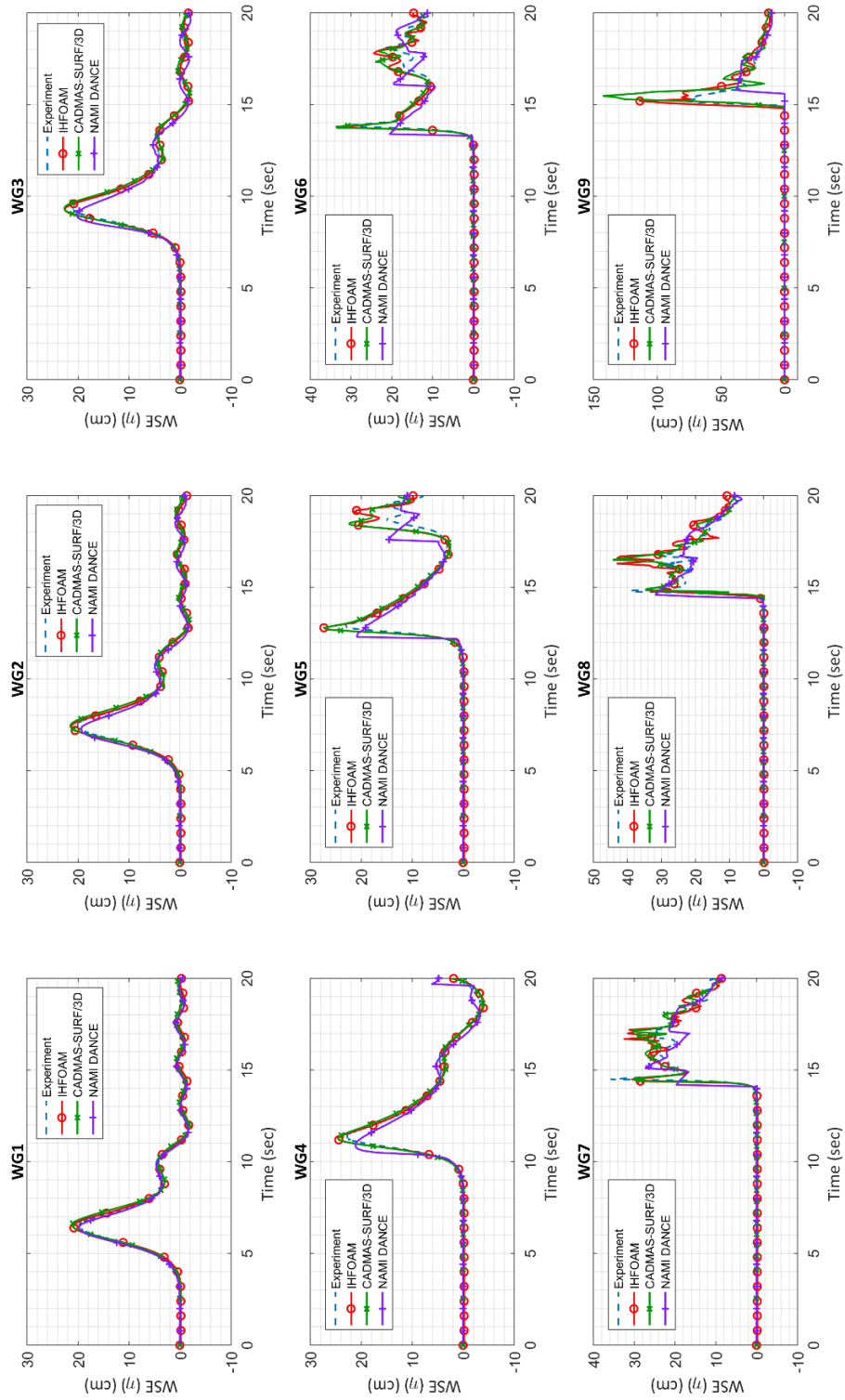


Figure 6.8 Comparison of Water Surface Elevations of All Models with Experimental Measurements for Case 2 with Laminar Approach

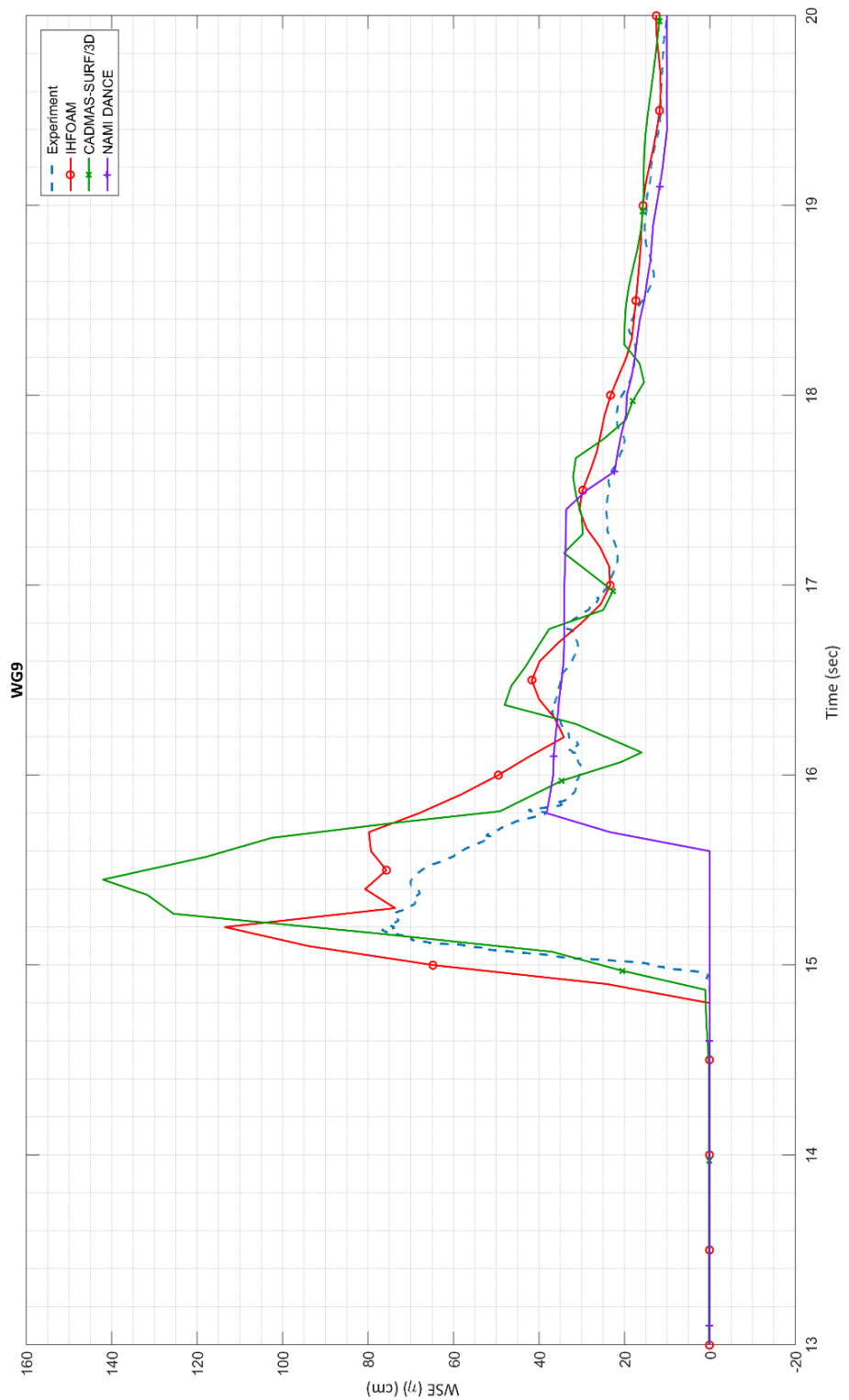


Figure 6.9 Comparison of Water Surface Elevations of All Models with Experimental Measurements at WG9 for Case 2 with Laminar Approach

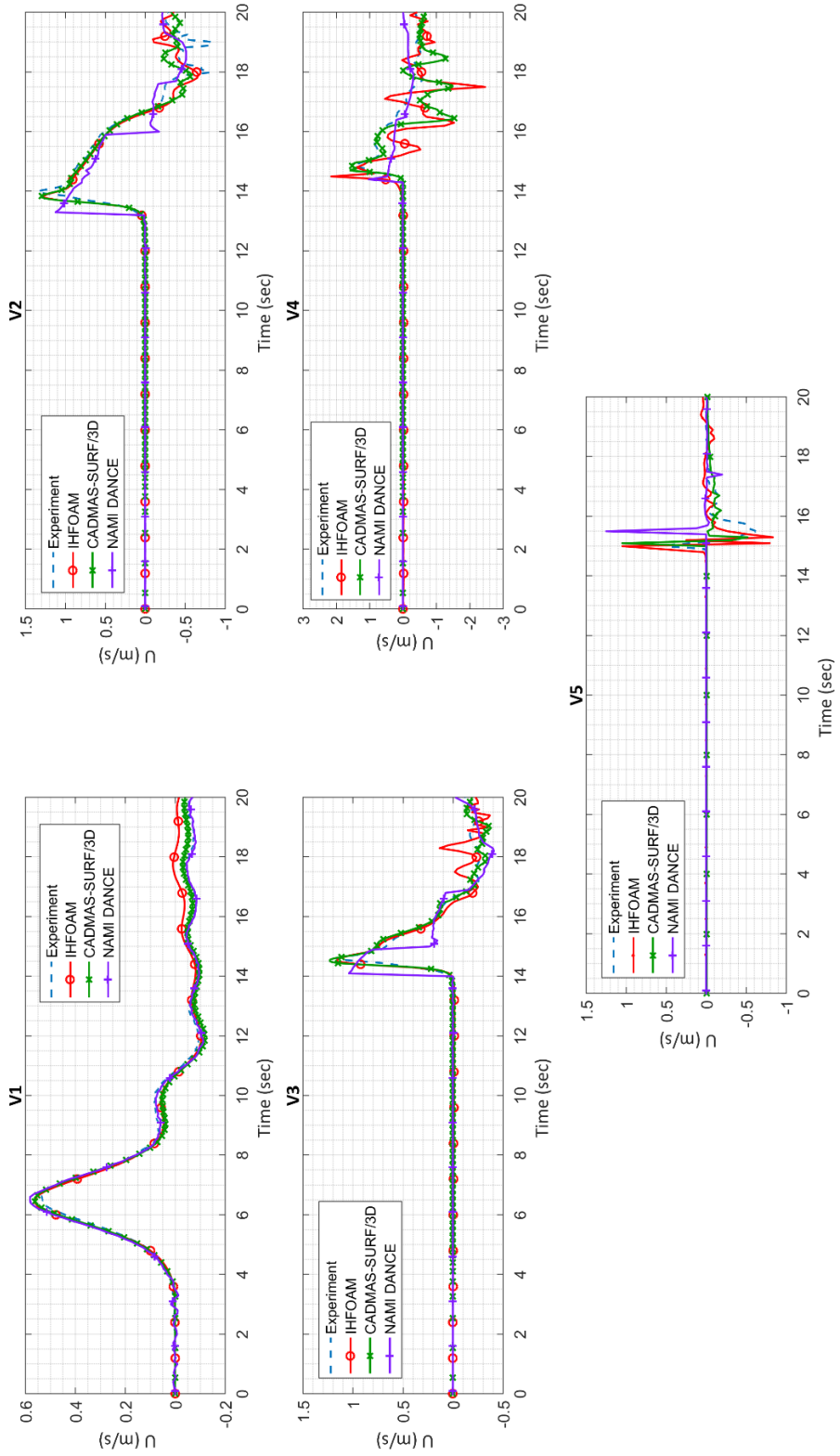


Figure 6.10 Comparison of Particle Velocities in x-direction, U of All Model with Experimental Measurements for Case 2 with Laminar Approach

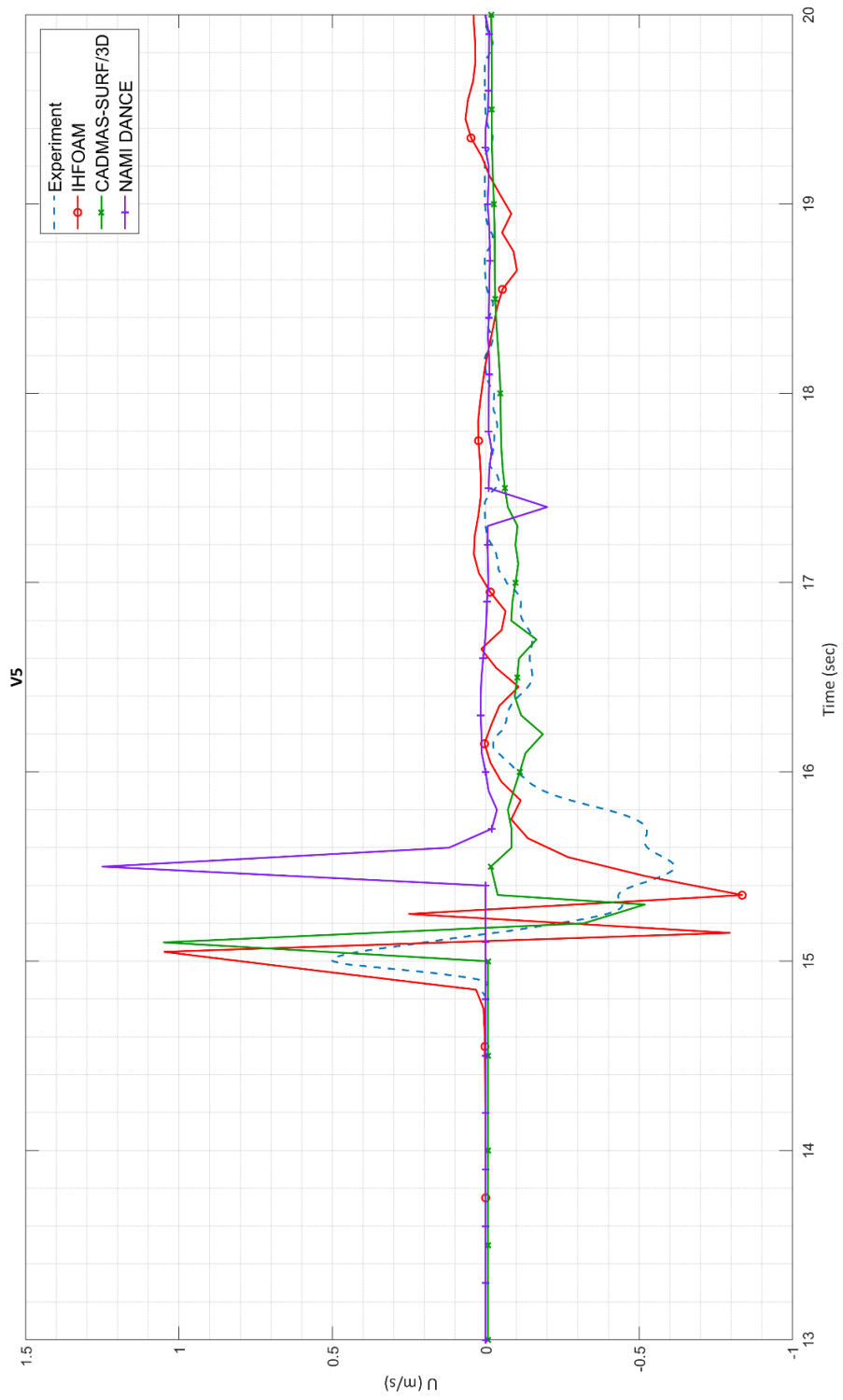


Figure 6.11 Comparison of Particle Velocities in x-direction, U of All Models with Experimental Measurements at V5
for Case 2 with Laminar Approach

For Case 3 results, the graphical comparison of water surface elevation is given in Figure 6.12 for all wave gauges and a closer look for the wave gauge located just in front of the vertical wall is given in Figure 6.13 to see the differences between the numerical model result and the experimental data. Similarly, graphical comparison of the water particle velocities for the three models are given in Figure 6.14 and a closer look of the velocity gauge located right in front of the vertical wall is presented in Figure 6.15. To have a better understanding of the differences between the experimental data and the results of the different numerical models with laminar approach, the percent errors of each wave gauge for Case 3 are presented in Table 6.5 only for the peak water surface elevations. Similarly, water surface elevations and water particle velocities are in reasonably well agreement with the experimental data for all three models in Case 3. The differences can be observed with the start of wave breaking process where the vertical velocities are dominant in the flow. The time lag for the NAMI DANCE results are much apparent in this case. Since the solitary wave comes as a broken wave in this case, the motion is more complicated than those previous cases. At the WG10, it can be seen that NAMI DANCE could not estimate the water surface elevations accurately. The percent error is around 77%. For the water surface particles, NAMI DANCE could not provide accurate results. Again, these results were expected due to the nature of the depth-averaged NSW equations. For IHFOAM and CADMAS-SURF/3D, it is seen that the water surface elevations and water particle velocities results are very similar with each other until the solitary wave starts to break. From that point, the differences between these two numerical models become more distinguishable. At WG10, CADMAS-SURF/3D provided higher peak water surface elevations results than IHFOAM. While the IHFOAM gives around 19% error, the percent error calculated for CADMAS-SURF/3D is nearly 13%. In Figure 6.13 it is seen that CADMAS-SURF/3D has more or less the same trend with the experimental data however, IHFOAM could not provide accurate results for the reflected wave. For the water particle velocities at V6, it is seen that IHFOAM overestimated the peak value. On the other hand, it is clearly seen that CADMAS-SURF/3D could not solve the reflected water particle velocities.

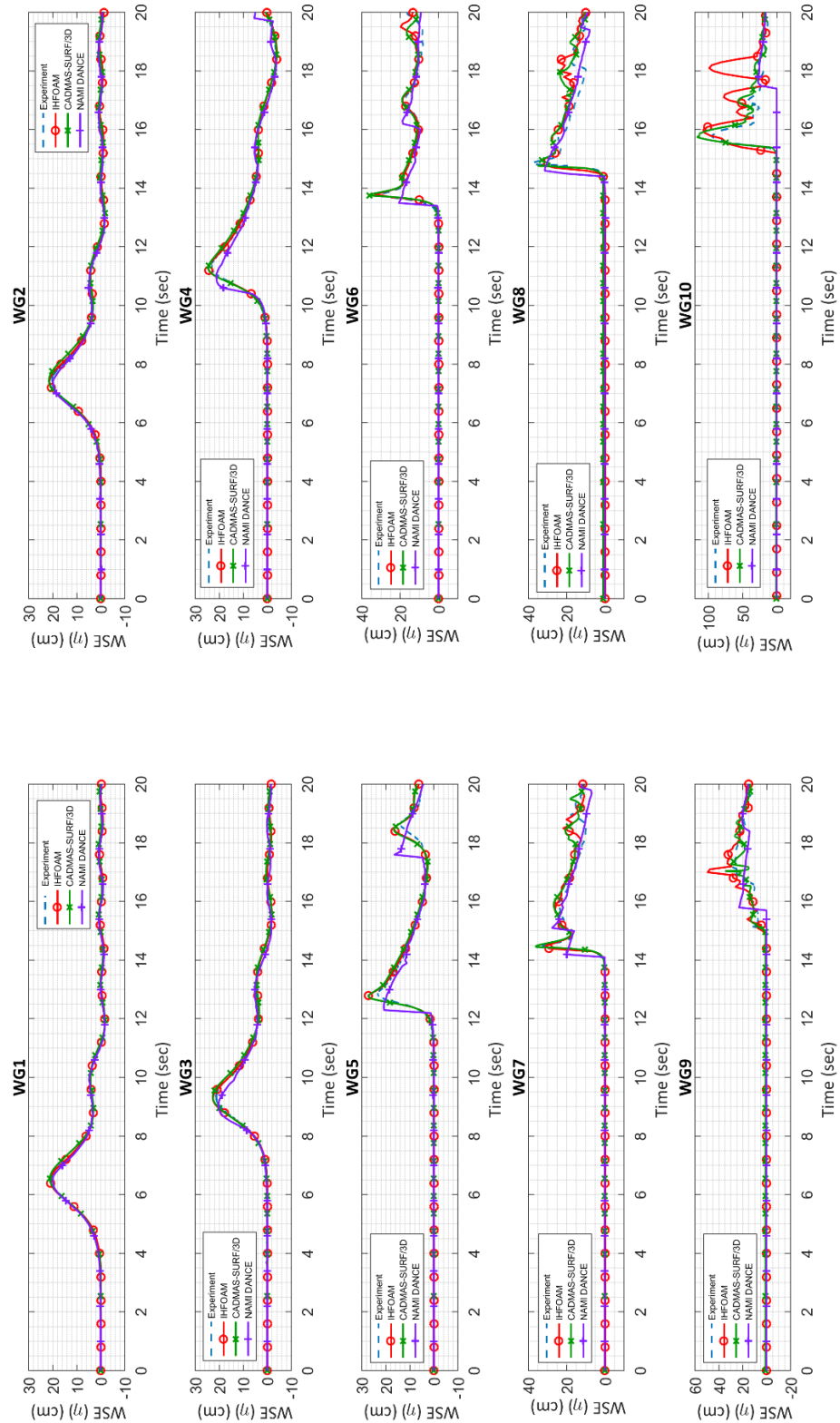


Figure 6.12 Comparison of Water Surface Elevations of All Models with Experimental Measurements for Case 3 with Laminar Approach

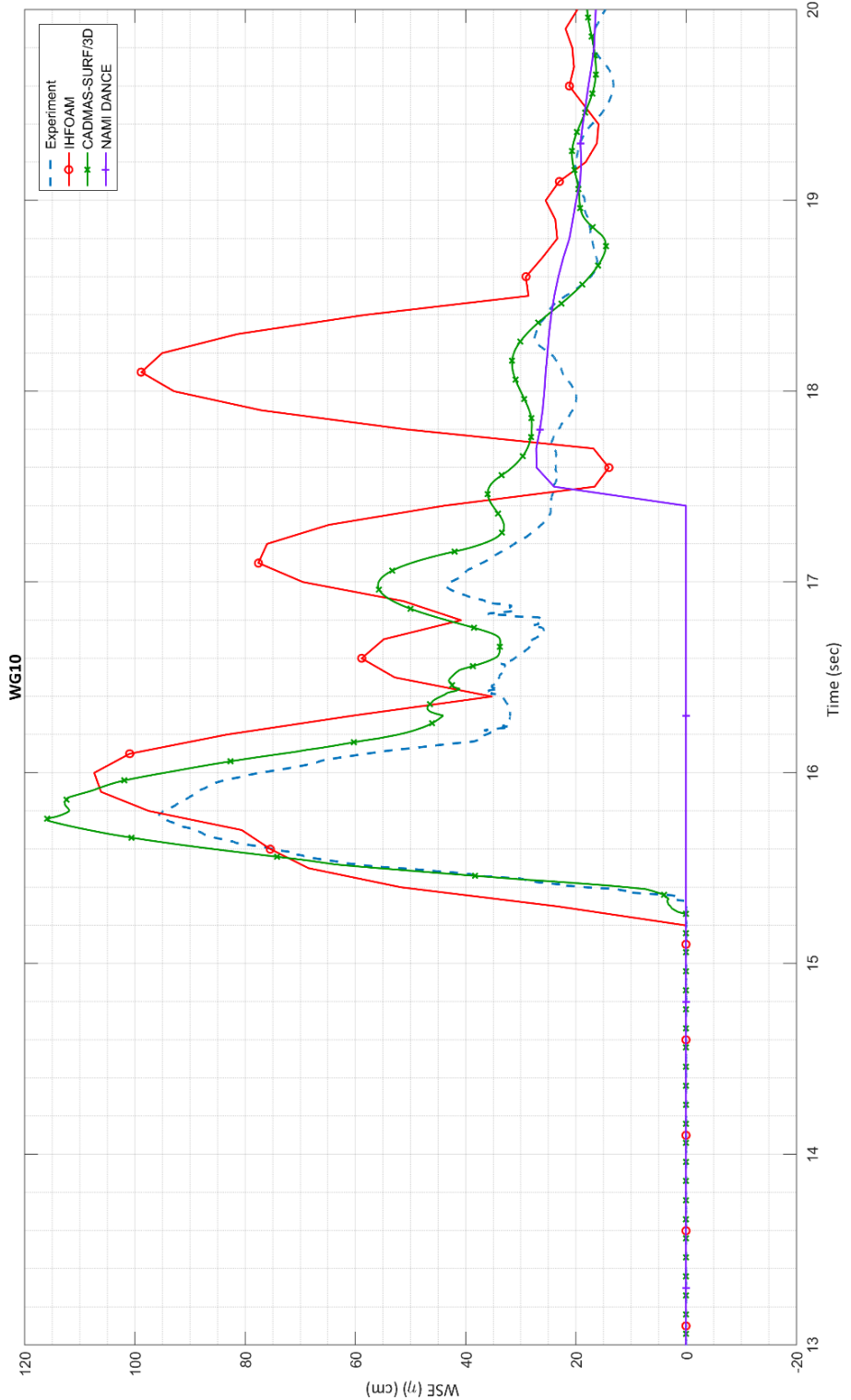


Figure 6.13 Comparison of Water Surface Elevations of All Models with Experimental Measurements at WG10 for Case 3 with Laminar Approach

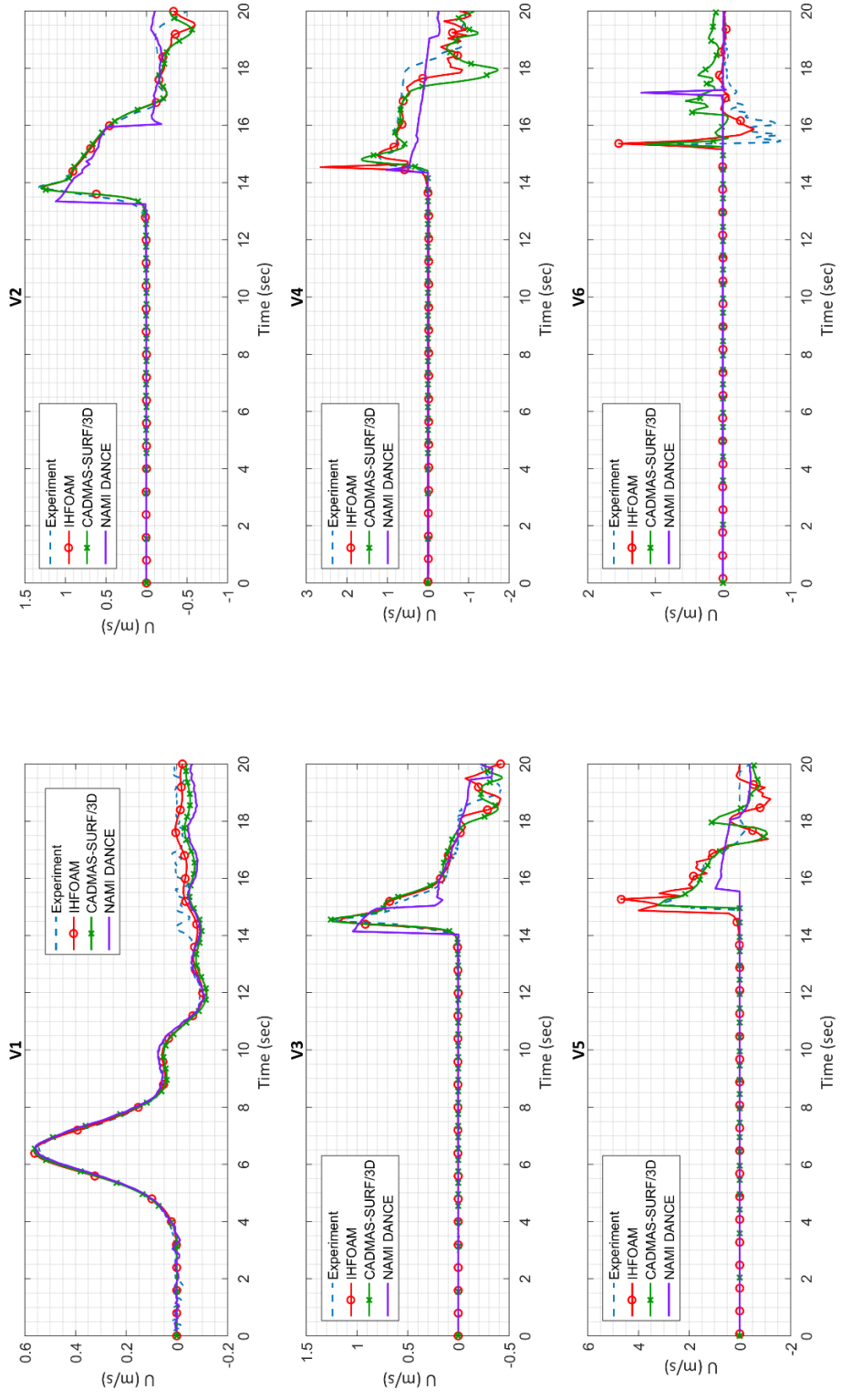


Figure 6.14 Comparison of Particle Velocities in x-direction, U of All Model with Experimental Measurements for Case 3 with Laminar Approach

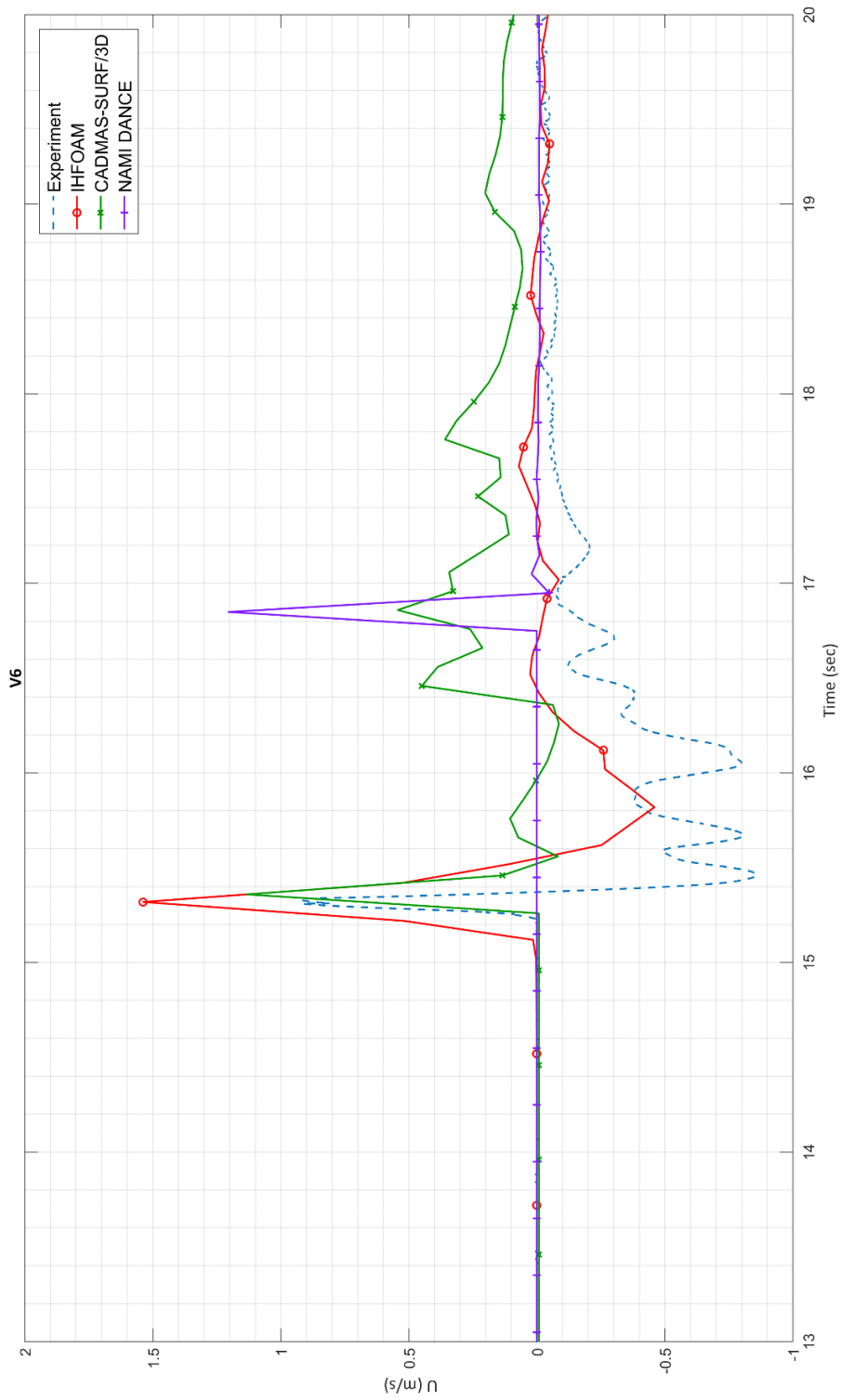


Figure 6.15 Comparison of Particle Velocities in x-direction, U of All Models with Experimental Measurements at V6
for Case 3 with Laminar Approach

Table 6.5. Percent Error of Each Wave Gauge for Laminar Approach in Case 3

Wave Gauges	Case 3		
	NAMI DANCE	IHFOAM	CADMAS- SURF/3D
	Percent Error	Percent Error	Percent Error
WG1	0.00	4.92	7.09
WG2	1.24	5.34	2.27
WG3	4.39	6.57	3.31
WG4	8.14	6.75	3.05
WG5	9.63	17.25	13.29
WG6	34.93	2.63	10.35
WG7	41.18	12.10	2.25
WG8	15.61	14.14	8.45
WG9	120.33	38.76	6.46
WG10	77.34	19.32	12.86

6.3. Comparison for k- ϵ Turbulence Model

Results of the peak water surface elevations obtained from IHFOAM and CADMAS-SURF/3D simulations with k- ϵ turbulence model and the measured maximum water surface elevation data of physical model experiments are presented in Table 6.6 for all cases at each wave gauge.

The graphical comparison of water surface elevation for Case 1 is given in Figure 6.16 for all wave gauges and a closer look for the wave gauge located just in front of the vertical wall is given in Figure 6.17 to see the differences between the numerical model result and the experimental data. Similarly, graphical comparison of the water particle velocities for the three models are given in Figure 6.18 and a closer look of the velocity gauge located right in front of the vertical wall is presented in Figure 6.19. To have a better understanding of the differences between the experimental data and the results of the different numerical models with laminar approach, the percent errors of each wave gauge for Case 1 are presented in Table 6.7 only for the peak water surface elevations.

Figures 6.16 and 6.18 shows that results of the water surface elevations and water particle velocities obtained from IHFOAM and CADMAS-SURF/3D simulations are almost identical with each other along the channel. The averaged percent errors along the channel are around 2.5% and 2.7% for IHFOAM and CADMAS-SURF/3D respectively excluding the WG1. As the wave approaches to the vertical wall, differences between the results of the two numerical models are observed. At WG8, CADMAS-SURF/3D provided higher peak for the water surface elevations than IHFOAM. The percent errors calculated for IHFOAM and CADMAS-SURF/3D are around 14% and 2%, respectively in front of the vertical wall. For the peak value for the water particle velocities calculated by these two models, it can be said that they are nearly same however, the trend of the CADMAS-SURF/3D results are more similar with the experimental data than IHFOAM.

Table 6.6. Peak Surface Water Elevation (in cm) of Each Wave Gauge for All Cases Under k-ε Approach

Wave Gauges	IHFQAM			CADMAS-SURF/3D			EXPERIMENT		
	Case 1	Case 2	Case 3	Case 1	Case 2	Case 3	Case 1	Case 2	Case 3
WG1	20.89	20.88	20.88	21.1	21.11	21.31	20.51	19.7	19.9
WG2	21.34	21.3	21.3	21.48	21.48	20.68	21	19.99	20.22
WG3	22.58	22.55	22.55	22.66	22.67	21.87	22.07	20.93	21.17
WG4	24.55	24.5	24.5	24.46	24.47	23.67	23.7	22.75	22.97
WG5	27.26	27.2	27.24	27.12	27.13	26.34	24.22	22.95	23.25
WG6	33.2	33.13	33.12	36.36	34.11	35.6	33.61	31.43	32.26
WG7	29.01	29.41	29.23	35.85	31.01	35.36	35.35	35.72	34.63
WG8	131.3	28.74	28.49	149.2	32.94	31.12	152	39.04	37.4
WG9	-	86.28	13.22	-	110.1	12.23	-	150	11.61
WG10	-	-	66.05	-	-	96.15	-	-	133

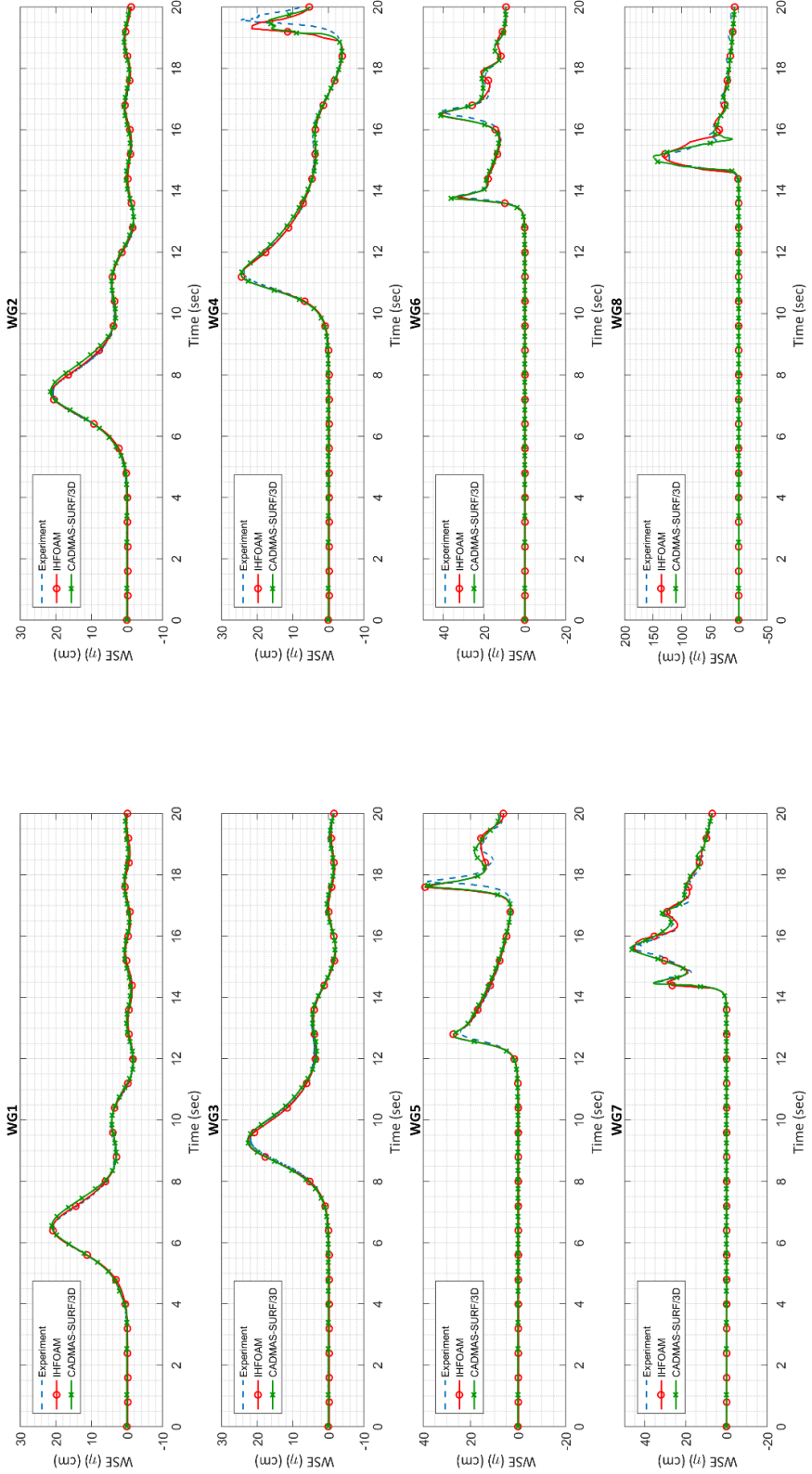
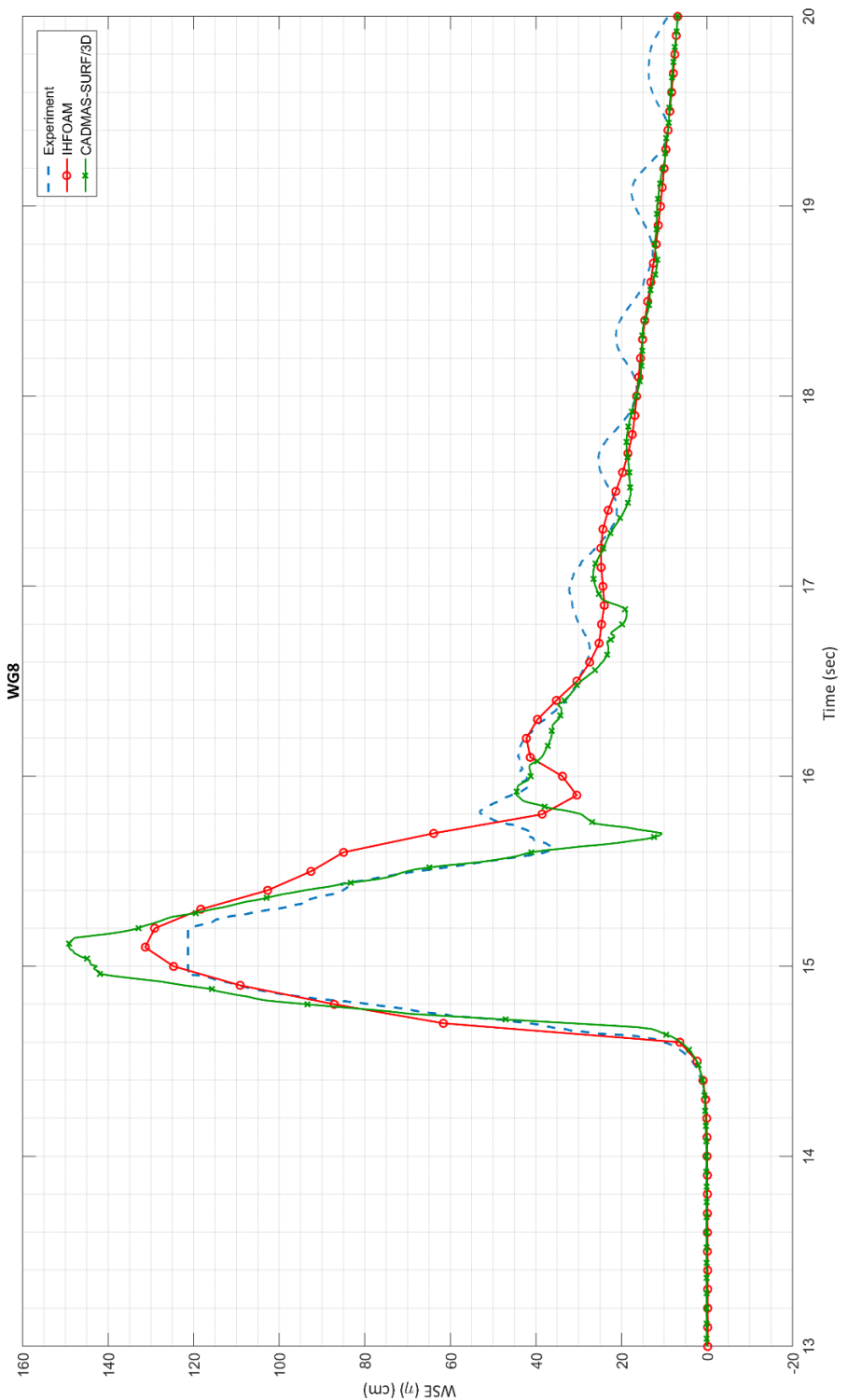


Figure 6.16 Comparison of Water Surface Elevations of IHFOAM and CADMAS-SURF/3D with Experimental Measurements for Case 1 with $k-\epsilon$ Turbulence Model



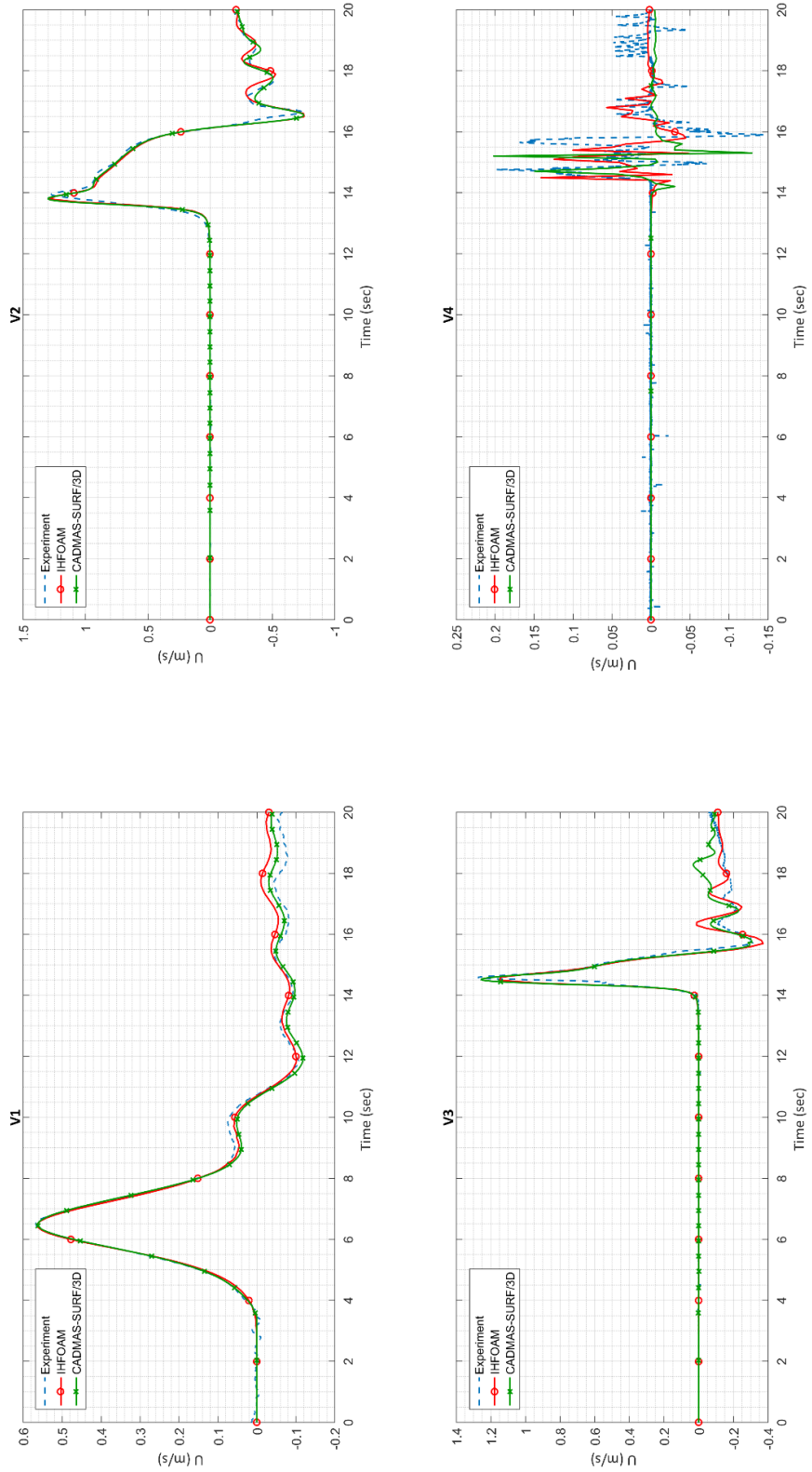


Figure 6.718 Comparison of Water Surface Elevations obtained by IfFoAM and CADMAS-SURF/3D model
Experimental data were obtained with Taffululent Model

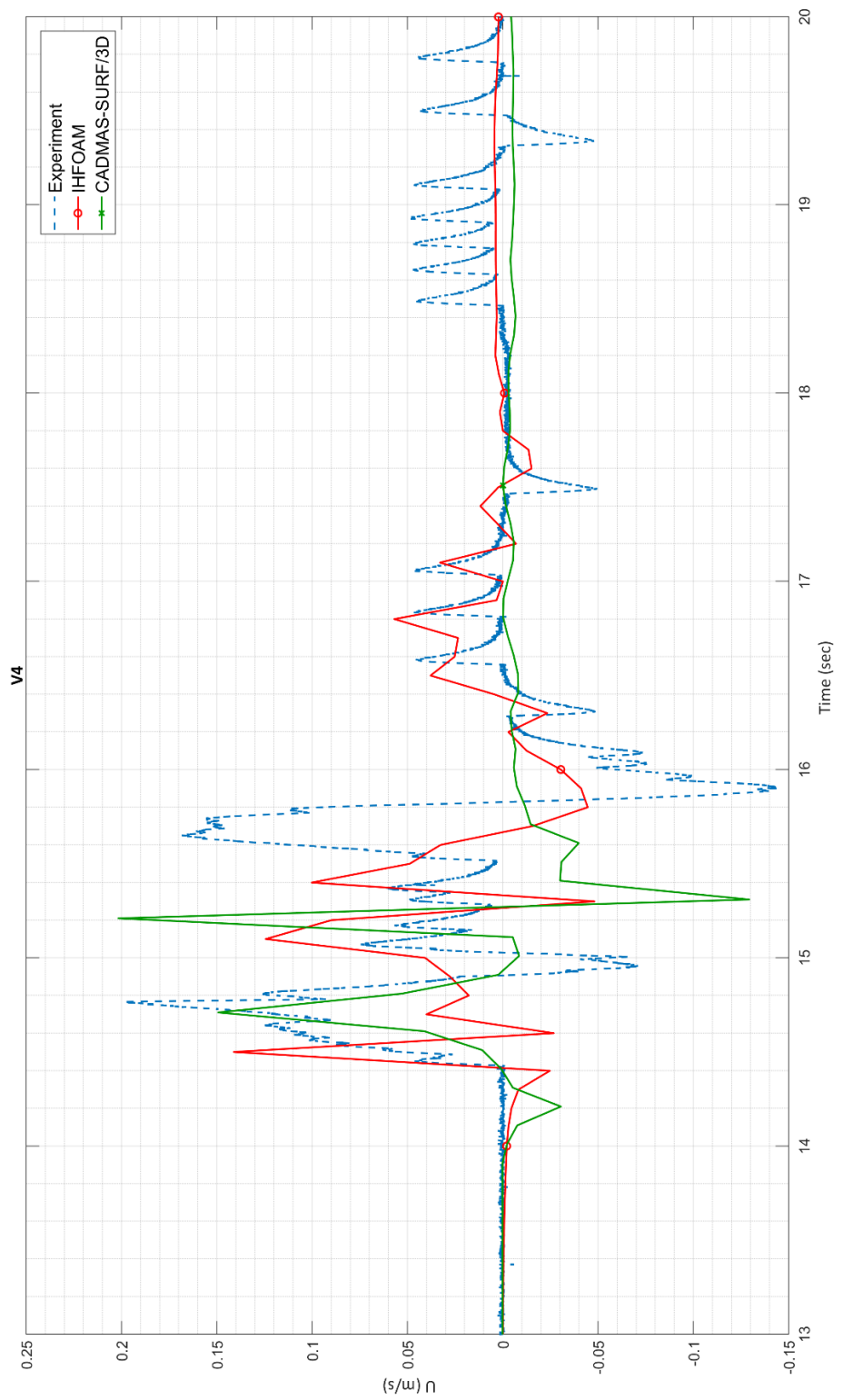


Figure 6.19 Comparison of Particle Velocities in x-direction, U of IHFOAM and CADMAS-SURF/3D with Experimental Measurements at V4 for Case 1 with $k-\epsilon$ Turbulence Model

Table 6.7. Percent Error of Each Wave Gauge for k- ϵ Approach in Case 1

Case 1		
Wave Gauges	IHFOAM	CADMAS- SURF/3D
	Percent Error	Percent Error
WG1	1.85	2.88
WG2	1.62	2.29
WG3	2.31	2.67
WG4	3.59	3.21
WG5	12.55	11.97
WG6	1.22	8.18
WG7	17.93	1.41
WG8	13.62	1.84

The graphical comparison of water surface elevation for Case 2 is given in Figure 6.20 for all wave gauges and a closer look for the wave gauge located just in front of the vertical wall is given in Figure 6.21 to see the differences between the numerical model result and the experimental data. Similarly, graphical comparison of the water particle velocities for the three models are given in Figure 6.22 and a closer look of the velocity gauge located right in front of the vertical wall is presented in Figure 6.23. To have a better understanding of the differences between the experimental data and the results of the different numerical models with laminar approach, the percent errors of each wave gauge for Case 2 are presented in Table 6.8 only for the peak water surface elevations.

The averaged percent errors along the channel are around 7.3% and 7.6% for IHFOAM and CADMAS-SURF/3D respectively excluding the WG1. It can be seen from the Figure 6.21 that underestimation of the peak water surface elevations starts with the wave breaking process. Table 6.8 indicates that percent errors for Case 2 are significantly increased compared to the laminar approach particularly for the wave gauge located in front of the vertical wall due to the breaking of the solitary wave. The percent errors for IHFOAM and

CADMAS-SURF/3D are around 42% and 26%, respectively at WG9. Based on the discussions made in Section 6.1, it is clearly seen that IHFOAM could not catch and highly underestimated the accurate splash height on the vertical wall. For the water particle velocities, it is seen that while IHFOAM provides similar peak value with the experimental data, CADMAS-SURF/3D gives overestimated result for the peak water particle velocities. Moreover, the trend of the negative velocities in the experimental data is more similar with the IHFOAM results.

Table 6.8. Percent Error of Each Wave Gauge for k- ϵ Approach in Case 2

Wave Gauges	Case 2	
	IHFOAM	CADMAS- SURF/3D
	Percent Error	Percent Error
WG1	5.99	7.16
WG2	6.55	7.45
WG3	7.74	8.31
WG4	7.69	7.56
WG5	18.52	18.21
WG6	5.41	8.53
WG7	17.67	13.19
WG8	26.38	15.63
WG9	42.48	26.60

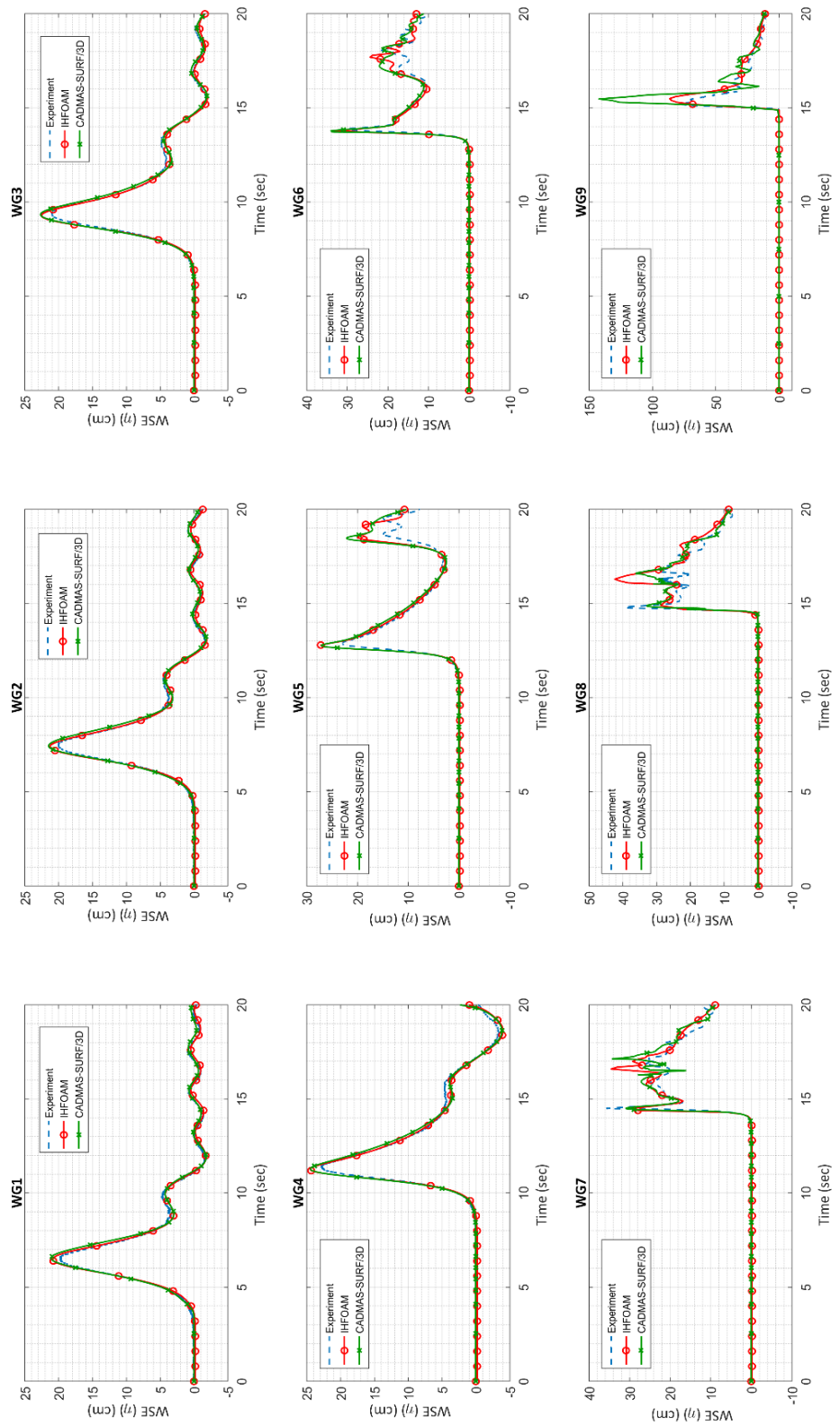


Figure 6.20 Comparison of Water Surface Elevations of IHFOAM and CADMAS-SURF/3D with Experimental Measurements for Case 2 with k- ϵ Turbulence Model

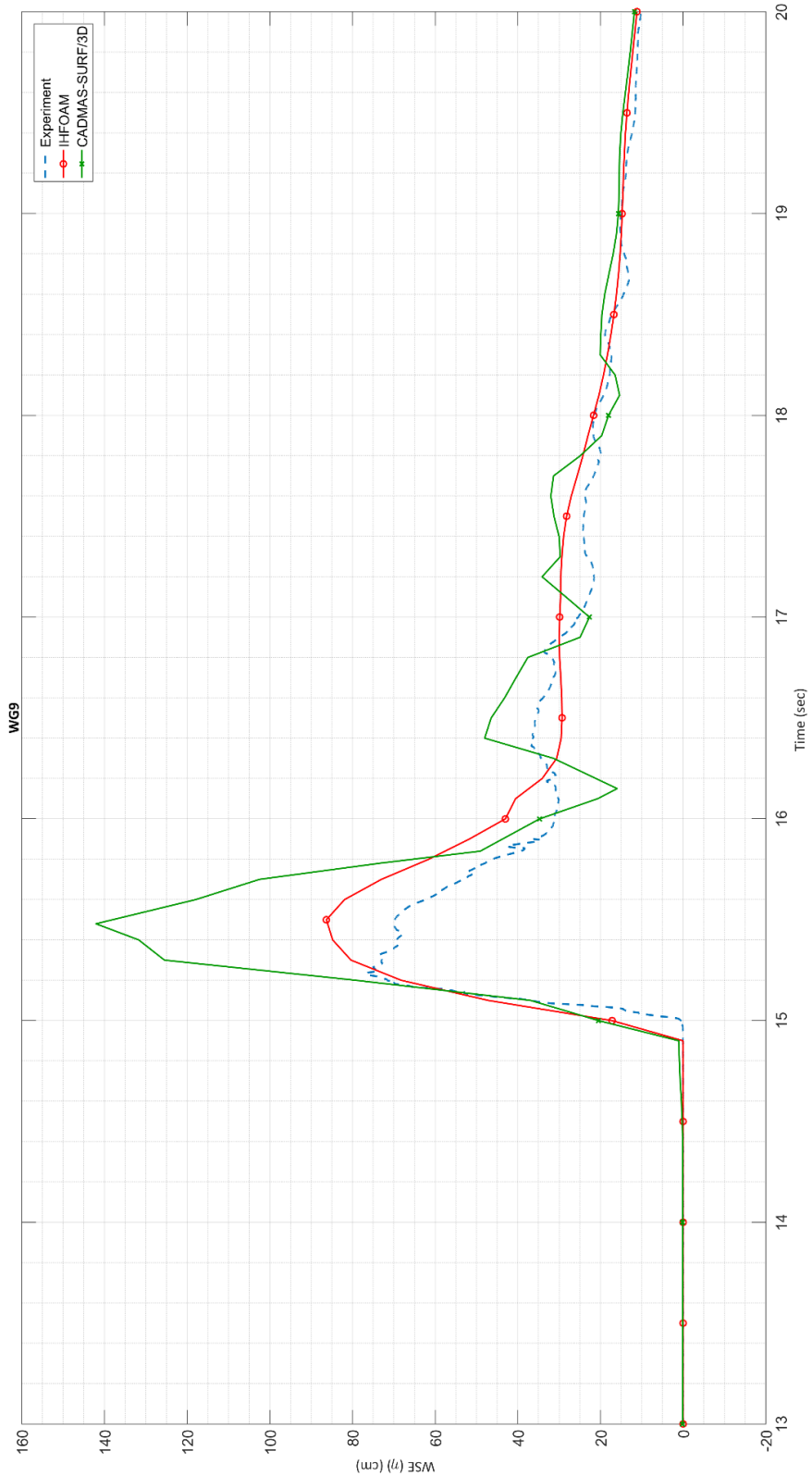


Figure 6.21 Comparison of Water Surface Elevations of IHFOAM and CADMAS-SURF/3D with Experimental Measurements at WG9 for Case 2 with k-ε Turbulence Model

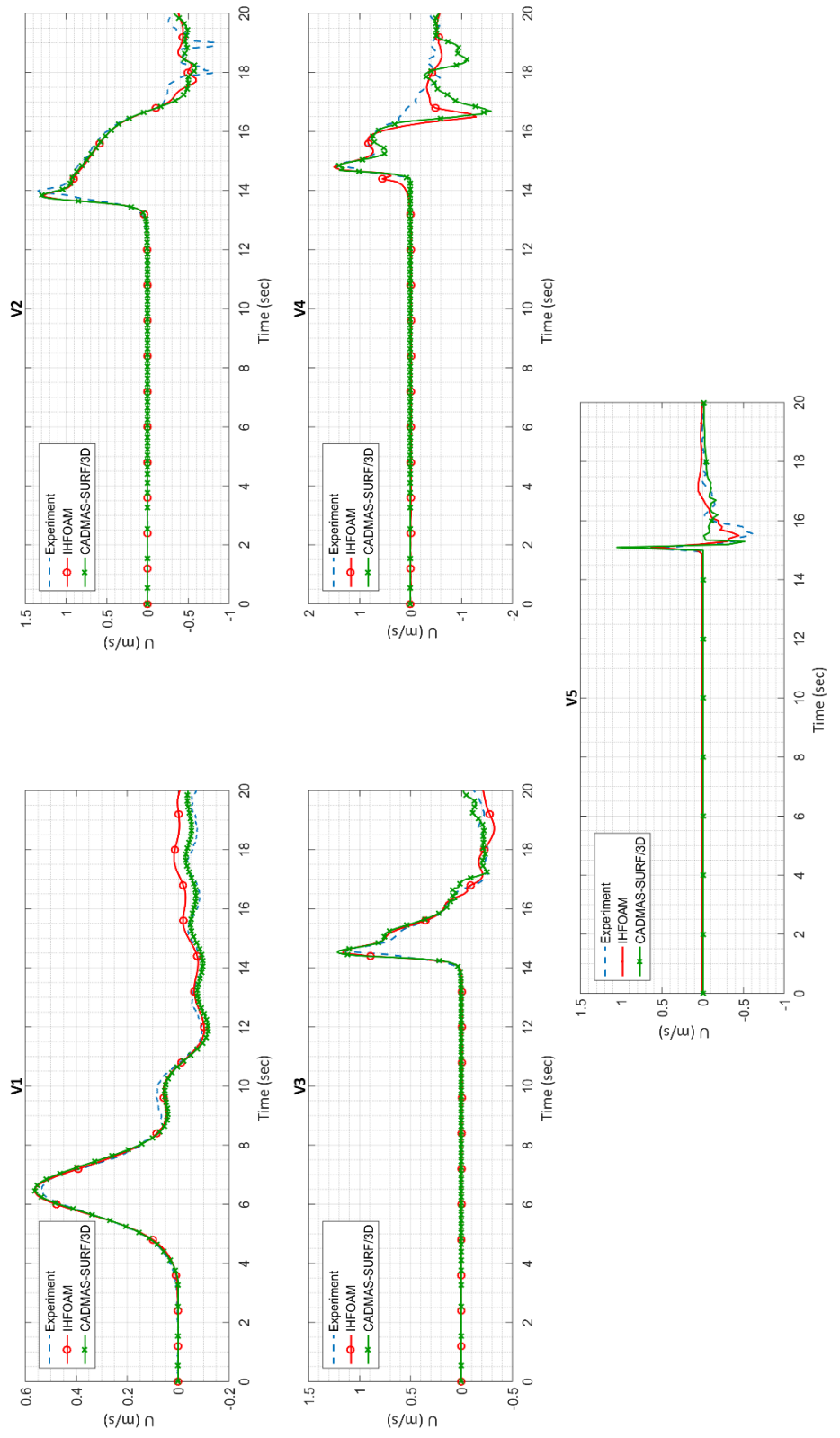


Figure 6.22 Comparison of Particle Velocities in x-direction, U of IHFOAM and CADMAS-SURF/3D with Experimental Measurements for Case 2 with $k-\epsilon$ Turbulence Model

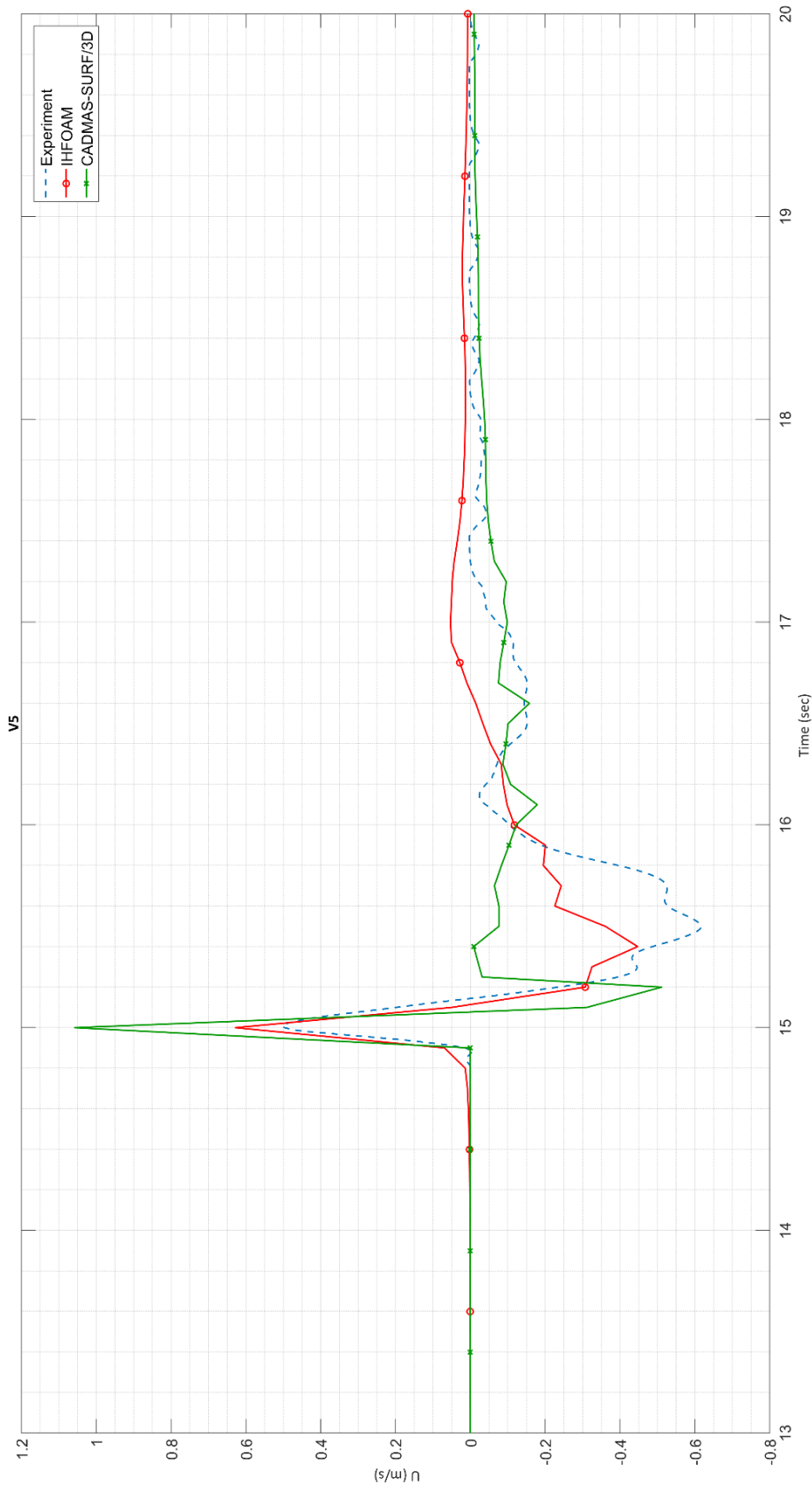


Figure 6.23 Comparison of Particle Velocities in x-direction, U , at V_5 for Case 2 with $k-\epsilon$ Turbulence Model Measurements at V_5 for Case 2 with $k-\epsilon$ Turbulence Model

The graphical comparison of water surface elevation for Case 3 is given in Figure 6.24 for all wave gauges and a closer look for the wave gauge located just in front of the vertical wall is given in Figure 6.25 to see the differences between the numerical model result and the experimental data. Similarly, graphical comparison of the water particle velocities for the three models are given in Figure 6.26 and a closer look of the velocity gauge located right in front of the vertical wall is presented in Figure 6.27. To have a better understanding of the differences between the experimental data and the results of the different numerical models with laminar approach, the percent errors of each wave gauge for Case 3 are presented in Table 6.9 only for the peak water surface elevations. Similar with Case 1 and Case 2, results of the water surface elevations and water particle velocities obtained from IHFOAM and CADMAS-SURF/3D are fairly well agreement with the experimental data along the wave channel until the point where the solitary wave starts breaking. The averaged percent errors along the channel are around 6.2% and 2.9% for IHFOAM and CADMAS-SURF/3D respectively excluding the WG1. It can be seen from the Table 6.8 that percent errors for Case 3 are higher than Case 2 particularly for the wave gauges after the small step since the process is more complicated than the previous one. The percent errors for IHFOAM and CADMAS-SURF/3D are around 50% and 28%, respectively at WG10. Error is quite high especially for IHFOAM however, possible reasons for that is discussed in Chapter 7. It is clearly seen that IHFOAM could not catch and highly underestimated the accurate splash height on the vertical wall. Similarly, water particle velocities are underestimated by IHFOAM at V6. On the other hand, although CADMAS-SURF/3D provided overestimated results for the peak water particle velocities, based on the discussions in Section 6.1 it is seen that CADMAS-SURF/3D underestimated the peak water surface elevations at WG10. Moreover, it is clearly seen that both models could not provide accurate results for the negative velocities after the incident of wave impact. In Table 6.9, it can be concluded that percent errors of Case 3 in $k-\epsilon$ approach are importantly higher than the laminar approach only for the water surface elevations at the WG10 which is located in front of the vertical wall. Along the channel, there is not much difference between the laminar and $k-\epsilon$ turbulence models.

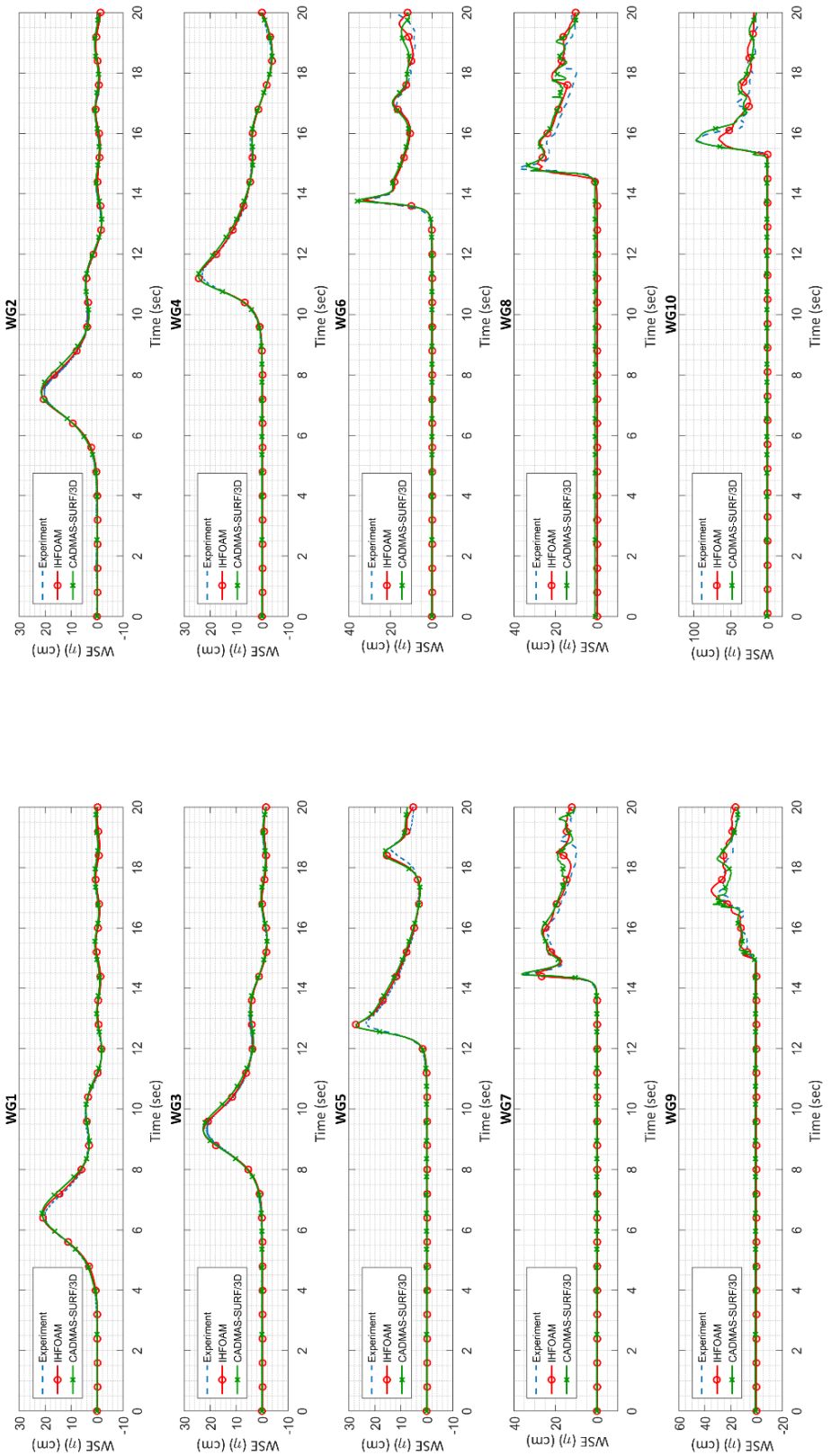


Figure 6.24 Comparison of Water Surface Elevations of IHFOAM and CADMAS-SURF/3D with Experimental Measurements for Case 3 with k-e Turbulence Model

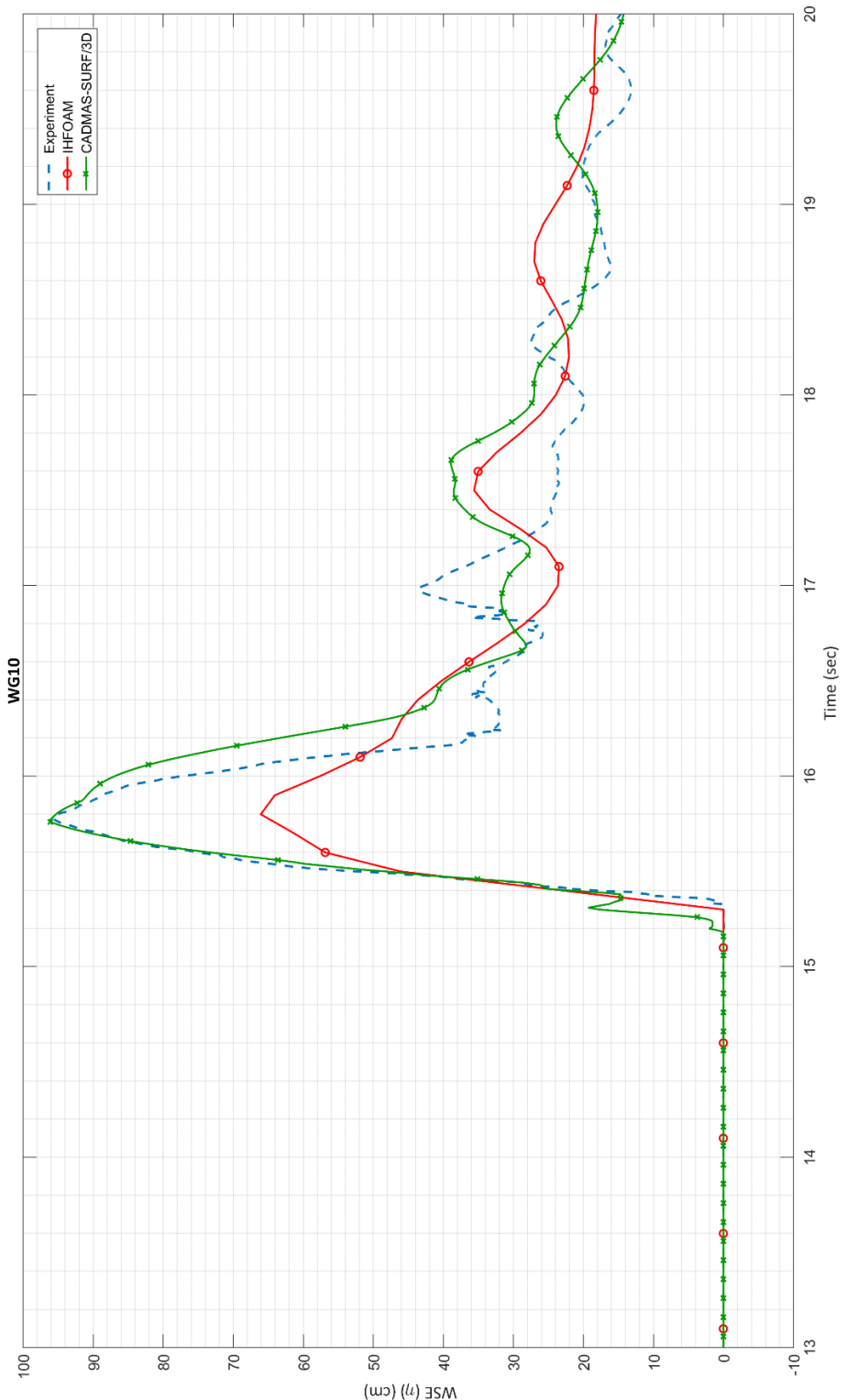


Figure 6.25 Comparison of Water Surface Elevations of IHFOAM and CADMAS-SURF/3D with Experimental Measurements at WG10 for Case 3 with $k-\epsilon$ Turbulence Model

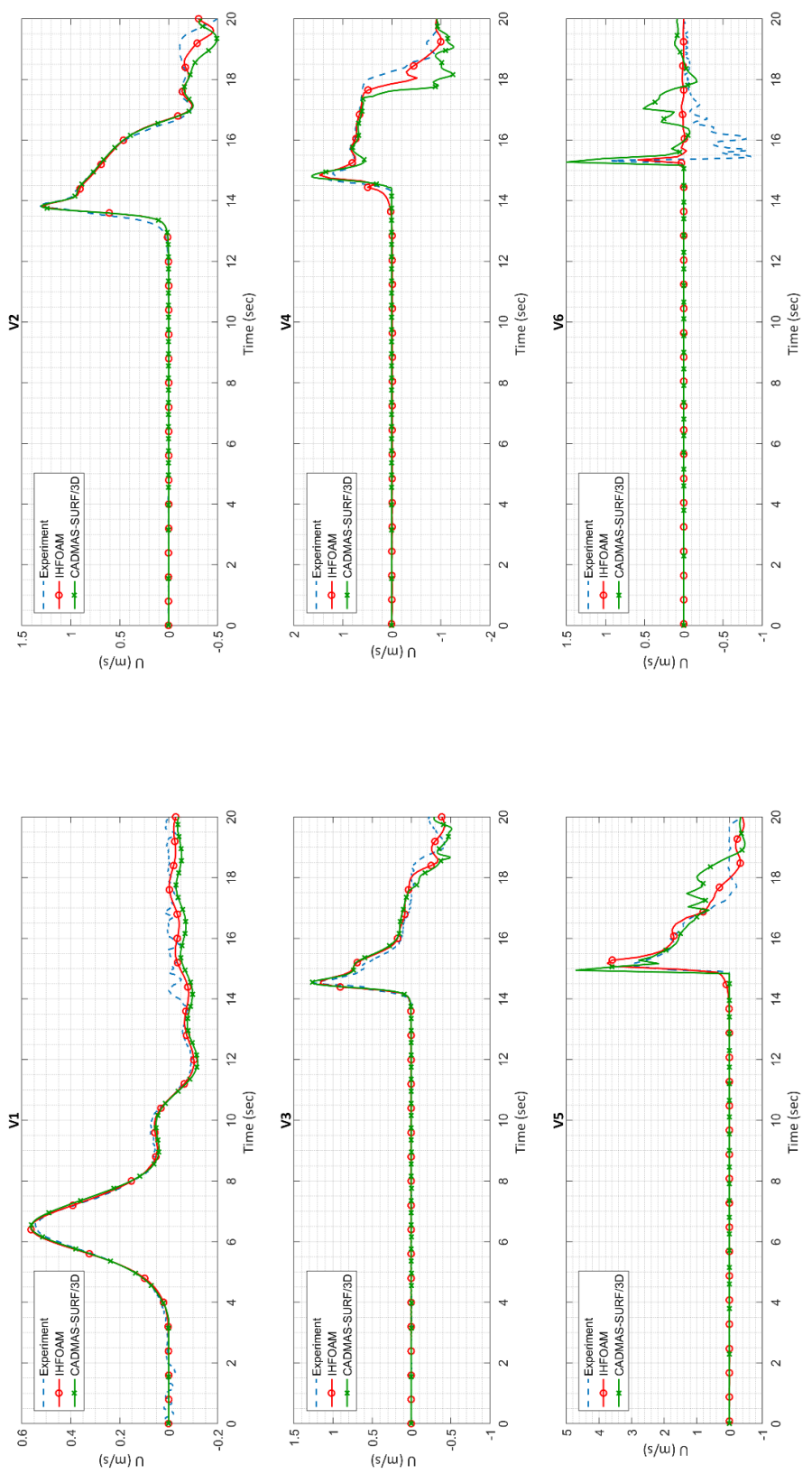


Figure 6.26 Comparison of Particle Velocities in x-direction, U of IHFOAM and CADMAS-SURF/3D with Experimental Measurements for Case 3 with k-ε Turbulence Model

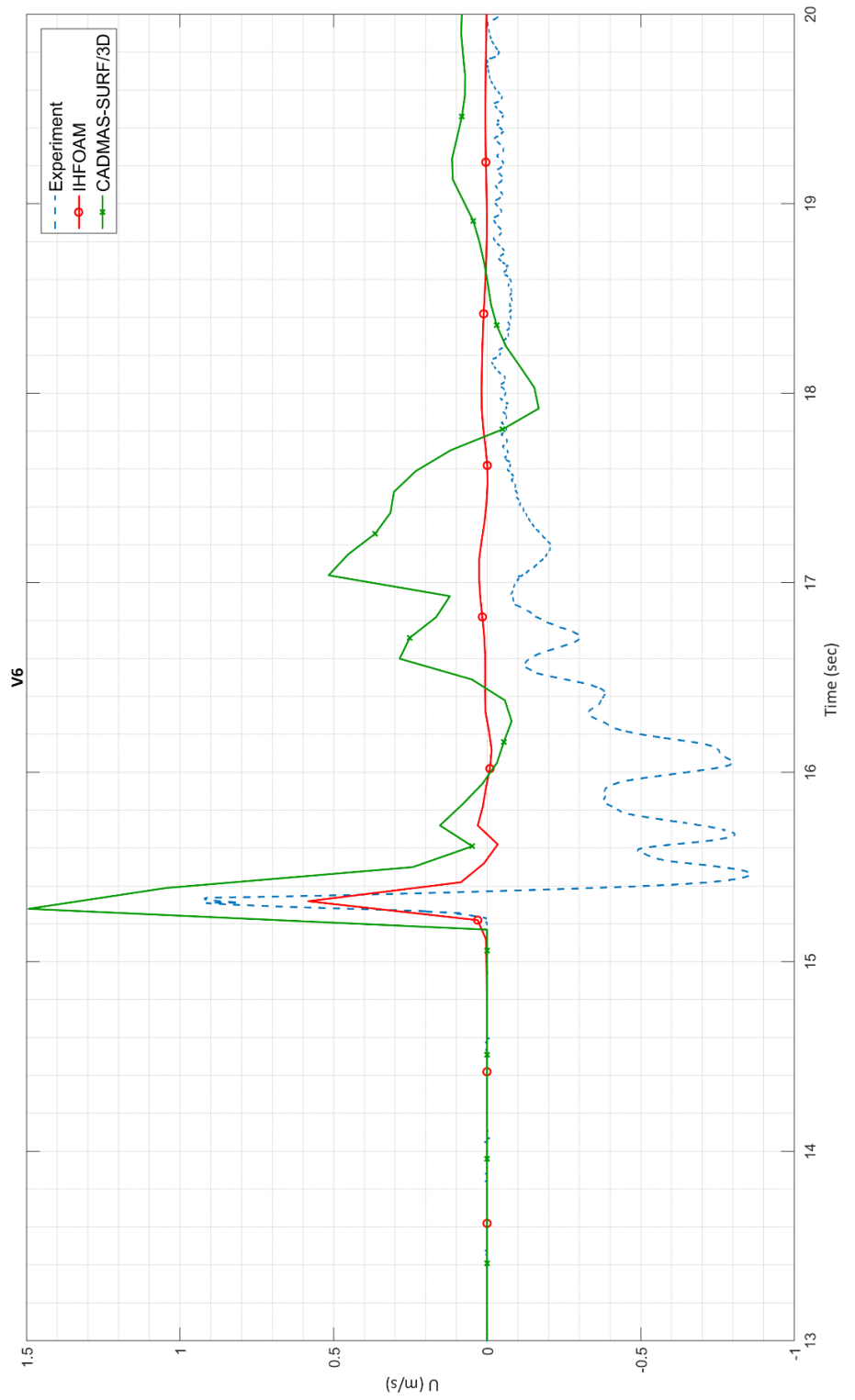


Figure 6.27 Comparison of Particle Velocities in x-direction, U of IHFOAM and CADMAS-SURF/3D with Experimental Measurements at V_6 for Case 3 with $k-\epsilon$ Turbulence Model

Table 6.9. Percent Error of Each Wave Gauge for k- ϵ Approach in Case 3

Wave Gauges	Case 3	
	IHFOAM	CADMAS- SURF/3D
	Percent Error	Percent Error
WG1	4.92	2.06
WG2	5.34	2.27
WG3	6.52	3.31
WG4	6.66	3.05
WG5	17.16	13.29
WG6	2.67	10.35
WG7	15.59	2.11
WG8	23.82	16.79
WG9	13.87	5.34
WG10	50.34	27.71

6.4. Comparison for k- ω -SST Turbulence Model

Lastly for k- ω -SST comparison, since this turbulence model only available in IHFOAM, the results of the peak water surface elevations obtained from the simulations and the measured maximum water surface elevation data of the physical model experiments are presented in Table 6.10 for all cases at each wave gauge. Percent errors are also provided for Case 1, Case 2 and Case 3 of IHFOAM results with different turbulence approaches after the comparison of the numerical results with the experimental data in Table 6.11 only for the water surface elevations. The graphical comparison of water surface elevation for Case 1, Case 2 and Case 3 were given in Chapter 4. Therefore, in this section only the percent errors are presented.

Comparing the numerical simulation results of the three cases within the IHFOAM numerical model with different turbulence model approaches, it can be seen that k- ω -SST turbulence model performed well computing the maximum water surface elevation at the wave gauge in front of the vertical wall. It can be seen from Table 6.13

that the results are very similar at the gauges located along the channel. At the wave gauge in front of the vertical wall in Case 1, the percent error of the k- ω -SST compared to the experimental data is around 11%. For Case 2, again the results are not very different from each other along the channel compared to the laminar approach except for the WG9 where the percent error for k- ω -SST model is similar with Case 1 as around 11%. Lastly for Case 3, the maximum water surface elevation computed by k- ω -SST model in front of the vertical wall at the incident of wave impact deviates from the experimental data around 14%. It can be resulted that the turbulence modeling is effective particularly around the wall area or at the breaking zones. Under these physical model experiments it can be discussed whether the rate of improvement is considerable or not in the engineering point of view for design purposes.

Table 6.10. Peak Surface Water Elevation (in cm) of Each Wave Gauge for All Cases Under k- ω -SST Approach

Wave Gauges	IHFOAM			EXPERIMENT		
	Case 1	Case 2	Case 3	Case 1	Case 2	Case 3
WG1	20.89	20.88	20.89	20.51	19.7	19.9
WG2	21.33	21.3	21.29	21	19.99	20.22
WG3	22.57	22.54	22.55	22.07	20.93	21.17
WG4	24.53	24.49	24.49	23.7	22.75	22.97
WG5	27.24	27.02	27.21	24.22	22.95	23.25
WG6	33.21	33.07	33.14	33.61	31.43	32.26
WG7	29.54	29.02	29.79	35.35	35.72	34.63
WG8	134.9	29.51	29.27	152	39.04	37.4
WG9	-	133.1	12.93	-	150	11.61
WG10	-	-	113.3	-	-	133

Table 6.11. Percent Error of Each Wave Gauge for k- ω -SST Approach in All Cases

IHFOAM			
Wave Gauges	Case 1	Case 2	Case 3
	Percent Error	Percent Error	Percent Error
WG1	1.85	5.99	4.97
WG2	1.57	6.55	5.29
WG3	2.27	7.69	6.52
WG4	3.50	7.65	6.62
WG5	12.47	17.73	17.03
WG6	1.19	5.22	2.73
WG7	16.44	18.76	13.98
WG8	11.25	24.41	21.74
WG9	-	11.27	11.37
WG10	-	-	14.81

CHAPTER 7

CONCLUSION

In this thesis study, physical model experiments on solitary wave-vertical wall interaction for three different location of the vertical wall structure at the end of the wave channel performed by Arikawa (2015) are numerically studied using three different numerical models named as NAMI DANCE, IHFOAM solver of OpenFOAM® and CADMAS-SURF/3D.

NAMI DANCE solves Non-linear Shallow Water Equations (NSWE) using staggered leap-frog finite difference method with no special treatment for the free surface. The time series of water surface elevations and water particle velocities are given as input to the system at the exact location of first wave gauge.

IHFOAM solves three-dimensional Volume Averaged Reynolds Averaged Navier Stokes (VARANS) equations for multiphase and porous media flow using finite volume technique tracking the free surface by Volume of Fluid method. Numerical simulations assuming laminar flow, volume averaged $k-\varepsilon$ and $k-\omega$ -SST models for turbulence closure are performed for each case. The time series of water surface elevation and water particle velocity are given as inputs to the system 0.6 m behind the first wave gauge.

CADMAS-SURF/3D solves three-dimensional RANS for single-phase incompressible fluid based on porous body model and trace the free surface with VOF method. Numerical simulations performed assuming laminar flow and using $k-\varepsilon$ turbulence model in every case. Similarly, the time series of water surface elevation

and water particle velocity are given as inputs to the system 0.6 m behind the first wave gauge.

Overall, it can be inferred from the graphical comparisons of water surface elevations and particle velocities given in Chapter 3, Chapter 4, Chapter 5 and Chapter 6 that all models performed well in the free flow region away from the vertical wall. There are some differences between the results in front of the vertical wall. However, it should be noted that it is not trivial to catch the exact peak water surface elevation in front of the vertical wall as complex wave breaking and a splash of the water body are observed in the experiments.

For NAMI DANCE it is seen that numerical results are fairly well agreement in consideration of wave propagation along the channel. For all three cases, it is seen that at the end of the slope as the solitary wave starts breaking, NAMI DANCE could not solve the water surface elevation in a good accuracy. For each case, the results of the peak water surface elevations observed due to extreme splashes at the wave gauges in front of the vertical wall are underestimated by NAMI DANCE. However, the performance of NAMI DANCE is highest for the Case 1 when comparing with Case 2 and Case 3 since the wave breaking is more dominant in Case 2 and Case 3 which causes turbulence and vertical velocities to govern the motion. Because of the nature of depth-averaged NSWE, lower water surface elevations and higher horizontal water particle velocities are computed in front of the vertical wall.

IHFOAM results for all cases and turbulence models shows fairly well agreements with the experimental data at the gauges located along the channel. The differences start with the process of breaking of the solitary wave and alteration of the results compared to the experimental data becomes noticeable in front of the vertical wall. Comparison of the numerical results with different turbulence approaches showed that using $k-\omega$ -SST turbulence model improved the peak water surface elevations on the vertical wall and provided much closer results for the water particle velocities in each case in comparison with the experimental data. It can be concluded from the graphical

comparison of the water surface elevations in front of the vertical wall that k- ϵ turbulence model is much dissipative than the k- ω -SST approach.

It can be concluded that CADMAS-SURF/3D performed quite well both for laminar and k- ϵ models. For all cases along the channel, the results of the numerical simulations are in a fairly good agreement with the experimental data. The discrepancies are started with the breaking of the solitary wave, and the maximum deviations among the results are observed at the gauges in front of the vertical wall at the incident of impact. It is seen that laminar approach of the CADMAS-SURF/3D overestimated the peak water surface elevation caused by the extreme splashes in front of the vertical wall. It also had some difficulties to compute the correct water particle velocities in front of the vertical wall at the incident of wave impact. It can be seen for all cases that k- ϵ turbulence model in CADMAS-SURF/3D shows a dissipative behavior, and provide lower water surface elevation results and higher water particle velocities than the laminar approach in front of the vertical wall.

For the comparison of IHFOAM and CADMAS-SURF/3D, it is seen that the results of these numerical models are very similar both along the channel and in front of the vertical wall. However, there are some non-negligible deviations from the results of these models. It can be seen from the graphical comparisons that while CADMAS-SURF/3D provided closer water surface elevations to the experimental data near the vertical wall, IHFOAM provided underestimated results. One of the reasons for the differences can be that IHFOAM is a multiphase solver and CADMAS-SURF/3D uses single phase for its calculations. In IHFOAM, the fluid properties (density and viscosity) in each cell are calculated just by weighting them by the VOF function. Therefore, to obtain the density of the fluid in a cell, density of water and density of air are inputted in the VOF function together with the indicator of phase function defining the quantity of water per unit volume in each cell. The same procedure is also applied for the viscosity. Since the experiments include breaking that air entrainment is highly important in this process, IHFOAM results are very sensitive for the alterations due to the amount of air entrainment calculation.

The physical model experiments used in this thesis are highly challenging for accurate numerical modeling. It is important to know the limits of the NSWE in these type of challenging cases and determine the possible role of these type of models in engineering applications.

Computational time for IHFOAM and CADMAS-SURF/3D for same turbulence model was 63.10 hours and 112.89 hours, respectively. For NAMI DANCE; which uses GPU acceleration, computational time only took for half an hour.

After all, comparisons performed in this study, it can be concluded that two-dimensional depth-averaged NSWE are reasonably accurate to investigate wave transformation and propagation. However, it is more convenient to use three-dimensional Navier-Stokes equations for wave-structure interaction problems in engineering applications even if it is required to improve the results by paying special attention to air entrainment in the wave breaking process.

In the end, recommendations for future studies for applications and further development of the numerical modeling are itemized as follows:

- Local mesh refinement should be considered to obtain more accurate results in front of the vertical wall.
- Adaptive mesh refinement technique can be an alternative approach to acquire refinement around the flow and splashes.
- Three-dimensional numerical modeling studies should be carried out to eliminate the 2D-3D effect which can be the cause of the differences between the numerical and experimental results.
- Since the air entrainment affects the solution of the breaking process significantly, extended studies should be carried out on the investigation of air entrainment effects.
- Detailed analysis should be performed to investigate the different behavior of WG5.
- Pressure distribution on the vertical wall should be investigated.

REFERENCES

- Al-Faesly, T., Palermo, D., Nistor, I., & Cornett, A. (2012). Experimental Modeling of Extreme Hydrodynamic Forces on Structural Models. *International Journal of Protective Structures*, 3(4), 477–505. <https://doi.org/10.1260/2041-4196.3.4.477>
- Aniel-Quiroga, I., Vidal, C., Lara, J. L., González, M., & Sainz, Á. (2018). Stability of rubble-mound breakwaters under tsunami first impact and overflow based on laboratory experiments. *Coastal Engineering*, 135(August 2017), 39–54. <https://doi.org/10.1016/j.coastaleng.2018.01.004>
- Arikawa, T. (2015). Consideration of Characteristics of Pressure on Seawall by Solitary Waves Based on Hydraulic Experiments. *Journal of Japan Society of Civil Engineers, Ser. B2 (Coastal Engineering)*, 71(2), 889–894.
- Arikawa, T., Hayashi, T., Suzuki, T., & Shimosako, K. (2014a). Stability analysis of breakwaters under tsunami overflow based on numerical wave tank. *Journal of Japan Society of Civil Engineers, Ser. B2 (Coastal Engineering)*, 70(2), 366–371.
- Arikawa, T., Ikeda, T. and Kubota, K. (2014b). Experimental study on scour behind seawall due to tsunami overflow. *Journal of Japan Society of Civil Engineers, Ser. B2 (Coastal Engineering)*, 70(2), 926–930. https://doi.org/https://doi.org/10.2208/kaigan.70.I_926
- Arikawa, T., Sato, M., Shimosako, K. & Gen, H. (2013). Stability of breakwaters under tsunami overflow. *Journal of Japan Society of Civil Engineers, Ser. B2 (Coastal Engineering)*, 69(2), 916–920.
- Arikawa, T., Sato, S., Shimosako, K., Tomita, T., Hasegawa, I., Yeom, G. S. & Tomita, T. (2012). Failure mechanism of Kamaishi breakwaters due to Great East Japan Earthquake Tsunami. In COPRI (Ed.), *The International Conference on Coastal Engineering (ICCE) Proceedings 2012* (p. 52). ASCE.

- Arikawa, T., Yamano, T., & Akiyama, M. (2007). Advanced deformation method for breaking waves by using CADMAS-SURF/3D. *Annual Journal of Coastal Engineering, JSCE*, 54, 71–75. Retrieved from (in Japanese)
- Arikawa, T., Yamada, F., & Akiyama, M. (2005). Study of the applicability of tsunami wave force in a three-dimensional numerical wave flume. *Annual Journal of Coastal Engineering, JSCE*, 52, 46–50. Retrieved from (in Japanese)
- Arnason, H. (2005). *Interactions between an incident bore and a free-standing coastal structure*. University of Washington, Seattle.
- Azadbakht, M., & Yim, S. C. (2015). Simulation and Estimation of Tsunami Loads on Bridge Superstructures. *Journal of Waterway, Port, Coastal, and Ocean Engineering*, 141(2), 04014031. [https://doi.org/10.1061/\(ASCE\)WW.1943](https://doi.org/10.1061/(ASCE)WW.1943)
- Bricker, J. D., & Nakayama, A. (2014). Contribution of trapped air, deck superelevation, and nearby structures to bridge deck failure during a tsunami. *Journal of Hydraulic Engineering*, 140(5), [https://doi.org/10.1061/\(ASCE\)HY.1943-7900.0000855](https://doi.org/10.1061/(ASCE)HY.1943-7900.0000855).
- Bricker, J. D., Takagi, H., & Mitsui, J. (2013). Turbulence model effects on VOF analysis of breakwater overtopping during the 2011 Great East Japan tsunami. In *in Proc. 35th IAHR World Congress, Chengdu, Sichuan, China*.
- Briggs, M. J., Synolakis, C. E., Harkins, G. S. and Hughes, S. T. (1995). Large scale three-dimensional laboratory measurements of tsunami inundation. In “*Tsunami: Progress in Prediction, Disaster Prevention and Warning*” (Y. Tsuchiya and N. Shuto, Eds.), Kluwer Academic Publishers, Dordrecht, The Netherlands, 129–149.
- Briggs, M. J., Yeh, H., & Cox, D. T. (2009). Physical Modeling of Tsunami Waves. In *Handbook of Coastal and Ocean Engineering*. <https://doi.org/10.1142/9789812819307>

Casey, M., & Wintergerste, T. (2000). *Best practise guidelines*. ERCOFTAC Publication.

Chella, M., Bihs, H., Myrhaug, D., & Muskulus, M. (2017). Breaking solitary waves and breaking wave forces on a vertically mounted slender cylinder over an impermeable sloping seabed. *Journal of Ocean Engineering and Marine Energy*, 3(1), 1–19. <https://doi.org/10.1007/s40722-016-0055-5>

Chen, C., Melville, B. W., Nandasena, N. A. K., Shamseldin, A. Y., & Wotherspoon, L. (2016). Experimental study of uplift loads due to tsunami bore impact on a wharf model. *Coastal Engineering*, 117, 126–137. <https://doi.org/10.1016/j.coastaleng.2016.08.001>

Chen, Q., Zang, J., Kelly, D. M., & Dimakopoulos, A. S. (2017). A 3-D numerical study of solitary wave interaction with vertical cylinders using a parallelised particle-in-cell solver. *Journal of Hydrodynamics*, 29(5), 790–799. [https://doi.org/10.1016/S1001-6058\(16\)60790-4](https://doi.org/10.1016/S1001-6058(16)60790-4)

Cho, M., Shin, S., Yoon, H.-D., & Cox, D. T. (2017). Numerical simulation of tsunami force acting on vertical walls. In *Journal of Coastal Research: Special Issue 79 - The 2nd International Water Safety Symposium* (pp. 289–293). <https://doi.org/https://doi.org/10.2112/SI79-059.1>

Dao, N. X., Adityawan, M. B., Tanaka, H., & Sundar, V. (2014). SENSITIVITY ANALYSIS OF RELATIONSHIP BETWEEN TSUNAMI DISASTER AND COASTAL. *Journal of Japan Society of Civil Engineers, Ser. B1 (Hydraulic Engineering)*, 70(4), 43–48.

del Jesus, M. (2011). *Three-dimensional interaction of water waves with maritime structures*. Ph.D. Thesis, University of Cantabria.

del Jesus, M., Lara, J. L., & Losada, I. J. (2012). Three-dimensional interaction of waves and porous coastal structures Part I: Numerical model formulation. *Coastal Engineering*, 64, 57–72.

<https://doi.org/10.1016/j.coastaleng.2012.01.008>

Douglas, S., & Nistor, I. (2015). On the effect of bed condition on the development of tsunami-induced loading on structures using OpenFOAM. *Natural Hazards*, 76, 1335–1356. <https://doi.org/10.1007/s11069-014-1552-2>

Douglas, S., Nistor, I., & St-Germain, P. (2015). 3-D Multi-phase numerical modelling of tsunami-induced hydrodynamic loading on nearshore structures. In *E-proceedings of the 36th IAHR World Congress 28 June - 3 July, 2015, The Hague, the Netherlands*.

Engelund, F. (1953). On the laminar and turbulent flow of ground water through homogeneous sand. *Trans. Dan. Acad. Techn. Sci.*, 3.

Esteban, M., Izumi, M., Tomoya, S., Aranguiz, R., Mikami, T., Thao, N. D., ... Ohtani, A. (2012). Stability of Rubble Mound Breakwaters Against Solitary Waves. In *Coastal Engineering Proceedings* (pp. 1–13). <https://doi.org/10.9753/icce.v33.structures.9>

Ghosh, D., Mittal, A. K., & Bhattacharyya, S. K. (2016). Multiphase modeling of tsunami impact on building with openings Governing equations. *The Journal of Computational Multiphase Flows*, 8(2), 85–94. <https://doi.org/10.1177/0010836716653881>

Goto, C., & Ogawa, Y. (1991). *Numerical method of tsunami simulation with the leap-frog scheme. Translated for the TIME Project by Prof. Shuto, N.* Sendai, Japan.

Guler, H. G., Arikawa, T., Oei, T., & Yalciner, A. C. (2015). Performance of rubble mound breakwaters under tsunami attack, a case study: Haydarpasa Port, Istanbul, Turkey. *Coastal Engineering*, 104, 43–53. <https://doi.org/10.1016/j.coastaleng.2015.07.007>

Guler, H. G., Baykal, C., Arikawa, T., & Yalciner, A. C. (2018). Numerical assessment of tsunami attack on a rubble mound breakwater using OpenFOAM®. *Applied*

Ocean Research, 72, 76–91. <https://doi.org/10.1016/j.apor.2018.01.005>

- Guzzo, A. Del, Panizzo, A., Bellotti, G., Longo, D., & Girolamo, P. De. (2007). Simulation of Fluid-Structure Interaction Using Smoothed Particle Hydrodynamics and Nonlinear, (1).
- Hall, J. V. and Watts, J. W. (1953). Laboratory investigation of the vertical rise of solitary waves on impermeable slopes. *Technical Report, Beach Erosion Board, US Army Corps of Engineering*, 33.
- Harbitz, C. B., Nakamura, Y., Arikawa, T., Baykal, C., Dogan, G. G., Frauenfelder, R., ... Yalciner, A. C. (2016). Risk assesment and design of prevention structures for enhanced tsunami disaster resilience (RAPSODI)/Euro-Japan Collaboration. *Coastal Engineering Journal*, 58(4). <https://doi.org/doi:10.1142/S057856341640012X>
- Higuera, P., Lara, J. L., & Losada, I. J. (2013a). Realistic wave generation and active wave absorption for Navier – Stokes models Application to OpenFOAM ®. *Coastal Engineering*, 71, 102–118. <https://doi.org/10.1016/j.coastaleng.2012.07.002>
- Higuera, P., Lara, J. L., & Losada, I. J. (2013b). Simulating coastal engineering processes with OpenFOAM ®. *Coastal Engineering*, 71, 119–134. <https://doi.org/10.1016/j.coastaleng.2012.06.002>
- Higuera, P., Lara, J. L., & Losada, I. J. (2014a). Three-dimensional interaction of waves and porous coastal structures using OpenFOAM ® . Part I : Formulation and validation. *Coastal Engineering*, 83, 243–258. <https://doi.org/10.1016/j.coastaleng.2013.08.010>
- Higuera, P., Lara, J. L., & Losada, I. J. (2014b). Three-dimensional interaction of waves and porous coastal structures using OpenFOAM ® . Part II : Application. *Coastal Engineering*, 83, 259–270. <https://doi.org/10.1016/j.coastaleng.2013.09.002>

Horrillo, J., Kowalik, Z., & Shigihara, Y. (2006). Wave Dispersion Study in the Indian Ocean- Tsunami of December 26 , 2004. *Marine Geodesy*, 29(3), 149–166. <https://doi.org/10.1080/01490410600939140>

Hsiao, S-C., Lin, T.-C. (2010). Tsunami-like solitary waves impinging and overtopping an impermeable sealwall: Experiment and RANS modeling. *Coastal Engineering*, 57(1), 1–18.

Hughes, S. A. (1993). *Physical models and laboratory techniques in coastal engineering*. Singapore: World Scientific.

Imamura, F. (1989). *Tsunami numerical simulation with the staggered leap-frog scheme (Numerical code of TUNAMI-N1)*.

Imamura, F., Yalçiner, A. C., & Özyurt, G. (2006). *TUNAMI N2 tsunami modeling manual*.

Isobe, M., Yu, X., Umemura, K., & Takahashi, S. (1999). Study on development of numerical wave flume. In *Proceedings of Coastal Engineering* (p. 36–40 (in Japanese)).

Jesus, M. del, Lara, J. L., & Losada, I. J. (2012). Numerical Modeling of Tsunami Waves Interaction with Porous and Impermeable Vertical Barriers. *Journal of Applied Mathematics*, 2012, 27. <https://doi.org/10.1155/2012/263839>

Kanoğlu, U. and Synolakis, C. E. (1998). Long wave runup on piecewise linear topographies. *Journal of Fluid Mechanics*, 374, 1–28.

Kanoğlu, U. (1998). *The runup of long waves around piecewise linear bathymetries*. University of Southern California, Los Angeles, California, 900809-2531.

Kawasaki, Y., Nakao, H., & Izuno, K. (2015). Multiphase flow analysis of tsunami forces associated pressures on a rectangular-section bridge girder. *Journal of Japan Society of Civil Engineers, Ser. A1 (Structural Engineering & Earthquake Engineering (SE/EE))*, 71(2), 199–207.

- Larsen, E. B., Fuhrman, D. R., Baykal, C., & Sumer, B. M. (2017). Tsunami-induced scour around monopile foundations. *Coastal Engineering*, 129(January), 36–49. <https://doi.org/10.1016/j.coastaleng.2017.08.002>
- Leschka, S., & Oumeraci, H. (2011). 3D numerical simulations of the effect of large roughness elements on the propagation of solitary waves. In *6th Annual International Workshop & Expo on Sumatra Tsunami Disaster & Recovery 2011 in Conjunction with 4th South China Sea Tsunami Workshop*.
- Leschka, S., Oumeraci, H., & Larsen, O. (2014). Hydrodynamic forces on a group of three emerged cylinders by solitary wave and bores: Effect of cylinder arrangements and distances. *Journal of Earthquake and Tsunami*, 8(3), 144005 (36 pages).
- Liu, P., Cho, Y., Briggs, M. J., Kânoglu, U. & Synolakis, C. E. (1995). Runup of solitary waves on a circular island. *Journal of Fluid Mechanics*, 302, 259–285. <https://doi.org/doi:10.1017/S0022112095004095>
- Liu, P. L.-F., Wu, T. R., Raichlen, F., Synolakis, C. E. and Borrero, J. (2005). Runup and rundown generated by three-dimensional sliding masses. *Journal of Fluid Mechanics*, 536, 107–144.
- Madsen, P. A., Fuhrman, D. R., & Schäffer, H. A. (2008). On the solitary wave paradigm for tsunamis. *Journal of Geophysical Research: Oceans*, 113(12). <https://doi.org/10.1029/2008JC004932>
- Menter, F. (1994). Two-equation eddy viscosity turbulence models for engineering applications. *AIAA J.*, 32, 1598–1605.
- Nistor, I., Palermo, D., Cornett, A., & Al-Faesly, T. (2010). Experimental and Numerical Modeling of Tsunami Loading on Structures. In ASCE (Ed.), *International Conference of Coastal Engineering, ICCE 2010 Proceeding*. Shanghai, China. <https://doi.org/http://dx.doi.org/10.9753/icce.v32.currents.2>

- Nistor, I., Palermo, D., Nouri, Y., Murty, T., & Saatcioglu, M. (2009). Tsunami-induced forces on structures. In *Handbook of Coastal and Ocean Engineering*. <https://doi.org/10.1142/9789812819307>
- Ozer, C., & Yalciner, A. C. (2011). Sensitivity study of hydrodynamics parameters during numerical simulations of tsunami inundation. *Pure and Applied Geophysics*, 168(11), 2083–2095.
- Pringle, W. J., Yoneyama, N., & Mori, N. (2016). Two-way coupled long wave-RANS model: Solitary wave transformation and breaking on a plane beach. *Coastal Engineering*, 114, 99–118.
- Rahman, M. M., & Nakaza, E. (2016). Experimental and Numerical Simulation of Tsunami Bore Impact on a Building. In *International Journal of Civil Engineering and Technology (IJCIET)* (Vol. 7, pp. 13–23). Retrieved from <http://www.iaeme.com/IJCIET/index.asp%5Cnhttp://www.iaeme.com/IJCIET/issues.asp%5Cnwww.jifactor.com%5Cnhttp://www.iaeme.com/IJCIET/issues.asp?JType=IJCIET&VType=7&IType=4>
- Ramsden, J. D. (1993). Tsunamis: Forces on a vertical wall caused by long waves, bores, and surges on a dry bed. *Ph.D. Thesis, California Institute of Technology*.
- Robertson, I. N., Riggs, H. R., & Mohamed, A. (2008). Experimental Results of Tsunami Bore Forces on Structures. *Proceedings of the ASTM 2011 30th Internal Conference on Ocean, Offshore and Arctic Engineering*, (October 2014), 1–9. <https://doi.org/10.1115/OMAE2008-57525>
- Rodi, W. (2017). Turbulence Modeling and Simulation in Hydraulics: A Historical Review. *Journal of Hydraulic Engineering*, 143(5), 1–20. [https://doi.org/10.1061/\(ASCE\)HY.1943-7900.0001288](https://doi.org/10.1061/(ASCE)HY.1943-7900.0001288).
- Sakakiyama, T. (2013). Flow Fields of Tsunamis Passing on Rubble Mound Breakwater. In *Proceedings of the Twewnty-third (2013) International Offshore and Polar Engineering* (Vol. 9, pp. 111–118). Anchorage, Alaska, USA.

Sarjamee, S. (2016). *Numerical Modelling of Extreme Hydrodynamic Loading on Coastal Structures*. University of Ottawa.

Sassa, S., Takahashi, H., Morikawa, Y., & Takano, D. (2016). Effect of overflow and seepage coupling on tsunami-induced instability of caisson breakwaters. *Coastal Engineering*, 117, 157–165. <https://doi.org/10.1016/j.coastaleng.2016.08.004>

Shuto, N., Goto, C., & Imamura, F. (1990). Numerical simulation as a means of warning for near field tsunamis. *Coastal Engineering in Japan*, 33(2), 173–193.

Sozdinler, C. O., Yalciner, A. C., & Zaytsev, A. (2014). Investigation of tsunami hydrodynamics parameters in inundation zones with different structural layouts. *Pure and Applied Geophysics*, 3(4), 931–952.

Sozdinler, C. O., Yalciner, A. C., Zaytsev, A., Suppasri, A., & Imamura, F. (2015). Investigation of hydrodynamic parameters and the effects of breakwater during the 2011 Great East Japan Tsunami in Kamaishi Bay. *Pure and Applied Geophysics*, 172(12). <https://doi.org/DOI: 10.1007/s00024-015-1051-8>

St-Germain, P., Nistor, I., & Townsend, R. (2012). Numerical Modeling of Tsunami-Induced Hydrodynamic Forces on Onshore Structures Using Sph. In *Coastal Engineering Proceedings* (pp. 1–15). <https://doi.org/10.9753/icce.v33.structures.81>

Suppasri, A., Latcharote, P., Bricker, J. D., Leelawat, N., Hayashi, A., Yamashita, K., ... Imamura, F. (2016). Improvement of Tsunami Countermeasures Based on Lessons from The 2011 Great East Japan Earthquake and Tsunami — Situation After Five Years. *Coastal Engineering Journal*, 58(04), 1640011. <https://doi.org/10.1142/S0578563416400118>

Synolakis, C. E. (1987). The runup of solitary waves. *Journal of Fluid Mechanics*, 185(May), 523–545. <https://doi.org/10.1017/S002211208700329X>

Synolakis, C. E., Bernard, E. N., Titov, V. V., Kânoğlu, U., & González, F. I. (2008).

Validation and verification of tsunami numerical models. *Pure and Applied Geophysics*, 165(11–12), 2197–2228. <https://doi.org/10.1007/s00024-004-0427-y>

Takahashi, H., Sassa, S., Morikawa, Y., Takano, D., & Maruyama, K. (2014). Stability of caisson-type breakwater foundation under tsunami-induced seepage. *Soils and Foundations*, 54(4), 789–805. <https://doi.org/10.1016/j.sandf.2014.07.002>

Takahashi, T. (1996). Benchmark problem 4; The 1993 Okushiri tsunami-Data, conditions and phenomena. In *In Long-Wave Runup Models* (pp. 384–403). World Scientific.

van Gent, M. R. A. (1995). *Wave interaction with permeable coastal structures*. Ph.D. Thesis, Delft University.

Velioglu, D. (2017). *Advanced two-and three-dimensional tsunami models: Benchmarking and validation*. Middle East Technical University.

Wang, D., Shaowu, L., Arikawa, T., & Gen, H. (2016). ISPH simulation of scour behind seawall due to continuous tsunami overflow. *Coastal Engineering Journal*, 58(3).

Wilcox, D. C. (1993). *Turbulence modeling for CFD*. DCW Industries, La Canada, CA.

Williams, I. A., & Fuhrman, D. R. (2016). Numerical simulation of tsunami-scale wave boundary layers. *Coastal Engineering*, 110, 17–31. <https://doi.org/10.1016/j.coastaleng.2015.12.002>

Xiao, H., & Huang, W. (2008). Numerical modeling of wave runup and forces on an idealized beachfront house. *Ocean Engineering*, 35, 106–116. <https://doi.org/10.1016/j.oceaneng.2007.07.009>

Xu, G., Cai, C., & Deng, L. (2017). Numerical prediction of solitary wave forces on a typical coastal bridge deck with girders. *Structure and Infrastructure*

Engineering, 13(2), 254–272. <https://doi.org/10.1080/15732479.2016.1158195>

Xu, G., & Cai, C. S. (2015). Numerical simulations of lateral restraining stiffness effect on bridge deck-wave interaction under solitary waves. *Engineering Structures*, 101, 337–351.

Yalciner, A. C., Pelinovsky, E., Zaytsev, A., Chernov, A., Kurkin, A., Ozer, C., & Karakus, H. (2006). *NAMI DANCE Manual*. Ankara, Turkey: METU, Civil Engineering Department, Ocean Engineering Research Center. Retrieved from <http://namidance.ce.metu.edu.tr>

Yalciner, A. C., Synolakis, C. E., Gonzales, M., & Kanoglu, U. (2007). *Joint Workshp on Improvements of Tsunami Models, Inundation Map and Test Sites of EU TRANSFER Project, June 11-14*. Fethiye, Turkey.